UNIVERSITAT DE BARCELONA

Pore pressure build-up in mixed contourite-turbidite systems: the SW Iberian margin

Davide Mencaroni

Pore pressure build-up in mixed contourite-turbidite systems: the SW Iberian margin

Memòria de tesi doctoral presentada per:

Davide Mencaroni

Per optar al Grau de Doctor per la Universitat de Barcelona

Aquesta memòria s'ha dut a terme dins el Programa de Doctorat de Ciències de la Terra de la Universitat de Barcelona sota la direcció de:

Dr. Roger Urgeles Esclasans i Dr. Jaume Llopart Serra

I la tutela de:

Dra. Marta Guinau Selles

Barcelona, Novembre de 2021

A mamma e babbo

Acknowledgements

This thesis represents the end of an intense 4-year-long journey that started during a sunny day of July in Bremen and finishes with the notions, calculations and concepts contained in the next pages. However, not all the results from my PhD are contained in this book. The more important and meaningful are not an object of interest for this thesis and have to do with a personal growth resulting from many moments of excitements and discomforts, good and bad days, adventures, late nights, friendships, loneliness and love that enriched me as a man. Many people contributed to make this a wonderful journey and deserve to be acknowledged.

Firstly, thanks to the supervisor of this thesis Roger Urgeles for letting me embark in this ambitious project, for his feedbacks and for sharing his scientific knowledge.

This thesis would probably not have come to an end without the invaluable contribution of the co-supervisor Jaume Llopart. The help, support, guidance and mentoring that I received in the office, in the lab or in front of a beer went way beyond his duties and exceeded what I could possibly hope from a supervisor. I will not forget it.

I am very grateful to Morelia Urlaub and Angelo Camerlenghi for hosting me at GEOMAR and OGS, for their valuable time and support and for teaching me to look at things from a different perspective.

I had the great pleasure and honor to get through these PhD years together with my dear colleague Cristina. Your positive attitude, empathy and friendship have been so precious for me during this journey, making me feel your support during the most challenging periods and your genuine joy when there was something to celebrate. A special hug goes also to Claudia, Slaven and Will, for creating a fun and stimulating environment in the office that made me feel home from the first day. Thanks to all the other amazing people I had the pleasure to meet at the Institut de Ciències del Mar (ICM), and especially to all the master students, PhDs and post-docs from the BCSI group I had the pleasure to meet and share time with.

Thanks to the great group of brilliant PhD colleagues and new friends from the SLATE project. It was always very inspiring and fun to meet up.

Finally, thanks to Marta for all the love and understanding during these years, especially during these last, tough months. Thanks for bringing me back to earth and for never making me forget to live.

Thank you.

Funding

This research received funding by the European Union's Horizon 2020 research and innovating program under the Marie Sklodowska-Curie grant via project ITN-SLATE (grant agreement No 721403). The Spanish "Ministerio de Ciencia e Innovación" and the European Regional Development Fund are also acknowledged for funding through grant CTM2015-70155-R (project INSIGHT). This work was carried out within the Laboratory of Seafloor and Subseafloor Geological Processes (LS3GP) group based at the Dept. of Marine Geoscience of the Institute of Marine Science of Barcelona (ICM – CSIC).

Table of contents

Summary

Contourite drifts are the depositional expression of bottom currents, which are capable of shaping the morphology of the seafloor by transporting, eroding and reworking marine sediments, and are distributed on continental slopes worldwide. Synchronous interaction between bottom currents and turbidity currents have been reported often in channel-levée systems where the thickness of the turbidity current exceeds that of the levées. Such interplay between along-slope and down-slope sedimentary process is one of the mechanisms by which "mixed turbidite-contourite systems" can originate. Being composed by the winnowed finest part of turbidity currents and potentially able to deposit at sedimentation rates of several m/kyr, mixed systems constitute a potential source of overpressure development in marine sediments.

The Alentejo basin is located in the northern edge of the Gulf of Cadiz (SW Iberian margin), from which is separated by the São Vicente Canyon, one of the most prominent geomorphological features in SW Iberia. The area is characterized by an extensive contourite depositional system, generated by the Mediterranean Outflow Water (MOW) bottom current. The Alentejo basin hosts multiple mass transport deposits (MTDs) and scars, which are typically considered to be triggered by the frequent seismic activity related to the movement of multiple active faults present in the area. The combined presence of a contourite depositional system, a deeply incised canyon, mass wasting processes and potentially seismogenic faults makes the Alentejo basin the ideal study area to assess: a) how does contour currents interact with sediments transported along deeply incised canyons? b) How does mixed contourite – turbidite systems affect the development of overpressure within marine sediments, and consequently the stability of submarine slopes?

To answer these questions, in this thesis we first adopted a workflow that included reinterpretation of existing seismic data in the Alentejo basin as well as acquisition and interpretation of geophysical and sediment core data collected during two scientific cruises in 2018 (INSIGHT-Leg1) and 2019 (INSIGHT-Leg2). The study focuses in the area between ~ 1000 and 3000 m water depth around the São Vicente Canyon. Grain size and physical properties (i.e. water content, Atterberg limits, porosity, permeability and compression index) of sediments collected in the study area have been analysed through geotechnical laboratory experiments. The updated stratigraphic model and sediment physical properties have been integrated into Finite Element numerical models in order to derive the fluid flow and overpressure evolution of the Alentejo basin, focusing on the potential influence of mixed-system deposition in the emplacement of the MTDs detected in the basin and in the overall stability of the slopes.

This thesis identifies a previously unknown mixed contour current – turbidity current deposit, the Marquês de Pombal Drift, located on the NW flank of the São Vicente Canyon and generated by the interaction between the MOW, particularly during cold periods, and turbidity currents flowing along the canyon itself. Because the canyon is incised significantly deeper (~ 1.5 km) than the thickness of turbidity currents, interaction between down-slope and along-slope currents requires intermediate nepheloid layers, forming at the boundary between major water masses (i.e., the MOW and the North Atlantic Deep Water), to export the finer-grained fraction of turbidity currents out of the canyon. Such mechanism is likely active in other canyons worldwide. Stratigraphic interpretation and gravity core analysis reveal that the Marquês de Pombal Drift is characterized by sedimentation rates up to 2 m/kyr and fine-grained sediments (mean grain size of 8.6 μm). Despite those characteristics, the hydrogeological models presented in this thesis show development of overpressure associated with the Marquês de Pombal Drift deposition up to a maximum of 20% of the lithostatic load.

Factor of safety (FoS) analysis indicates that overpressure development decreases the stability of the slopes in the study area by 18% under static conditions, and that slope gradients play a more important role as pre-conditioning factor for slope failures as the highest overpressures are recorded in relatively flat terrains. The pseudo-static slope stability analysis, on the other hand, indicates that earthquake-induced accelerations given the fault characteristics in the area (i.e. earthquake shaking) have a much stronger influence on slope stability in the Alentejo basin. Therefore, trigger mechanisms seems to be the predominant component in slope stability compared to pre-conditioning factors (i.e., overpressure development, slope gradients).

The results indicate that the Marquês de Pombal Drift is a relatively stable feature and its deposition has a minor influence in the stability of the Alentejo basin. However, in other settings, fine-grained sediments and potential high sedimentation rates associated with mixed contour current – turbidity current systems could have the potential to develop higher overpressure and thus play a more important role in submarine slope stability. Our results show that multiple conditions related with the physical properties of sediments (i.e. high degree of compressibility and low permeability), high sedimentation rate and the morphology of the slope (i.e. slope gradients) must all be present to efficiently influence slope instability.

Structure and organization of this thesis

Part I: Introduction	**Chapter 1:**	Introduction
	Chapter 2:	Geological and oceanographic settings
Part II: Methodology	**Chapter 3:**	Data and methods
Part III: Results	**Chapter 4:**	Characterization of the Marquês de Pombal Plateau area: stratigraphy and sediments distribution
	Chapter 5:	Influence of measured physical properties in finite-element overpressure models
	Chapter 6:	Modelling overpressure in the Marquês de Pombal Plateau area
Part IV: Discussion	**Chapter 7:**	A mixed turbidite – contourite system related to a major submarine canyon: The Marquês de Pombal Drift
	Chapter 8:	Factors influencing overpressure development in the Alentejo basin
	Chapter 9:	Slope instability in mixed contour current – turbidity current systems: balance between pre-conditioning factors and trigger mechanisms
Part V: Conclusions and forward look	**Chapter 10:**	Conclusions
	Chapter 11:	Forward look
References		

PART I

INTRODUCTION

Chapter 1: Introduction

Excess pore pressure controls a variety of shallow earth processes, ranging from fault localization and mediation of earthquake slip through its control on effective normal stress (Saffer and Tobin, 2011), propagation of rupture and migration of microseismicity (Johnson and Mcevilly, 1995; Screaton, 2010), fault slip behaviour along subduction thrusts (Obana and Kodaira, 2009), the biogeochemical cycles related with fluids, heat and hydrocarbon fluid migration (Neuzil, 1995). Interest in studying overpressure development in marine sediments started for oil and gas exploration purposes, as it plays a fundamental role in fluid flow focalization, controlling the distribution of hydrocarbons and heat (Dugan and Sheahan, 2012; Grauls and Baleix, 1994; Micallef et al., 2009). An accurate assessment of overpressure conditions of a oil and gas production well is also paramount for safety reasons, as it can cause major borehole stability issues during the drilling and in the long term (Hickman et al., 2010). Finally, overpressure development in marine sediments is a major pre-conditioning factor that favours slope instability by decreasing the amount of gravitational driving stresses required to mobilize sediments (Dugan and Sheahan, 2012). If the pressure of the water contained in the pore space exceeds the hydrostatic condition (Figure 1.1), failures can be initiated in low angle submarine slopes by a relatively minor trigger such as small magnitude earthquakes (Urlaub et al., 2015).

Downslope displacement of marine sediments, or submarine landslides, are one of the main threats for offshore infrastructures (Clare et al., 2017). They can damage oil and gas recovery platforms and pipelines (Barley, 1999), posing potentially devastating environmental and economic risks. Turbidity currents generated from disintegration and dilution of subaqueous landslides have also been responsible for the breaking of telecommunication cables offshore Algeria (Cattaneo et al., 2012), Taiwan (Carter et al., 2014, 2012) and in occasion of the notorious "Grand Banks" earthquake in 1929 (Piper et al., 1999). In the last cited example, turbidity currents affected an area that ranges from 650 to 2800 m water depth, breaking submarine telegraph cables and depositing to a distance greater than 850 km from the scar (Piper et al., 1999; Piper and Aksu, 1987). The event had great impact on deep sea sedimentology research, increasing the understanding of the now well-known concept of turbidity currents (Paull et al., 2018; Talling et al., 2013). Submarine landslides are also a risk for the safety of increasingly growing coastline populations, being able to generate devastating tsunamis. Amongst many others, the most recent example of the consequences that submarine landslides can have on people safety is the tsunami event that took place on September 28th 2018 on Sulawesi Island, Indonesia. The Mw 7.5 earthquake caused a submarine landslide that generated a tsunami causing more than 4000 fatalities, especially in the city of Palu (Heidarzadeh et al., 2019; Takagi et al., 2019).

Slope failures generate from the interaction between pre-conditioning factors and triggering mechanisms. Pre-conditioning factors are long-term processes, inherited by the slope and related with steady conditions such as the tectonic history, sediment properties and fluid flow regime (Hampton et al., 1996). Pre-conditioning factors also include properties acquired during the depositional processes, like aspects of the gross structure and stratigraphy of the sediments (e.g., presence or absence of surfaces that could potentially evolve in failure planes), water content, pore pressure related to deposition (Canals et al., 2004; Masson et al., 2010). Excess pore pressure, defined as the fluid pressure in excess of hydrostatic equilibrium (Revil et al., 1998) (Figure 1.1), decreases the effective stresses, therefore the frictional strength of submarine slopes. The low strength allows failure to be initiated in low angle submarine slopes by a relatively minor trigger like small magnitude earthquakes (Urlaub et al., 2015).

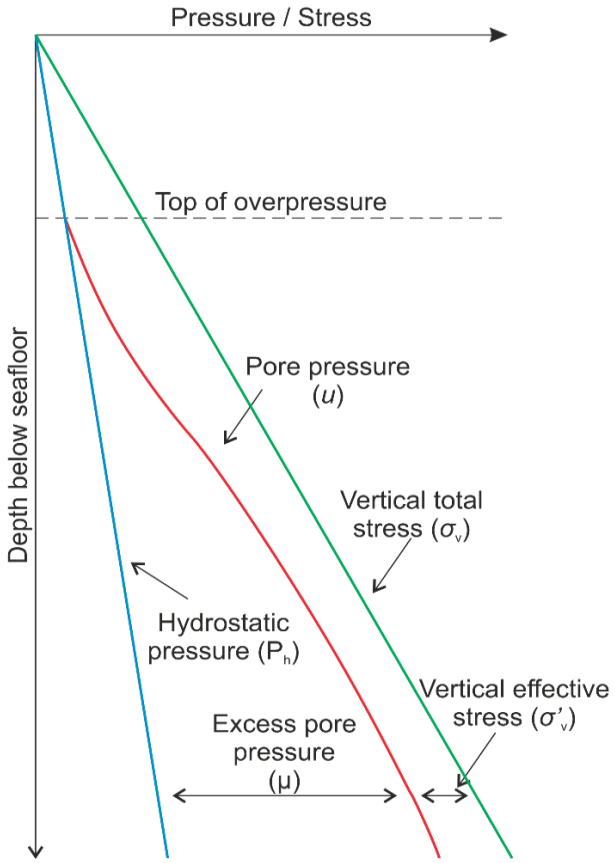

Figure 1.1: Schematic representation of overpressure related to hydrostatic pressure, pore pressure, vertical total stress and vertical effective stress. Modified after Bruce and Bowers (2002).

On the other hand, triggering mechanisms are related to external, relatively short-duration stimulus (Badhani, 2020; Masson et al., 2010; Sultan et al., 2004a; Urgeles et al., 2006). According to Locat & Lee (2002), the most common trigger mechanisms include (1) oversteepening, (2) seismic loading, (3) storm-wave loading, (4) rapid accumulation of sediments, (5) gas charging, (6) gas hydrate dissociation, (7) low tides, (8) seepage, (9) glacial

loading, and (10) volcanic island growth. These events influence slope stability in two ways: by decreasing the shear strength of a slope and/or by inducing additional shear stress (Figure 1.2).

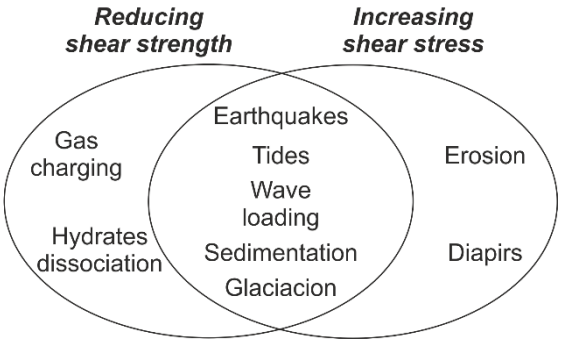

Figure 1.2: Causes of submarine landslides (Locat and Lee, 2002)

The nature/characteristics of pre-conditioning factors might be such that even relatively low magnitude triggering events are sufficient for the onset of a submarine landslide. While erosion and oversteepening (the latter typically related with salt or mud diapir growth) are directly related with an increase in shear stress (Figure 1.2), most of the triggering mechanism act on submarine slopes by both reducing the shear strength of sediments and increasing the shear stress. Earthquake shaking is often considered as the main triggering factor for most submarine landslides (Masson et al., 2010, 2006), as it produces a sudden increase in shear stress over submarine slopes while, at the same time, it is capable of generating a reduction of shear strength by increasing the pore pressure in the sediments. Nevertheless, it is also known that active margins, where the largest and more frequent earthquakes occur, experience a paucity of large submarine landslides (Urgeles and Camerlenghi, 2013) which has been explained by seismic strengthening of marine sediment. Repeated exposure to earthquake energy over time, in fact, gradually increases shear strength by shear-induced compaction (Locat et al., 2002; Sawyer and Devore, 2015).

1.1 Hypothesis

The study presented in this thesis is focused mainly in the Alentejo basin, in the SW Iberian margin. The area, as well as the entire Gulf of Cadiz, is characterized by an extensive contourite depositional system generated by the Mediterranean Outflow Water (MOW), a bottom current that exits the Strait of Gibraltar flowing northward and circulates especially along the middle slope (Rodrigues et al., 2020). The sediment transition from the shallower part of the basin to deeper water setting, extensively studied in the southern and central part of the Gulf of Cadiz (Brackenridge et al., 2013; Llave et al., 2011; Mestdagh et al., 2019; Mulder et al., 2003; Stow et al., 2013b) remains, however, somehow poorly understood in the Alentejo basin area. In this regard, most of the studies in the area focus on the downslope movement that transfers sediments from the shallower part of the slope towards the abyssal plains, as testified by multiple mass transport deposits and scars present in the deeper parts of the Alentejo basin (Collico et al., 2020;

Ford et al., 2021; Teixeira et al., 2019). Due to the recurrent seismic activity in the area, earthquakes are considered the most obvious trigger mechanism for submarine landslides (Collico et al., 2020; Garcia-Orellana et al., 2006; Lo Iacono et al., 2012; Teixeira et al., 2019; Urgeles and Camerlenghi, 2013). However, it is also well-known that, in contour current dominated environments, fine-grained sediments can accumulate at relatively high rates (Rebesco et al., 2014). Given the high compressibility and generally low permeability associated with fine-grained deposits there is also a potential in the Alentejo basin for development of overpressure. **The main hypothesis of this thesis is that the development of contourite system, further influenced by downslope sediment transport along the São Vicente Canyon, might have promoted the generation of overpressure in the Alentejo basin, facilitating the occurrence of submarine landslides in the area.**

The oceanographic and geological setting of the Alentejo basin represent a natural laboratory to understand the interactions between bottom currents, promoting contourite development, canyon erosion and associated turbidity currents, submarine landslides and earthquake activity. Occurrence of turbidity flows related with erosion along the São Vicente Canyon had (or still has) the potential to interact with the MOW circulation, which has originated a mixed contourite-turbidite depositional system: the Marquês de Pombal Drift.

1.2 Objectives and scientific goals

This thesis aims to contribute towards a better understanding of how the coupling of geological processes and sediment properties related with mixed contour current – turbidity current systems can affect the development of overpressure in marine sediments and the stability of submarine slope. The hypothesis mentioned in the previous section (1.1) have been tackled by pursuing four main objectives:

1. ***Identify the mechanisms of interaction between bottom current and sediment travelling within deeply incised submarine canyons.***

We reviewed the stratigraphic distribution in the Alentejo basin by making use of data collected by the International Ocean Discovery Program (IODP) at Site U1391, together with published as well as newly acquired multi-channel seismic profiles, focusing especially in the areas closer to the canyon in order to answer the questions:.

   a. *What type of interaction takes place between the Mediterranean Outflow Water (MOW) and the deeply incised São Vicente Canyon?*
   b. *How does contourite deposition and São Vicente Canyon erosion influence the sedimentation in deeper areas of the Alentejo basin, such as the Marquês de Pombal Plateau?*

2. ***Understand how do sediment physical properties and sedimentation rates of mixed contour current – turbidity current systems affect the development of pore pressure.***

This objective has been tackled by performing laboratory analysis to derive physical properties of the sediments collected in the study area. The results from the laboratory tests have been integrated with the stratigraphic interpretation of the area into finite-element numerical models in order to answer the questions:

   a. *How does fine-grained sediments and sediment accumulation rates influence the development of overpressure in the Marquês de Pombal Plateau?*
   b. *How does lateral fluid flow towards the São Vicente Canyon and the Marquês de Pombal Fault contribute to overpressure buildup/dissipation?*

3. ***Evaluate the suitability of hydrogeological models based on literature-derived physical properties of sediments collected from similar depositional environments and with comparable grain size distributions.***

We made use of finite-element numerical models to quantify the differences in computed overpressure generated by fine-grained hemipelagic sediments from three different offshore locations and geological settings (SW Iberia, Lesser Antilles and Gulf of Mexico). The question that we aimed to answer was:

   a. *How does the definition of hydrogeological model with physical properties parameters (porosity, permeability and compressibility) measured from sediments collected in the study area affect the reliability of resulting overpressure?*

4. ***Assess the significance of pre-conditioning factors versus trigger mechanisms in a seismically active area.***

The overpressure modelling results from objective n.2 have been spatially propagated through the study area in order to visualize the locations most impacted by development of overpressure as a result of the mixed contour current – turbidity current deposition. Static and pseudo-static factor of safety (FoS) analyses have been performed in order to answer the questions:

   a. *What is the contribution of pore pressure development generated by the mixed contour current – turbidity current on the overall stability in the Alentejo basin?*
   b. *What is the influence of pre-conditioning factors (i.e. overpressure development, slope gradient) compared with triggering mechanisms (i.e. earthquake shaking) in decreasing the slope stability in the area?*

1.3 Pore pressure development

Pore pressure development is effectively described by Terzaghi's principle of effective stress (Terzaghi, 1926) (eq. 1):

$$|\sigma'| = |\sigma_i| - |u| \quad (1)$$

where σ'_i is the effective stress, σ_i is the total stress and u is the pore pressure. $|\sigma_i|$ reflects the maximum, intermediate and minimum stress components (σ_1, σ_2 and σ_3), and it is common to assume that, in passive margins and for shallow sediments, σ_1 is associated with the total vertical stress (σ_v), allowing to define the maximum principal effective stress as (eq. 2):

$$\sigma'_1 = \sigma'_v = \sigma_v - u \quad (2)$$

The total vertical stress, commonly associated with lithostatic stress, is defined as the depth-integrated bulk density times gravity. The total pore pressure is controlled by the hydrostatic pressure, which is the depth-integrated bulk density times gravity and overpressure. The maximum principal effective stress equation (eq. 1) can be then expanded as follow (Revil et al., 1998) (eq. 3):

$$\sigma'_1 = \sigma'_v = \sigma_v - u = \int (\rho_b - \rho_f)\, g dz - \lambda \quad (3)$$

where ρ_b is the bulk density, ρ_f is the fluid density, g is the gravity, z is the depth of interest and λ is the overpressure. The bulk density (ρ_b) primarily depends on the density of the grains and on the porosity of the sediments. Most of the overpressure models relate porosity to vertical effective stress (Dugan and Flemings, 2000; Hart et al., 1995; Llopart et al., 2019; Mencaroni et al., 2020; Urgeles et al., 2010; Urlaub et al., 2015), since the horizontal stresses (σ_2 and σ_3) are often assumed to be equal. This approximation is appropriate near the seafloor and far from faults, since in presence of relevant horizontal stresses σ_2 can exceed σ_3 and the relative orientation of the stresses may cause changes in λ (Osborne and Swarbrick, 1997; Revil et al., 1998).

1.4 Mechanisms driving overpressure

1.4.1 Rapid sedimentation (1-D consolidation)

Since vertical loading of sediments increases during burial, sediments tend to compact, reducing the pore volume and forcing out the fluids contained in the pore space (Osborne and Swarbrick, 1997). When the sediment deposition rate exceeds the sediment consolidation rate, fluids cannot be expelled fast enough and pore pressure builds up above the hydrostatic equilibrium, generating overpressure (Gibson, 1958). This process is known as disequilibrium compaction (or underconsolidation), and it is commonly found in thick low-permeability successions (e.g. clay, mud, marl, shale) during continuous rapid burial (Osborne and Swarbrick, 1997). If the sediment deposition decreases below the consolidation rate, pore water dissipates, following hydraulic

gradients towards areas of lower pressure. In this way, excess pore pressure gradually decreases until it returns to equilibrium values and the sediments return into a normally consolidated state (Osborne and Swarbrick, 1997; Urlaub, 2013) (Figure 1.3).

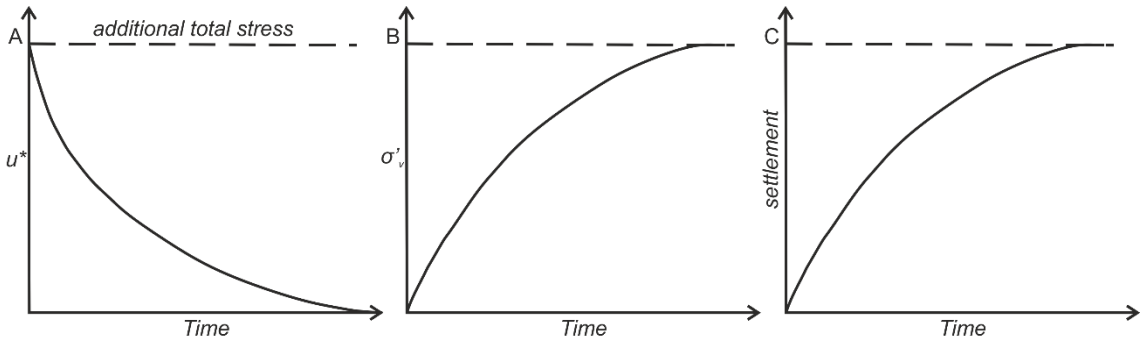

Figure 1.3: Time-dependent response to an increase in total stress. A: excess pore pressure (u^*); B: vertical effective stress (σ'_v); C: settlement. Modified after Urlaub (2013).

The evolution of overpressure within saturated sediments on a basin scale depends on the depositional history of the basin, especially the sedimentation rate, fluid migration patterns and sediments physical properties (Dickinson, 1953; Gibson, 1958; Neuzil, 1995; Revil et al., 1998). In case of rapid sedimentation of low-permeability sediments, the increasing lithostatic stress does not generate a significant loss in porosity (i.e., no significant increase in bulk density), since the low permeability prevents the pore water to escape (Bethke and Corbet, 1988; Bredehoeft and Hanshaw, 1968; Flemings et al., 2008; Reece et al., 2012; Urlaub et al., 2012; Wangen, 1997). This type of dynamics favours the development of overpressure. On the other hand, slow deposition of highly permeable sediments allows pore pressure to dissipate and the sediments to consolidate. The increase of overpressures results in lower effective stress (eq. 1 and 2), leading to a decrease in shear resistance, potentially resulting in sediment failures that can involve faulting, hydraulic fracturing or landslides (Revil et al., 1998). Development of overpressure can also drive fluid flow phenomena such as mud volcanism (Kopf, 2002), seafloor pockmarks (Hustoft et al., 2009), pipe structures (Berndt, 2005), hydrocarbon seepage (Hickman et al., 2010) and solute transport (Spinelli et al., 2006).

If we consider 1D burial systems (i.e. $\sigma_2 = \sigma_3$), the overpressure development due to sedimentation can be described with the consolidation equation (Gibson, 1958; Revil et al., 1998) (eq. 4):

$$\frac{\partial u^*}{\partial t} = c_v \frac{\partial^2 u^*}{\partial z^2} + B\gamma' \frac{\partial h}{\partial t} \tag{4}$$

where γ' is the buoyant unit weight of the sediment being deposited, B is Skepton's pore pressure build-up coefficient ($\partial u^*/\partial \sigma v$), and $\partial h/\partial t$ is the sedimentation rate. In soft and fully saturated sediments it is usually assumed that B = 1, implying that the entire load generated by the sedimentation is initially sustained by the pore fluid. C_V is the coefficient of consolidation, defined as (Revil et al., 1998) (eq. 5):

$$C_V = k/(m_v \gamma_w) \quad (5)$$

where k is the permeability of the sediments, m_v is the coefficient of volume compressibility and γ_w is the unit weight of water.

Eq. 4 and 5 indicate that the rate of overpressure generation is controlled by the pore water flow rate out of the system, determined by the magnitude of C_V, and the stress applied to the system by the sedimentation ($\partial h/\partial t$). Thus, the degree and duration of consolidation is driven by compressibility and permeability of the sediments. Compressibility measures the volume change in relation with the stress applied, and controls the total volume of pore water that is displaced and leave the system (Long et al., 2011), while permeability defines the velocity at which pore water flows out of the system (Reece et al., 2012; Urlaub, 2013). For these reasons, the hydromechanical properties of sediments (compressibility and permeability) are dominant processes for overpressure development, as the more pore water has to be displaced and the further the pore water has to travel at low velocities, the longer sediments take to consolidate (Reece et al., 2012; Urlaub, 2013). Overpressure generated by quick deposition of low-permeability and high compressibility sediments can extend from near the seafloor to depths of many kilometres, and can be sustained for periods of times in the order of magnitude up to 10^6 years (Bredehoeft and Hanshaw, 1968).

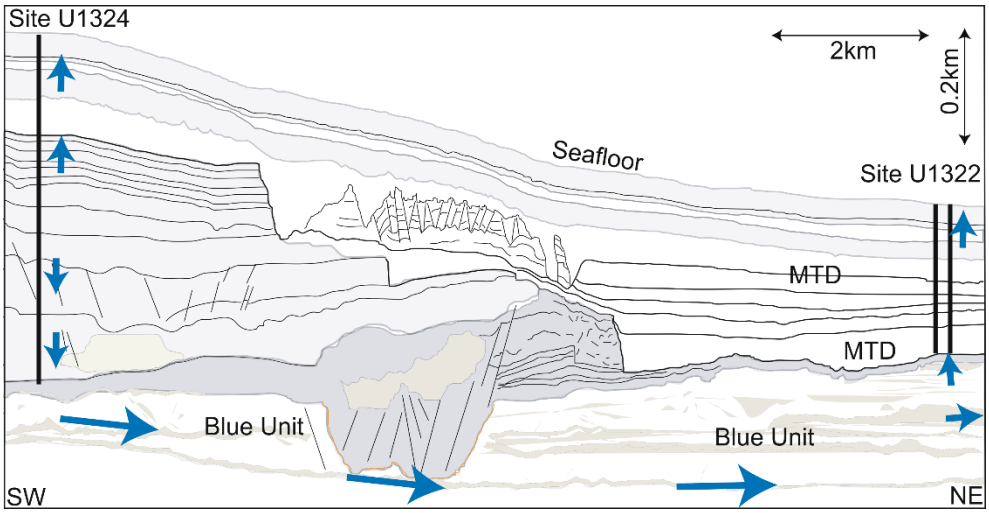

Figure 1.4: Geological interpretation of seismic profile connecting IODP sites U1324 and U1322 in the Ursa basin, Gulf of Mexico, by Flemings et al. (2008). Blue arrow added by Screaton (2010) indicates the interpreted fluid flow system transferring pore pressure from Site U1324 towards U1322, through the channel-levee deposits composing the Blue Unit.

1.4.2 Fluid migration (2D/3D consolidation)

The dissipation of overpressure is strongly dependent by length and continuity of drainage paths, such as laterally and well-connected sand levels, within which the displaced pore water flows under the influence of hydraulic gradients and reaches regions of lower pore pressure (Behrmann et al., 2006; Osborne and Swarbrick, 1997). Fluid focusing, taking place within semi-isolated

higher-permeability pathways, represents a second category of overpressure development mechanism due to consolidation (Figure 1.4) (Revil et al., 1998). Fluid flow though a permeable medium occurs in response to a hydraulic potential field, as described by the Darcy's Law (Freeze, 1979). Thus, the amount of fluid flowing through sediments or rocks depends on their hydraulic conductivity and difference in pore-water pressure between the two end points of the flow path, known as hydraulic head (Berndt, 2005). In continental margins, the hydraulic head is typically generated by compaction, since burial depth increases the density of sediments and decreases their porosity and permeability accordingly. Permeable and continuous layers can, for example, transfer pore pressure generated in deep zones towards upper stratigraphic levels where lithostatic stress is lower or connect areas of higher lithostatic stress to areas where sediment load and/or sedimentation rate is lower (Figure 1.5) (Behrmann et al., 2006). This process equilibrates the fluid pressure within the entire aquifer, potentially resulting in overpressure contained in the permeable layer being higher than in the fine-grained sediments (Figure 1.5, Figure 1.6 and Figure 1.7).

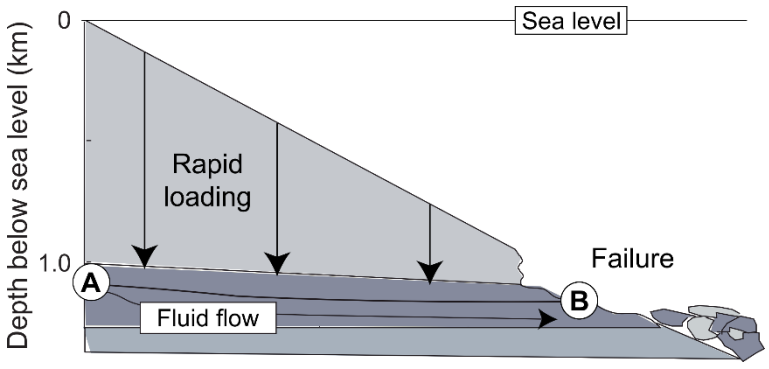

Figure 1.5: Schematic representation of flow-focusing conditions in the Ursa basin. Rapid deposition of low permeability sediments over point A promote fluid flow within deeper sand-dominated Blue Unit, generating overpressure and slope instability in point B. Behrmann et al. (2006).

One of the most iconic example of this phenomena is the Ursa basin, in the northern part of the Gulf of Mexico, an area characterized by gentle continental slope (2º) and large slope failures (Flemings et al., 2006, 2008). Hart et al. (1995) documented overpressure ratios up to almost 90% in the shelf sediments, at depths greater than 2 km. The Integrated Ocean Drilling Program (IODP) Expedition 308 performed *in-situ* pore pressure measurements at two sites (U1324 and U1322) (Figure 1.4) (Flemings et al., 2006, 2008), consolidation experiments (Long et al., 2011, 2008; Reece et al., 2012) and hydrogeological models (Behrmann et al., 2006; Stigall and Dugan, 2010; Urgeles et al., 2010). These studies demonstrated that high overpressure (up to 70% of the lithostatic stress) due to rapid sedimentation of highly compressible sediments developed also at shallow depth, starting in the first 10 m below the seafloor (Dugan and Germaine, 2008; Long et al., 2011), affecting the stability of the slope and promoting submarine landslides (Stigall and Dugan, 2010; Urgeles et al., 2007). However, excess pore pressure at Site U1324 were observed to decrease below 200 m while at Site U1322 pore pressure continued to increase with depth

(Figure 1.4) (Flemings et al., 2008). The IODP expedition results demonstrated lateral transfer of pore pressure from Site U1324 to U1322 through the deeper Blue Unit, composed by interbedded high permeability sand and mud, resulting in pore pressure at Site U1322 much higher than what would be produced by only high rate of sedimentation (Figure 1.4) (Flemings et al., 2008; Stigall and Dugan, 2010). These new evidences provided a fundamental field reference about the importance of low permeability sediments in generating high overpressures (Reece et al., 2012), and also demonstrated how lateral fluid flow can transfer pore pressure to areas displaying relatively low sedimentation rates (Behrmann et al., 2006; Revil et al., 1998). Overpressure generated within highly permeable sand layers in response to loading by low-permeability clays has also been demonstrated offshore New Jersey (Dugan and Flemings, 2000), leading to high overpressures in an area where sedimentation rates are not extremely high (<1 m/kyr). Another example where lateral migration of fluids within a high permeability layer played a fundamental role in generating overpressure is the Storegga Slide region, offshore Norway. The Storegga Slide is one of the largest and best studied submarine landslides in the world (Bryn et al., 2005; Bugge et al., 1987; Haflidason et al., 2004; Kvalstad et al., 2005). The sedimentation in the region is dominated by the interplay between glacial-interglacial depositional cycles and bottom currents that deposit clay-rich contourite sediments (Kvalstad et al., 2005). The rapid sedimentation of glacial sediments over the fine-grained, high-porosity drift deposits is believed to be responsible for excess pore pressure build up that led to the giant slope failure emplaced on a slope that, before the mass wasting event, averaged less than 1º (Kvalstad et al., 2005; Solheim et al., 2005).

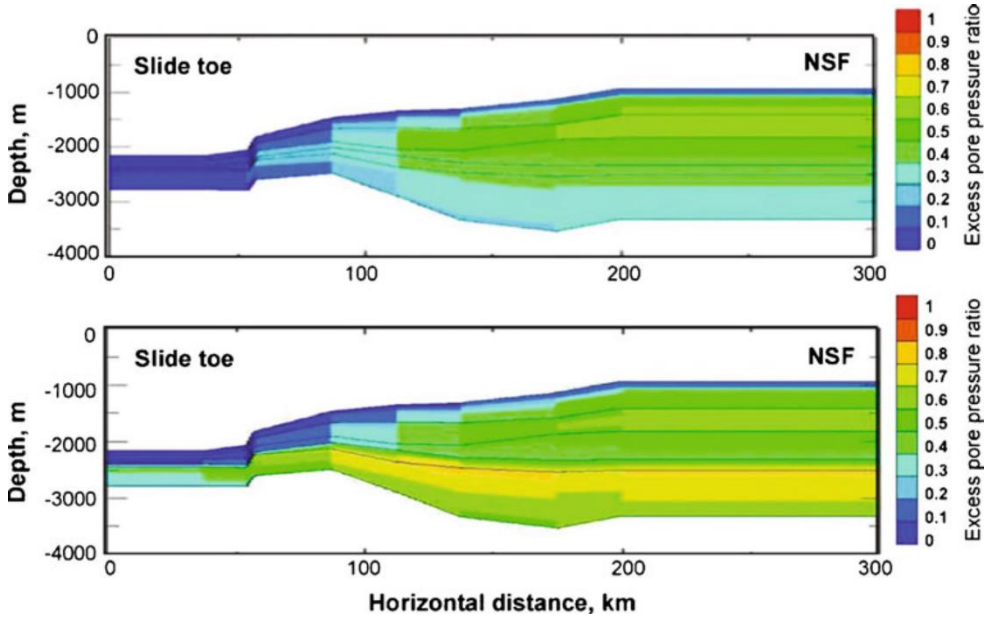

Figure 1.6: Overpressure ratio (λ*) for 2D models of Storegga Slide region from Kvalstad et al. (2005). Lower figure show the impact of a high permeabiility ooze layer buried by low permeability fine sediments in overpressure development compared with homogeneous fine-grained sedimentation with horizontal permeability one order of magnitude higher than vertical permeability (upper figure).

Even though the unloading generated by the Storegga slide event most likely reduced pore pressures in the area to nearly hydrostatic (Hustoft et al., 2009), fluid flow simulations demonstrate that pore pressure can be transmitted laterally from the North Sea Fan through an ooze layer, resulting in significantly higher overpressure conditions (Figure 1.6) (Kvalstad et al., 2005; Screaton, 2010).

According to Masson et al. (2010), lateral transfer of pore pressure through high permeability layers is the main driver for the onset of giant submarine landslides in mid continental slopes. The basic observation behind this statement is that sedimentation rates are usually higher in the upper part of the slopes, creating high pore pressures that could potentially lead to slope failures. This model fits well in submarine deltas environments, such as those created by the Nile and Mississippi rivers, where mass movements detach from the areas of maximum sediment deposition (Loncke et al., 2002; Prior and Coleman, 1982). However, it is now well established that landslide headwalls related with large scale mass wasting events are located mostly in the mid-slope, where sedimentation rates are generally lower compared with submarine deltas (Bugge et al., 1987; Masson et al., 2010; Urgeles and Camerlenghi, 2013). Furthermore, many of those major mass wasting events are affected by retrogressive failures (Badhani et al., 2020; Bugge et al., 1987; Canals et al., 2004; Micallef et al., 2009). In Masson et al. (2010)'s model (Figure 1.7), excess pore pressure generated in the shallower part of the slope is transferred through the continental slope sediment sequence to the lower slope, where landslides initiate.

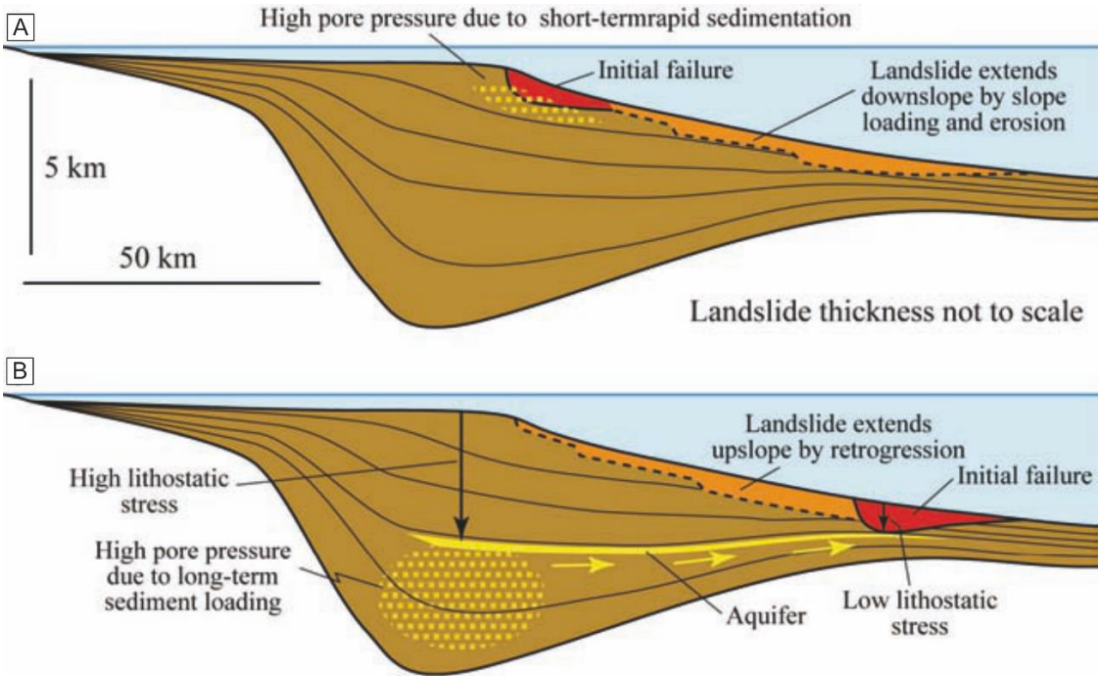

Figure 1.7: Schematic representation of the mechanism of initiation for mid-slope giant landslides proposed by Masson et al. (2010). (A) Landslide initiated in the upper slope due to rapid sedimentation; (B) Landslide initiated in lower slope due to lateral migration of high pore pressure through a permeable aquifer. From Masson et al. (2010).

This can happen in case of: (1) quick deposition of a thick sediment pile takes place in the upper slope (i.e., allowing overpressure generation); (2) presence of a permeable layer bounded by lower permeability units, within which pore fluids are driven to migrate laterally instead of vertically; and (3) good lateral continuity of the aquifer-seals system allows fluid flow for long distances (Figure 1.7).

The emplacement of mass failure in the mid slope is more likely to trigger retrogressive failures because the sediments above loose lateral support (Figure 1.7) (Masson et al., 2010). This is especially the case in presence of sediment layers characterized by specific properties that tend to loose strength and concentrate strain (Badhani et al., 2020; Gatter et al., 2020; Kvalstad et al., 2005; Locat et al., 2014). Such surfaces are most commonly known as weak layers and have been defined by Locat et al. (2014) as "layers consisting of sediment or rock that show lower strength than that of adjacent units to provide a potential focus for the development of a surface of rupture".

1.4.3 Artesian pressures in marine aquifers

A similar process that has the potential to generate overpressure in submarine shelf sediments through the combination of hydraulic head and the presence of a continuous aquifer overlain by a seal is the development of a potentiometric head (Figure 1.8) (Bachu and Underschultz, 1993; Osborne and Swarbrick, 1997). In this case, the hydraulic pressure gradient generates from the elevation of the water table in highland regions, in the same way as for an overpressured aquifer generating artesian wells. In the case of potentiometric head, the amount of overpressure cannot exceed the pressure resulting from the differential elevation in the water table along the aquifer, although this pressure-driven circulation can be enhanced by density-driven circulation if the groundwater passes through evaporite formations (Schultheiss, 1990).

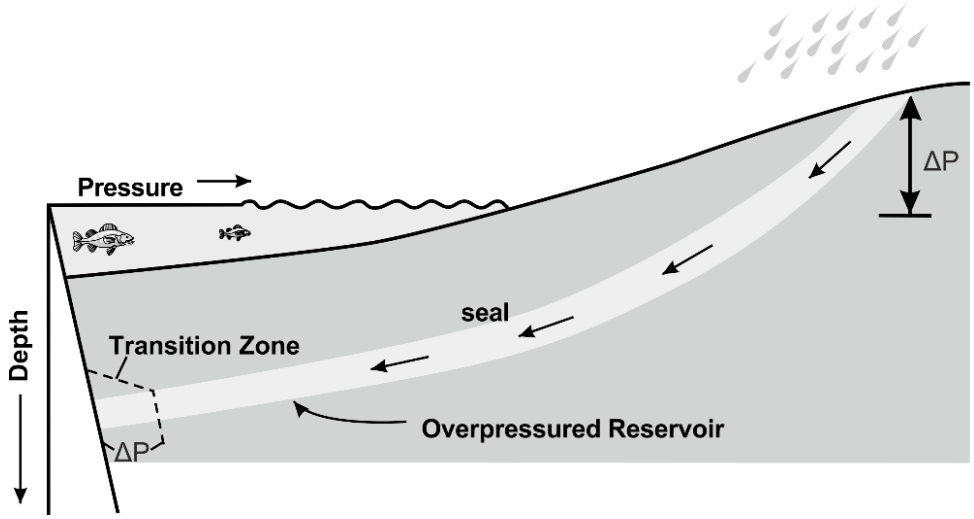

Figure 1.8: Schematic representation of how potentiometric head can generate overpressure in the subsurface. From Osborne and Swarbrick (1997).

1.4.4 Changes in pore fluids volume

Fluid migration can also induce overpressure as a result of fluid expansion, which is a typical feature if hydrocarbons are present in the system. Oil and gas tend to rise to the top of the aquifers due to their lower density compared with water. When reaching shallower stratigraphic levels, hydrocarbons tend to expand under reduced hydrostatic pressure, causing increased fluid pressure also within high porosity and high permeability sediments (Revil et al., 1998). This process does not only drive the hydrocarbon migration, but it also facilitates trapping by generating the so-called capillary seal phenomena, which take place when hydrocarbons fill the pore space in mudrocks. The reduction of hydrostatic pressure, in fact, expands oil and gas contained in the pore space, generating a capillary seal that prevent migration of fluid by generating high capillary entry pressure. In presence of fine-grained sediments, however, overpressure may exceed the capillary entry pressure of the seal resulting in hydrofracturing and loss of sealing capacity. As this failure releases fluids in the system, this process can increase the overpressure within shallow sediments, potentially favouring sediment failures (Dugan and Sheahan, 2012; Revil et al., 1998).

As for the capillary seal formation, other thermal and chemical processes can increase the volume of pore fluids and their pressure until they can generate fractures in the sediments. Despite expansion of pore water due to thermal processes is not considered a relevant cause for overpressure development in shallow sediments, such effect can be more pronounced at burial depths higher than 1 km (Revil et al., 1998). This process, known as aquathermal expansion, takes place in perfectly sealed rock systems. However, it has been measured that fresh water heated from 54.4º to 93.3º between 609.6 and 1524 mbsf (2000 to 5000 ft) increases its volume only by 1.65% (Daines, 1982), thus the effect of aquathermal pressuring alone is unlikely to generate considerable overpressure (Osborne and Swarbrick, 1997; Revil et al., 1998).

Finally, the combination of loose sediments, small amount of gas and low tides has been proved to potentially generate gas expansion that can lead to failures in shallow water environments. Methane gas resulting from decomposition of organic matter is quite common in marine soil and decreases their degree of saturation (Chillarige et al., 1997). Tidal drawdown promotes expansion of those gases increasing the pore pressure and potentially favouring the collapse of soil structure and liquefaction in fjords and active river deltas (Chillarige et al., 1997; Clare et al., 2016; Riboulot et al., 2013).

1.4.5 Chemical processes and phase changes

Chemical processes that can lead to changes in pore fluid volume and overpressure development in marine sediments include gas hydrates dissociation and dissolution (Kvenvolden, 1993; Sultan et al., 2004b). Under stable conditions, gas hydrates can act as an efficient seal, preventing fluids migration and promoting overpressure generation in the underlying units (Flemings et al., 2003; Grauls, 2001). Gas hydrate are induced to dissociation if pressure conditions decrease (e.g.

lowered sea level) (Liu and Flemings, 2009; Maslin et al., 2004; Sultan et al., 2004b) and/or if water temperature increases (Kvenvolden, 1993). The dissociation of gas hydrates produces an expansion in the gas volume, increases the pressure of the surrounding fluids, thus decreasing the effective stress of the system (Sultan et al., 2010). Gas hydrates dissociation can therefore reduce the degree of stability of relatively shallow submarine slopes and/or trigger submarine landslides (Kvenvolden, 1993; Liu and Flemings, 2009; Revil et al., 1998; Sultan et al., 2004b) and represent a potential link between climate changes and submarine slope stability.

Gas hydrates can generate overpressure even when they are contained in the stability zone. When temperature and pressure conditions are favourable for their stability, in fact, dissolution of hydrate crystals in the pore water take place in case the gas concentration in the ambient is unsaturated (Nihous and Masutani, 2006; Tessarolo et al., 2021). In this case, gas hydrate becomes mixture of water and dissolved gas (Sultan et al., 2010). Since the compressibility of systems containing free gas is much higher than the ones containing just liquid (Sultan, 2007), a decrease in hydrates concentration within the gas hydrates stability zone involves compaction of sediments where gas hydrates were originally contained, promoting excess pore pressure generation, and potentially triggering sediment deformation and seafloor collapse (Sultan et al., 2010).

1.4.6 Diagenesis and mineral transformations

Diagenesis and mineral transformations can also be the source of overpressure by releasing water in the system. The most relevant transformations are montmorillonite or smectite to illite, gypsum to anhydrite and opal-A to opal-CT (Neuzil, 1995; Osborne and Swarbrick, 1997). The smectite-to-illite reaction generates the first pulse of water release at approximately 60º of temperature (Colton-Bradley, 1987), while the gypsum-to-anhydrite transformation can release water starting from 40º. The reaction involves a 38% reduction of volume of the solids, but generates a 48% increase in pore water volume, with a net volume increase of approximately 10% (Jowett et al., 1993). Therefore, the gypsum-to-anhydride transformation could represent a relevant source of overpressure if temperatures are high enough (Bjørlykke and Høeg, 1997; Osborne and Swarbrick, 1997; Revil et al., 1998). Also in this case, temperatures in shallow sediments along passive margins are usually too low to trigger the transformations, thus they should be considered as a realistic source of overpressure only in deep sediments (Neuzil, 1995; Osborne and Swarbrick, 1997; Revil et al., 1998). Volpi et al. (2003), however, demonstrated how the presence of biogenic opal within shallow sediments is able to affect slope stability in the Pacific margin of the Antartic Peninsula. At approximately 500 mbsf, early diagenetic processes initiate the transformation of opal-A to opal-CT, destroying the rigid microfabric built by fragments of diatoms and resulting in resumed consolidation, involving a decrease in porosity and overpressure generation (Volpi et al., 2003).

1.4.7 Osmotic pressures

In case of a semipermeable membrane dividing formation fluids with large contrast in brine concentration, fluid transfer from fresh water to saltier water can be facilitated by osmosis. In this process, electrical restrictions allow water to cross the membrane while anions and cations are excluded (Osborne and Swarbrick, 1997). Marine and Fritz (1981) first demonstrated the importance of the process in fluid flows related with geological studies, taking place where the membrane is constituted by clay and clay-rich sediments, suggesting that osmosis could be an explanation for some cases of overpressure development in sediments (see also Neuzil, 2000). According to Osborne and Swarbrick (1997), however, osmotic processes could produce considerable and widespread overpressure only if clay sediments acts like a near-perfect and continuous membrane in order to generate a great temperature and salinity contrast across it. On the other hand, porosity of fine sediments is almost always too high to act as a barrier for prolonged periods, also for the common presence of microfractures. Furthermore, the non-perfect membrane represented by clays allows the transit of ions in the opposite direction to the movement of water. This allows the salinity contrast between the waters divided by the membrane to slowly equilibrate, reducing the salinity gradient and weakening the osmosis process (Osborne and Swarbrick, 1997).

1.4.8 Tectonic compression

As explained in section 1.3, when studying overpressure development in shallow unconsolidated sediments far from fault systems, horizontal stresses are often assumed to be equal (Revil et al., 1998), thus relating porosity only to vertical effective stresses. However, lateral stresses are also able to increase pore pressure (Osborne and Swarbrick, 1997). Lateral compression associated with ductile creep of the San Andreas Fault in California generate extended overpressure areas in partially sealed fault zones at seismogenic depths (7 to 20 km depth) (Sleep and Blanpied, 1992). In the same way, tectonic compression generated overpressure ratios up to 91% of the lithostatic load, extending 55 km landward from the Nakai subduction plate boundary megathrust offshore SW Japan (Kitajima and Saffer, 2012) as well as at 25-45 km depth in the Cascadia subduction zone, beneath Vancouver Island (Canada) (Peacock et al., 2011). Overpressure development due to tectonic compression can be very rapid due to the large volume of pore water that can be mobilized and the very low permeability values that can be reached along fault planes. On the other hand, immediately postfailure, faults can become highly permeable conducts promoting overpressure dissipation. This behaviour, known as fault-valve (Sibson, 1990), allows overpressure to rapidly build up due to tectonic compression, but also to be rapidly released during fault movements or openings (Osborne and Swarbrick, 1997). Tectonic compression is normally not taken into account when studying overpressure development in shallow sediments, since it typically affects sediments at greater depths.

1.4.9 Pore pressures in response to cyclic loading

The generation of overpressure in coarse sediments during cycling loading, such as earthquakes or wave induced loadings, has been extensively studied. The shaking induced by earthquakes over coarse sand or silt is able to potentially re-organize the disposition of the grains, generating excess pore pressure and promoting liquefaction failures which can now be accurately predicted and analysed (e.g. Seed and Idriss, 1971). More recently, interest in studying the relation between cycling loading and overpressure development in clays has also increased and constitutive models to predict the relation between cycles and excess pore pressure have been proposed (Biscontin et al., 2004; Polito et al., 2008). Those models are mainly based on the concept of residual excess pore pressure, resulting from the plastic deformations that progressively collapse the soil skeleton (Polito et al., 2008) and influence the strength and stiffness of fine sediments.

1.5 Assessing overpressure in marine sediments

1.5.1 Piezometers

Free falling piezometers are the most efficient method to perform *in-situ* measurements of vertical pore pressure gradients in the seafloor (Figure 1.9) (Sultan et al., 2010; Urgeles et al., 2000).

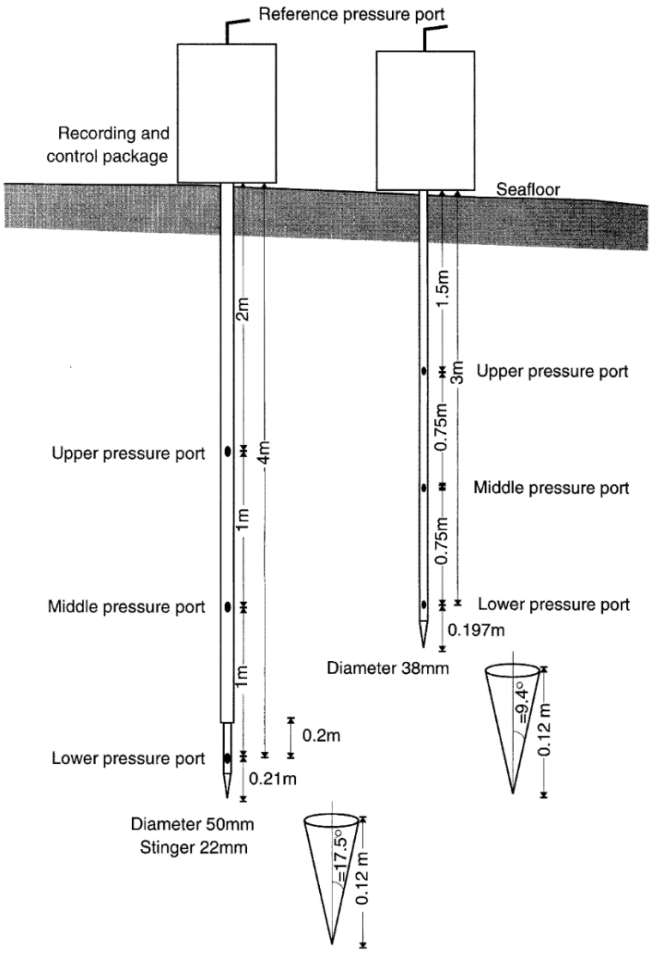

Figure 1.9: Configuration of PoP Up Pore Pressure Instrument (POPPI) free falling piezometer described by Urgeles et al. (2000).

These instruments can be ballasted with lead or still weights and are equipped with lances of different lengths (typically 4 to 6 m) depending on the expected stiffness of the sediments to penetrate.

When the instrument penetrates the sediments, it generates an initial high insertion pressure that, in case of low-permeability marine clays, can require tens of hours to dissipate (Urgeles et al., 2000). During this period of time the probes are left in the seafloor, and porous ports on the lance allow to measure the pore pressure decay in relation with hydrostatic conditions (Sultan and Lafuerza, 2013; Urgeles et al., 2000).

1.5.2 Piezocones/penetrometers

The fastest way to assess *in-situ* pore pressure conditions in soft marine sediments is by using piezocones. These tools are pushed within sediments, creating a pore pressure perturbation that subsequently decays to or close to the background pore pressure conditions (Long et al., 2007) in a similar way as for piezometers. The pore pressure is determined by analysing the decay of the induced fluid pressure pulse (Flemings et al., 2008; Long et al., 2007; Orange et al., 2003; Revil et al., 1998; Screaton, 2010; Sultan and Lafuerza, 2013).

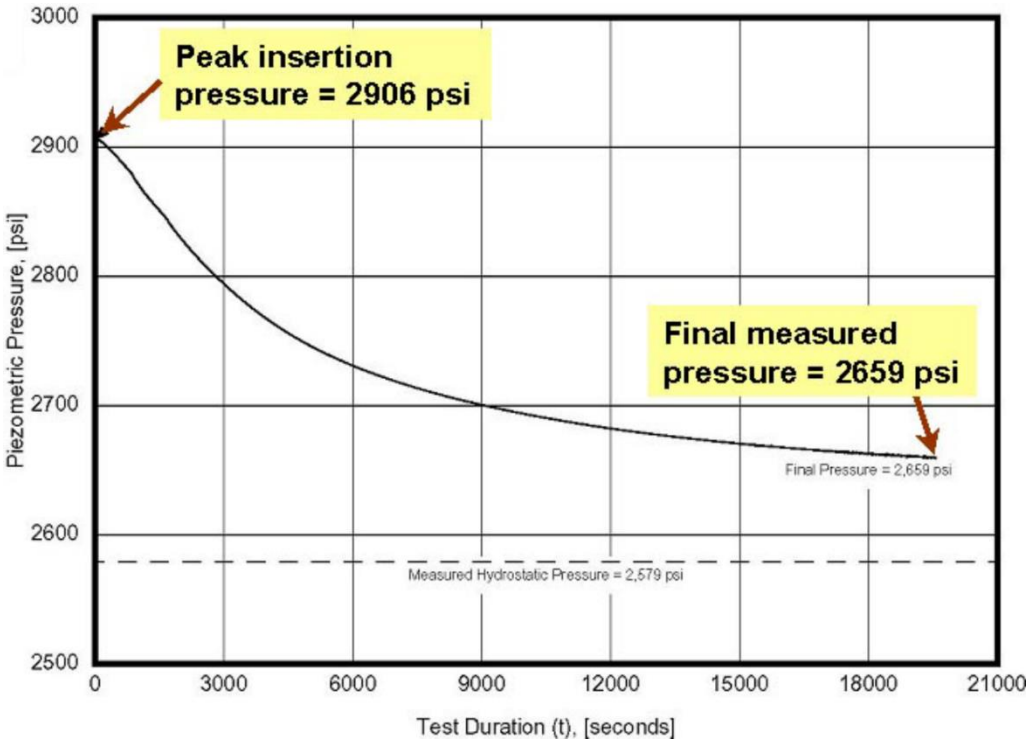

Figure 1.10: Example of piezoprobe insertion record from Orange et al. (2003). 5.5 hours after the insertion, the pore pressure has not completely decayed to the hydrostatic, indicating probable presence of overpressure.

In-situ pore pressure measurements have been performed for scientific purposes during IODP expeditions such as leg 204 offshore Oregon (Tréhu et al., 2004) and 308 in the Gulf of Mexico (Flemings et al., 2008). In these expeditions two types of penetrometers, one Davis-Villinger

Temperature/Pressure Probe (DVTPP) and one "Temperature/2 Pressure" (T2P) Piezoprobe have been used (for details about the two configurations of penetrometer see Long et al., 2007).

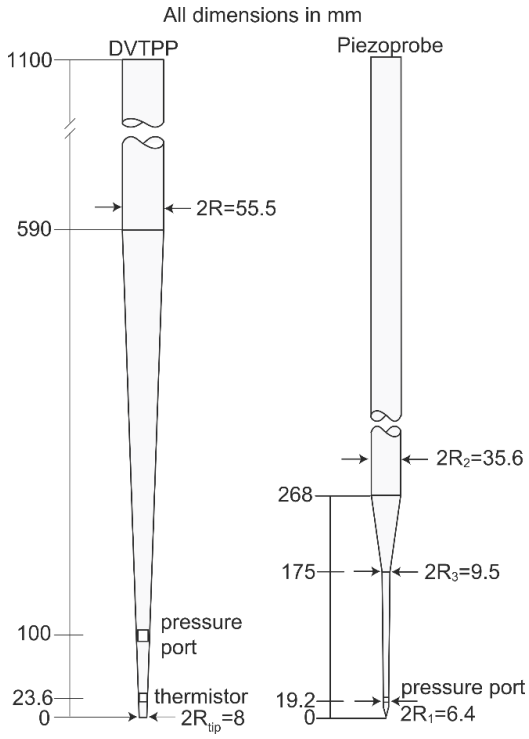

Figure 1.11: DVTPP and T2P piezoprobe pore pressure penetrometers used during IODP legs 204 and 308. From Long et al. (2007).

In-situ pore pressure measurements have been performed for scientific purposes during IODP expeditions such as leg 204 offshore Oregon (Tréhu et al., 2004) and 308 in the Gulf of Mexico (Flemings et al., 2008). In these expeditions two types of penetrometers, one Davis-Villinger Temperature/Pressure Probe (DVTPP) and one "Temperature/2 Pressure" (T2P) Piezoprobe have been used (for details about the two configurations of penetrometer see Long et al., 2007). When analysing penetrometer results, a detailed knowledge of the geological setting is paramount for a correct interpretation of the data, since heterogeneous sediments, overconsolidation and presence of gas can lead to potentially unreliable estimations (Strout and Tjelta, 2005; Sultan and Lafuerza, 2013).

In onshore and offshore geotechnical projects, the most widely used *in-situ* test for geotechnical characterization of shallow sediment is the Cone Penetration Test (CPTU) (Figure 1.12). The test consists of pushing a piezocone penetrometer into the sediment at a steady controlled rate. The penetrometer can be deployed in marine settings from offshore platforms or drilling vessels (Figure 1.12A), and it is equipped with sensors to measure the cone tip resistance, sleeve friction and pore pressure (Figure 1.12B) continuously with depth providing information about the subseafloor sedimentary sequences and geotechnical properties (Lunne et al., 1997).

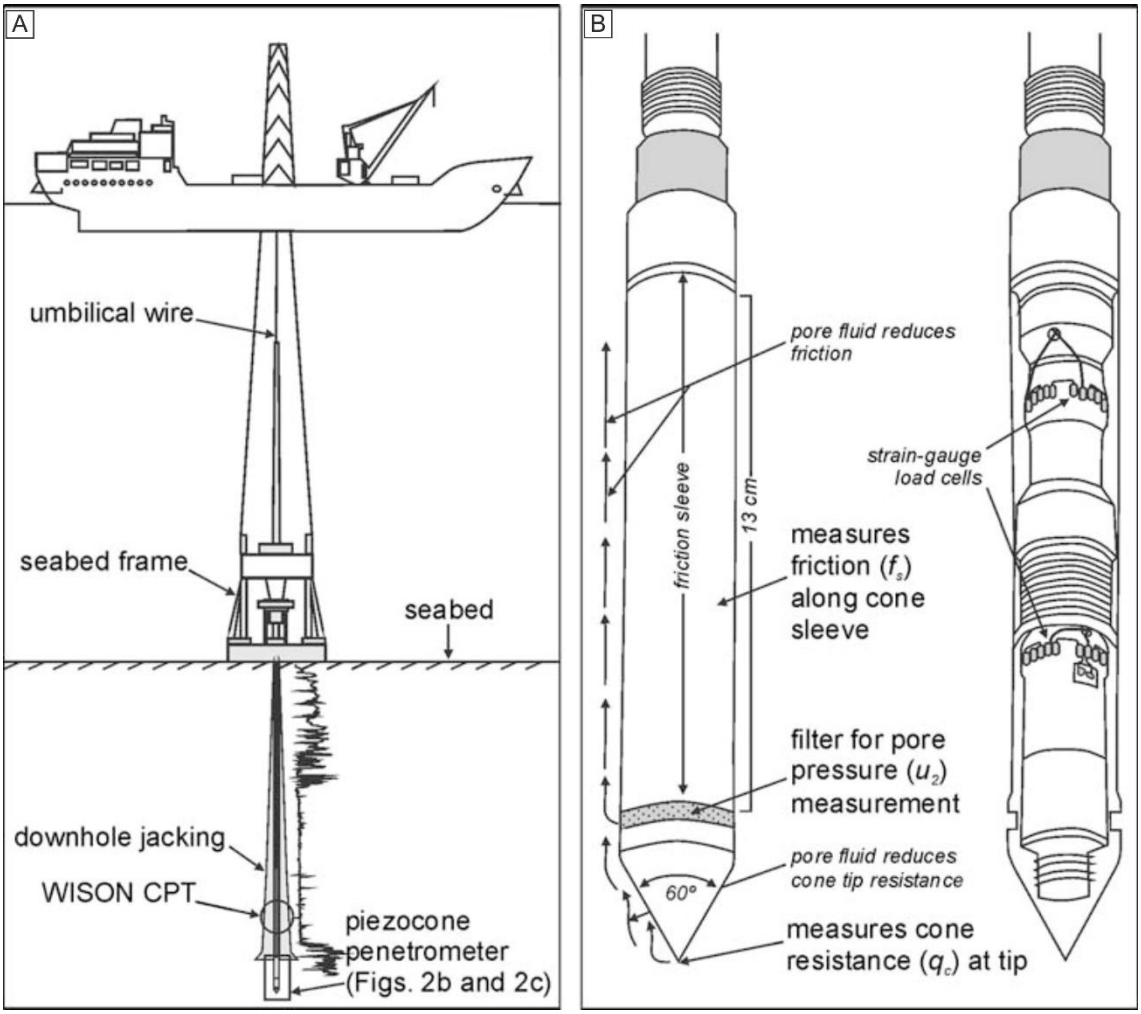

Figure 1.12: (A) CPTU deployment from a drilling vassel; (B): CPTU setting and components.

Besides its capacity to be used as a standard piezocone by temporally halting penetration and recording the pore pressure decay, the CPTU tests can be used to detect indirectly overpressure in marine sediments by estimating the pre-consolidation pressure (σ'_p). The pre-consolidation pressure is defined as the highest pressure the sediments have ever experienced (Lafuerza et al., 2009). Overpressure can be then assessed as the difference between the vertical effective stress assuming hydrostatic conditions (σ'_{v0}) and the pre-consolidation pressure as follows (Lafuerza et al., 2009) (eq. 6):

$$\lambda = \sigma'_{v0} - \sigma'_p \quad (6)$$

Although σ'_p is derived using empirical formulations and not measured directly (Lunne et al., 1997), CPTU tests have demonstrated to provide reliable *in-situ* estimations of the pre-consolidation pressure for a variety of fine-grained sediments (Demers and Leroueil, 2002; Lafuerza et al., 2009).

1.5.3 Long-term observatories

A direct way to perform *in-situ* measurements of pore water pressure is by setting up long-term observatories. An example of such long-term observatories are IODP's CORKs (Circulation Obviation Retrofit Kits) (Becker and Davis, 2005; Dugan and Sheahan, 2012). CORKs consist of isolated fluid pressure sensors deployed in sealed boreholes, avoiding fluid exchanges between the borehole environment and ocean bottom waters (Figure 1.13) (Becker and Davis, 2005). As it has been summarized by Kopf et al. (2015), the main advantages of long-term monitoring are related with measurement of episodic phenomena: (1) they provide a reliable measurement of ambient pore pressure, since significant time after the drilling operations is often needed to equilibrate pore pressures with real *in-situ* conditions; (2) they can be used to monitor hydrological properties in response to tidal and seismic loading (Davis and Villinger, 2006; Wang and Davis, 1996); and (3) CORKs can record hydraulic transients in response, for example, of seismic and aseismic slip, fluid flow events and possible precursory phenomena (Davis et al., 2006). Finally, modern versions of CORKs are equipped with other sensors able to (4) measure anomalies associated with fluid flow episodes and (5) changes in the chemical composition or the seepage rate (Brown et al., 2005).

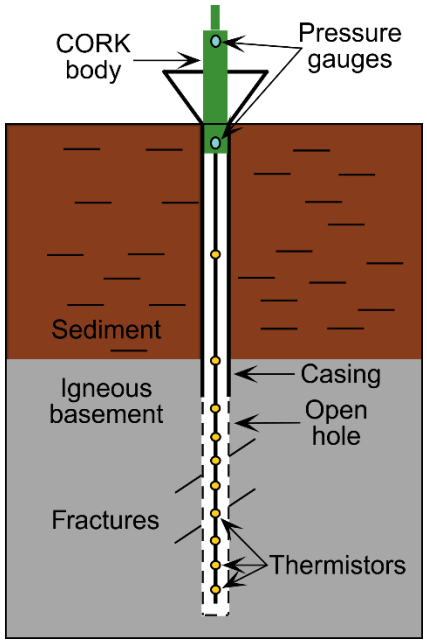

Figure 1.13: Schematic representation of a CORK hydrological observatory. From Becker & Davis (2005).

This technology has been used for scientific purposes in the frame of ODP and IODP expeditions to study the development of overpressure in fault zones (Screaton et al., 1995), the influence of overpressure in fault dynamics and to observe fluid migration in basaltic aquifer systems (Becker and Davis, 2005; Davis et al., 2006). However, at present CORK systems have never been adopted to study long term fluid flow in shallow sediments in passive margins (Dugan and Sheahan, 2012). The main limitations related with CORKs are that the installation requires using

expensive and logistically challenging drillships, and the installation becomes longer and more challenging with the increasing complexity of the tools (Kopf et al., 2015). The development of tethered seafloor drills deployed on the seabed and remotely controlled from a sea vessel such as the MARUM-MeBo (Bremen, Germany; Freudenthal and Wefer, 2013), might represent an affordable solution for the installation of borehole observatory in the near future. This new technology has been successfully tested in the Nakai Trough (Japan) in 2012, where the MeBoCORK was able to collect pore pressure data down to a depth of 35 mbsf (Kopf et al., 2015, 2013), and also in the Alboran Sea and in the Gulf of Cadiz (Hüpers et al., 2020).

1.5.4 Core measurements and geophysical data

The occurrence of overpressure within marine sediments can be evaluated also by analysing the properties of sediment samples taken from sediment cores. In particular, porosity measurements from uniaxial consolidation tests have been one of the first methods adopted to estimate excess pore pressure. This method is based on the assumption that occurrence of excess pore pressure limits sediments compaction, results in higher porosity values than what would be expected for hydrostatic conditions (Athy, 1930). By considering vertical effective stress instead of depth, *in-situ* porosity can be expressed as (Hart et al., 1995; Rubey and Hubbert, 1959) (eq. 7):

$$Ø = Ø_0 e^{-\beta \sigma_v'} \quad (7)$$

where Ø is the observed porosity, $Ø_0$ is the porosity at depositional conditions (i.e. at zero vertical effective stress) and β is the bulk compressibility of the sediments. According to the vertical effective stress (σ_v') definition from eq. 1, the porosity measured through core, logging or laboratory moisture and density data, can be used to estimate *in-situ* overpressure (Dugan and Flemings, 2002; Hart et al., 1995; Revil et al., 1998; Saffer, 2003). Similarly, the relationship between porosity and effective stress can also be expressed by relating void ratio ($e = Ø/(1- Ø)$) to the vertical effective stress (eq. 8):

$$e = e_0 - C_C \log \sigma_v' \quad (8)$$

where C_C is the compression index, defined as the change in void ratio per logarithmic cycle of vertical effective stress, and e_0 is the reference void ratio (Hart et al., 1995; Revil et al., 1998).

The same relation between pore space, effective stress and overpressure allows also to estimate pore pressure through velocity data, determined from wireline logging, logging while drilling or seismic data (Bowers, 2002; Sayers et al., 2002; Screaton, 2010). Shear (*S*) and compression (*P*) wave velocities increase as sediments consolidate and porosity decreases. In presence of high overpressures, consolidation is prevented and high porosities are maintained. Since the normal velocity trend for velocity is to increase with depth, detecting areas of constant or decreasing velocity might indicate overpressured sectors (Bowers, 2002; Marín-Moreno et al., 2013; Revil

et al., 1998). Porosity and velocity data from the ODP Site 1073 has been used, for example, to define the regional overpressure condition offshore New Jersey (Dugan and Flemings, 2002, 2000; Revil et al., 1998).

On the other hand, although in soil mechanics sediments are generally assumed to change their properties mainly in response to mechanical compaction, the reduction in pore space is not a direct function of the vertical effective stress, since mechanical properties are also a function of mineralogical and chemical processes, especially in deeply buried systems (Bjørlykke and Høeg, 1997). For example cementation, intended as precipitation of minerals around clastic grains, provides cohesion to the sediments making them more brittle in their behaviour, thus reducing the loss of porosity with depth (Bjørlykke and Høeg, 1997). Lithological changes, unloading generated by erosion or development of fluid pressure after burial (e.g., due to diagenetic processes) are other variables capable of varying the linearity of porosity trend with depth. Therefore, *in-situ* overpressure should be calculated from porosity and consolidation data only in settings where burial is the major contributor to the principal stress, erosion is minimal and there are no evidences of fluid pressure genesis after burial or cementation processes. These conditions typically exist in shallow sediments along passive margins where slope failures have not taken place (Revil et al., 1998; Screaton, 2010).

1.5.5 Acoustic/geophysical data interpretation

Signs of overpressure can be inferred also from interpretation of conventional seismic reflection and bathymetric data.

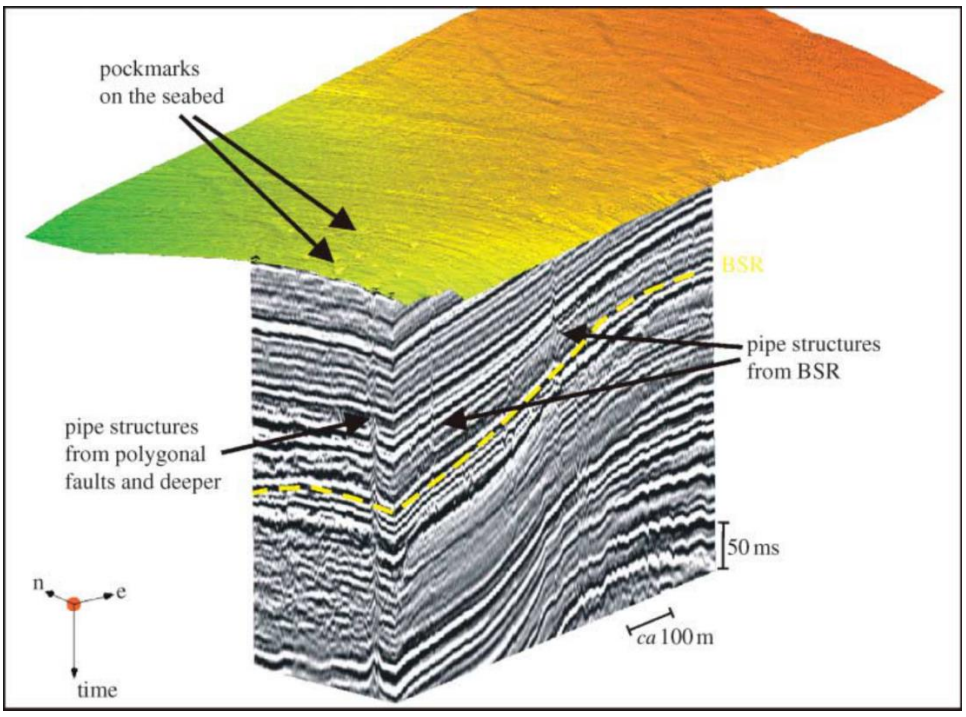

Figure 1.14: 3D seismic data showing pipe structure due to blow-out of overpressured pore fluids after compaction of fine-grained hemipelagic sediments, offshore mid-Norway. From Berndt (2005).

Berndt (2005) describe that episodic blow-out of fluids occurs in response to overpressure generated by compaction of water-rich sediments, volcanic intrusions or hydrocarbon migration, leading to the formation of pipe structures well visible from multi-channel seismic profiles (Figure 1.14).

Orange et al. (2003) suggested that overpressure related to submarine slope failures can be deduced from bathymetric data by analysing the shape of the headscarps. In their interpretation, validated with *in-situ* piezometer measurements and hydrogeological models, amphitheatre-shaped headscarps of submarine failures in the Green Canyon area (Gulf of Mexico), with steep headwalls, sharp inflection points at the top and bottom, linear trend and flat basis, indicate that slope failures are related with overpressure development within shallow sediments.

1.5.6 Overpressure modelling

Overpressure development and evolution over geological time scales can be evaluated using hydrogeological models (Figure 1.15). By coupling sedimentation, consolidation and fluid flow, numerical models are able to simulate the origin of overpressure and their impact in offshore slope stability (e.g. Revil et al., 1998; Orange et al., 2003; Kvalstad et al., 2005b; Hustoft et al., 2009; Screaton, 2010; Urgeles et al., 2010; Urlaub et al., 2015, 2012; Llopart et al., 2019, 2021; Mencaroni et al., 2020). While modelling overpressure development in shallow sediments of passive continental margins, the most important driving mechanism is sediment loading. For this reason, an accurate reproduction of the response to burial load (e.g. porosity and permeability responses to load and compaction) is essential (Revil et al., 1998; Stigall and Dugan, 2010).

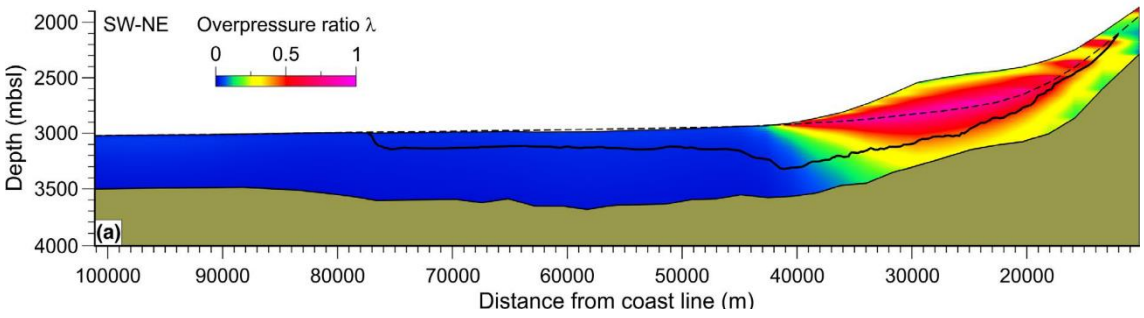

Figure 1.15: Example of overpressure modelling from Llopart et al. (2021). The figure refers to the overpressure generated after the emplacement of debris avalanches in the Grenada basin, offshore Martinique.

The influence of sedimentation rate and physical properties of sediments on the overpressure development can be quantified by using 1D sedimentation-consolidation analysis (e.g. Viesca & Rice, 2012; Urlaub et al., 2015; Mencaroni et al., 2020). 1D simulations, in fact, are able to reproduce the loss in pore space and permeability with increasing burial depth. Lateral flow and spatial distribution of stresses can only be analysed from 2D models that couple fluid flow and stress analysis in porous medium (Urlaub et al., 2015). Typical 2D finite-element hydrogeological

models returns deterministic results that can accurately reproduce the fluid flow of simple slopes, where stratigraphic architecture and anisotropy of physical properties can be reproduced in two dimensions (Dugan and Flemings, 2000; Llopart et al., 2019; Urlaub et al., 2015). 3D stochastic fluid-flow models are broadly used in the oil and gas field with specific tools that aim to calculate, for example, heat flow and hydrocarbons migration (Tømmerås et al., 2018). Various geotechnical and hydrogeological software adopt a 3D approach in solving pore fluid migration problems at smaller scale. The use of 3D tools for basin-scale hydrogeological models is, however, still not common, especially because the size and characteristics of the numerical models generates significant CPU load that cannot be easily handled on regular desktop computers.

1.6 Influence of overpressure in slope stability

The application of overpressure evolution numerical models at a basin scale, in some cases, aims to provide a broad understanding of the conditions that may have generated previous slope instabilities (Bellwald et al., 2019; Gutierrez and Wangen, 2005; Llopart et al., 2019; Orange et al., 2003; Urlaub et al., 2012). The examples cited in this chapter (Gulf of Mexico, offshore New Jersey and the Storegga Slide) demonstrated that development of high excess pore fluid pressure has a primary influence in the generation of large submarine landslides in passive margins, also in areas characterized by very gentle slopes (< 2º) (Stigall and Dugan, 2010; Urlaub et al., 2015). Urlaub et al. (2015) calculated that a 2º steep submarine slope could only be destabilized with $\lambda \geq 0.9$. In absence of extreme hydromechanical properties of sediments (e.g. very high compressibility or very low permeability), those overpressure ratio values can be reached only in presence of high sedimentation rates values. Sedimentation rates in the order of 0.15 m/kyr, in fact, would not be sufficient to generate overpressure nor lateral fluid flow sufficient to destabilize a low-angle slope (Urlaub et al., 2015).

1.7 Depositional systems in mid-latitude continental margins: basic concepts

This section aims to provide a brief overview on key aspects related to depositional systems of mid-latitude continental margins that are discussed in this thesis. In particular, to bring a general physiography of continental margins, sedimentary processes such as mass wasting and bottom current sediment transport and related depositional systems.

1.7.1 Continental margins physiography

Continental margins represent the transition between the ocean domain and the subaerial parts of the continents. Covering about the 28% of the submarine areas in the world (Figure 1.16), continental margins are one of the key domains of oceanic floors, together with deep-ocean basins and mid-ocean ridges.

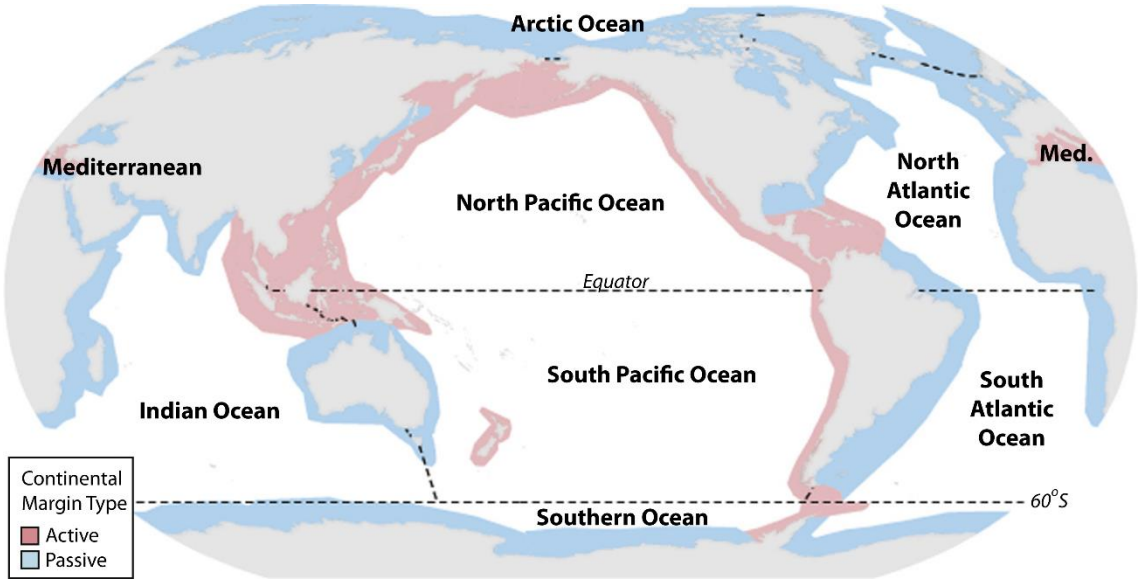

Figure 1.16: Locations of active and passive continental margins from Harris et al. (2014).

Continental margins are typically differentiated in active margins, if associated with lithospheric plate boundaries, and passive margins, located in the interior of lithospheric plates and often away from plate boundaries (Figure 1.16). Active and passive continental margins show differences in morphology that can be related to their formation processes. The morphology of passive margins, in fact, is mainly controlled by deposition and erosion processes, whereas in active margins tectonics and magmatism are often the dominant processes (Harris & Whiteway, 2011; Harris et al., 2014).

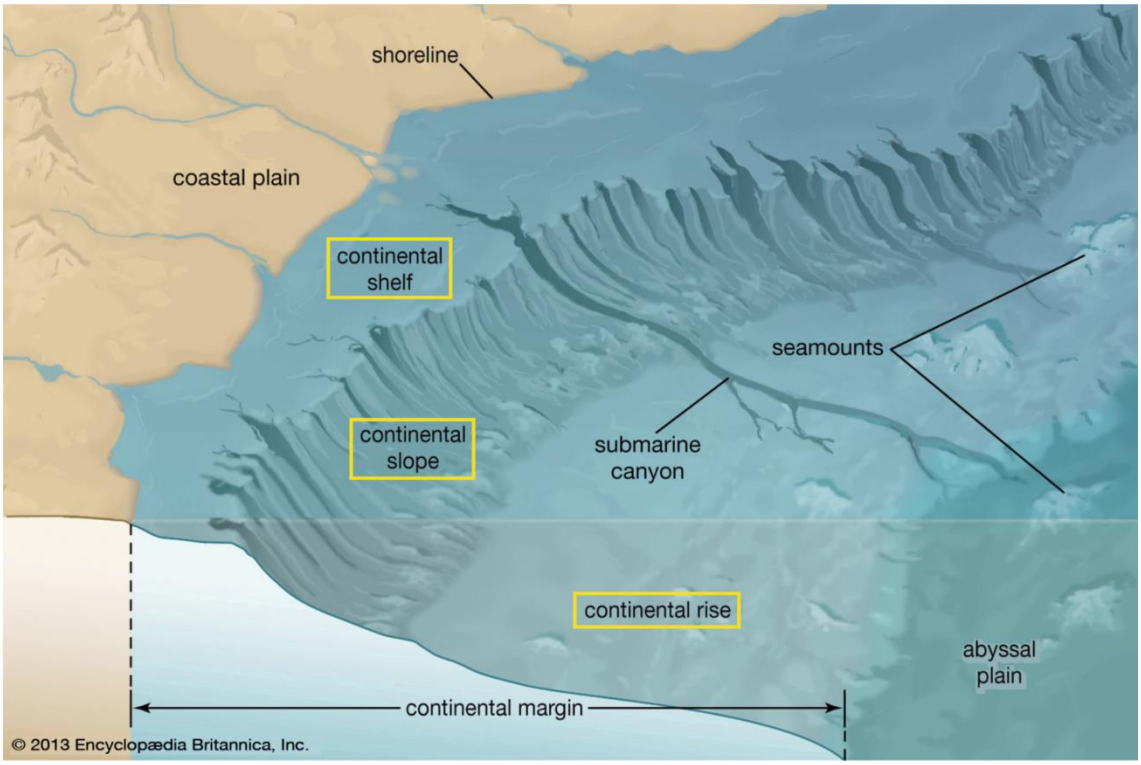

Figure 1.17: Physiographic domains of continental passive margins. Modified from (Encyclopedia Britanica, 2021).

Three physiographic domains are present in typical continental margins (Figure 1.17):

1. Continental shelf: it is the area closer to the shoreline. By definition, the continental shelf is covered with shallow waters (typically down to 200-300 m) and it is inclined seawards at low angles. Generally, continental shelves end with an abrupt drop towards the sea called shelf-break or shelf-edge. The morphology of present-day mid-latitude continental shelves has been shaped especially during the Last Glacial Maximum (LGM), approximately 20000 years ago, when the maximum extent of ice sheets corresponded to sea level lowstands and periods of intense erosion of present-day continental shelfs. The world average continental shelf width is 80 km, although it can vary from almost not-existing, especially in active margins (Harris et al., 2014) to very wide in passive margins, where they can reach 1,500 km (e.g., the Siberian shelf in the Arctic ocean) (Harris et al., 2014; Kennett, 1982).
2. Continental slope: it is generally the steepest part of a continental margin. It extends from the shelf-break (usually 200-300 m) to the upper limit of the continental rise down to 3000-4000 m), where there is a general decrease in steepness. The typical gradient for a continental slope is between 2-4º, although it can locally reach much steeper gradients. In general, it has been observed that continental slopes are steeper in active than in passive margins (Harris et al., 2014). Depending on the slope angle, the continental slope can reach a width of hundreds of kilometres (Kennett, 1982). Submarine canyons often erode continental slopes. Those geomorphological features act as major transfer conduits for water and sediments from the continents to the deep sea. Submarine canyons found off the mouth of major rivers in passive margins are usually developed from erosion by sediment gravity flows, while in active margins the genesis of canyons is also controlled by tectonics and they emplace along structural boundaries. Most of the canyons end at the base of continental slopes, where they extend towards the sea as channels into fan systems (Kennett, 1982). Canyons in mid-latitude continental margins can reach hundreds of kilometres in length, although the larger and longer canyon systems in the world are found in polar regions and developed under the discharge of sediments derived from glaciated catchments during the Quaternary (Harris et al., 2014; Harris and Whiteway, 2011).
3. Continental rise: it connects the continental slope with the abyssal plain, representing the deeper continental margin element before transitioning toward the deep ocean. It is marked by a gentle slope dipping towards the sea and decreasing towards the abyssal plain. It usually hosts thick sediment accumulations coming from mass wasting events generated in shallower parts of the continental slope. The presence of continental rises is more commonly associated with passive margins, while it is often absent in active

margins where often the slope feeds directly an ocean trench at subduction plate boundaries (Harris et al., 2014).

1.7.2 Mass wasting processes: submarine landslides and turbidity currents

Submarine landslides are volumetrically one of the key transport processes that redistribute large volumes of sediments from the upper continental slope, where the majority of sediments tend to accumulate, to the deep sea (Masson et al., 2006). The volume of sediment mobilized in individual events can exceed by several orders of magnitudes those of any terrestrial landslides (Talling et al., 2014) and are widespread across every continental margin in the world.

The term "landslide" can refer generically to any form of slope failure. Landslides' classification is based on the process that generated the failure and the rheology of the flow (see Hampton et al., 1996; Locat and Lee, 2002; Mulder and Cochonat, 1996; Nardin et al., 1979 for more information about nomenclature of submarine mass movements). Masson et al. (2006) summarized the four main types of landslides as (Figure 1.18):

- Slide: movement of a coherent mass of sediments bounded by distinct failure planes;
- Debris flow: laminar, cohesive flow with clasts in a fine-grained matrix;
- Debris avalanche: rapid flow of cohesionless rock fragments with energy dissipation by grain contact;
- Turbidity current: gravity flow in which sediment grains are maintained in suspension by fluid turbulence.

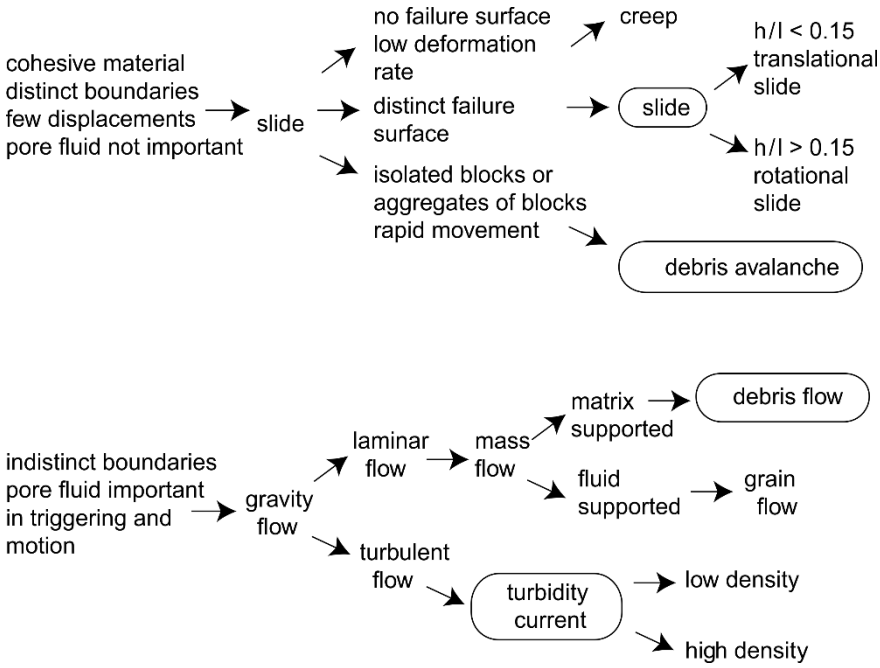

Figure 1.18: Dynamic submarine landslides classificaiton proposed by Masson et al. (2006).

Rheology of mass movements can be deduced by analysing source and depositional areas with geophysical techniques, although distinguishing between different types of flow is often difficult because of their destructive nature and the tendency of mass movements to evolve while proceeding (Masson et al., 2006; Talling, 2014). The general paradigm is that landslides evolve downslope from slides to debris flows to turbidity currents by disintegrating and gradually incorporating volumes of water (Bryn et al., 2005). However, this model most likely oversimplifies the actual submarine landslides flow behaviour. Some landslides travel many hundreds of kilometres without evolving into turbidity currents, indicating that, in reality, the formation of large turbidity currents is still a poorly understood process (Masson et al., 2006).

The inclination of the slope control size and frequency of the failures. Steeper areas such as fjords and canyons generate smaller and more frequent landslides (Hampton et al., 1996), while low angles slopes are where less frequent but larger landslides detach from (Urlaub et al., 2015). In the same way, it has been observed that active margins generate frequent but smaller landslides compared with passive margins (Figure 1.19). Higher seismic activity in active margins, in fact, triggers sediment mobilization more often than in passive margins, where the rarer occurrence of earthquakes allows the build-up of thicker sediment columns (Urgeles and Camerlenghi, 2013) while promoting overpressure generation as explained in section 1.3.

Besides the already mentioned differences in volumes, subaqueous landslides differ from those in the subaerial environment for other key characteristics (Urgeles and Camerlenghi, 2013):

1. They occur in fully saturated sediments, except for the possible presence of localized free gas. If sediments contain gas, they become more susceptible to failures due to environmental conditions. If the load imposed by the water column decreases (i.e. lowstand conditions), the undrained unloading of gas-charged sediments can decrease the stability of the slope (Sultan et al., 2004b; Vanoudheusden et al., 2004). On the other hand, increase in water temperature can dissociate and expand gas hydrates, leading to similar sediment instability conditions (Maslin et al., 2010; Sultan et al., 2004b) (see section 1.3.2.3).
2. Physical properties of marine sediments differ from the ones of subaerial sediments. This is especially the case if sediments contain relevant percentages of microfossils, that can affect their compressibility behaviour (Locat et al., 2003; Tanaka and Locat, 1999).
3. Marine sediments are subject to environmental stresses which are not found in the subaerial environment, e.g. tides, surface waves and internal waves (Mestdagh et al., 2020; Stow et al., 2013b; Urgeles and Camerlenghi, 2013).
4. Large submarine landslides occur often in submarine slopes much gentler than terrestrial landslides (< 2º) (Talling et al., 2014; Urlaub et al., 2015). In presence of such low slope angles, the necessary condition to generate failures is the development of overpressure

within sediments. When the pressure of the water contained in the pore spaces exceeds the hydrostatic condition, in fact, the shear strength of the sediments is reduced and so is the stability of a slope (Revil et al., 1998) while the runout of the slide is sustained by dynamics such as hydroplaning (De Blasio, 2004) (see also section 1.3).

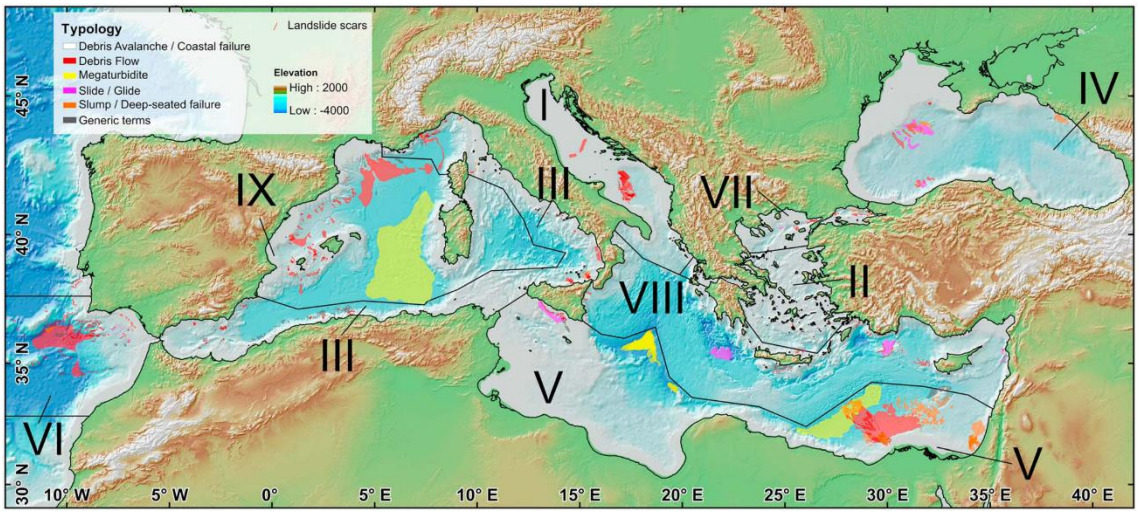

Figure 1.19: Map of landslides distribution in the Mediterranean Sea according to margins' typology. Areas I, II, III, VII, VIII corresponds to active margins and show more frequent, smaller MTDs. Areas IV, V and IX are passive margins, with larger but less frequent landslides. From Urgeles & Camerlenghi (2013).

The most critical difference between subaqueous and terrestrial landslides remains, however, the disparity of complexity regarding observation, mapping and monitoring, hence understanding. Satellite data, broadly used to detect and study subaerial landslides (e.g. Kimura & Yamaguchi, 2000; Nichol & Wong, 2005), do not penetrate thick sea-water columns. The acquisition of geophysical data, key to imaging submarine mass movements, is only possible using expensive and logistically challenging expeditions with research vessels equipped with high technology tools. An example are the two recent INSIGHT cruises on which part of this thesis is based (Gràcia et al., 2018; Urgeles and Shipboard Scientific Party, 2019). Conventional geophysical methods such as sub-bottom profiles, multibeam bathymetric data or side-scan sonars allow quantifying the extent of landslide runout of past events. Repeated surveys of the same area allow to create detailed time-lapse seabed images and detect changes that took place in within submarine channels (e.g. Heijnen et al., 2020), such as the emplacement of new mass transport deposits. Modern monitoring campaigns integrate geophysical methods with moorings or frames installed on the seafloor (e.g. Azpiroz-Zabala et al., 2017) (Figure 1.20), despite deploying those instruments on the deep seafloor is challenging and the power of the flows can damage the instruments (Clare et al., 2020, 2017).

Even in presence of the highest technological standards, however, we are far from producing reliable forecasts on individual landslide events, especially because they are often triggered by other episodic and unpredictable events such as earthquakes (Masson et al., 2006; Talling et al.,

2014). In this sense, numerical models represent one of the key ways forward in order to improve our understanding on submarine landslides and predict their impact on offshore infrastructure and coastal population safety (Masson et al., 2006).

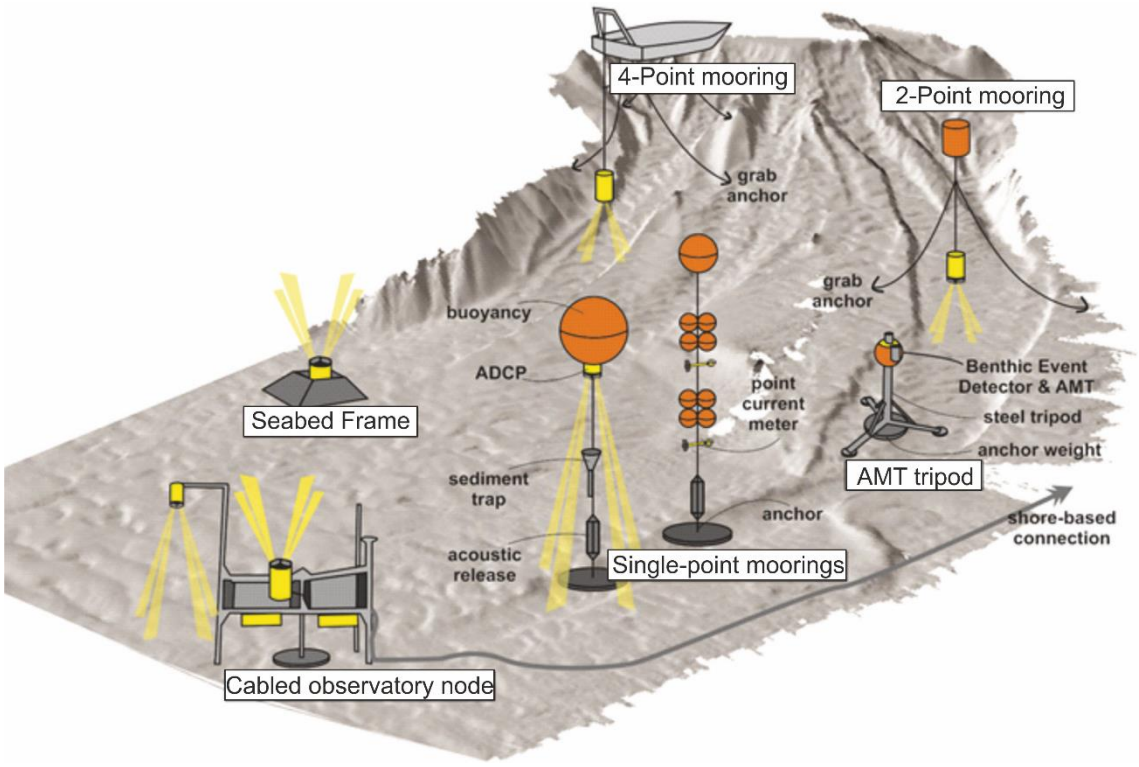

Figure 1.20: Examples of turbidity current monitoring platforms from Clare et al. (2020).

1.7.3 Contour current and mixed sediment transport processes

Contourite drifts are thick and extensive sedimentary deposits built under the persistent action of along-slope contour currents (Rebesco et al., 2014; Rebesco and Camerlenghi, 2008; Stow et al., 2002). Over the last few decades, examples of ancient and modern contourite drifts, showing a wide variety of grain-size distributions, sediment compositions and stratigraphic architectures, have been found worldwide in almost all continental margins (Rebesco et al., 2014) (Figure 1.21). As proposed by Rebesco et al. (2014), in the present terminology the term "contourites" does not only refer to the sediments deposited in the deep sea by contour-parallel currents *sensu stricto*, but it embraces "all those sediments that are affected to various extents by different types of currents". This more generic definition can represent better the real nature of contourite sedimentation, since they are almost always found interbedded with other sediment types (e.g. hemipelagic, turbiditic) and "interaction of processes is the norm rather than the exception" (Rebesco et al., 2014).

Contourite systems along continental margins are associated with both erosional and depositional features, with erosion usually taking place where the bottom current circulation is more vigorous and drifts developing adjacent to them (Rebesco et al., 2014; Stow et al., 2002).

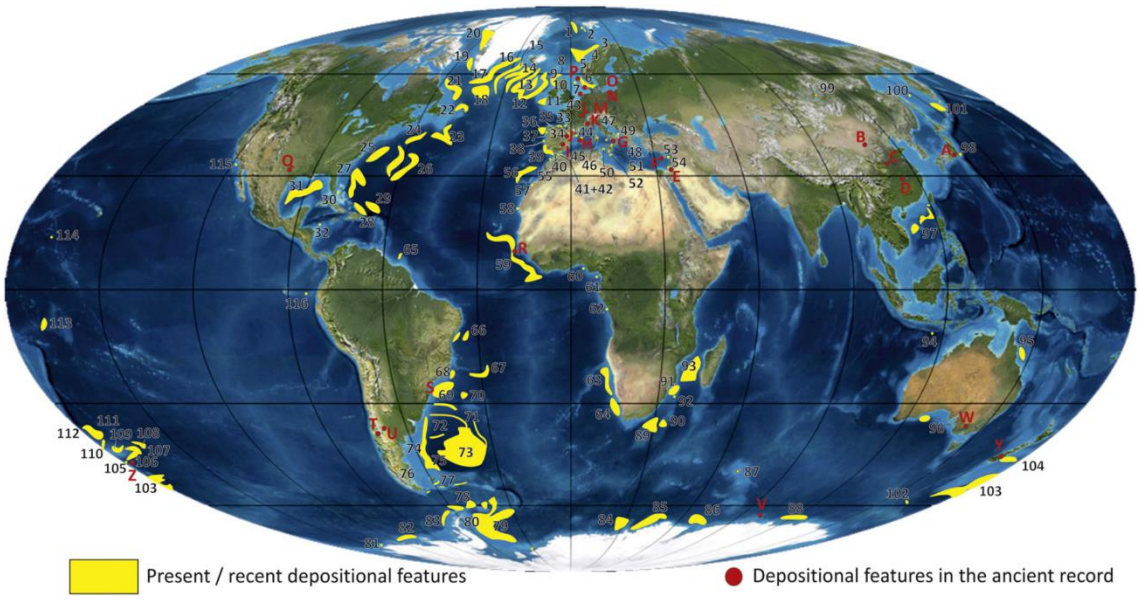

Figure 1.21: Present day large contourite depositional systems (yellow) and ancient sedimentary record (red points). From Rebesco et al. (2014).

The resulting configuration of drifts varies from sheeted to mounded, and both depositional and erosional features are classified also based on location within the slopes, morphology and evolution (Faugères et al., 1999; Rebesco et al., 2014; Stow et al., 2002). Figure 1.22 shows the classification for (A) drifts and (B) erosional features proposed by Rebesco et al. (2014).

Interest in contourite depositional systems has increased simultaneously with their use as palaeoceanographic indicators (Camerlenghi et al., 1997; Llave et al., 2007a; Miramontes et al., 2019; Rebesco et al., 1996; Voelker et al., 2014), palaeoclimatic recorders (Grützner et al., 2003), and for their economic importance in the frame of hydrocarbon exploration (Brackenridge et al., 2013; Fonnesu et al., 2020; Sansom, 2018; Stow et al., 2013b; Viana and Rebesco, 2007). Recent studies also demonstrated the key role of bottom currents in the spreading and accumulation of microplastics in oceanic sediments (Kane et al., 2020). Finally, the identification of contourite deposits is of paramount importance for offshore geohazard assessment (Casas et al., 2015; Laberg and Camerlenghi, 2008; Miramontes et al., 2016a; Rebesco et al., 2014). Climatic variations modify the intensity and depth of contour current pathways, producing an alternation of poorly sorted, low-permeability, fine-grained sediments with coarser sand beds (Brackenridge et al., 2018; de Castro et al., 2020; Gatter et al., 2020; Knutz, 2008; Laberg et al., 2005; Miramontes et al., 2018, 2016b; Rebesco and Camerlenghi, 2006; Yu et al., 2020). Such alternation favours the generation of weak layers (Gatter et al., 2020; Laberg et al., 2005; Laberg and Camerlenghi, 2008; Nicholson et al., 2020) and overpressure development (Solheim et al., 2005), which increase the likelihood of failure.

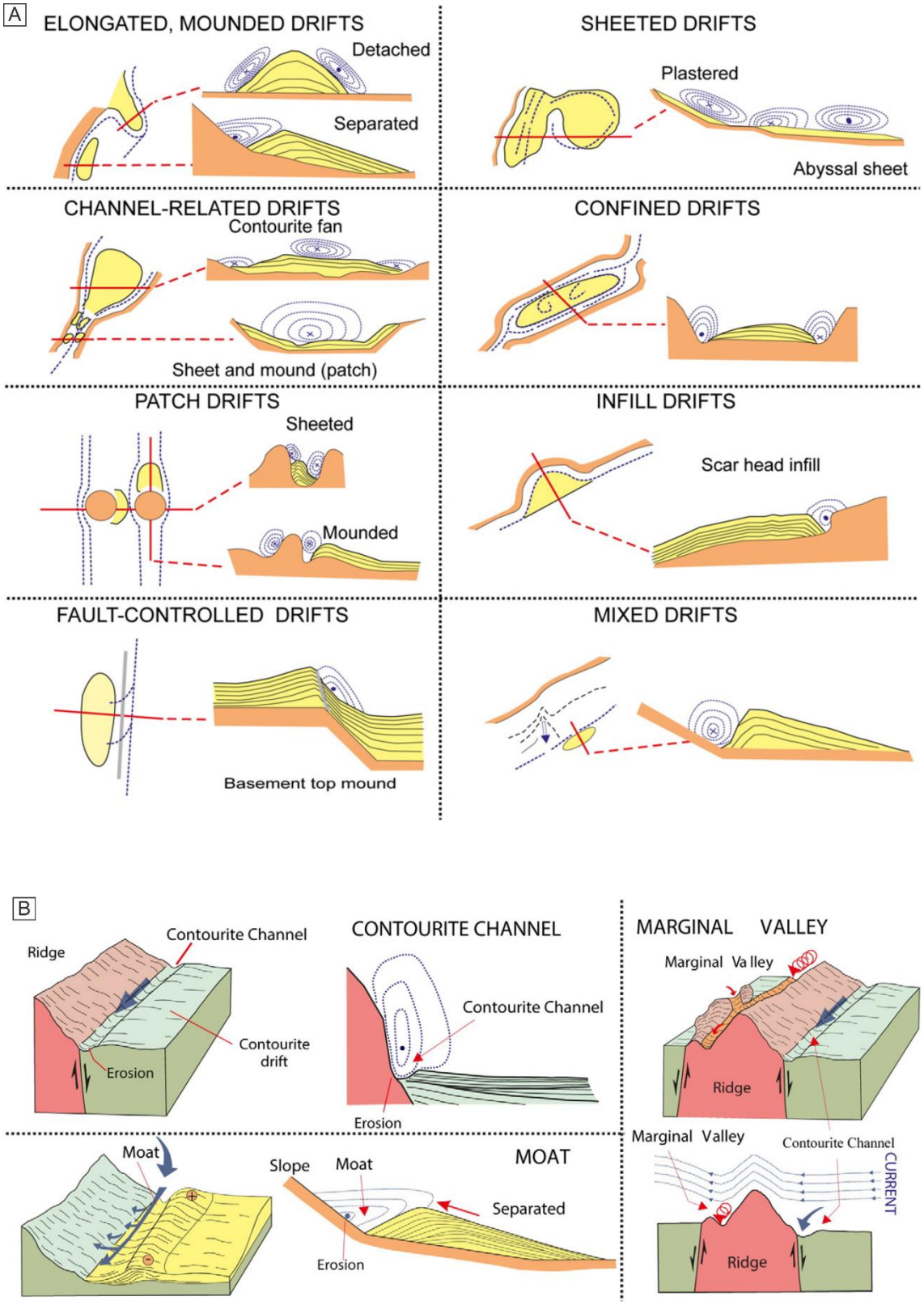

Figure 1.22: Sediment drift types (A) and large-scale contourite erosional features (B) with inferred bottom-current paths from Rebesco et al. (2014).

Interaction between along-slope contour currents and down-slope sediment gravity flows such as turbidity currents generates what it is commonly known as mixed turbidite-contourite systems (Mulder et al., 2008). Such interplay has been found in many areas worldwide (Edwards et al., 2018; Fuhrmann et al., 2020; Gong et al., 2013; Lucchi and Rebesco, 2007; Rasmussen et al., 2003; Rebesco et al., 1996) and it is recorded when there is an energy balance that allows preservation of the influence of both currents (Mulder et al., 2008; Rebesco et al., 2014). This is also the case in many areas within the Gulf of Cadiz, where depositional features generated by the Mediterranean Outflow Water (MOW) crossing the pathway of turbidity currents have already been documented (Alonso et al., 2016; Brackenridge et al., 2013; de Castro et al., 2020; Hanquiez et al., 2010; Marchès et al., 2007; Mulder et al., 2006).

Turbidity and bottom currents can interact in three different ways, producing diagnostic deposits described in detail by Mulder et al. (2008) and Fonnesu et al. (2020). The type of interactions depends on the relative timing between turbidity current deposition and contour-current action (Figure 1.23).

1. Contourite-turbidite alternations (Figure 1.23A): contourite and turbidite systems develop at different times. A contour current can be deviated by a previously imposed turbidite channel (e.g., the Portimão Canyon in the Gulf of Cadiz) (Marchès et al., 2007). On the other hand, an existing contourite drift can change the pathways of a turbidity flow, as shown by examples from the US Atlantic margin (e.g. Locker & Laine, 1992), Greenland (Rasmussen et al., 2003) and offshore Tanzania (Sansom, 2018).
2. Redistribution of gravity flow deposits by bottom currents (Figure 1.23B): in this case, bottom currents rework turbidity or debris flow deposits right after their deposition, spreading the sediments in the direction of the bottom current even for very long distances. The reworked sediments fill local sea-floor depressions and often show erosional or tractional features, as it is has been detected in the Faroe-Shetland Channel (Akhurst et al., 2002) and, again, in the Gulf of Cadiz, where the fine grained components of lobes generated by turbidity currents are winnowed by the MOW and transported down-current (Hanquiez et al., 2010).
3. Interaction of synchronous contour and turbidity currents (Figure 1.23C): typically occur when bottom currents affect synchronous turbidity flows. Asymmetric levees are generated with preferential extension in the contour-current direction. This scenario has been observed in several areas worldwide, including offshore Antarctica (Escutia et al., 2002; Lucchi and Rebesco, 2007; Rebesco et al., 2007, 1996), China (Gong et al., 2013), Mozambique (Fonnesu et al., 2020) and Tanzania (Fuhrmann et al., 2020). In all of those cases, lobes formed by turbidity currents are deflected in the direction of the bottom current. If the contour current has enough power, the whole lobe can be deflected while

it deposits, while if the energy is not so high the bottom current can pirate only a part of the finest sediment in suspension (Mulder et al., 2008).

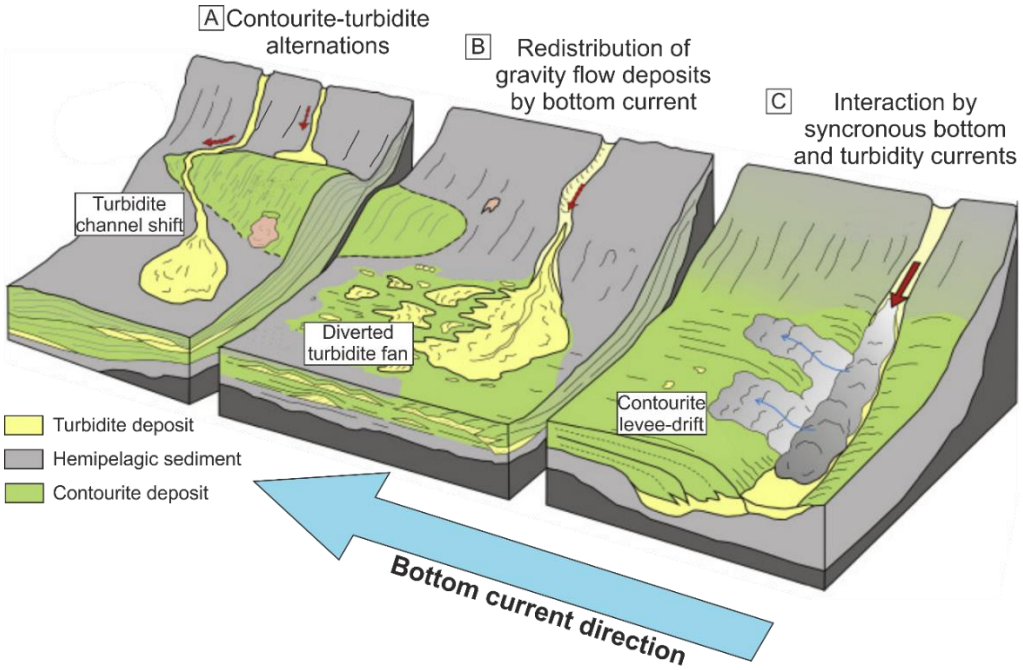

Figure 1.23: Conceptual representation of possible interactions between gravity flows and bottom currents at different temporal scales. A: Contourite-turbidite alternation; B: Redistribution of gravity flow deposits by bottom currents; C: Interaction by sincronous bottom current and turbidity currents. The bottom current direction is indicated by the light blue arrow, while the red arrows indicate the gravity flows pathways. Modified after Fonnesu et al. (2020).

Miramontes et al. (2020) performed three-dimensional flume tank experiments to simulate the synchronous interaction between turbidity currents and contour currents at different velocities. The experiments show that high contour current velocities favour asymmetric levee formation downstream of the contour current due to overbanking, if the submarine channels incision is not so high. At these conditions, the runout distance is reduced and less sediments accumulate within the channel terminal lobe. On the other hand, lower bottom currents velocity generates lower sediment accumulation within and around the channel, as the lobe is located further downslope (Miramontes et al., 2020).

Chapter 2: Geological and oceanographic settings

This study is mainly focused on the Alentejo basin, located in the northernmost edge of the Gulf of Cadiz, SW Iberian margin (Figure 2.1). The scientific production related with the area reflects three aspects for which the Alentejo basin and, in a more general way, the whole Gulf of Cadiz is broadly recognized as an area of significant geological interest.

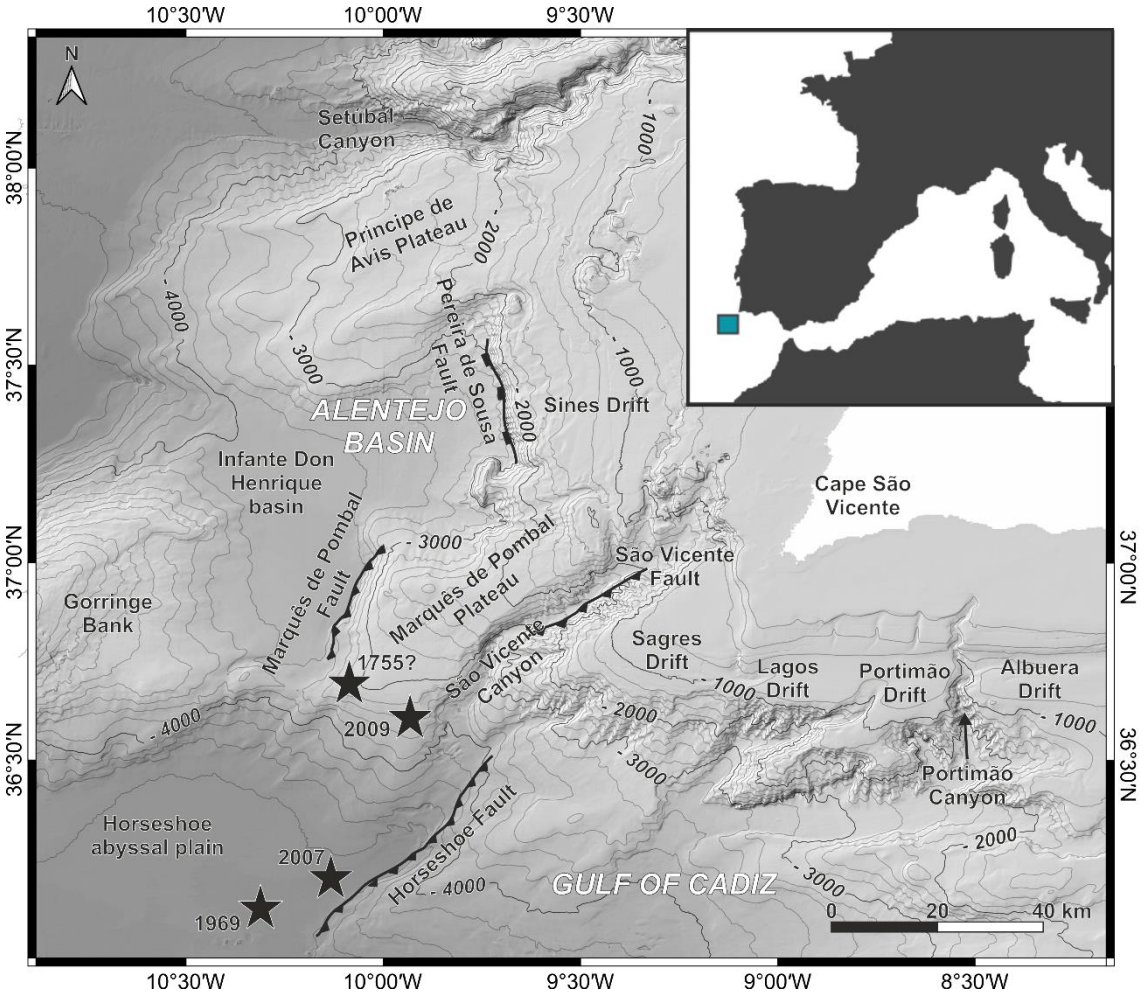

Figure 2.1: Location and main morphological features of the study area mentioned in this thesis. Stars indicate the epicenters and years of the cited earthquakes.

First, the Alentejo basin is considered a possible epicentre for the 1755 Lisbon earthquake (Mw $\geq$ 8.5) and tsunami event and still represents a threat in terms of earthquake geohazard. The historical event is tragically known as the most devastating natural catastrophe in western Europe, as it caused some 10000 casualties, about 1000 of which attributed exclusively to the tsunami, within Portugal, Spain and western Morocco (Baptista et al., 1998). Until recently, none of the multiple proposed geological structures and tsunami models (e.g. Zitellini et al., 2001, 2009; Gutscher et al., 2002; Gràcia et al., 2003b; Gutscher, 2004; Stich et al., 2007; Terrinha et al.,

2009) have been able to explain the magnitude of the 1755 Lisbon earthquake or the tsunami arrival times. On the other hand, a recent study from Martínez-Loriente et al. (2021) demonstrated that an intra-plate thrust fault located in the Horseshoe Abyssal Plain (Figure 2.1) could have suitable dimension and fault-rock properties to generate the 1755 earthquake and tsunami event. This study confirms the fact that the whole area is under a compressive deformation regime, with numerous active structures having high tsunamigenic potential (Gràcia et al., 2003b, 2003a; Martínez-Loriente et al., 2018, 2013; Terrinha et al., 2009, 2003; Zitellini et al., 2004). During recent years, earthquakes of considerable magnitude have nucleated in the area such as those of 1969 (Mw ≥ 7.9-8.0), 2007 (Mw ≥ 6.0) and 2009 (Mw ≥ 5.5) (Stich et al., 2007a) (Figure 2.1).

Second, the whole Gulf of Cadiz receives the influence of a strong bottom current, the Mediterranean Outflow Water (MOW), which originates in the Mediterranean Sea and has swept the continental slope starting from the opening of the strait of Gibraltar in the Early Pliocene (Ambar et al., 1976; Ambar and Howe, 1979; Hernández-Molina et al., 2014b). The flow depth and power of the MOW is strictly related to the conditions at which the waters exit the Mediterranean basin, which vary according to both long term climatic cycles (e.g. glacial vs interglacial cycles) (Hernández-Molina et al., 2014a; Rogerson et al., 2012a; Sánchez-Leal et al., 2017) and seasonal changes (Bahr et al., 2015; Sánchez-Leal et al., 2020).

The MOW is also responsible for the **third** key feature commonly associated with the Alentejo basin, which is the emplacement of one of the most well-known contourite depositional systems worldwide (Hanquiez et al., 2010; Hernández-Molina et al., 2016a, 2014b; Mulder et al., 2003; Stow et al., 2013b). The contourite system dominates the sediment distribution of the upper slope along the entire Gulf of Cadiz until the Alentejo basin, with stratigraphic architecture and grain sizes reflecting the changes in the MOW hydrodynamics through time.

2.1 Geodynamic setting of the Gulf of Cadiz

The Gulf of Cadiz hosts the Azores Gibraltar Line (AGL) (or Fault Zone), which represents the present-day boundary between the African and Eurasian plates and extends from the Strait of Gibraltar to the Azores triple junction (Roest and Srivastava, 1991) (Figure 2.2). Within the Gulf of Cadiz, the exact location of the AGL is not precisely established since the deformation expands over an area of approximately 200 km (Roest and Srivastava, 1991; Sartori et al., 1994; Srivastava et al., 1990). However, this eastern segment of the AGL follows a NW-SE direction, connecting the Strait of Gibraltar with the Gorringe Bank (Martínez-Loriente, 2013). At present, the Gulf of Cadiz is subject to compressive stresses. The African plate is moving to the NW-NNW at a rate of 4-5 mm/kyr (Calais et al., 2003; DeMets et al., 2010) (Figure 2.2) with respect to the Eurasian plate, causing frequent low to intermediate magnitude earthquakes (Mw < 5.5) (Silva et al., 2017) as well as less frequent, but larger magnitude events, such as the already cited catastrophic 1755 Lisbon earthquake (Mw > 8.5) and the more recent 1969 event (Mw 7.9 to 8) (Baptista and

Miranda, 2009; Gràcia et al., 2010, 2003a; Martínez-Loriente et al., 2018; Sallarès et al., 2013; Stich et al., 2007a, 2005).

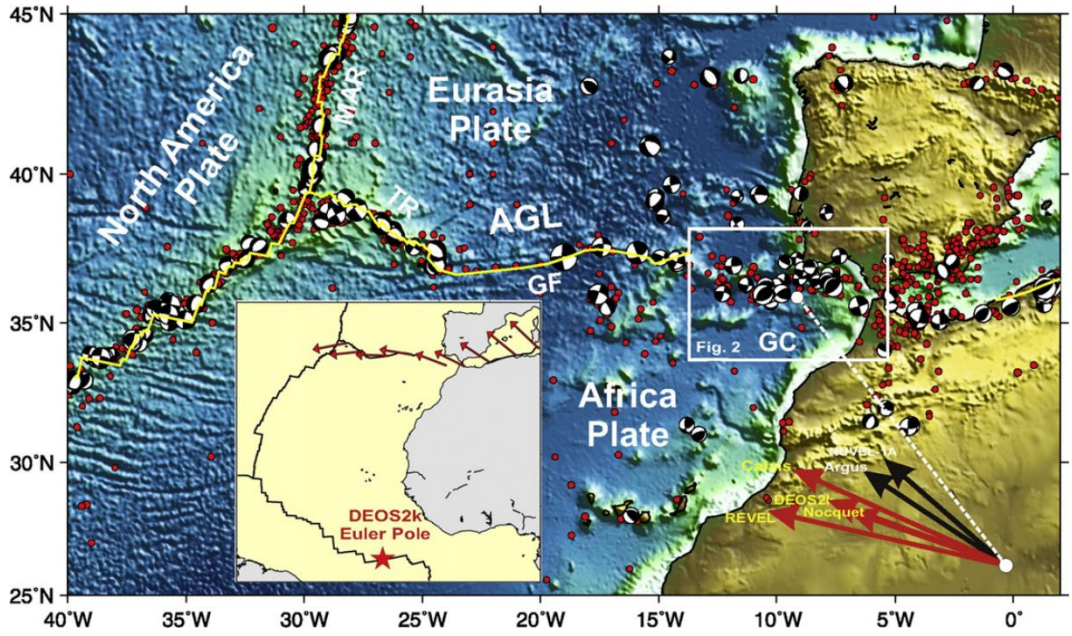

Figure 2.2: Bathymetry map of Iberia, NW Africa and Central Atlantic indicating the main plate boundaries and focal mechanisms. AGL: Azores-Gibraltar Line; GC: Gulf of Cadiz; GF: Gloria Fault; MAR: Mid-Atlantic Ridge; TR: Terceira Ridge; yellow line: plate boundaries. Arrows at right bottom corner show the relative movement of Africa with respect to Eurasia at the centre of the Gulfof Cadiz, deduced from geological indators (black arrows) and from GPS measurements (red arrows). Inset: location of the Euler pole and the relative movement of Nubia with respect to Eurasia. From Zitellini et al. (2009).

The genesis of the current SW Iberian continental margin started in the Lower Jurassic, with the opening of the Central Atlantic Ocean that thinned the lithosphere generating graben and half-graben structures aligned NNE-SSW to NE-SW (Figure 2.3). The extensional stage continued until the Early Cretaceous, with the emplacement of an oblique rifting between Iberian and African plates (Malod and Mauffret, 1990; Pereira and Alves, 2011; Schettino and Turco, 2009). During this period, a pull apart basin generated within a wide transform zone, involving transcurrent faults that controlled the evolution of the South Iberian and North African margin (Gràcia et al., 2003b; Srivastava et al., 1990) (Figure 2.3). At the end of the Cenomanian (Late Cretaceous), the relative trajectory of Africa with respect to Eurasia changed from NW-SE to SW-NE (Srivastava et al., 1990). This change provoked a rotation of Iberia and the beginning of the Pyrenean orogeny starting from the Late Cretaceous and, later on, the Betic orogeny in the Neogene (De Vicente et al., 2011) (Figure 2.3). In the Early Oligocene, the continuous compression activated several new plate boundaries and promoted the development of the AGL (Figure 2.2 and Figure 2.3). The Pyrenees orogeny stopped and the deformation generated by the African and Eurasian convergence started being accommodated by the AGL itself (Martínez-Loriente, 2013; Sartori et al., 1994; Schettino and Turco, 2009).

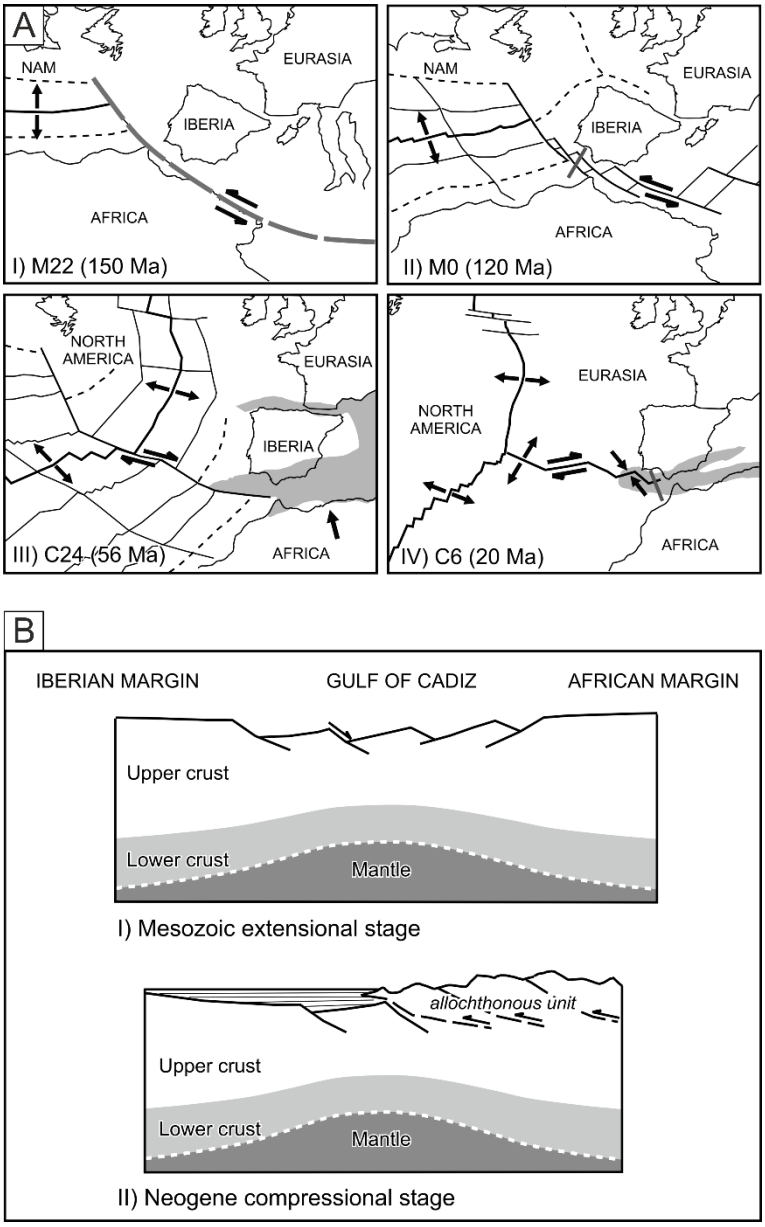

Figure 2.3: A: Schematic representation of the Eurasian, North American and African plates relative movements. Gray areas indicates main compressional zones. B: Simplified cross-section of the Gulf of Cadiz evolution: (I) During the Mesozoic extensional stage and (II) during the Neogene compression (from Gràcia et al. 2003b).

The presence of the Africa-Eurasia plate boundary, however, generated collision and compression events in the present-day SW Iberia during the Late Miocene (Figure 2.3). During the Tortonian (Late Miocene), the regional compression rotated towards the NNW-SSE, reactivating the extensional NE-SW trending reverse faults activated in the Mesozoic as WNW–ESE trending dextral strike slip faults (Gràcia et al., 2003b; Sallarès et al., 2013; Zitellini et al., 2009, 2004). These structures controlled the emplacement of large allochthonous units within the Gulf of Cadiz during this period (Gràcia et al., 2003a; Martínez-Loriente et al., 2018; Terrinha et al., 2009, 2003). Another effect of this collisional period was the closure of the oceanic gateway between the Atlantic Ocean and the Mediterranean Sea about 7-6.1 Ma ago (Flecker et al., 2015). This event isolated the Mediterranean region and started the so-called Messinian Salinity Crisis (5.96-

5.33 Ma) (Krijgsman et al., 1999; Roveri et al., 2014). Only with the beginning of the Pliocene, the emplacement of a transtensional regime re-connected the Atlantic Ocean and the Mediterranean Sea, giving origin to the present-day Strait of Gibraltar that ended the Messinian Salinity Crisis (Krijgsman et al., 1999; Maldonado et al., 1999) (Figure 2.3).

2.2 Alentejo basin: morphology and main structures

The Alentejo basin is located in the northernmost edge of the Gulf of Cadiz, from which is separated by the São Vicente canyon (Figure 2.1 and Figure 2.4). The morphology of the area, dominated by a poorly organized network of gullies and canyons, is the expression of the complex geodynamic history of the Southwest Iberian Margin (SWIM) (Terrinha et al., 2009). Rodrigues et al. (2020) and Teixeira et al. (2019) described three main physiographic domains in the area: shelf, slope (upper, middle and lower), and basin plains. The shelf area corresponds to the shallower domain, down to 200 m of water depth. Submarine canyon heads such as the São Vicente or the Setúbal Canyons or, within the eastern Gulf of Cadiz, the Portimão canyon, are located in this shallower parts of the basin (Figure 2.1). Below the shelf area, the upper slope extends until 750 m water depth, while the middle slope reaches water depths of 1800 m. The main contourite depositional systems in the area, such as the Sines and the Sagres drift, are located within the middle slope domain (Figure 2.1). The lower slope is located at water depths ranging between 1800 and 3000 meters, and hosts the structurally controlled Marquês de Pombal Plateau and Principe de Avis Plateau (Figure 2.1). Steep slopes, often corresponding with fault scarps, mark the transition from the lower slope to the abyssal plains. Within the basin plain domain are located the Infante Don Henrique basin and the Horseshoe Abyssal Plain (Figure 2.1). According to Teixeira et al. (2019), most of the slope instability in the area generates within the steep transition between the lower slope domain and the abyssal plains.

2.2.1 Structural highs, plateaus and abyssal plains

The most conspicuous morphometric structure in the study area is the Gorringe Bank, a Middle Miocene northwest-vergent thrust block, 200 km long and 80 km wide (Lo Iacono et al., 2012; Zitellini et al., 2004) (Figure 2.1). This uplifted block of crustal and upper mantle rocks (Sallarès et al., 2013) rises more than 4500 m above the Horseshoe Abyssal Plain, from 5000 m to less than 100 m below the sea level, and divides the Tagus Abyssal Plain in the north from the Horseshoe Abyssal Plain in the south (Figure 2.1).

The Horseshoe Abyssal Plain constitutes the deepest part of the study area, reaching almost 5000 m water depth. It is extremely flat, with a slope gentler than 0.1º, in contrast with the surrounding slopes ranging between 5º and 10º (Terrinha et al., 2009). The Infante Don Hernique basin is located in shallower water depths than the Horseshoe Abyssal Plain (approximately 4000 m water depth) (Figure 2.1). It lies west from the Gorringe Bank and separates it from the Marquês de Pombal Plateau, a rectangular and rather flat surface (0.5-1.5º in the shallower part to 1-5º towards

the São Vicente Canyon) located at water depths between 1300 and 3800 m water depth. The plateau represents the hanging-wall block of a NW-verging thrust fault, the Marquês de Pombal Fault, and is bounded by the São Vicente Canyon in the east and the fault scarp to the west (Gràcia et al., 2003a, 2003b; Terrinha et al., 2009; Zitellini et al., 2004) (Figure 2.1 and Figure 2.4). The São Vicente Canyon separates the Marquês de Pombal Plateau to the NW from the Sagres Plateau to the SE. Similar to the Marquês de Pombal Plateau, the Sagres Plateau shows a rectangular shape, divided by a diagonal NE-SW trending crest (Terrinha et al., 2009) (Figure 2.1). To the NW, the Sagres Plateau is bounded by the Horseshoe reverse fault scarp (Figure 2.1 and Figure 2.4), which represents also the SE boundary of the Horseshoe Abyssal Plain. Finally, in the northernmost part of the study area there is the Principe de Avis Plateau (2500 to 5000 m water depth) (Rodrigues et al., 2020; Zitellini et al., 2004). It represents the northern and steep limit of the Infante Don Enrique basin, separating this basin from the Setúbal Canyon.

2.2.2 Main faults

The N-S trending Marquês de Pombal reverse fault scarp (Figure 2.4 and Figure 2.5) divides the Marquês de Pombal Plateau in the SE from the Infante Don Henrique basin in the NW, reaching a maximum uplift of 1.2 km in the northern part (Figure 2.1). The fault extends for 55 km in length and dips 24º towards the SE, forming a very steep monoclinal fold at the hanging-wall (Gràcia et al., 2003a; Martínez-Loriente, 2013; Rovere et al., 2004; Terrinha et al., 2003; Zitellini et al., 2001) (Figure 2.1, Figure 2.4 and Figure 2.5). Gràcia et al. (2003a; b) and Terrinha et al. (2003) show that the fault originated as a N-S trending continent-wards directed extensional fault before tectonic inversion processes transformed it in a westward directed thrust. This tectonic inversion led to the development of the Marquês de Pombal Plateau (Figure 2.1 and Figure 2.4). The thrust fault has been described as active in the Quaternary (Gràcia et al., 2003a, 2003b; Terrinha et al., 2009, 2003; Zitellini et al., 2001, 1999), and its steep scarp has originated intense mass wasting activity, as testified by a series of superimposed mass transport deposits detected at its footwall (Figure 2.6) (Collico et al., 2020; Ford et al., 2021; Gràcia et al., 2003a; Mencaroni et al., 2021; Minning et al., 2006; Vizcaino et al., 2006).

The Marquês de Pombal Fault was proposed as a possible source for the 1755 Lisbon Earthquake (Baptista et al., 1998), but further studies demonstrated that the configuration of the fault does not allow to reach the magnitude Mw ≥ 8.5 at the origin of this historic event (Martínez-Loriente et al., 2021; Zitellini et al., 2001). The landslides interpreted to result from the Marquês de Pombal Fault activity have been also initially proposed as a possible contributor for the 1755 Lisbon tsunami (Gràcia et al., 2003a). However, further studies and sediment dating demonstrated that the mass transport deposit related with the 1755 earthquake did most likely produce only a turbidity current event with no tsunamigenic potential (Minning et al., 2006; Vizcaino et al., 2006).

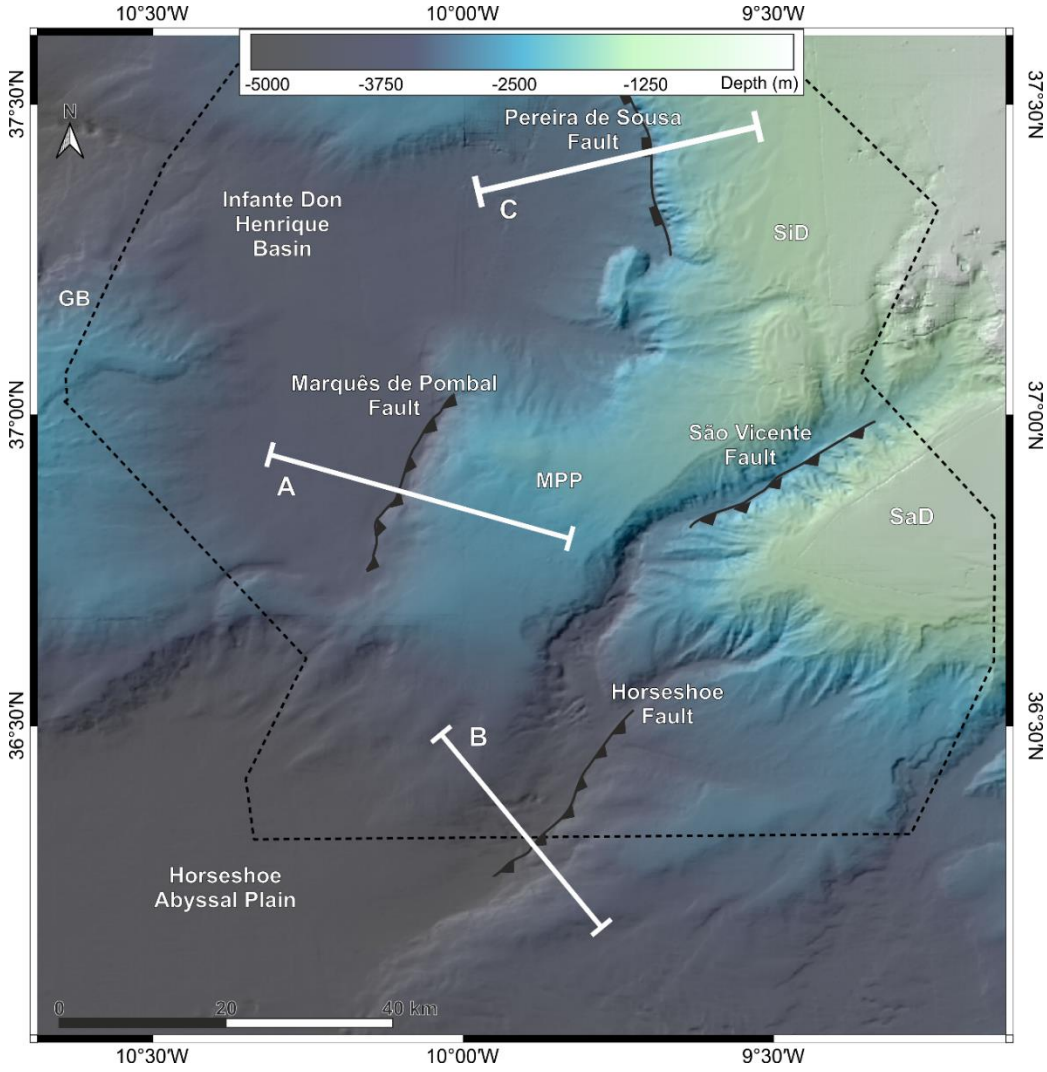

Figure 2.4: Bathymetric map of Alentejo basin and the northern part of the Gulf of Cadiz the main faults described in this paragraph. White lines (A, B, C) indicate the locaiton of the schematic profiles showed in Figs. 2.5 to 2.8. The dashed polygon bounds the area of interest of this study. GB: Gorringe Bank; MPP: Marquês de Pombal Plateau; SaD: Sagres Drift; SiD: Sines Drift.

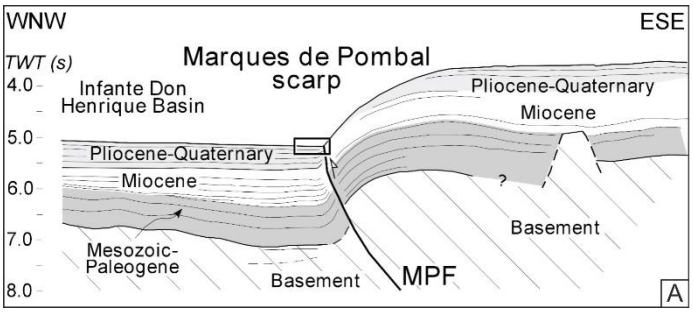

Figure 2.5: Schematic interpretation of multichannel seismic profile across the Marquês de Pombal Fault (MPF). From Gràcia et al. (2003a).

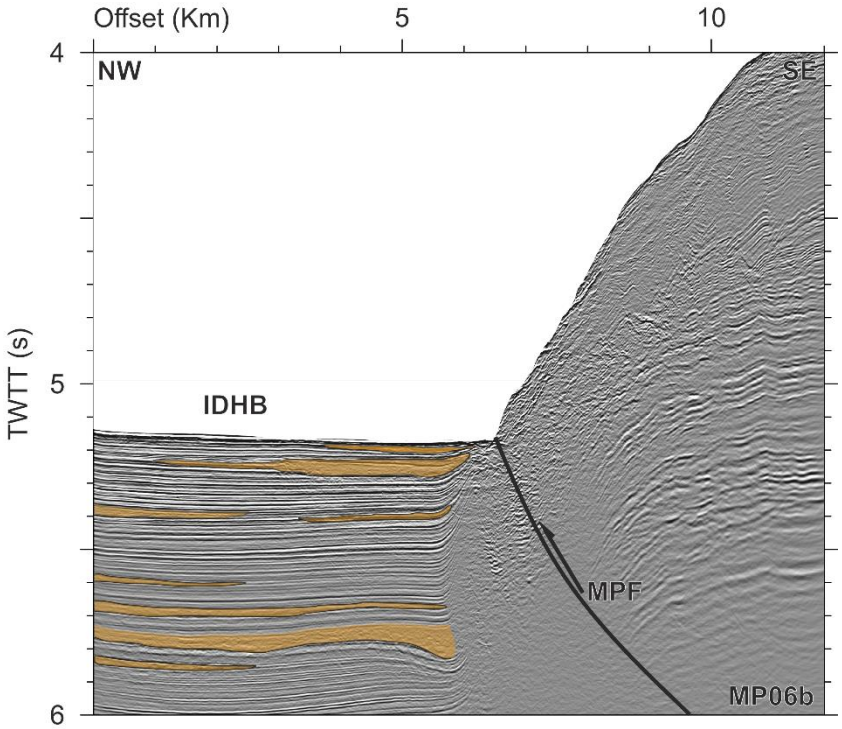

Figure 2.6: MCS profile MP06b showing MTDs (orange bodies) interpreted by Ford et al. (2020) at the footwall of the Marquês de Pombal Fault. IDHB: Infante Don Henrique basin; MPF: Marquês de Pombal Fault. Vertical exaggeration ~ 1:4.

The NE-SW oriented Horseshoe reverse fault scarp (Figure 2.4 and Figure 2.7), which constitutes the eastern boundary of the Horseshoe Abyssal Plain, is well developed only in its northern segment, while in the southern part it has been mainly eroded (Terrinha et al., 2009). The NW-verging blind Horseshoe thrust started to develop during the Miocene and, similarly to the Marquês de Pombal Fault, it has been interpreted to be presently active (Gràcia et al., 2003a, 2003b; Zitellini et al., 2004), as testified by the seismicity cluster in the area (Stich et al., 2007b).

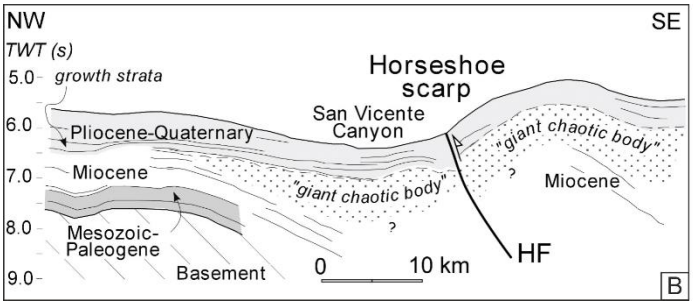

Figure 2.7: Schematic interpretation of multichannel seismic profile across the Horseshoe Fault (HF). From Gràcia et al. (2003a).

The 1400 to 2000 m-high Pereira de Sousa Fault scarp is a steep feature that divides the Sines area from the Infante Don Henrique basin (Figure 2.1 and Figure 2.8). It is a N-S trending normal fault that originated during the Mesozoic rifting (Gràcia et al., 2003a, 2003b; Martínez-Loriente, 2013; Terrinha et al., 2003). The scarp is affected by several erosional features, as testified by many head scarps gullies and MTDs at the footwall (Gràcia et al., 2003a; Teixeira et al., 2019).

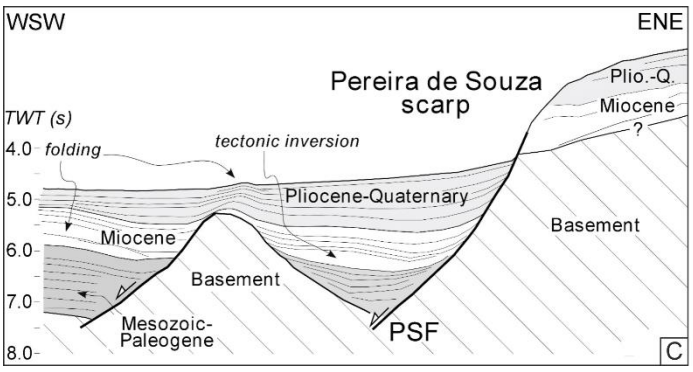

Figure 2.8: Schematic interpretation of multichannel seismic profile across the Pereira de Souza Fault (PSF). From Gràcia et al. (2003a).

Finally, the São Vicente Fault (Figure 2.1) is located along the SE flank of the São Vicente canyon. It is a west-verging NNE-SSW trending thrust that becomes a blind thrust towards the SSW, progressively attenuating until disappearing (Serra et al., 2020).

2.2.3 The São Vicente Canyon

The 150 km long and 20 km wide São Vicente Canyon (Figure 2.1 and Figure 2.9) is the largest canyon in the SWIM and constitutes the southernmost boundary of the Alentejo basin. The development of the canyon is linked to the NE-SW trending São Vicente, Horseshoe and Marquês de Pombal thrust faults (Figure 2.1, Figure 2.4 and Figure 2.5), which evolved under the influence of the present-day African-Eurasian plate convergence (Bartolome et al., 2012; Gràcia et al., 2003b; Martínez-Loriente et al., 2018, 2013; Terrinha et al., 2003; Zitellini et al., 2001). Motion of the two thrust faults since the Late Miocene generated a syncline fold in between them that triggered retrogressive erosion (Serra et al., 2020). The incision of the canyon developed mainly during the late Quaternary and it is nowadays still in progress, transferring sediments from the canyon upper reaches to the Horseshoe Abyssal Plain (Lebreiro et al., 1997; Serra et al., 2020). In its present-day configuration, the canyon head is located in the shelf area, at 200 m water depth, and it is bounded by the Sagres Plateau on its southern side and the Sines Drift and Marquês de Pombal Plateau areas on its northern one (Figure 2.1 and Figure 2.9). Based on the orientation of its longitudinal axis, the canyon can be subdivided into: (i) upper section (between 200 m and 3200 m water depth); (ii) central section (3200 to 4400 m); and (iii) lower section (4400 to 4900 m) (Serra et al., 2020) (Figure 2.9).

The incision is deeper in the upper section and clearly asymmetrical between the two flanks: the SE flank is steeper and incised up to 1700 m, while the north-west flank dips more gently and the incision reaches ~ 1100 m. The shallower part of the central section shows similar asymmetry, while the deeper parts of the central section and the lower section display reversed asymmetry, with the north-west flank incised up to 880 m and the south-east flank up to 750 m (Serra et al., 2020) (Figure 2.9).

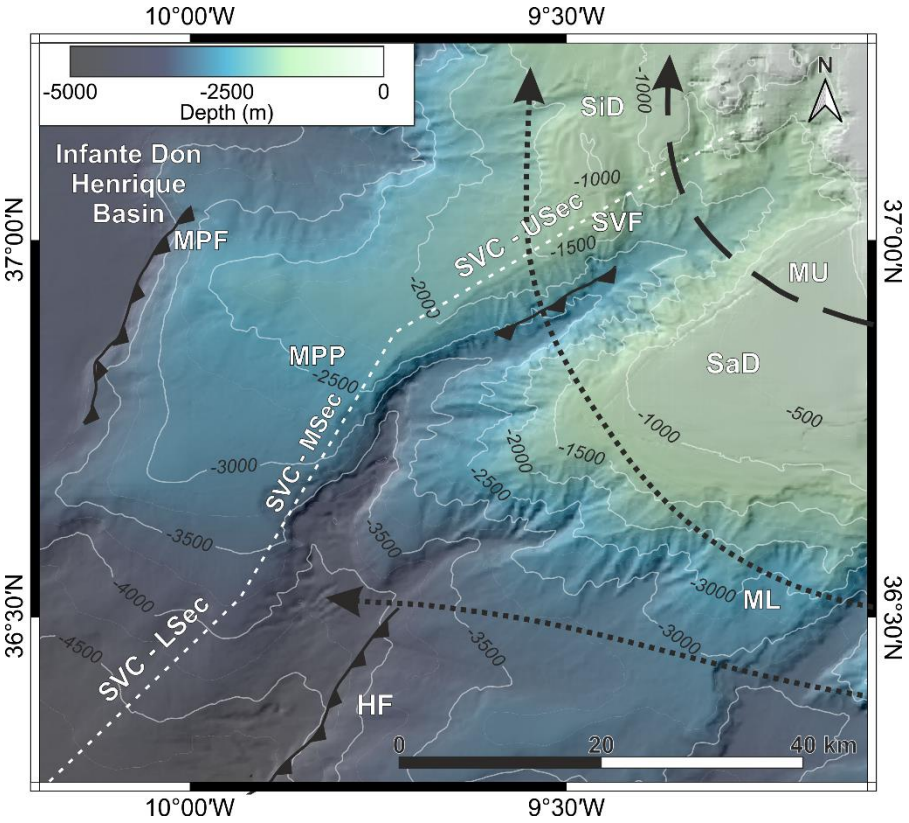

Figure 2.9: Detailed bathymetry of the São Vicente Canyon. SVC-LSec, MSec and USec indicates the Lower, Middle and Upper sectors of the canyon described by Serra et al. (2020). MU: MOW Upper core, ML: MOW Lower core; MMP: Marquês de Pombal Plauteau; SaD: Sagres Drift; SiD: Sines Drift; HF: Horseshoe Fault; MPF: Marquês de Pombal Fault; SVF: São Vicente Fault.

Numerous landslide scars located at the canyon flanks, especially in the north-west upper sector, suggest intense mass wasting activity within the São Vicente Canyon. These mass wasting processes favour the occurrence of turbidity currents travelling along the canyon axis (Serra et al., 2020). Because the canyon extends significantly into the continental shelf, many turbidity currents could also be generated at the shelf edge. Piston cores collected in the Horseshoe Abyssal Plain reveal Quaternary turbidites alternating with hemipelagic sediments covering the entire abyssal plain (Gràcia et al., 2010; Lebreiro et al., 1997). This suggests that the turbidity currents generated within the São Vicente Canyon are able to travel the entire 356 km length of the Horseshoe Abyssal Plain, from the mouth of the São Vicente Canyon to its westernmost end.

2.3 Oceanographic setting

Three major water masses are present in the SWIM: the Atlantic Inflow Water (AIW), the Mediterranean Outflow Water (MOW) and the North Atlantic Deep Water (NADW) (Figure 2.10). The AIW is the shallowest current, and flows southward entering the Mediterranean Sea (Serra et al., 2005; Thorpe, 1975). In the proximity of the Strait of Gibraltar, the AIW is characterized by high temperatures (12 to 16˚C) and moderate salinities (34.7 to 36.25‰) (Llave et al., 2006). Flowing below the AIW, the MOW is a current generated by the warm (13˚C average temperature) and saline (37.2‰ average salinity) waters from the Mediterranean Sea that leave

the Strait of Gibraltar, deflect to the west due to the Coriolis force and flow northward along the Atlantic continental slope of the Iberian Peninsula (Figure 2.10). The onset of the MOW began with the opening of the Gibraltar gateway, 5.3 Ma ago, and gradually increased to become a major contributor to the North Atlantic oceanic circulation in the Late Pliocene (Hernández-Molina et al., 2014b). Since then, it has had a major influence on the sedimentation of the entire SWIM, generating one of the most extensive contourite depositional systems in the world (Ambar et al., 1976; Ambar and Howe, 1979; Hanquiez et al., 2007; Hernández-Molina et al., 2002; Llave et al., 2007a; Mulder et al., 2003). The velocity of the MOW varies from 2.5 ms^{-1} at the Strait of Gibraltar, where the gateway narrows the current to a width of approximately 10 km (Baringer and Price, 2002; Hernández-Molina et al., 2016a; Mulder et al., 2003) to less than 0.2 ms^{-1} off Cape São Vicente (Johnson et al., 2002; Mulder et al., 2003). While moving northward, the MOW flows above the colder (3 to 8˚C) and less saline (34.95 to 35.2‰) NADW (Hernández-Molina et al., 2014a; Llave et al., 2006), a current that flows from the Greenland–Norwegian Sea region southward (Figure 2.10). The MOW begins to raft above the NADW in correspondence with the Cape São Vicente, where it reaches a neutral buoyancy and detaches from the seabed (Ambar and Howe, 1979; Hernández-Molina et al., 2016a).

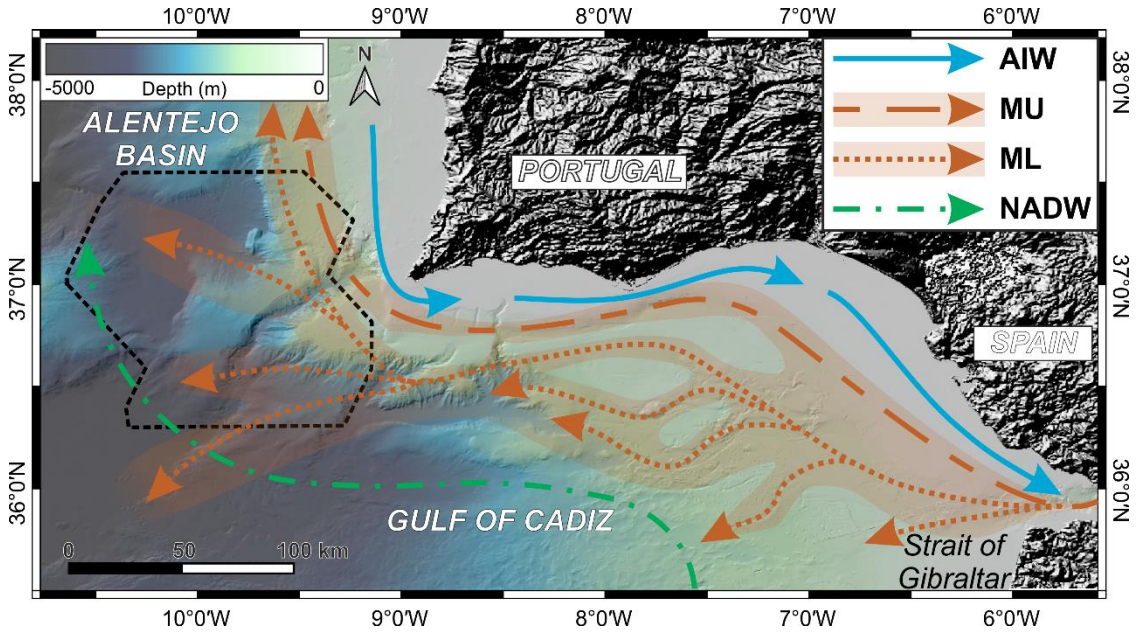

Figure 2.10: Bathymetric map of the Southwest Iberian Margin (SWIM) indicating the main water masses. Dashed polygon indicates the area of interest of this thesis. AIW: Atlantinc Inflow Water; MU: Mediterranean Outflow Water (MOW) Upper core; ML: Mediterranean Outflow Water (MOW) Lower core; NADW: North Atlantic Deep Water.

The complex seafloor morphology of the SWIM, dominated by a set of continuous crests and troughs, diapirs and canyons, transforms the MOW single-stream, dense overflow into a multicore saline plume. Distinct channels located in the upper and mid slope constrain the MOW spreading and promote the formation of several MOW branches, that travel with velocity, salinity and density values that increase with depth (Sánchez-Leal et al., 2017) (Figure 2.10). The two major MOW pathways that are generally distinguished in the literature are the MOW upper core (MU),

warmer and less saline, that flows between 500 m and 800 m, and the deeper MOW lower core (ML), flowing between 800 m and 1500 m (Ambar and Howe, 1979; Cacho et al., 2000; Mulder et al., 2003; Serra et al., 2005). The differentiation between upper and lower core is most likely directly inherited from the two water masses exiting the Mediterranean Sea: the Western Mediterranean Deep Water (WMDW) and, especially, the Levantine Intermediate Water (LIW) (Hernández-Molina et al., 2014a; Rogerson et al., 2012a; Sánchez-Leal et al., 2017). Seasonal climatic variations and longer term changes (e.g. glacial and interglacial cycles) influence the production of the LIW. During cold periods, lower water temperatures and reduced freshwater input into the Mediterranean basin (Bahr et al., 2015) increase the density of the current exiting the Strait of Gibraltar, resulting in an enhanced ML circulation and favouring periods of sand deposition or erosion. On the other hand, higher Mediterranean water temperatures during interglacial periods such as at present, favour a more vigorous MU circulation in the upper slope (Hernández-Molina et al., 2014b; Jiménez-Espejo et al., 2015; Rogerson et al., 2005).

2.4 Depositional history

The sedimentary record of the SWIM started developing in the Mesozoic over a deformed Paleozoic basement (Pereira, 2013). A multitude of studies have described in great detail the stratigraphic architecture and sediment distribution of the Gulf of Cadiz starting from the emplacement of the contourite depositional systems from the Late Miocene (e.g. Mulder et al., 2003; Llave et al., 2007a; Stow et al., 2013b; Hernández-Molina et al., 2016; Rodrigues et al., 2020). However, there is not as much information on the pre-Miocene stratigraphy of the area, which is mostly restricted to onshore outcrops and few commercial wells located in the inner part of the Gulf of Cadiz. The data from these outcrops and wells have been correlated with relatively deep, low resolution MCS profiles offshore (Alves et al., 2003; Pereira, 2013; Pereira and Alves, 2013).

2.4.1 SWIM stratigraphy

The brief summary of the pre-Miocene stratigraphic units for the Alentejo basin reported herein is mainly based on the comprehensive description provided by Pereira (2013) (and the summary focused on the Alentejo basin based provided by Rodrigues, 2017). Those studies are based on outcrops, exploration wells and dredges and with reference to the regional units described in other areas within the SWIM (e.g. Algarve, Lusitanian, Peniche and Porto basin).

2.4.1.1 The Palaeozoic Basement

The Palaeozoic units in the SWIM are made of a deformed succession of the South Portuguese zone (Oliveira, 1984) and are visible as outcrops in Southwest Portugal. Depending on the locations, Palaeozoic units include (Pereira, 2013):

2.4.1.2 Mesozoic deposition

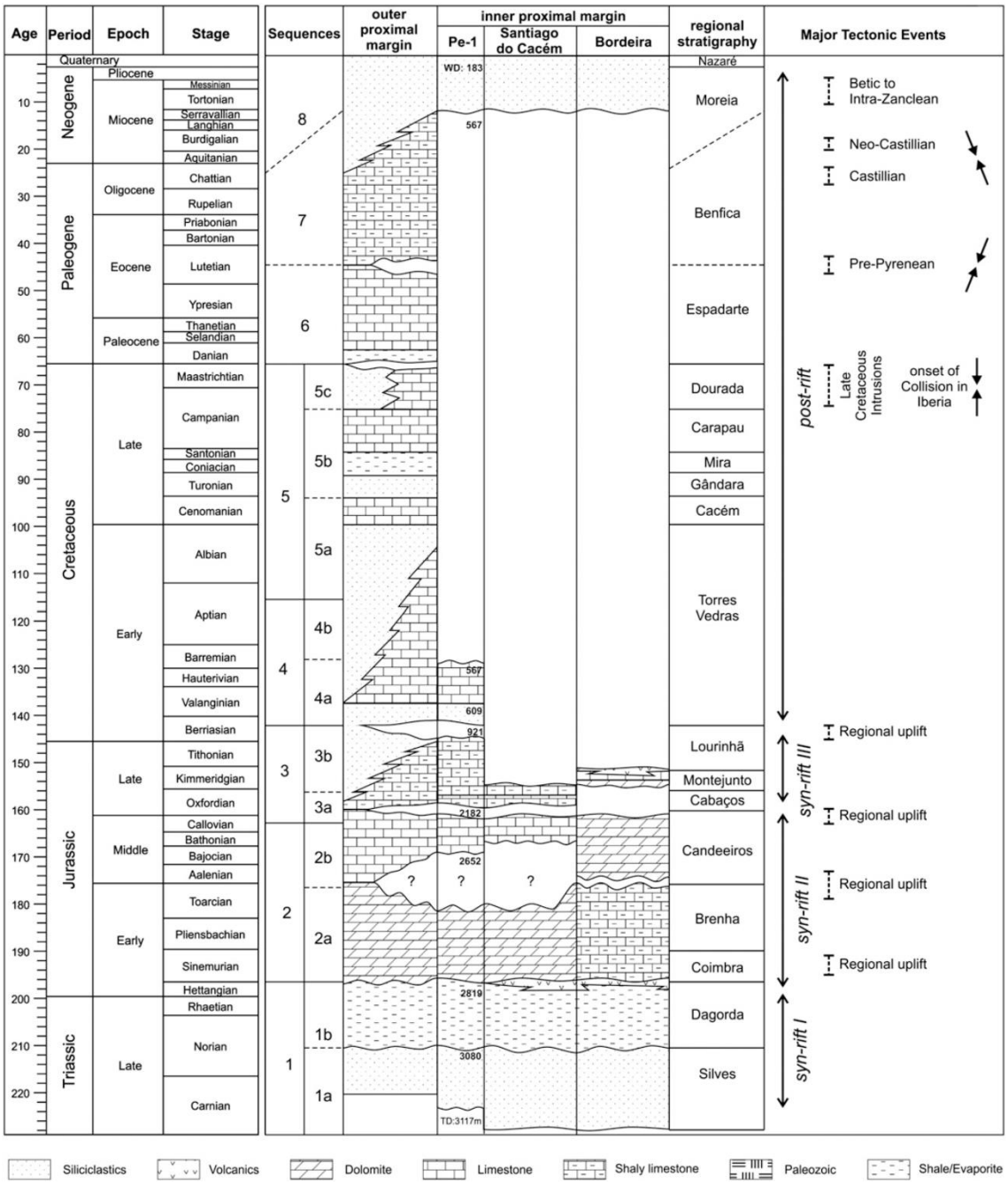

Figure 2.11: Lithostratigraphy and seismic stratigraphy of the Southwest Iberian margin with the major tectonic events of the Alentejo basin. From Pereira & Alves (2013). Location of exploration well Pescada-1 (Pe-1) and outcrops Santiago de Cacem and Bordeira are showed in Figure 2.12.

- Tercenas Formation (Late Devonian): deep marine shales and sandstones;
- Volcanic Complex of Cercal (Late Devonian);
- Carrapateira Group (Carboniferous): includes the Bordalete, Murração and Quebradas Formations, composed by metasedimentary sandstones, silts, black shales, limestones, schists;
- Mira Formation (Carboniferous): turbidites, conglomerates and sporadic interbedded limestones.
- The Brejeira Formation (Late Carboniferous): widespread turbidites.

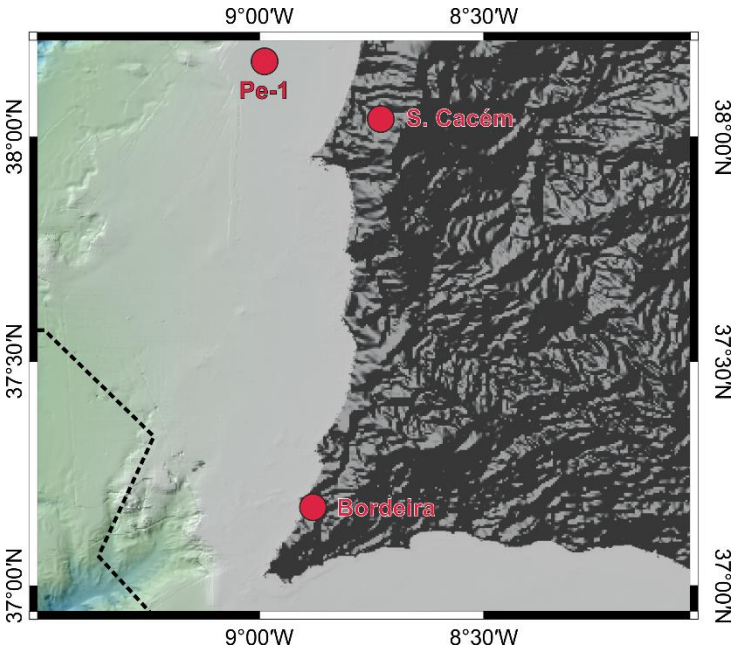

Figure 2.12: Location of exploration well Pe-1 and outcrops Santiago do Cacém (S. Cacém) and Bordeira mentioned in Figure 2.11.

The Mesozoic deposits in the SWIM start with the Silves Formation (Late Triassic), composed by fluvial red beds, with rarer marls and dolomites (Inverno et al., 1993; Ribeiro et al., 1987). Above it, the Dagorda Formation (Norian-Hettangian) is characterized by evaporites, dolomites, marls and shales (Inverno et al., 1993; Oliveira, 1984; Ribeiro et al., 1987) (Figure 2.11).

With the opening of the Central/Northern Atlantic, in the Early Jurassic the SWIM was under shallow marine condition and carbonate succession started developing (Azerêdo et al., 2002). In the Alentejo basin, the Coimbra Formation (Early Jurassic), composed by dolomitic carbonates, represents this phase. During the Pliensbachian, tectonic subsidence generated deep water conditions in the southern Alentejo basin with the emplacement of the marly limestones of the Forno unit (Oliveira, 1984; Ribeiro et al., 1987), while in other areas of the basin dolomite diagenesis developed (Inverno et al., 1993) (Figure 2.11).

A period of regional uplift during the Toarcian-Aalenian generated a depositional hiatus that lasted until the Bajocian, when carbonate deposition started again (Ribeiro et al., 1987; Terrinha et al., 2002). The carbonate ramp shallowed and the landward domains during this phase were uplifted to exposure and eroded, generating an extensive unconformity from the Mid-Callovian to the Early Oxfordian (Azerêdo et al., 2002; Mougenot, 1979). The dolomitic carbonates generated in this period gave origin to the Dolomias Inferiores unit (Toarcian – Callovian) in Bordeira (Figure 2.11 and Figure 2.12), while in the Santiago do Cacém (Figure 2.11 and Figure 2.12) the Bathonian-Callovian was characterized by open, shallow marine limestone with marls and dolomites that compose the Rodeado and Monte Branco Formations (Inverno et al., 1993).

A new rift phase and tectonic subsidence stage during the Late Jurassic generated a widespread unconformity during the Late Callovian – Middle Oxfordian (Azerêdo et al., 2002). This period is followed, in the Alentejo basin, by the deposition of lacustrine to shallow marine marls and limestone of the Cabaços Formation (Early Oxfordian) (Azerêdo et al., 2002), which underlie the Oxfordian-Kimmeridgian deep-marine limestone deposited during the maximum period of subsidence (Alves et al., 2009). Shallow marine sandstones, pelagic limestones and marls characterize the Late Jurassic deposits in the Alentejo basin (Inverno et al., 1993). In the Berriasian, the last rifting phase in the SWIM is marked by a regional angular unconformity. No sediment deposition is associated with this period in the Alentejo basin, while siliciclastic and carbonate deposition took place in other parts of the SWIM (Mougenot, 1979) (Figure 2.11).

2.4.1.3 Cenozoic deposition

In the proximal areas of the Alentejo basin, the Cenozoic is composed by Paleogene to Quaternary sediments, sourced by surrounding areas and by canyon sediment bypass (Alves et al., 2003; Oliveira, 1984; Rodrigues, 2017). The Paleogene deposition in the offshore Alentejo basin was dominated by limestones, dolomites and continental to shallow marine siliciclastic sediments that form the Benfica and Moreia Formations (Mougenot, 1979). Margin inversion during the Eocene possibly generated periods of mass movement deposits (Mougenot, 1979; Rodrigues, 2017) while extended erosional surfaces generated by tectonic uplift of the margin characterize the Oligocene (Mougenot, 1979). A rise in sea-level from the Chattian onwards covered these erosional surfaces with fault-bounded successions (Alves et al., 2000). Finally, the beginning of the Neogene was characterized by the deposition of shallow marine siliciclastic sediments from the Burdigallian to the Miocene (Mougenot, 1979). During the Pliocene to the Pleistocene, limestones and marls were deposited in deep waters, while, starting from the end of the Miocene, the extensive contourite depositional system generated by the MOW started dominating the deposition in the upper and middle SWIM continental slope (Hernández-Molina et al., 2016a) (Figure 2.11 and Figure 2.13).

2.4.2 Contourite depositional system in the Alentejo area

The Plio-Quaternary sedimentary history of the SWIM is strictly connected with the MOW hydrodynamic conditions and its variability through time (Hanquiez et al., 2010; Hernández-Molina et al., 2014a, 2014b; Llave et al., 2011, 2007b; Lofi et al., 2016; Mestdagh et al., 2019; Mulder et al., 2003; Stow et al., 1986). An extensive contourite drift extends along the entire margin, from the Strait of Gibraltar to Cape São Vicente (Brackenridge et al., 2013; Hernández-Molina et al., 2011; Llave et al., 2019; Mulder et al., 2003). The drift consists of mixed terrigenous and biogenic sediments, where the siliciclastic fraction enters the basin through Iberian rivers, especially the Guadalquivir River (Hernández-Molina et al., 2016a; Mulder et al., 2003; Nelson et al., 1999). The MOW transports, deposits and reworks the sediments in the SWIM, resulting in

varying grain size that reflects the hydrodynamic conditions of the bottom current. Offshore Cape São Vicente the deposits are characterized by silt and mud waves, with sporadic presence of sand layers (Brackenridge et al., 2018; Mulder et al., 2003).

The Integrated Ocean Drilling Program (IODP) Expedition 339 acquired borehole geophysical and geological data along a transect, including six sites following the path of the MOW in the Gulf of Cadiz and in the Alentejo basin (Hernández-Molina et al., 2016a; IODP Expedition 339 Scientists, 2013a). Significant regional unconformities have been interpreted as periods of MOW intensification and are typically associated with local erosion, dolomite diagenesis and mass movements originating from the shallower parts of the slope (Brackenridge et al., 2013; Hernández-Molina et al., 2016a, 2002; Llave et al., 2007a, 2006). Three main hiatuses are especially evident both in seismic profiles and from the recovered cores at 3.2 to 3 Ma (Late Pliocene Discontinuity, LPD), at 2.4 to 2.1 Ma (Early Quaternary Discontinuity, EQD) and at 0.8 Ma (Middle Pleistocene Discontinuity, MPD).

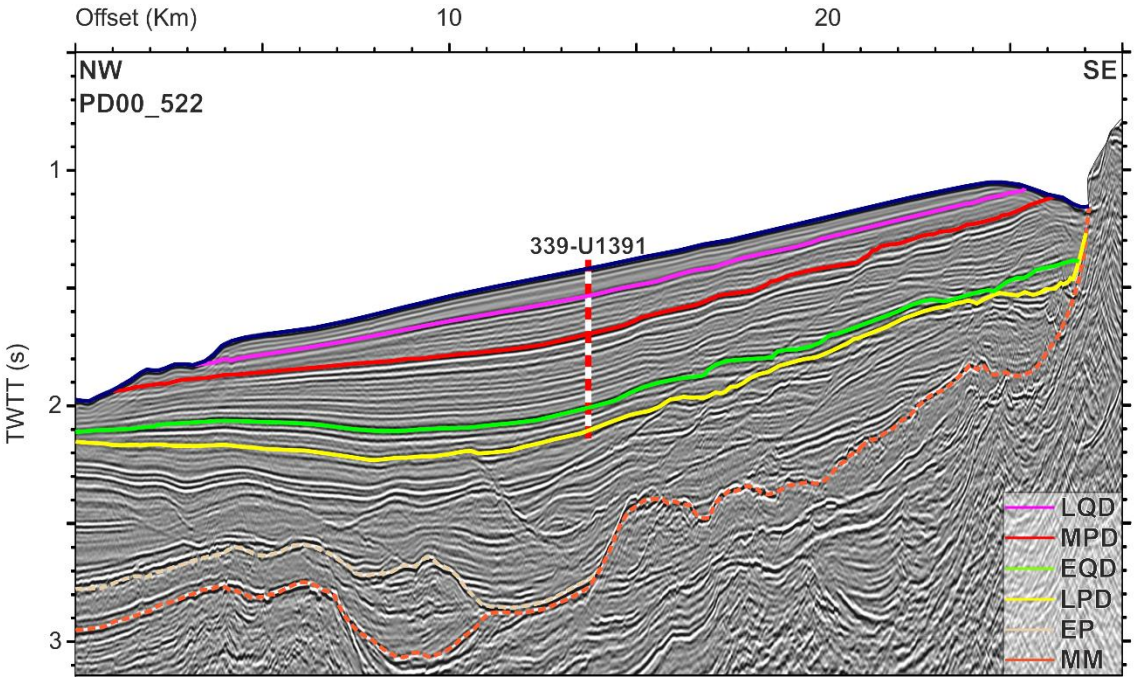

Figure 2.13: Stratigraphic interpretation of MCS line PD00-522. Horizons LPD (Late Pliocene Discontinuity), EQD (Early Quaternary Discontinuity), MPD (Middle Pleistocene Discontinuity) and LQD (Late Quaternary Discontinuity) correspond to the main Plio-Quaternary discontinuities described by Hernández-Molina et al. (2016) after the drilling of borehole 339-U1391. MM (Middle Miocene) and EP (Early Pliocene) refer to deeper horizons mapped by Martínez-Loriente et al. (2018, 2013). Profile image modified after Hernández-Molina et al. (2016).

A fourth, younger unconformity, more pronounced in the northern part of the Gulf of Cadiz and in the Alentejo basin, is due to a hiatus that took place approximately between 0.4 Ma and 0.3 Ma (Late Quaternary Discontinuity, LQD) (Hernández-Molina et al., 2016a; Lofi et al., 2016) (Figure 2.13).

Although influence of the MOW on the sediment distribution in the deep part of the Alentejo basin is restricted to some studies on slope failures detaching from drift areas (Neves et al., 2016;

Teixeira et al., 2019), the depositional evolution of the Sines Drift (middle slope) has been recently documented by Rodrigues et al. (2020) (Figure 2.14). This study relates the core data from Site U1391 with the stacking patterns that characterize different stages of the Sines Drift deposition. Three main stages of contourite sedimentation have been recognized for the Sines Drift that could be related more in general to the Alentejo basin middle slope.

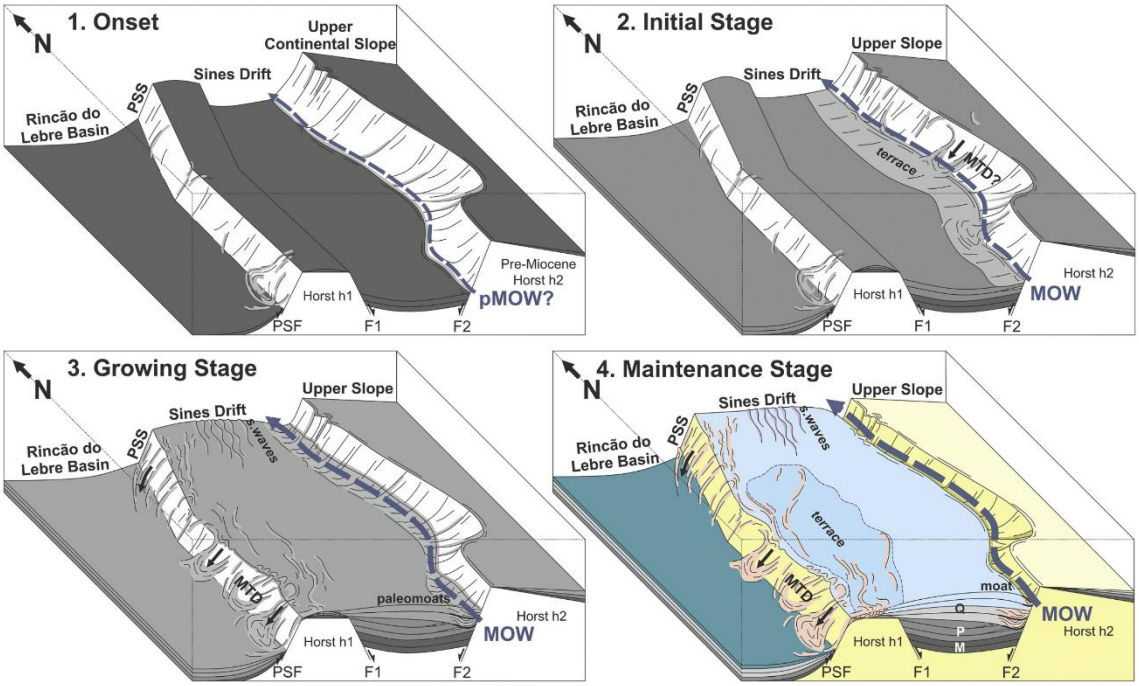

Figure 2.14: Depositional evolution of the Sines Drift (Alentejo margin middle slope) proposed by Rodrigues et al. (2020). Rincão do Lebre basin: subsector of the Infante Don Henrique basin; PSF: Pereira de Sousa Fault; PSS: Pereira de Sousa Scarp. From Rodrigues et al. (2020).

2.4.2.1 Initial stage – Late Miocene to Late Pliocene

Even if the beginning of contourite deposition in the Gulf of Cadiz is typically assumed to take place in the beginning of the Pliocene (Hanquiez et al., 2010; Hernández-Molina et al., 2014a, 2014b; Llave et al., 2011, 2007b; Lofi et al., 2016; Mulder et al., 2003; Stow et al., 1986), the Sines drift shows signs of ancient contourite deposition starting from the Late Miocene (5.33 Ma). This preliminary phase of contourite formation is expressed with sheeted drifts confined within paleo-reliefs, generated during previous extensional phases (Rodrigues et al., 2020).

The beginning of the Pliocene marks the beginning of the modern contourite system deposition (Figure 2.14). The drift was initially emplaced by weak bottom current, as suggested by low sedimentation rates (13 cm/kyr) (Hernández-Molina et al., 2016a; IODP Expedition 339 Scientists, 2013a; Rodrigues et al., 2020; Stow et al., 2013b) and by the fine-grained composition of the deposit (IODP Expedition 339 Scientists, 2013b). Recovery of mud rich contourite together with biogenic carbonate, dolomite mudstone and debrites associated with this early stage interval (i.e., until LPD) at Site U1391 (IODP Expedition 339 Scientists, 2013c) indicates that this initial stage of contourite deposition was not entirely dominated by alongslope processes, since downslope sediment transport might have played an important role (Rodrigues et al., 2020). The

initial stage of weak paleo-MOW has been associated with humid conditions in the Mediterranean basin until 3.4 Ma. Increasing summer aridity in the Mediterranean basin from the Late Pliocene, on the other hand, led to the production of cooler, saltier and denser MOW, with consequent enhancement of the current (Bahr et al., 2015; Hernández-Molina et al., 2014b).

2.4.2.2 Growing stage – Late Pliocene to Middle Pleistocene

Starting from the Early Quaternary, the growing stage of the contourite system begins (Figure 2.14). This stage is marked by the transition from sheeted to mounded drift in the Sines area (Rodrigues et al., 2020). Sedimentation rate increases from 17 cm/kyr between 2.58 and 1.5 Ma to 27 cm/ky after 1.5 Ma (Hernández-Molina et al., 2016a; IODP Expedition 339 Scientists, 2013a). The deposit shifted from fine, biogenically dominated sediments, debrites and biogenic contourites that dominated the initial stage to mud-rich contourites (IODP Expedition 339 Scientists, 2013b, 2013c; Rodrigues et al., 2020). This change has been related to an important global cooling period and sea level fall that took place in correspondence of the EQD, and that might have let to denser MOW exiting the Mediterranean basin, thus to more active circulation in the North Atlantic (Bartoli et al., 2005; Hernández-Molina et al., 2016a, 2014b; Rodrigues et al., 2020).

2.4.2.3 Maintenance stage – Middle Pleistocene to Present Day

Starting from the MPD, the transition from mounded to plastered stacking pattern in the Sines Drift indicates the transition from the growing to the maintenance stage of the drift (Rodrigues et al., 2020) (Figure 2.14). Sedimentation rates increases to > 27 cm/kyr, and levels of coarser sediment start being deposited (Brackenridge et al., 2018; Hernández-Molina et al., 2016a; IODP Expedition 339 Scientists, 2013b). The almost constant supply of contouritic sediments favour processes of slope instability and emplacement of MTDs towards deeper parts of the basin (Neves et al., 2016; Teixeira et al., 2019). The occurrence of discontinuities such as the MPD (also associated with higher sand deposition) and LQD marks periods of MOW enhancement related with global cooling events (Bartoli et al., 2005; Hernández-Molina et al., 2016a, 2014b; Rodrigues et al., 2020).

2.5 Other areas

Besides the Alentejo basin (Figure 2.15A), this study makes use of hydromechanical properties of hemipelagic sediment samples collected from other two oceanic regions: the Grenada basin (offshore Martinique) (Figure 2.15B) and the Ursa basin (Gulf of Mexico) (Figure 2.15C). The areas represent very different depositional settings, and have in common well-documented subaqueous slope instabilities processes (e.g. Deplus et al., 2001; Sawyer et al., 2007; Flemings et al., 2008; Urgeles et al., 2010; Le Friant et al., 2015; Llopart et al., 2021).

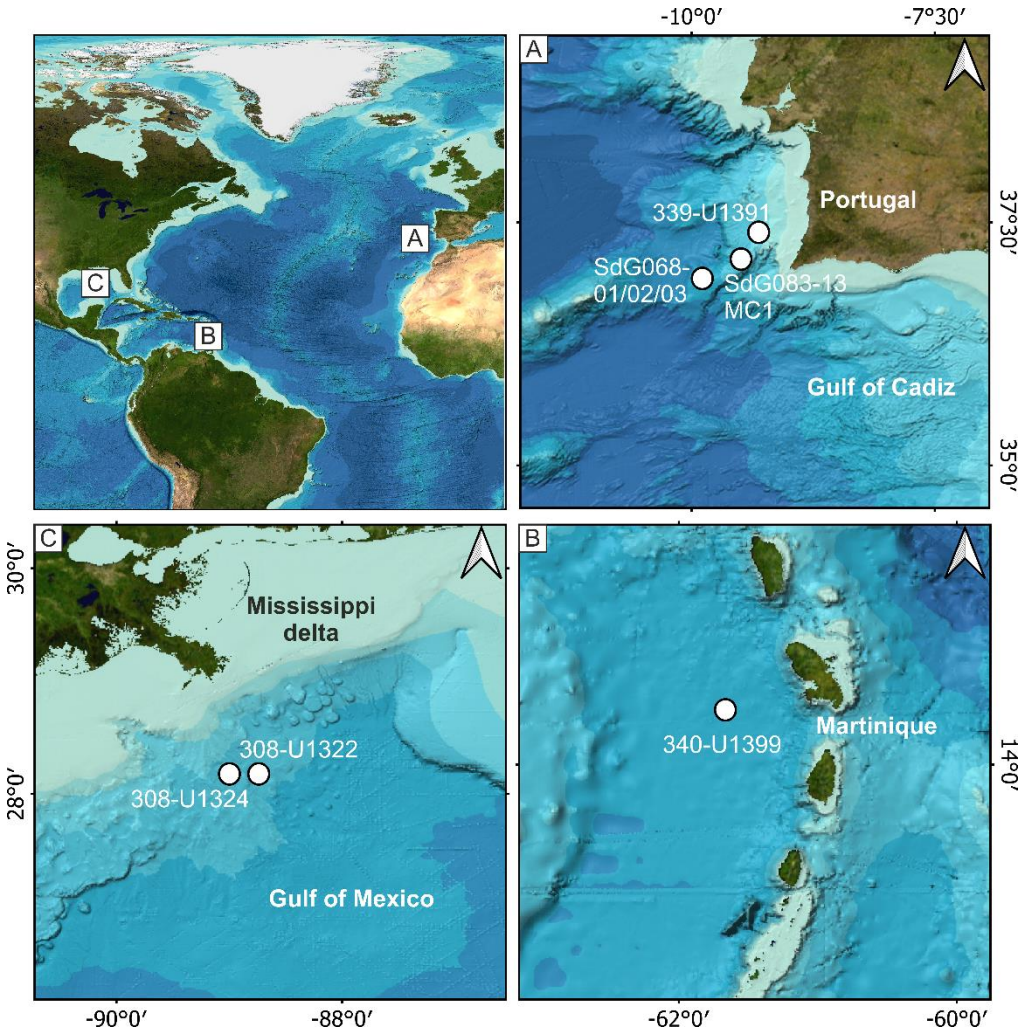

Figure 2.15: Areas considered in this study: (A) Alentejo basin, (B) Grenada basin and (C) Ursa basin. White circles indicate core locations (see description in section 3.2.3).

2.5.1 Grenada basin (offshore Martinique)

Martinique is a volcanic island that originated from the westward subduction of the Atlantic oceanic crust beneath the Caribbean plate that gave origin to the Lesser Antilles islandic arc (Westercamp et al., 1972) (Figure 2.15B). Volcanic activity took place in the island since 40 Ma, although in the northern part it started ~ 5.3 Ma and it has been particularly intense especially from 550 ka to present (Germa et al., 2011, 2010). The Montagne Pelée Volcano is located in Northern Martinique, and experienced three major flank collapses dated 127, 127-45 and 36 ka, respectively (Brunet et al., 2016; Germa et al., 2011; Le Friant et al., 2015). The three events removed tens of cubic kilometres of the western subaerial flank and generated three Debris Avalanches Deposits (DAD) (Le Friant et al., 2015, 2003), visible from bathymetric data as distinct lobes, within the 2900 m deep back-arc Grenada basin, located west of Martinique (Figure 2.16 and Figure 2.17).

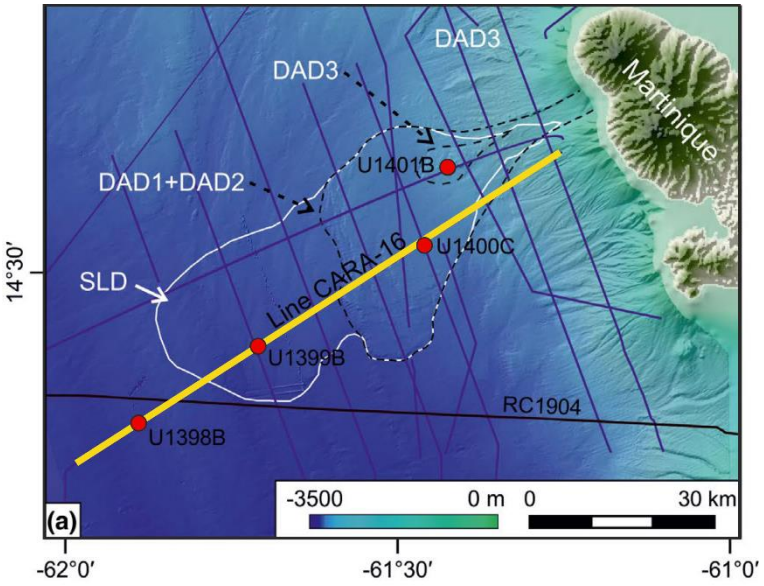

Figure 2.16: Shaded relief showing the location of seismic line CARAVAL-16 (yellow line) (Figure 2.17) and the IODP sites drilled in the area during expedition 340 (red dots). The distribution of Debris Avalanche Deposits (black dashed lines) from Le Friant et al. (2015) and Submarine Landslide Deposit (white line) from Brunet et al. (2016) are showed. Modified after Llopart et al. (2021).

Besides DAD, the Grenada basin represents a major depocenter for mass-wasting, turbiditic and hemipelagic deposits (Boudon et al., 2007; Deplus et al., 2001). The MTDs extend offshore Martinique 40 km beyond the debris avalanche deposits, as testified by the series of boreholes drilled during the IODP expedition 340 in 2012 (Brunet et al., 2016; Deplus et al., 2001; Le Friant et al., 2015, 2013) (Figure 2.16 and Figure 2.17). Numerical models show that emplacement of the DADs favoured the generation of these submarine landslides. The almost instantaneous deposition of the DADs, in fact, led to the development of high overpressure ratios and created localized fluid flow patterns that reduced the sediments' bearing capacity and shear strength, favouring their mobilization (Llopart et al., 2021). Recurrent earthquakes related with volcanic activity has also favoured the emplacement of frequent turbidites, that increase the sedimentation rate in the deep part of the basin up to 20 cm/kyr (Le Friant et al., 2015). The volcanic setting has also had a strong influence over the hemipelagic sediments composition in the area, which are influenced by volcanic ashes released by the extensive series of volcanos in the Lesser Antilles volcanic arc (Wiemer and Kopf, 2015).

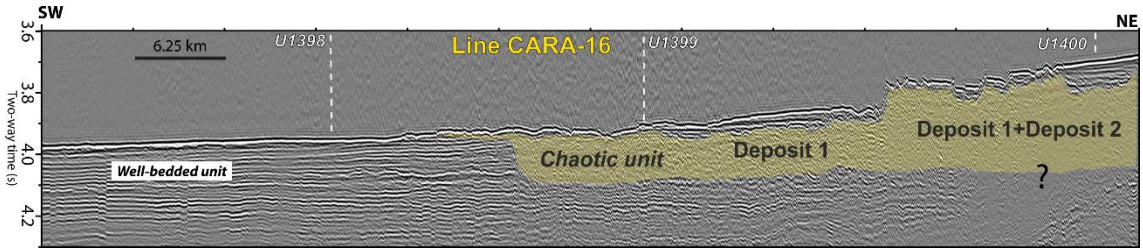

Figure 2.17: Seismic reflection profile revealing the presence of chaotic deposits offshore Martinique from Le Friant et al. (2015). See Figure 2.16 for location of the profile.

2.5.2 Ursa basin (Gulf of Mexico)

The Ursa basin is located in the NE Gulf of Mexico, 210 km S-SW of New Orleans, between 800 and 1400 m water depth (Figure 2.15 and Figure 2.18). The region is bounded to the west by the Mars Ridge, a north-south trending bathymetric high related to a buried channel-levee system (Winker and Booth, 2000). The basin was affected by intense deposition of sediments derived from the Mississippi River during the Late Pleistocene and depositing upon a salt substrate (Worrall and Snelson, 1989). The deposition started in response to the North American continental glaciation, and it is associated with four channel-levee systems that filled the region and migrated westward, transporting sediments from the continental margin to the Mississippi Fan during the Late Pleistocene (Winker and Booth, 2000).

Four depositional elements constitute the stratigraphy of the Ursa basin in the last 70 kyr and are described by Sawyer et al. (2007) (Figure 2.18):

- The Blue Unit: interbedded sand and mud, generated by turbidity currents that ponded within a depression in the Ursa Region.
- The Ursa Canyon channel-levee system: composed by channel fills, channel-margin slides and levees. It is composed by sand, sand transitioning upwards to mud, and thin-bedded sand and mud.
- The Southwest Pass Canyon channel-levee system: alternation of sand and mud layers.
- Mass transport deposits: present within mud-rich levee deposits generated above the Blue Unit.

Above those units, a mud-drape deposited during the last ~20ky (Behrmann et al., 2006; Flemings et al., 2008).

This area is characterized by well-documented overpressure due to sedimentation rates exceeding 25 m/ky during some intervals in the Pleistocene (Flemings et al., 2006; Sawyer et al., 2007; Urgeles et al., 2010). IODP expedition 308 performed *in-situ* pore pressure measurements using the DVTPP and T2P piezoprobes (see Flemings et al., 2008; Long et al., 2008 for further details on the measurements), and documented high overpressure associated with the high sedimentation rates in the area and lateral transfer of fluids (Expedition 308 Scientists, 2005). Previous studies (Urgeles et al., 2010, 2007) modelled the stratigraphic evolution of the margin considering the physical properties of the different units in the Ursa basin, with the aim of understanding the present-day pore pressure condition revealed by the *in-situ* measurements. Despite the significant scatter observed in the direct overpressure measurement, especially within the uppermost hemipelagic drape, 1D simulations reproduced the general vertical overpressure distribution at Site U1324 (for more information about previous overpressure modelling see Stigall & Dugan, 2010; Urgeles et al., 2010).

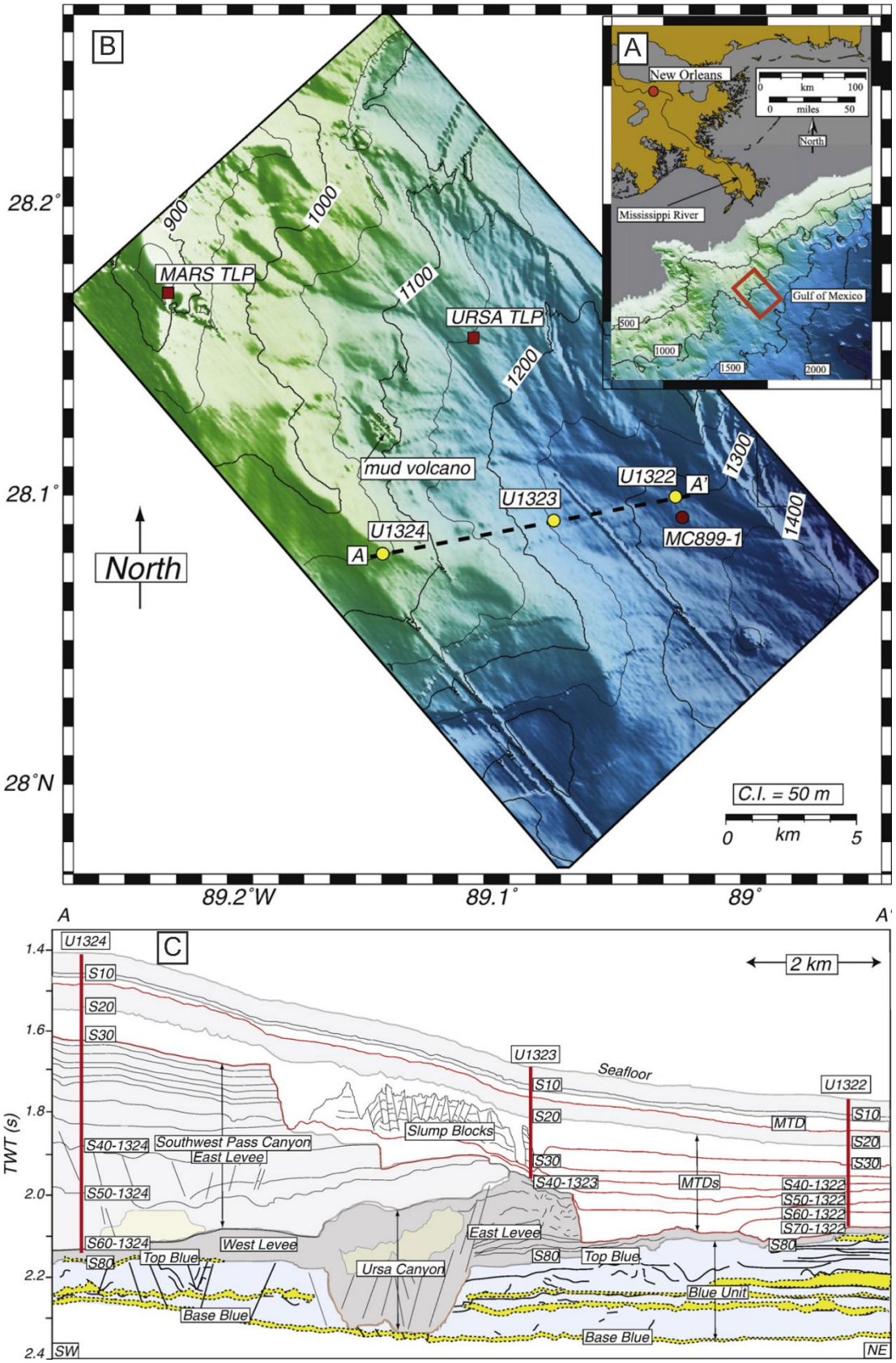

Figure 2.18: Location (A) and bathymetry (B) of the Ursa basin. (C): Interpreted cross section A-A'. Light and dark gray represent mud-rich levee, slides and hemipelagic drape. Yellow indicates sand-rich channel fill within the Blue Unit (light blue). Red color indicates dechatment surfaces at the base of the MTDs. From Flemings et al. (2008).

PART II

METHODOLOGY

Chapter 3: Data and methods

3.1 Dataset used in this thesis

3.1.1 The INSIGHT project

A significant amount of geophysical and core data used for this study have been collected in the frame of the INSIGHT (ImagiNg large SeismogenIc and tsunamiGenic structures of the Gulf of Cadiz with ultra-High resolution Technologies) project, lead at the Institut de Ciències del Mar (ICM-CSIC) of Barcelona and granted by the Spanish *Ministerio de Ciencia e Innovación*. The main scientific objectives of the INSIGHT project were:

1. To characterize the 4D architecture of major elements at the origin of geohazards (faults and submarine landslides) in the Gulf of Cadiz and to understand their relation with fluid seepage;
2. To evaluate the role of large faults and associated submarine landslides as potential sources of tsunamis.

Two scientific cruises, onboard the R/V Sarmiento de Gamboa, were carried out in the frame of the INSIGHT project and I have been personally involved in both. The first leg (April-May 2018) was devoted to acoustic and high-resolution seismic investigation to search for surface ruptures, seafloor deformation, submarine landslide characterization and fluid flow mud-volcano structures (Gràcia et al., 2018). We surveyed active seismogenic faults and large submarine landslides in the Gulf of Cadiz, in both Portuguese and Moroccan margins (Marquês de Pombal Fault and slides, Lineament South-West, Portimão Bank Fault and slides, and Lineament South-East), making use of an Autonomous Underwater Vehicle (AUV) and 2D-high-resolution multi-channel seismic system to survey. During the second leg (September-October 2019) the same structures have been revisited with Controlled Source ElectroMagnetic (CSEM) methods and a 2D High-Resolution multi-channel seismic system (Urgeles and Shipboard Scientific Party, 2019). Both legs made use of other acoustic and geological methods such as shipborne swath-bathymetry, parametric sub-bottom profiler and gravity coring.

The data from the INSIGHT cruises that have been used in this thesis are the multi-channel seismic profiles and the gravity cores collected within the Alentejo basin (Figure 3.1) (more information in sections 3.2 and 3.3).

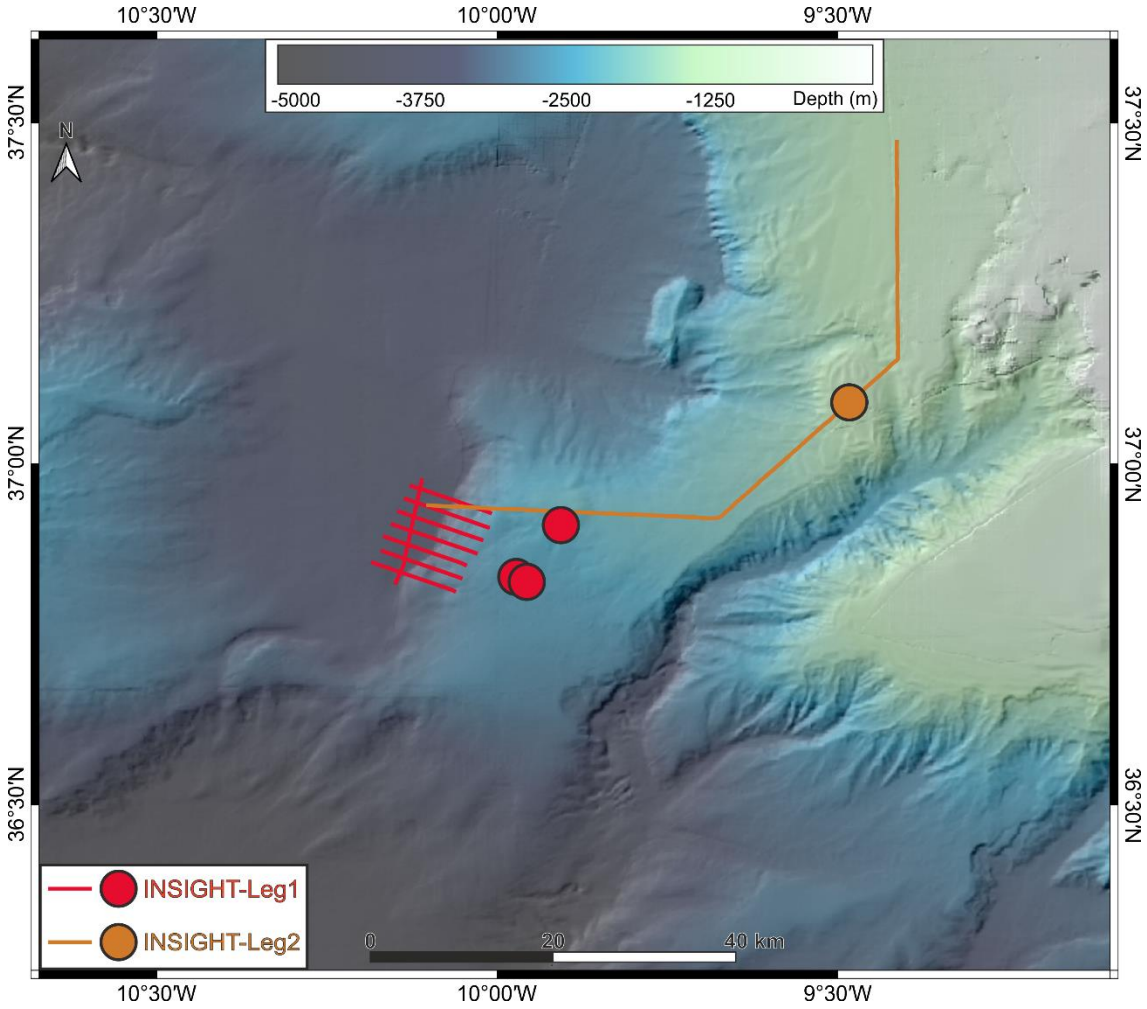

Figure 3.1: Multi-channel seismic profiles (lines) and gravity cores (circles) collected during the INSIGHT cruises in the Alentejo basin and used for this thesis.

3.1.2 Other data

Beside the multi-channel and gravity core data acquired during the INSIGHT cruises (Figure 3.1), this study makes use of geophysical and core data collected during various scientific cruises that investigated the area offshore Cape São Vicente in the last three decades. The geophysical data from those projects are part of the ICM-CSIC database, while additional core data have been obtained from IODP's Janus database and the scientific literature. The seismic and core data used in this study were collected in the following cruises:

- *ARRIFANO* (Arco Rifano) (1992): The project led by the Italian National Research Council (CNR), investigated the plate boundary between Africa and Eurasia by shooting seismic lines from the Gibraltar arc to the Horseshoe Abyssal Plain onboard the R/V OGS Explora (Sartori et al., 1994). The portions of the lines acquired within the Alentejo basin have been used in this study (section 3.2.2).

- *BIGSETS* (Big Sources of Earthquake and Tsunami) (1998): Project led by the Italian National Research Council (CNR), investigated the geological and geophysical properties

of seismogenetic areas off Cape São Vicente (Zitellini et al., 2010, 2004, 2001). In this study we made use of multi-channel seismic data acquired during the BIGSET 1998 cruise onboard the R/V Urania (see section 3.2.2).

- *VOLTAIRE* (Valuation Of Large Tsunamis And Iberia Risk for Earthquakes) (2002): the project was co-funded by the Italian and Portuguese funding Agencies and led by the Italian Research Council (CNR) and by the Portuguese Instituto de Ciências da Terra e do Espaço (ICTE). The VOLTAIRE cruise, onboard the R/V Urania, investigated the active tectonic processes occurring at continental margins of SW Iberia (e.g., the Marquês de Pombal Fault, the Horseshoe Faults and the Guadalquivir Bank), by acquiring multi-channel seismic data and magnetic profiles. The portions of seismic lines acquired within the Alentejo basin have been used in this study (Terrinha et al., 2009; Zitellini et al., 2002).

- *PD00*: The one multi-channel seismic line included in our database was acquired by TGS-NOPEC in 2000 and it is part of a multi-client 2D seismic survey (TGS, 2005).

- *HITS* (High resolution Imaging of Tsunamigenic Structures in the southwest Iberian margin) (2001): the research cruise was carried out by the Spanish Research Council (CSIC) onboard the R/V Hesperides and it aimed to determine the detailed geometry of active seismogenic structures of the South West Iberian Peninsula (Gracia and Danobeitia, 2001). The cruise acquired TOBI sidescan sonar high resolution images. In addition, dating on sediment samples were performed for palaeoseismological purposes. The published information about one of those sediment cores (MC1) (Garcia-Orellana et al., 2006) have been used for the aim of this thesis (see section 3.3.2).

- *Integrated Ocean Drilling Program (IODP) Expedition 339 (2011-2012)*: the expedition took place between November 2011 and January 2012 onboard the drilling R/V Joides Resolution with the aim of increase our understanding over: 1) the onset of the MOW after the opening of the Gibraltar Gateway; 2) the MOW paleocirculation and global climate significance; 3) the rapid climate change taking place during the Pleistocene; 4) the external controls on the sediment architecture in the Gulf of Cadiz; and 5) the syn-sedimentary neotectonic control on the evolution of the contourite system (IODP Expedition 339 Scientists, 2013a). To accomplish these goals the IODP expedition drilled 5 wells within the Gulf of Cadiz and 1 (well 339-U1391) in the Alentejo basin (Hernández-Molina et al., 2016a; IODP Expedition 339 Scientists, 2013c; Stow et al., 2013a). Grain size distribution, ages and borehole log data resulting from Site U1391 drilling have been extensively used for the aim of this thesis (see section 3.3.2).

Although most of the study is based on geophysical and core data from the Alentejo basin, data from the Lesser Antilles volcanic arc and the Gulf of Mexico (see also section 2.5) have also been used.

- *Integrated Ocean Drilling Program (IODP) Expedition 308 (2005):* the IODP expedition drilled three sites within the Ursa basin, in the Gulf of Mexico, onboard the drilling R/V Joides Resolution (Expedition 308 Scientists, 2006; Flemings et al., 2012, 2008). The scientific objective of the expedition were: 1) to document how pressure, stress and geology couple to control fluid migration on passive margins; 2) to understand the controls on slope stability in order to predict future potential slope failure and estimate what drove past mass transport deposits; 3) to understand sedimentation rates and timing of mass transport deposits; 4) to derive geotechnical and petrophysical properties of shallow sediments; and 5) to provide a dataset to observe ponded and channelized turbidite systems (Expedition 308 Scientists, 2006). In the frame of this thesis, we made use of published hydromechanical properties of sediments collected in two of the drilled sites (Long et al., 2008; Stigall and Dugan, 2010; Urgeles et al., 2007).

- *Integrated Ocean Drilling Program (IODP) Expedition 340 (2012)*: the expedition took place in 2012 onboard the drilling R/V Joides Resolution and investigated the constructive and destructive processes related with island arc volcanos by drilling 9 boreholes offshore Montserrat, Martinique and Dominica, in the Lesser Antilles volcanic arc (Le Friant et al., 2015). The main objectives of the expedition were 1) to understand timing and emplacement processes of potentially tsunamigenic debris avalanches; 2) to better understand the eruptive and 3) magmatic evolution of the arc (cycles of construction and destruction); 4) to document dispersal of sediments into the ocean; and 5) to determine processes and element fluxes associated with submarine alteration of volcanic material (Expedition 340 Scientists, 2013; Le Friant et al., 2015). This thesis made use of published geotechnical data resulting from testing of sediments collected during the IODP expedition 340 (Lafuerza et al., 2014).

3.2 Geophysical data

3.2.1 Swath bathymetry data

Multibeam echosounders (MBES) acquire bathymetric data using a fan of acoustic beams. They uses the returns of backscattered sound to define seabed elevation and infer the substrate (Figure 3.2). Compared with simpler single beam echosounders, MBES allow to examine three dimensional surfaces rather than the interpolation between sparse two dimensional profiles (Hughes Clarke, 2018). The choice of beam frequencies depends on the depth of the marine environment to be investigated: low frequency (e.g. 12 kHz) systems collect soundings up to

10,000 m depth, while high frequencies (e.g. 300+ kHz) are used to collect bathymetric data at water depths even lower than 20 m.

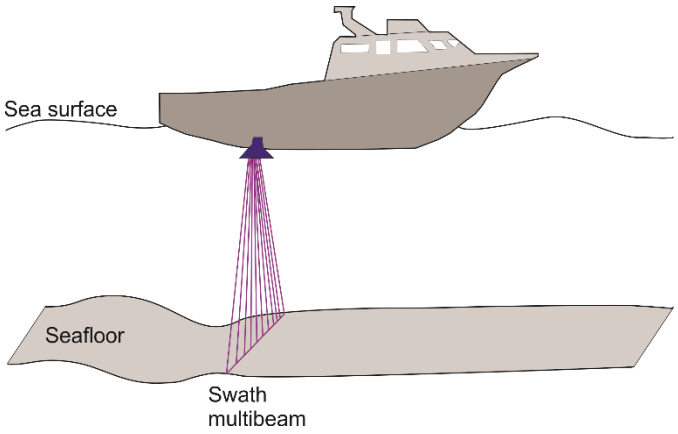

Figure 3.2: Schematic illustration of a multibeam echosounder system. Acoustic energy pathways are shown by the purple rays. Modified after USGS.

This study uses the high-resolution multibeam bathymetric compilation produced under the European Science Foundation (ESF) EuroMargins SWIM project, resulting from multiple marine cruises that were carried out between 1991 and 2006 (Zitellini et al., 2009) (Figure 3.3, Table 3.1):

Table 3.1: Bathymetry data composing the SWIM multibeam compliation (see location of each survey in Figure 3.3).

	Cruise	**Year**	**R/V**	**Instrument**	**Institute**	**Country**
1	ESPICHEL	1991	L'Atlante	Simrad EM12D	Ifremer	France
2	TASYO	2000	Hespérides	Simrad EM12S	IGME	Spain
3	PARSIFAL	2000	Hespérides	Simrad EM12S	CSIC-CMIMA	Spain
4	CADISAR-1	2001	Le Suroit	Simrad EM 300	Uni. Bordeaux	France
5	HITS cruise	2001	Hespérides	Simrad EM12S	CSIC-CMIMA	Spain
6	CADIPOR	2002	Belgica	Simrad EM 1002	Uni. Ghent	Belgium
7	GORRINGE	2003	Urania	Reason Seabat 8101	IAMC-CNR	Italy
8	TV-GIB	2003	Le Suroit	Simrad EM 300	Uni. Bretagne Occidentale	France
9	PICABIA	2003	Marion Dufresne	Thomson Sea Falcon 11	CSIC-CMIMA	Spain
10	GAP	2003	Sonne	Simrad EM 120	Uni. Bremen	Germany
11	MATESPRO	2004	D. Carlos I	Simrad EM 120	Uni. Lisboa	Portugal
12	CADISAR-2	2004	Le Suroit	Simrad EM 300	Uni. Bordeaux	France

13	DELILA	2004	D. Carlos I	Simrad EM 120	Uni. Bretagne Occidentale	France
14	DELSIS	2005	D. Carlos I	Simrad EM 120	Uni. Bretagne Occidentale	France
15	SWIM-2	2005	OGS Explora	Reason Seabat 8150	ISMAR	Italy
16	HERMES	2006	Charles Darwin	Simrad EM12S	NOC	UK
17	SWIM	2006	Hespérides	Simrad EM 120	CSIC_CMIMA	Spain
18	Digital Terrerin Model		D. Carlos I	Simrad EM 120	EMEPC	Portugal
19	Transit data		J. Charcot L'Atlante	Various	SISMER	France

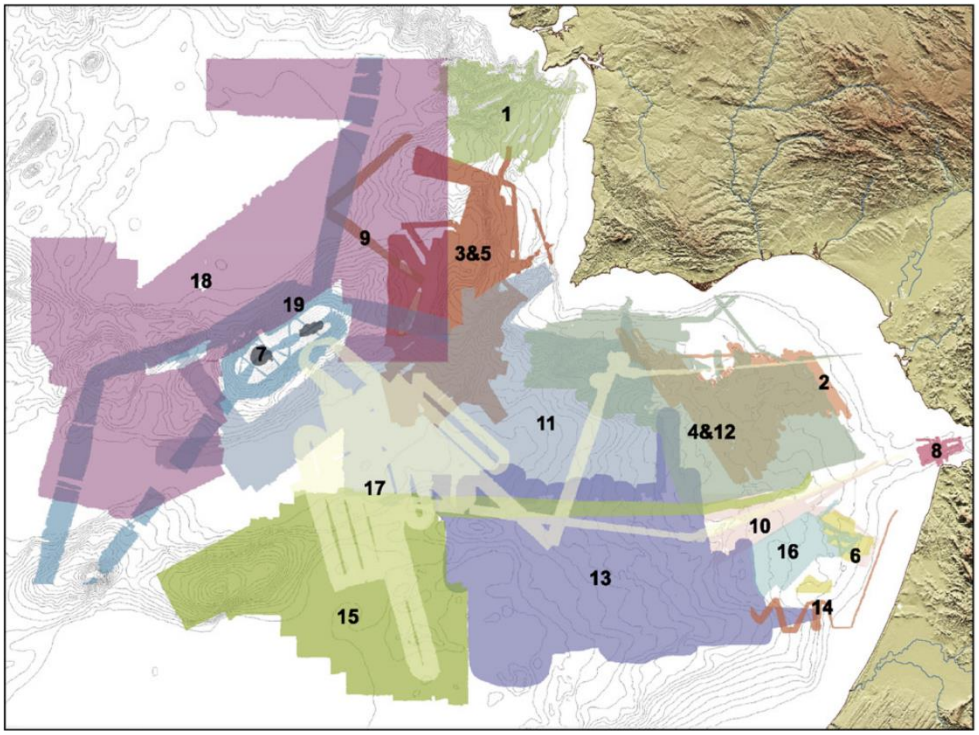

Figure 3.3: Location of the surveys composing the SWIM multibeam compliation and described in Table 3.1. From (Zitellini et al., 2009).

3.2.2 Multi-Channel seismic (MCS) reflection data

3.2.2.1 MCS acquisition and processing

Multi-channel seismic reflection is a geophysical method that uses the principle of seismology to estimate the properties of the Earth subsurface. The technique consists of using a sound source to produce sound pulses at a controlled frequency range and at regular time intervals. The sound waves propagate within the sediments, and when they encounter a boundary between two

materials with different acoustic impedances, part of the waves undergoes diffraction processes and travels deeper within the sediments, while the remaining fraction is reflected at the impedance boundaries. The reflected energy travels upwards and is recorded by hydrophones arranged in a streamer towed from the vessel (Figure 3.4). By processing the different times of arrivals of the reflected waves, it is possible to produce profiles of the sub-surface, which allow to characterize depositional and tectonic features in a variety of scales.

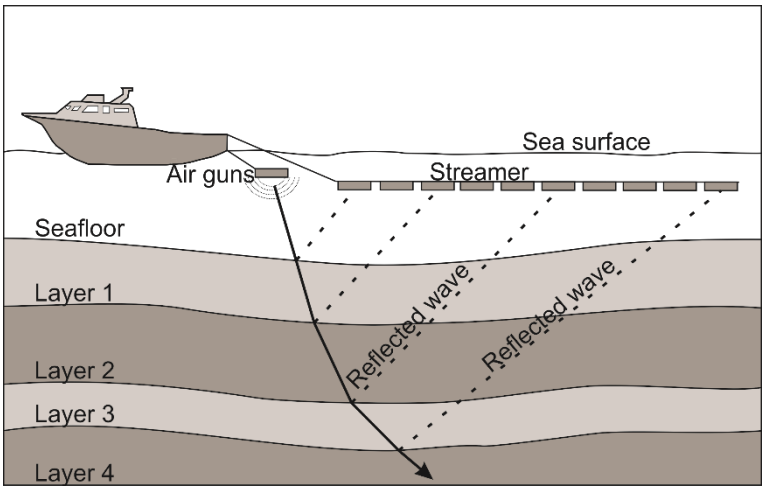

Figure 3.4: Schematic illustration of offshore multi-channel seismic acquisition. The air guns (source) generate acoustic pulses that penetrate downward within the subsurface and are partially reflected at the different interfaces (changes of acoustic impedance). Hydrophones located along a streamer record the amplitude and time of arrivals of the reflected waves.

Thirty-five Multi-Channel seismic (MCS) profiles are used for this study (Figure 3.5). The lines were acquired with different configurations during the ARRIFANO, BIGSETS, VOLTAIRE PD00 and INSIGHT marine surveys introduced in section 3.2.2.

8 MCS profiles have been acquired during the INISIGHT Leg1 (2018) and Leg2 (2019) cruises within the Alentejo basin (Figure 3.1) (Gràcia et al., 2018; Urgeles and Shipboard Scientific Party, 2019). The 7 profiles acquired during the INSIGHT Leg1 have been shot in the Marquês de Pombal Fault area, since the main objective was to image the thrust fault structure and the mass transport complex present at its footwall. The one line acquired during the second leg connects the IODP Site U1391 with the Marquês de Pombal Fault, following the axis of the São Vicente Canyon, and aimed to image the sedimentary patterns from the upper part of the slope to the plateau area. The INSIGHT MCS surveys used an airgun array of 10 GI-guns with a total capacity of 930 cubic inches shot at 25 m interval and an average speed of 4.5 kn. Data was collected with a 445 m long streamer with 72 channels for Leg1 and a 350 m long streamer with 56 active channels for Leg2, both with a channel spacing of 6.25 m (Table 3.2). In both cases the resulting CDP spacing was 3.125.

Seismic acquisition parameters related with the profiles used in this study (Figure 3.5) are reported in Table 3.2.

Table 3.2: Geophysical adquisition parameters for MCS profiles adopted in this study.

Surveys name	ARRIFANO	BIGSET	PD00	VOLTAIRE	INSIGHT (1-2)
Year	1992	1998	2001	2002	2018
Vessel	R/V OGS Explora	R/V Urania	(M/V Zephyr1)	R/V Urania	R/V Sarmiento de Gamboa
N. lines in database	2	17	1	6	9
Seismic source	32 airguns (80 l)	2 GI guns	Tuned Bolt array	2 GI guns	10 G-guns (15.2 l)
Shooting interval	50 m	25 – 37 – 50 m	25 – 30 m	50 m	12.5 m – 18.75 m
Length of streamer	3000 m	1200 m	6000 m	600 m	445 m – 350 m
N. of channels	120	48	480	48	72 – 56

Signals processing for the seismic data acquired during the ARRIFFANO cruise included spiking deconvolution, spherical divergence correction, NMO correction, finite-difference wave equation migration, time variant bandpass-frequency filter (Sartori et al., 1994; Terrinha et al., 2009). Seismic data from the BIGSETS cruise have been processed with interactive velocity analysis, NMO correction and stack, top mute, minimum phase predictive deconvolution, band pass filter, true amplitude recovery (Zitellini et al., 2010). The processing of the VOLTAIRE data included trace editing, shot delay removal, amplitude recovery, predictive deconvolution, velocity analysis every 200 CMPs, NMO correction, bandpass-frequency filtering and time migration using stacking velocities (Terrinha et al., 2009; Zitellini et al., 2002). The PD00 seismic dataset processing sequence included static correction, minimum phase conversion, trace decimation, amplitude recovery, forward and inverse NMO correction, threshold amplitude editing, FX deconvolution, time-variant filter (TGS, 2005).

The INSIGHT datasets were processed onboard using RadExPro seismic processing software. The pre-processing flow included a) resample to 1 ms, b) navigation/geometry application, c) trace editing, d) swell noise attenuation (low-cut filter, shot and channel domain time-frequency trim), e) source and receiver deghosting, f) debubble filter and zero-phase correction (operators derived by stacking the seafloor reflection), g) CMP binning (3.125 m spacing), and h) NMO correction and stacking. The stacked profiles were imaged using a post-stack Kirchhoff time migration, with migration velocities derived from a sediment velocity gradient model. The velocity in the water column was a constant 1500 ms^{-1}. The sediment velocity gradient was derived by running an ensemble of migrations with a range of gradients. Post-migration processing included a time-varying bandpass filter, F-X deconvolution and a water column mute.

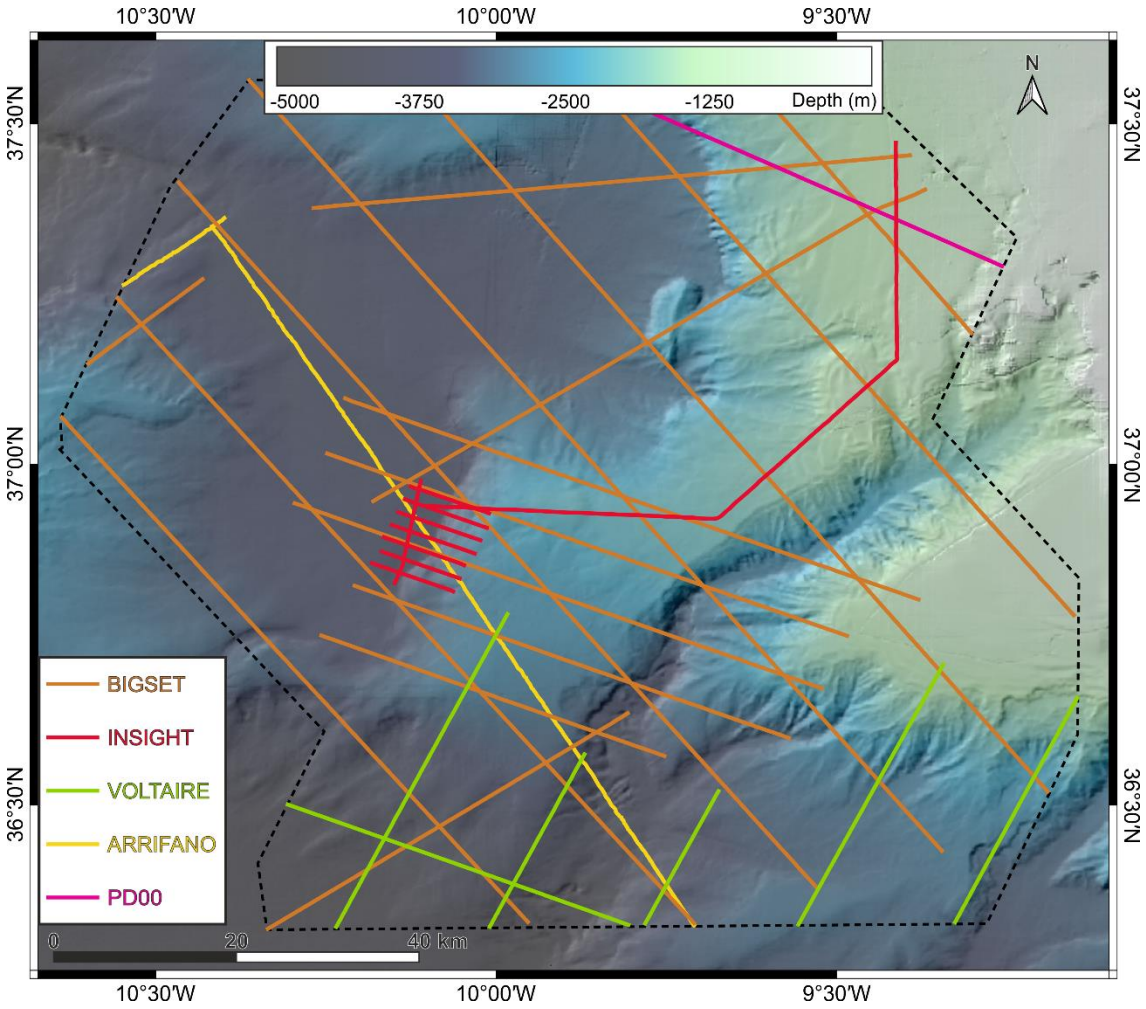

Figure 3.5: Location of the multichannel seismic (MCS) profiles used in this study (coloured according to survey, see legend). Dashed black polgon indicates the area of interest, within which the main stratigraphic horizons have been tracked.

3.2.2.2 Stratigraphic interpretation

Stratigraphic interpretation of the network of MCS profiles (Figure 3.5) has been carried out using the 'IHS Kingdom Suite' seismic interpretation package. Time to depth conversion was performed to generate the thickness and sedimentation rate maps. The interval velocity model assumed a constant water velocity and a linear velocity gradient with depth below the seafloor. The model parameters were calibrated at IODP Site U1391 (IODP Expedition 339 Scientists, 2013a) using the major discontinuities of the area proposed by Hernández-Molina et al. (2016) (LPD, EQD, MPD and LQD) (Table 3.3). The water velocity was set to 1514 ms^{-1} and the sediment velocity gradient was 491 ms^{-2}, derived using the measured depth and two-way travel time (TWTT) of the seafloor and LPD (deepest) horizon. The mismatch between the computed depths and the measured depth from the borehole using this gradient was less than 15 m for the deepest considered reflection. The seismo-stratigraphic interpretation in this study is focused on the sequence from the Upper Miocene to the Quaternary. The four main depositional discontinuities described by Hernández-Molina et al. (2016) (Table 3.3) for the Sines Drift have been tracked along the available MCS network over an area of approximately 14.750 km^2, which

included the shallower part of the slope (water depth of approximately 1000 m), the slope in the area of the Marquês de Pombal Fault and the proximal area of the Horseshoe Abyssal Plain (water depth of 4000 m). Further to the work by Hernández-Molina et al. (2016), the interpretation presented here is also based on the Upper Miocene and Early Pliocene reflectors identified by Serra et al. (2020) and Martínez-Loriente et al. (2018, 2013) (Table 3.3). The resulting stratigraphic model adopted in this study includes the Upper Miocene (UM) unit, Early Pliocene (EP), and four post-Pliocene seismic units bounded by the LPD, EQD, MPD and LQD, named sequentially from bottom to top (I to IV) (Table 3.3) (see also Mencaroni et al., 2021). A comparison between the units adopted in this study for the Alentejo basin and other stratigraphic models from previous studies (Hernández-Molina et al., 2016a; Llave et al., 2011, 2007a; Martínez-Loriente et al., 2018, 2013; Rodrigues et al., 2020; Teixeira et al., 2019) is reported in Table 3.3.

Table 3.3: Main seismic units and discontinuities adopted in this work compared with the stratigraphic models adopted in previous studies (Hernández-Molina et al., 2016a; Llave et al., 2011, 2007a; Martínez-Loriente et al., 2018, 2013; Rodrigues et al., 2020; Teixeira et al., 2019). Modified from Rodrigues et al. (2020).

Age (Ma)			This thesis	Base of unit depth (mbsf) (339-U1391)	Llave et al. 2007-2011	Hernandez-Molina et al., 2016		Teixeira et al., 2019	Rodrigues et al., 2020	Martinez-Loriente et al., 2013, 2018
0.34	Quaternary	Hol.	LQD Unit IV	91	QII	LQD QIII	Q	H1	U1	Ia
0.83		Pleistocene	MPD Unit III	196		MPD			H1	
1.5			Unit II		QI	QII			U2 H2	
2.25			EQD	566	BQD	EQD QI BQD		H2	U3 H3	
3.1	Neogene	Pliocene	Unit I LPD	634	P2	LPD PIII	PQ	H3	U4 H4	
			EP		LPR	IPD PII EPD	P		U5	
5.3			M/P		P1 M	PI M			H5	PQ
		Miocene	UM						U6	Ib

3.3 Core data and geotechnical tests

Gravity corers consist of a metal tube, equipped with a load head to enhance penetration within sediments. The instrument is let free falling within the last tens of meters of water column and plunging into muddy marine sediments driven only by gravity and inertia. The tube contains a plastic liner to accommodate the soil sample, and a core catcher at the bottom to prevent sediment to escape while it is recovered on board (Figure 3.6).

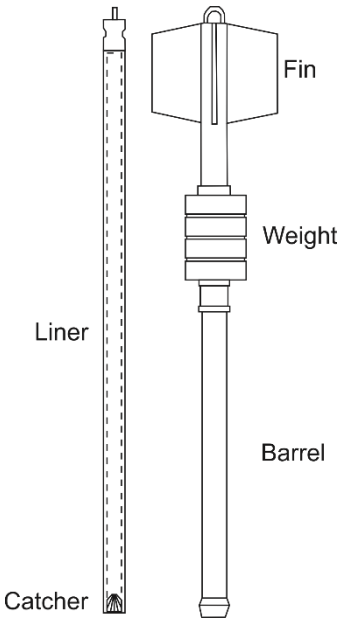

Figure 3.6: Gravity corer device main parts (after Llopart, 2016).

3.3.1 INSIGHT gravity cores

Four gravity cores collected in the Alentejo basin during the INSIGHT-Leg1 and Leg2 cruises have been used in the frame of this study (Figure 3.1, Figure 3.7 and Table 3.4) (Mencaroni et al., 2021, 2020). The coring operations were performed using a galvanized steel pipe of 9 cm in diameter, containing an internal PVC liner with 7 cm in diameter. The head of the gravity corer weighted ~800 kg. The coring operations consisted in sinking the instrument at controlled speed until an altitude of approximately 100 m above the seafloor. At this depth, the winch stopped to stabilize the corer from oscillations. Once the core reached a stable position perpendicular to the seafloor, it was sank at 100 m/min to ensure the maximum penetration.

Core SdG083-13 was located on the northern flank of the São Vicente Canyon, between the Sines Drift and the Marquês de Pombal Plateau. Cores SdG068-1, SdG068-2 and SdG068-3 were also collected within the Marquês de Pombal Plateau, but in deeper waters (Figure 3.1 and Figure 3.7 and Table 3.4). All the cores collected undisturbed sediments (e.g., not from landslide deposits). Core SdG068-02 was taken from one of the scars from where the Marquês de Pombal mass transport complex originated.

3.3.2 Other core data

In addition to the gravity cores collected during the INSIGHT Leg1 and Leg2 cruises, published physical properties and composition of the sediments in the Alentejo basin has been used (Figure 3.7 and Table 3.4). IODP expedition 339 played a fundamental role in revealing the sedimentary dynamics related with the MOW flow variability in the whole Gulf of Cadiz.

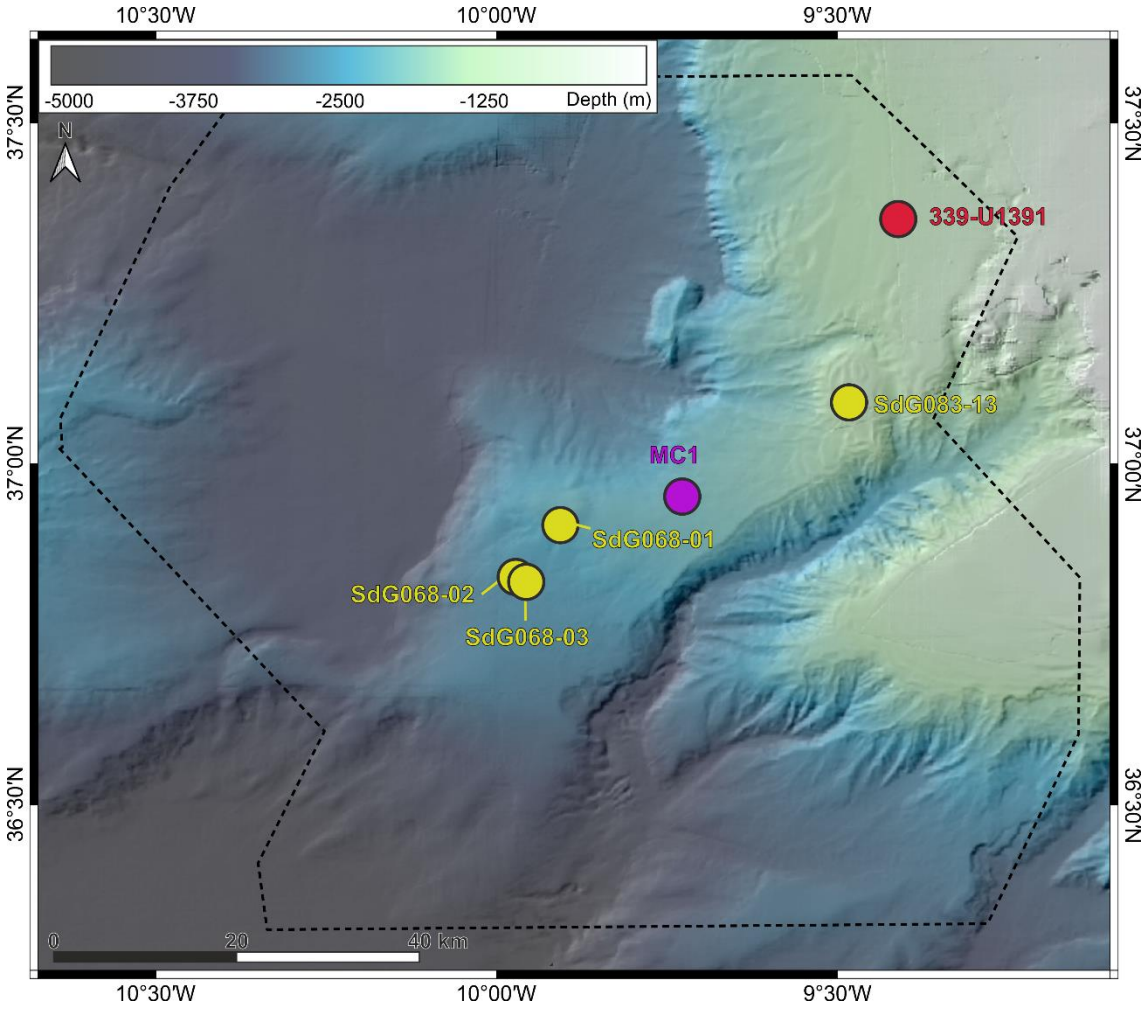

Figure 3.7: Location of the cores collected within the Alentejo basin and used in this thesis (dashed polygon bounds the area of interest). Yellow circles correspond to the gravity cores collected during the INSIGHT Leg1 (Gràcia et al., 2018) and Leg2 (Urgeles and Shipboard Scientific Party, 2019) cruises. Purple circle represent the Multicore MC1 collected and analyzed by Garcia-Orellana et al. (2006). Red circle indicates the location of IODP borehole U1391.

Within the 6 boreholes drilled during the expedition, we used especially the grain size distribution, petrophysical properties and ages information resulting from the drilling of borehole U1391, located approximately 60 km to the NE of the Marquês de Pombal slope area, in the upper slope (water depth of 1073 m) (Figure 3.7 and Figure 3.9). Site U1391 recovered more than 670 m of sediments and borehole logs. Percentage of sand, silt and clay have been defined through smear slide analysis (IODP Expedition 339 Scientists, 2013b).

Additional information about the shallow sediments composition in the Marquês de Pombal Plateau have been taken from the 20 cm long multicore MC1 collected during the HITS-01 cruise in 2001 (see section 3.1.2) and published by Garcia-Orellana et al. (2006) (Figure 3.7, Table 3.4). The authors constrained the sediment ages by ^{137}Cs and ^{210}Pb chronology. ^{210}Pb activity was determined by measuring the daughter nuclide, ^{210}Po, following the methodology described by Sanchez-Cabeza et al., (1998). ^{137}Cs was determined by γ-spectrometry using a high-purity well-type Ge detector. The mineral composition of the bulk and coarse fractions (>50 μm) was studied with X-ray scans and diffraction. Semi-quantitative estimation of mineral composition has been

performed by peak areas measurements, while major elements were identified using an X-ray spectrometer.

3.3.2.1 Sediments from other settings

One part of the modelling effort described in this study includes a comparison between 1D overpressure development models defined with sediment properties measured from the cores collected in the Alentejo basin, and physical properties from cores collected in very different geological settings such as the Grenada (offshore Martinique area) and Ursa (Gulf of Mexico) basins (Table 3.4).

Samples from Grenada basin (3 samples) and from the Ursa basin (9 samples) (Table 3.4) were recovered from wells drilled during two separate IODP expeditions. The samples from the Grenada basin used in this study have been drilled at well U1399 during the IODP expedition 340 (Le Friant et al., 2015) (Table 3.4) and their compressibility/permeability properties measured with 1D stepped loading consolidation tests (Lafuerza et al., 2014). Sediments from the Ursa basin have been taken from wells U1322 and U1324, drilled during the IODP expedition 308 (Expedition 308 Scientists, 2005; Flemings et al., 2006). In this case, their compressibility/permeability properties have been analysed using a combination of stepped loading and CRS oedometer tests (Long et al., 2008; Stigall and Dugan, 2010; Urgeles et al., 2010, 2007).

Table 3.4: Information about the core data used in this study.

Core	Cruise	Year	Basin	Lat. (º)	Lon. (º)	Depth (mbsl)	Recovery (m)	Coring system
MC1	HITS-01	2001	Alentejo	36.93	−9.75	2173	0.20	Multicore
SdG068-01	INS-Leg1	2018	Alentejo	36.92	−9.90	1703	2.43	Gravity Core
SdG068-02	INS-Leg1	2018	Alentejo	36.84	−9.97	2668	2.15	Gravity Core
SdG068-03	INS-Leg1	2018	Alentejo	36.84	−9.95	2664	2.48	Gravity Core
SdG083-13	INS-Leg2	2019	Alentejo	37.09	−9.48	1026	2.36	Gravity Core
U1391	IODP -339	2012	Alentejo	37.36	−9.41	1085	672	Borehole
U1322	IODP -308	2005	Ursa	28.10	-89.02	1319	238	Borehole
U1324	IODP-308	2005	Ursa	28.08	-89.14	1057	612	Borehole
U1399	IODP-340	2012	Grenada	14.39	-61.71	2900	274.7	Borehole

3.3.3 Multi-sensor core logging (MSCL)

Multi-sensor core loggers (MSCL) allow high-resolution, non-destructive measurements of the physical and chemical properties of sediment cores. The typical configuration of MSCL systems allow the simultaneous measurement of magnetic susceptibility, wet bulk density, P-wave velocity, electrical resistivity and natural gamma radiation on whole or split sediment cores (Figure 3.8) (Frigola et al., 2015). In this study, P-wave velocity and gamma-density were

measured on the whole cores collected during the INSIGHT cruises, with a Geotek® MSCL, at 0.5 cm intervals.

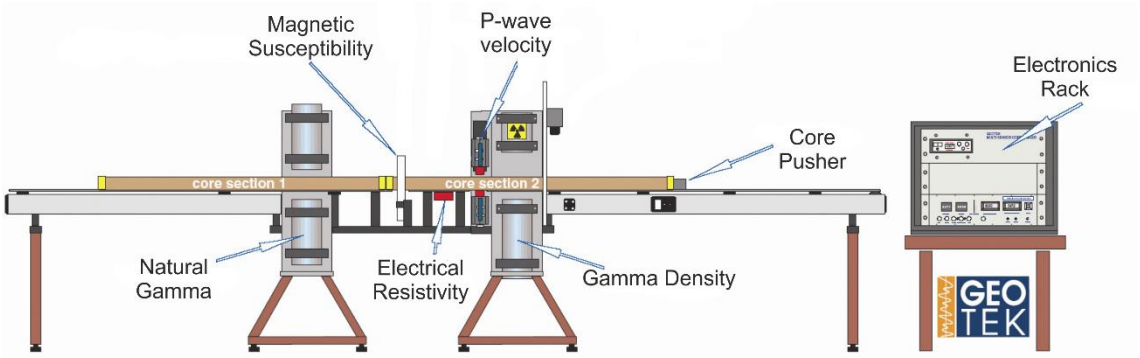

Figure 3.8: Geotek® Multi-sensor core logger, schematic configuration (modified after Vatandoost et al., 2009).

P-wave velocity is measured by a sensor consisting of a pair of transducers acting as transmitter and receiver, and allowing continuous measurements (Frigola et al., 2015). In general, P-wave velocity within sediments decreases with increasing bulk density. Changes in P-wave velocity is associated with variations in lithology, porosity, bulk density, lithostatic pressure, degrees of fracturing, consolidation and lithification, and the occurrence and abundance of free gas and gas hydrates (Blum, 1997). Thus, variation in P-wave velocity log can indicate changes in properties within the whole core.

The gamma-density log is used to measure the bulk density of sediments, which is a function of their mineralogy and degree of compaction and provides information about grain size, porosity and water content. The relevance of these information for geological studies makes density one of the most important properties to describe the physical state of marine sediments (Gerland and Villinger, 1995). In modern MSCL configurations, density is measured from the gamma ray attenuation (GRA) by using a ^{137}Ce source and a NaI (TI) scintillation detector, in conjunction with a universal counter. The GRA coefficient is a function of the detected gamma-ray energy, which is very sensitive to every individual device, to environmental conditions and to the characteristics of the sediments (Frigola et al., 2015). Thus, an accurate calibration process is normally made before every set of measurements using a standard of known density (normally a telescoping aluminium rod) in distilled water contained in a plastic liner of the same characteristics used to sample the sediments. The calibration allows to derive a linear regression curve between the GRA and the density from where calibration coefficients are extracted, allowing the determination of density variation in sediments (Best and Gunn, 1999; Blum, 1997).

Other log measurements used in this study are the downhole gamma ray (Figure 3.9C), compressional velocity (Figure 3.9D), resistivity logs (Figure 3.9E), and *in-situ* porosities (Figure 3.9B) measured at IODP Site U1391 down to 668 mbsf (Figure 3.7, Table 3.4) (Hernández-Molina et al., 2016a; IODP Expedition 339 Scientists, 2013a; Lofi et al., 2016; Stow et al., 2013a).

Natural gamma ray has been measured using the Hostile Environment Natural Gamma Ray Sonde (HNGS). HNGS signal is used as a proxy to track clay content, where greater percentages of K-rich minerals containing radioactive elements such as U and Th are usually present.

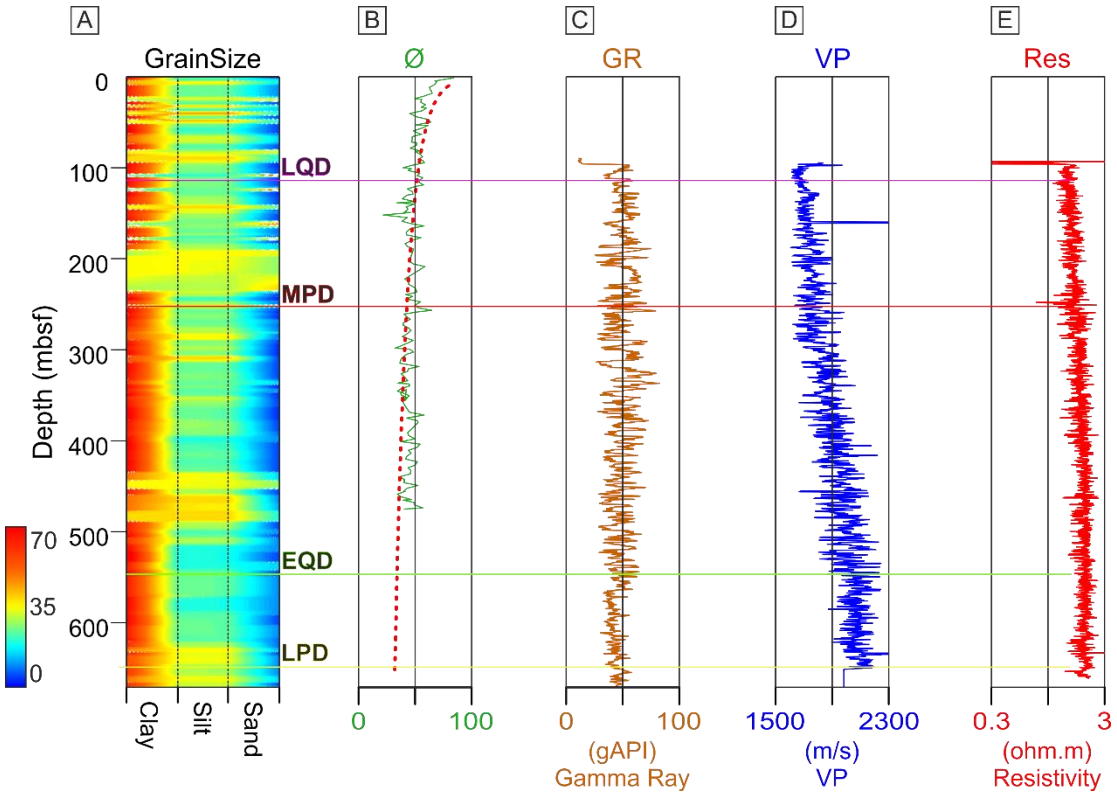

Figure 3.9: (A) Grain size distribution and borehole logs from IODP Site U1391 (IODP Expedition 339 Scientists, 2013b; Stow et al., 2013a); (B) Ø: porosity; C) GR: gamma ray log; (D) VP: compressional velocity. (E) Res: resisityvity log. Coloured horizontal lines correspond to main discontinuities detected in the cores recovered (see description in section 2.2): LQD: Late Quaternary Discontinuity (0.4 to 0.3 Ma); MPD: Middle Pleistocene Discontinuity (0.8 Ma); EQD: Early Quaternary Discontinuity (2.4 to 2.1 Ma); LPD: Late Pliocene Discontinuity (3.2 to 3.0 Ma). (IODP Expedition 339 Scientists, 2013b; Stow et al., 2013a).

3.3.4 Grain size analysis

Once MSCL measurements were performed, core SdG083-13 was split and sampled for measurement of grain-size distribution on bulk sediment at 5 cm spacing for the whole length (Table 3.5). Cores SdG068-1, SdG068-2 and SdG068-3 have been sampled for grain size measurements only at specific depth intervals because the rest of the core was preserved unsplit for additional geotechnical tests (Table 3.5) (see section 3.3.5). Grain-size distribution for all samples was measured using a Horiba LA950 Laser Diffraction particle size analyser (Horiba Scientific, Kyoto, Japan) for the grain size fraction <2 mm, while the fraction >2 mm was sieved and weighted. The results obtained with the laser diffractometer were converted to percent weight and combined with those of the sieves. We adopted the grain size classification proposed by Wentworth (Wentworth, 1922) to derive the amount of sand (2 mm - 62.5 μm), silt (62.5 μm – 4 μm) and clay (< 4 μm) in the sediments.

3.3.5 Atterberg limits and water content

By varying the water content, fine grained sediments go through four different stages of consistency: liquid, plastic, semi-solid and solid. The transitions from solid to semi-solid state (shrinkage limit, w_S) from plastic to semi-solid state (plastic limit, w_P) and from plastic to liquid state (liquid limit, w_L,) are known as Atterberg limits (Figure 3.10) (Casagrande, 1932; Seed et al., 1964). They provide useful information about shear strength, bearing capacity, compressibility, swelling potential and specific surface of sediments (McBride, 2002; Seed et al., 1964).

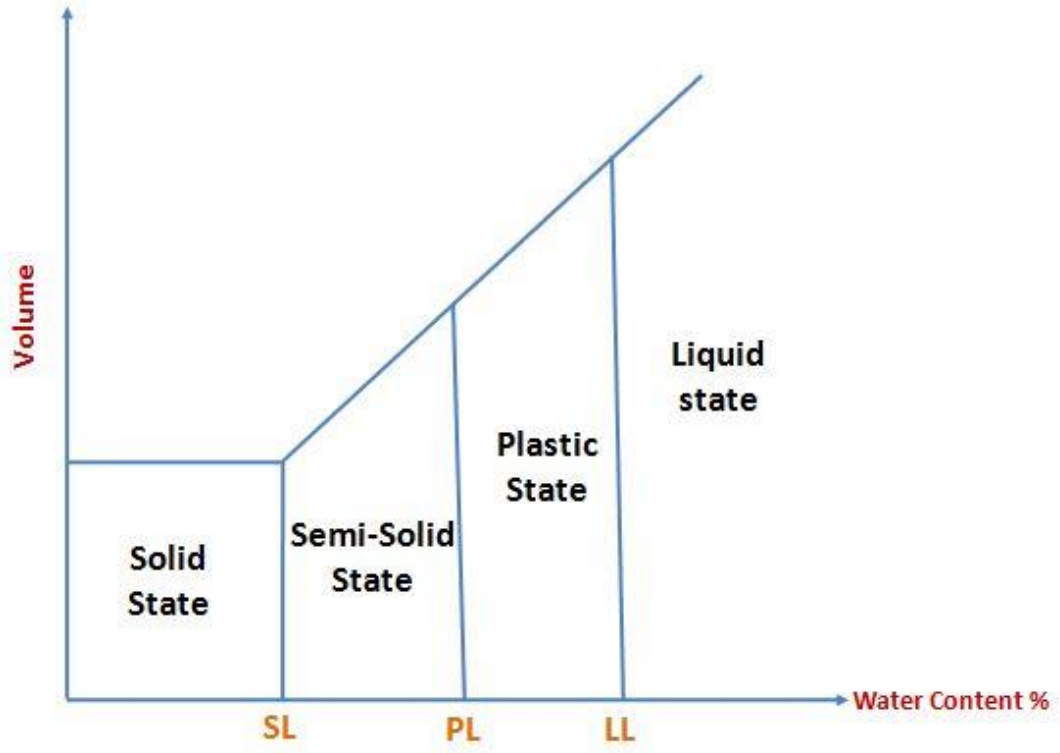

Figure 3.10: Atterberg limit consistency states of soils (downloaded from https://www.civilengineeringweb.com/).

Determination of liquid limit can be performed by using the fall cone test (Figure 3.11) and Casagrande cup (Casagrande, 1932). Nowadays, the fall cone test is preferred to the Casagrande method because it is more repeatable and less variable (Shimobe and Spagnoli, 2019). Accordingly, fall cone test method have been adopted to determine the liquid limit in this study. The method is described in D4318-10 (2010) and British Standards Institution (1990). After remoulding to break the internal structure, the sample is placed into a cup, removing the excess sediment to provide a smooth level surface. A cone is locked perpendicular to the sample surface, and a supporting assembly is lowered down so that the tip of the cone just touches the surface of the soil. When the correct position is reached, the cone is released and let penetrate the sample for 5 seconds. A gauge shows the amount of penetration (Figure 3.11). The test is repeated multiple times, by remoulding the sample and

adding increasing amounts of water each time, until the penetration exceeds 10 mm. The liquid limit is defined by the water content of the soil that allows the cone to penetrate for more than 10 mm.

Figure 3.11: Norwegian fall cone apparatus used in this study.

The plastic limit is determined by repeatedly remoulding a small ball of moist plastic soil by hand and manually rolling it out into a thread of 3 mm in diameter. The plastic limit is determined by the water content at which the thread crumbles before being completely rolled out. The standard method is described in British Standards Institution (1990). For this thesis, Atterberg limits have been determined for 10 samples extracted from the sediment cores SdG064-01, SdG064-02 and SdG064-03, collected during the INSIGHT Leg1 cruise (Figure 3.7 and Table 3.5).

Finally, the water content is determined by taking the difference in weight of the samples before and after oven-drying them at 105ºC for 24 hours, and dividing this difference by the oven-dried weight.

3.3.6 Consolidation and permeability tests

Consolidation testing consist of applying incremental loads on circular samples of undisturbed saturated sediments confined within a cell to prevent lateral deformation. Porous stones are placed on the top and bottom of the sample to ensure drainage. Incremental loading is applied on the sample and an axial displacement sensor measures the one-dimensional vertical deformation. By measuring the loss of sample thickness after (or during) the loading phase, it is possible to derive

the relationship between void ratio and effective stress for the soil. We carried out consolidation testing using Rowe & Barden cells and adopting stepped loading and Constant Rate of Strain (CRS) configurations.

A Rowe & Barden (Figure 3.12) cell is a type of oedometer where the sample is loaded hydraulically by water pressure acting on a porous disk. Drainage of the sample can be controlled and pore water pressure measured. The main difference with conventional oedometers is the presence of a back pressure controller, that can be used to achieve full sample saturation (Figure 3.12) (Rowe and Barden, 1966). The advantages of a Rowe and Barden cell over traditional oedometers are (Premchitt et al., 1995): 1) minimum vibration effects; 2) possibility to apply higher pressures; 3) negligible deformations of the loading system; 4) control on various drainage conditions; 5) measurement of pore water pressure; 6) measurement of water volume expelled from the sample; 7) saturation of sample under back pressure condition; 8) application of back pressure to simulate *in-situ* condition; 9) control on loading conditions.

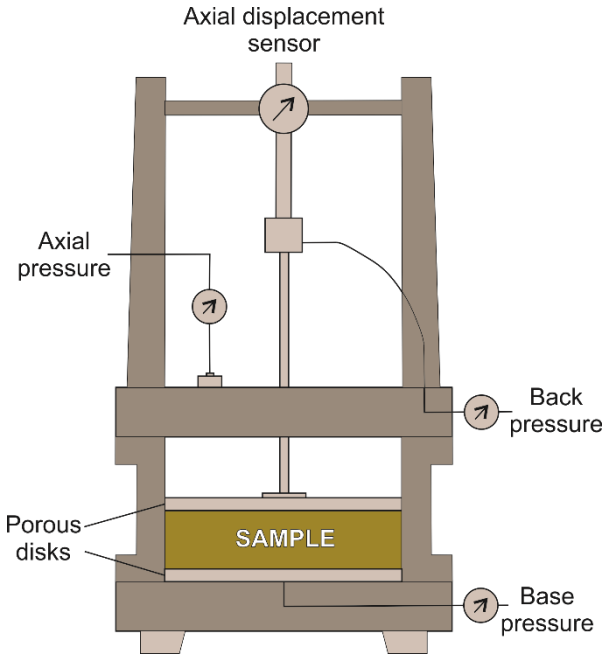

Figure 3.12: Schematic representation of an Rowe&Barden consolidation apparatus.

Consolidation and permeability tests have been carried out in the Geotechnical Laboratory of the Institut de Ciències del Mar in Barcelona (ICM – CSIC). The laboratory is equipped with one Rowe & Barden Type (Figure 3.13A) and one Constant Rate of Strain (CRS) (Figure 3.13B) cells from GDS Instruments®. In both configurations, load is applied on circular samples of saturated sediments of 5 cm diameter and 2 cm height, returning the void ratio variation under different effective stress. Specimens are laterally confined with a steel ring. Full saturation of the sediment sample is obtained by progressively increasing the water pressure in the chamber (i.e. axial and back pressure simultaneously). The increase in axial and back pressure between different saturation stages is distributed over 10 minutes and each saturation stage lasts 24 hours (British

Standards Institution, 1990). The specimen is considered fully saturated when applying a minimum increment in axial stress (10 kPa) without allowing fluid to drain from the sample to prevent any deformation, at least 90% of the additional stress is transferred to the pore pressure.

Although the sample dimensions and saturation procedure was the same for all the tests, we adopted different testing procedures on the two available cells given their characteristics:

1. On the Rowe and Barden type cell (Figure 3.13A), we performed stepped loading consolidation tests. In this configuration, the load is applied instantaneously on the sample, generating a pore pressure increment that is left dissipating before applying the following loading step. After each of the consolidation steps, we performed direct permeability measurement by adopting the constant head method. Constant head permeability measurement consist in creating a pressure gradient (10 kPa) between the two sides of the specimen and measure the water volume that circulates through the sample in a given time interval (10 min) (British Standards Institution, 1990). Darcy's law is then used to determine the sample permeability. The Rowe and Barden cell was equipped with three 2 MPa advanced pressure/volume controllers and sustained a maximum axial pressure of 2 MPa. Stepped loading configuration allows a better control over load, although waiting for excess pore pressure to dissipate after each loading step increase the time needed to perform tests (easily one month for low permeability sediments).

2. On the CRS cell (Figure 3.13B) we performed constant rate of strain tests. Contrary to the stepped loading, after reaching the specimen full saturation a constant rate of deformation, expressed as % of strain per hour, is assigned for the entire loading stage. The rate of deformation (0.1%/h in our tests) must be carefully set in order to allow fluid drainage from the sample and prevent generation of pressures exceeding 15% of the applied load (ASTM, 2012). Compared with the stepped loading configuration, the constant rate of strain test is more time-efficient as it does not involve waiting for pore pressure dissipation nor user input after each loading stage. Furthermore, by providing continuous loading data it is possible to obtain a more detailed view of compression behaviour (Long et al., 2008). The available CRS cell was equipped with 2 MPa pressure/volume controllers and 25 kN submersible load cell mounted on a 50 kN load frame, allowing higher loads compared with the Rowe and Barden cell to be achieved (up to ~10.2 MPa effective stress). Although the constant rate of strain configuration allows a better control over axial deformation, it does not allow a direct measurement of samples permeability.

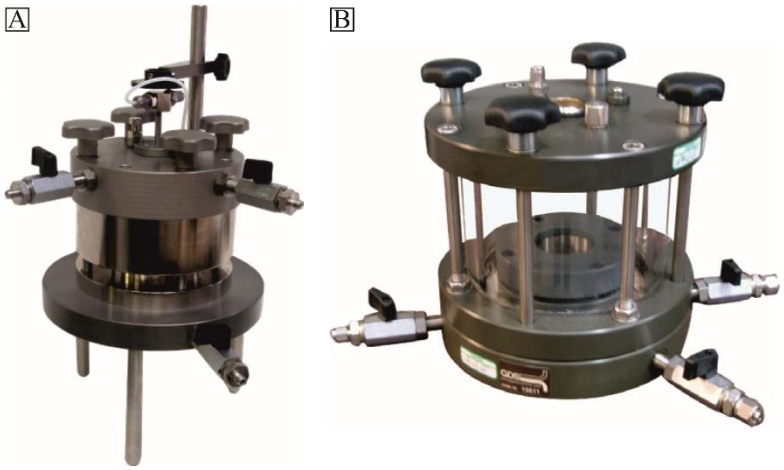

Figure 3.13: GDS® Rowe and Barden (A) and CRS (B) cells used for this study.

In this study, 8 consolidation tests have been performed on sediments sampled from the 3 gravity cores collected during the INSIGHT-Leg1 cruise (Figure 3.7, Table 3.5). 3 of the consolidation tests have been carried out using the Rowe and Barden cell, while 5 have been analysed with the CRS cell. The aim of the geotechnical tests was to derive compressibility and permeability characteristics, including initial void ratio (e_0), compression index (C_c) and initial hydraulic conductivity (k_0) values, to populate parameters for finite-element hydrogeological models (see sections 3.3 and 3.4).

Table 3.5: Summary table of the tests performed on sediment samples. Location of the cores is reported in Table 3.4.

Core	Depth interval (cm)	Grain size	Water content	Atterberg limits	Consolidation test	Permeability tests	Cell type
SdG064-01	187	✓	✓	✓	✓	×	CRS
SdG064-01	190	✓	✓	✓	✓	✓	R&B
SdG064-02	78	✓	✓	✓	×	×	
SdG064-02	84	✓	✓	✓	✓	×	CRS
SdG064-02	93	✓	✓	✓	×	×	
SdG064-02	102	✓	✓	✓	✓	×	CRS
SdG064-02	110	✓	×	×	×	×	
SdG064-02	207	✓	✓	✓	✓	×	CRS
SdG064-02	244	✓	✓	✓	✓	✓	R&B
SdG064-03	137	✓	✓	✓	✓	×	CRS
SdG064-03	144	✓	✓	✓	✓	✓	R&B
SdG083-13	Whole core	✓	✓	×	×	×	

Uniaxial loading data for the samples collected during IODP expedition 340 (see section 3.1.2) and adopted in this study have been calculated through incremental loading using a standard oedometer apparatus (Lafuerza et al., 2014). Hydraulic conductivity was measured by the falling head method. The falling head permeability in a standard oedometer apparatus is determined from

the time that a water column with height h1 takes to flow through a sample. The time starts when the technician opens a valve located on the bottom of the equipment and finalizes when h2 is reached (Sandoval et al., 2017).

Consolidation and permeability data from the sediments collected in the Ursa basin and measured from incremental loading consolidation experiments has been taken from Urgeles et al. (2010, 2007). Permeability values, in this case, were determined from the consolidation experiment itself.

3.4 Basin Analysis using Finite Element Method (FEM) models

Geophysical and geotechnical data described in the previous sections allow, respectively, to determine the stratigraphic architecture of a study area and to characterize their sediment physical properties. These data are used in this study as input for hydrogeological numerical models.

Finite-element method (FEM) numerical models allow solving partial differential equations of a given domain by dividing it into a set of nonintersecting subdomains of finite size (finite elements). This approach allows to approximate complicated functions related with large-scale problems into a set of smaller and easier to represent elements (Reddy, 2011). In the field of geotechnical engineering, for example, a displacement field problem is solved using FEM models by determining the displacement components of a finite number of nodes connecting the elements (Griffiths and Lane, 1999; Urlaub, 2013). FEM provide an approximation of natural processes, and their degree of accuracy greatly depends on the choice of element types and mesh. Generally, finer element grids increase the accuracy of the simulation as well as computational effort and timing to run the simulation. Fine meshes are required where a sharp transition in model properties is expected, while coarse meshes are adequate in areas of homogenous properties or low rate of change (Urlaub, 2013).

FEM software are adopted not only in the field of structural and geotechnical engineering (Griffiths and Lane, 1999), but also, for example, in mechanical, aerospace, civil and automotive engineering, and to simulate fluid flow, heat transfer and electromagnetic fields. In this thesis, we made use of FEM models to reproduce the sediment physical properties and fluid flow evolution of the basin over time. We did this by combining in FEM models the stratigraphy of the Alentejo basin obtained from seismic and core data with the properties of the sediments obtained from geotechnical tests.

Commercial software packages such as Plaxis® or Abaqus® are capable of creating 2D and 3D models coupled to soil constitutive models that reproduce the behaviour of specific types of sediment under different load conditions. However, the performance of those tools when applied to basin-scale studies, such as the one proposed in this study, can be the source of computational problems: a) big-scale models with fine FE meshes generate models too heavy to be handled for

desktop computers; and b) convergence issues appear when using a coarser mesh. On the other hand, basin-scale non-commercial codes provide better balanced resolution results versus computational requirements when applied to models of tens to hundreds of kilometres. In this thesis, the non-commercial software BASIN has been used because of its capabilities, computational requirements and reliable results (Bitzer, 1999; Llopart et al., 2021, 2019; Mencaroni et al., 2020).

3.4.1 BASIN

The finite element software BASIN (Bitzer, 1999, 1996) is based on a forward modelling approach. BASIN allows the calculation of non-equilibrium compaction and overpressure generation on sediments by coupling compaction and 2D fluid flow. The consolidation model incorporates porosity-dependent sediment compressibility through the equation (eq. 9) (Bitzer, 1996):

$$\left(\frac{\partial}{\partial x}\ \frac{k_{x(\emptyset)}\partial p}{\partial x}\right)+\left(\frac{\partial}{\partial x}\ \frac{k_{z(\emptyset)}\partial p}{\partial z}\right)=\ \frac{(1-\emptyset)\ \rho g\alpha_{(\emptyset)}\partial p}{\partial t} \tag{9}$$

where $k_{x(\phi)}$ is the porosity-dependent hydraulic conductivity in the *x*-direction, $\alpha_{(\phi)}$ is the porosity-dependent sediment compressibility, p the fluid pressure, ϕ the porosity, ρ is the sediment bulk density and g is the gravity constant. Sediment compressibility in BASIN is calculated from the specific storage (S_s), which is defined as the volume of water removed from a unit volume of a confined aquifer with an increase in the vertical stress. Specific storage is expressed as (eq. 10):

$$S_s = \rho_s g\alpha \tag{10}$$

Where ρ_s is the sediment density, g is the gravity and α is the sediment compressibility. Specific storage relates with the more commonly used compression index by (eq. 11) (Jorgensen, 1980):

$$s_s = \frac{0.434\ C_c\ \gamma_w}{\sigma'_v\ (1+e_0)} \tag{11}$$

where C_c is the compression index, γ_w is the specific weight of water, σ'_v is the effective vertical stress and e_0 is the void ratio at depositional conditions (1kPa).

In BASIN the depositional model can include a maximum of 40 layers, which must be input with their de-compacted thickness or, in other words, the depositional thickness prior to compaction. Decompacted thickness of the units is calculated using Van Hinte's equation (Van Hinte, 1978) (eq. 12):

$$H_i = H_f\frac{(1-\emptyset_f)}{(1-\emptyset_o)} \tag{12}$$

where $\emptyset_o$ is the initial porosity at deposition, $\emptyset_f$ is the present day porosity and H_f is the present day sediment thickness. Decompacted thickness and duration of deposition defines the sedimentation/loading rate associated to each layer. The facies (sediment characteristics) for each

layer is input as a mixture of maximum 4 sediment types, each one defined in terms of initial hydraulic conductivity (k_0), initial porosity ($Ø_0$) and initial specific storage (S_{s0}). The resulting physical properties of each layer are a function of the relative abundance of each sediment type for a given area and stratigraphic unit.

In the BASIN modelling approach, the physical properties of the sediments are input at their initial depositional conditions, to simulate their evolution and resulting pore pressure through time, down the stratigraphic column and along the margin. Therefore, initial porosity, hydraulic conductivity and specific storage are determined from extrapolation to 1 kPa loading conditions by using the logarithmic regression of the virgin consolidation line for each sediment sample (Figure 3.14). This approach allows to calculate the sediment hydromechanical parameters at deposition (σ' = 1 kPa) (Llopart et al., 2021, 2019; Mencaroni et al., 2020; Urgeles et al., 2010).

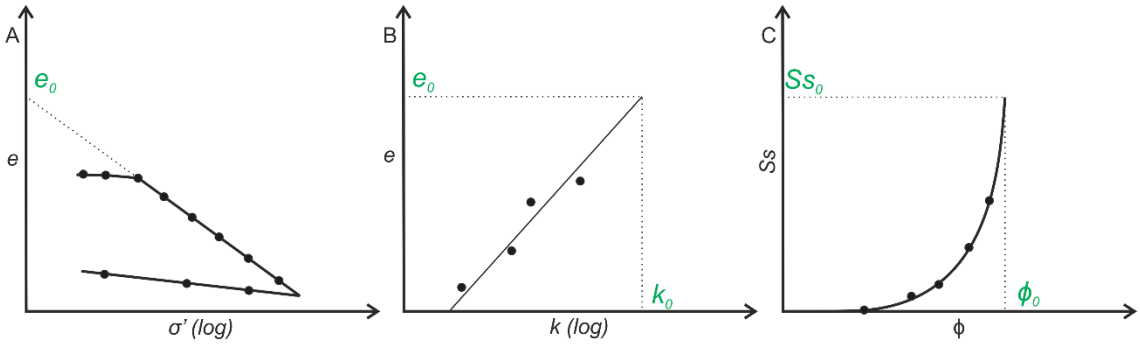

Figure 3.14: Schematic illustration of the method used to extrapolate depositional conditions of (A) porosity, (B) hydraulic conductivity and (C) specific storage from consolidation and permeability tests.

The rate of overpressure generation depends on sedimentation rate, sediment compressibility and permeability. The overpressure generation resulting from BASIN is expressed as overpressure ratio (λ*) (Flemings et al., 2008), defined as (eq. 13):

$$\lambda^* = \frac{(p - p_h)}{(\sigma_v - p_h)} \quad (13)$$

where p is pore pressure, p_h is the hydrostatic pressure and σ_v is the lithostatic or total vertical stress. A λ^* value of 0 means that pore pressure is hydrostatic, while a value of 1 means that the overburden is fully sustained by the pore water.

3.4.1.1 Boundary conditions

Left and right boundaries of BASIN models are constraint, allowing only vertical displacement. The bottom boundary of the model, represented by the basement, is vertical and horizontally fixed. The upper boundary (seafloor) is a hydrostatic boundary. Fluid flow out of the system is only allowed through the upper boundary (sediment-water interface), while it does not take place on the lateral boundaries. Flow in BASIN does not take place through the basement: this condition implies that, using BASIN for hydrogeological studies, the role of deeper units as relevant source

for fluid flow must be carefully considered when the model is conceptualized, since fluid flow input from deeper formations cannot be modelled.

3.4.2 Modelling the influence of sediment physical properties on overpressure development

The first modelling effort described in this thesis uses BASIN to evaluate the suitability of hydrogeological models based on literature-derived physical properties of sediments collected from similar depositional environments and with comparable grain size distributions. To this end, we built a series of one-dimensional finite-element models that simulate the development of overpressure on a hemipelagic unit rapidly buried by a series of mass wasting events. Using the same depositional scenario, the initial porosity, hydraulic conductivity and specific storage of the hemipelagic layer is replaced with values measured on sediments of similar grain size, but different depositional settings (hence physical properties): the Alentejo basin (Gulf of Cadiz, SW Iberian margin), Grenada basin (offshore Martinique, Lesser Antilles) and Ursa basin (Gulf of Mexico) (Table 3.4). All of the samples were composed by hemipelagic sediments, collected outside mass transport deposit areas: for this reason, we assumed they did not undergo heavy deformation or mixing processes and the extrapolation of their physical properties to 1 kPa can be considered a fair reproduction of their characteristics at depositional conditions (Figure 3.14 and Figure 3.16).

In a first instance, we built a series of 1D models to simulate deposition of a 500 m thick hemipelagic unit at a sedimentation rate of 30 cm/ky. This unit is followed by a series of turbidite events that deposit 250 m of sand-rich material during 10.000 years. Initial thickness of the units, sedimentation rates and boundary conditions, as well as physical properties of the turbidite unit, are kept constant through the different scenarios. Since no samples associated with turbidites were available in our database, we defined their physical properties with values taken from Reed et al. (2002). The only variables that change in between the different models are initial porosity, initial hydraulic conductivity and initial specific storage of the hemipelagic layer. In the first set of analysis (Scenario A), we defined the properties of the hemipelagic unit by averaging arithmetically the physical properties values for each study area. In the second series of tests (Scenario B), we assigned physical properties to each hemipelagic layer based on the average specific storage, porosity and hydraulic conductivity of the samples from each grain size class. The three-components textural classification for muddy sediments proposed by Flemming (2000) has been used to subdivide the analysed sediments in four classes based on their sand, silt and clay content: D-II (very silty slightly sandy mud), D-III (silty slightly sandy mud), E-II (slightly clayey silt) and E-III (clayey silt) (Figure 3.16).

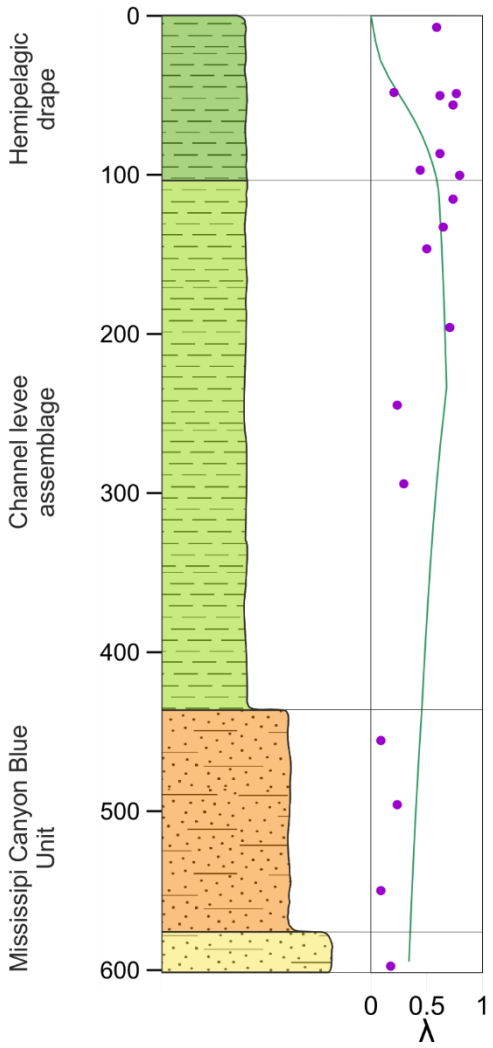

Figure 3.15: Site U1324 stratigraphic model adopted for the 1D simulation with corresponding overpressure: *in-situ* piezometer overpressure measurements (purple dots) (Expedition 308 Scientists 2005); reference 1D modelling result (green line) (Urgeles et al. 2010). Properties for overpressure models in Results section 5.2 are only changed for the upper hemipelagic drape.

Secondly, to evaluate the reliability of our results and their significance in terms of submarine slope stability, we applied our approach to the Ursa basin (Gulf of Mexico) case study, where *in-situ* overpressure has been grounthruthed with piezometer measurements during IODP expedition 308 (Flemings et al., 2008) (see section 1.3 for more information about the *in-situ* overpressure measurement methods, section 2.5.2 for the geological setting and section 3.1.2 for insights about the IODP expedition 308) (Figure 3.15 and Figure 3.16). The aim of this test was to adopt the actual sedimentary history at Ursa basin (Figure 3.15), and test the influence of using actual physical properties from the area versus physical properties taken from other depositional environments of similar grain size (Table 3.4).

Using BASIN, we reproduced the stratigraphic architecture, sedimentation rate, boundary conditions and lithologies of a 1D overpressure model at Site U1324 from Urgeles et al. (2010) (Table 3.4). Then, we replaced the original physical properties associated with the top hemipelagic drape with the ones measured from the sediments collected in the Alentejo (Figure

3.7 and Table 3.4) and Grenada basins (Table 3.4). By doing this, we aim to evaluate the differences in overpressure generated by defining hydrogeological models with physical properties measured from hemipelagic sediments collected in different areas, and compare them with the reference calibrated results from Urgeles et al. (2010). The overpressure evolution of the basin had been modelled and is modelled in this study since deposition of the sand-rich Blue unit (~ 100 ky ago), followed by the silt lithologies associated with the filling of the Ursa Canyon, and by the mud-dominated sediments from a channel levee assemblage and hemipelagic sediments (Figure 3.15 and Figure 3.16) (Urgeles et al., 2010, 2007).

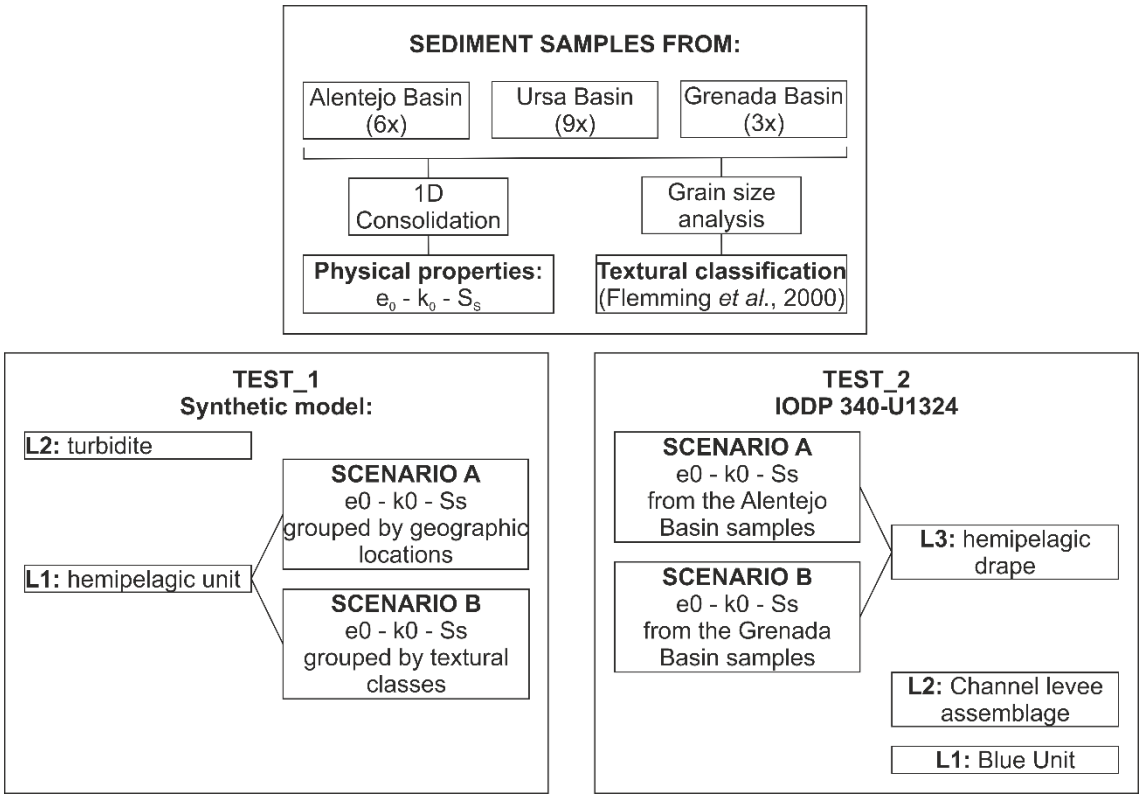

Figure 3.16: Flow chart of the set-up for the different 1D models using BASIN.

3.4.3 Modelling the pore pressure development in the Marquês de Pombal area

We also used BASIN to reconstruct the fluid-flow and pore pressure history in the Marquês de Pombal area. Our aim was to understand if the slope instabilities in the area, highlighted by well visible mass transport deposits and scars, could have been facilitated (or still are) by any excess pore pressure development or, to the contrary, if the major contributor towards the observed slope failures are the earthquakes that occur in the area.

While the series of synthetic models described in the previous section could be simulated through basic 1D simulations, reproducing the flow pattern and pore pressure development in the Marquês de Pombal area implied taking into account a series of additional elements. In the Marquês de Pombal area, multiple geomorphological and stratigraphic features such as the São Vicente Canyon, steep slopes, stratigraphic closures and areas of localized high sedimentation rate could

have the potential to affect the flow pattern within sediments. Ideally, the effect of those variables in the pore pressure distribution could be simulated accurately only by 3D models where all the lateral and vertical changes of properties could be modelled considering all the directions and their evolution through time. 3D fluid flow and overpressure modelling on a basin scale are adopted to study overpressure generation within deep and consolidated rock formations (Borge and Sylta, 1998; Broichhausen et al., 2005). However, as explained at the beginning of this chapter, at present 3D FEM models for geotechnical applications are mainly used for smaller scale simulations. This is because coupling compaction and fluid flow in unconsolidated sediment at the basin scale require high processor power and/or significant simulation time that cannot be handled by standard desktop computers. Furthermore, the reliability of 3D geotechnical software in solving problems with a scale of hundreds of square kilometres has never been tested.

Our attempt to bypass this limitation has been to build a network of 5 2D BASIN models within the Marquês de Pombal Plateau area, including the sediment transitions towards the Infante Don Henrique basin and the São Vicente Canyon (Figure 3.17). Our goal was to evaluate the influence of all the main geological and geomorphological variables on the pore pressure build up through 2D models. We interpolated the 2D results in order to obtain an overview of the pore pressure development along the area of interest and during the entire sedimentation history (Figure 3.20).

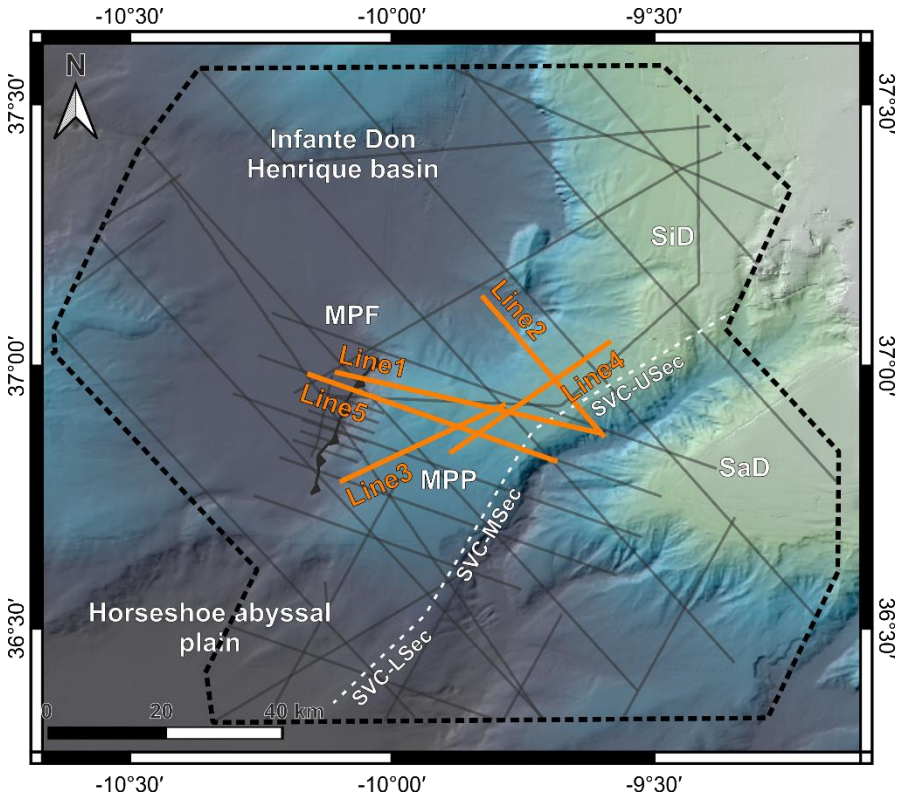

Figure 3.17: Location and names of the five 2D models used to model overpressure evolution in the Marquês de Pombal area.

3.4.3.1 Definition of the model's units

The main stratigraphic units adopted for this study are the ones included between the 7 regional reflectors tracked along the study area and reported in section 3.2.2.2 (Table 3.3). The horizons have been time-converted (see section 3.2.2.2), gridded (grid size: 100 m) and exported in correspondence of each of the 2D model profiles (Figure 3.17). In the models computed with BASIN, the mesh nodes are equally spaced up to a maximum of 40 nodes. Thus, the mesh node spacing for each line depends on the line length, with nodes spaced between approximately 800 m for Line_3 and 1150 m for Line_1 (Figure 3.17). The nodes spacing in the y-direction depends on the layers thickness, and it varies according with their geometric configuration.

Lateral transition of sedimentary facies (and associated physical properties) is modelled by changing the relative percentage of each of the four sediment types defined in BASIN along the x-direction. No vertical facies transitions are allowed within the same layer. To increase the vertical variability of the models, we split the seven main units into multiple sub-layers. To divide the units, we examined the grain size distribution at Site U1391 (Figure 3.9), and grouped depth intervals alternating levels of higher sand presence with intervals characterized by finer sediments. In this way, we aimed to represent in the stratigraphic model the alternation of potentially higher and lower permeability layers. We also made sure the thickness of the layers was roughly consistent with the stratigraphy at Site U1391. We split Unit I in 2 sub-layers, Unit II in 7 and Unit III in 3. Unit IV was divided in 10 sublayers of constant thickness to provide higher resolution to the uppermost part of the model, since the results will focus particularly on the overpressure development within this unit (Table 3.6).

Since Unit I was the deepest unit penetrated by well U1391, no grain size information were available below this unit. Thus, the subdivision of the Upper Miocene (UM) and Early Pliocene (EP) units have not been based on their grain size distribution and we divided them in regular thickness sub-layers (four for the UM and three for the EP). After units' subdivision, the model was composed by 30 sub-layers, bounded by 29 horizons (Table 3.6).

The depth of the horizons was first identified at Site U1391 location on seismic profile PD00_522 (Figure 2.13). Since the vertical resolution of the available MCS profiles was mostly too low to allow for tracking the reflectors related with each sub-layer, the sub-horizons have been projected along the basin by keeping their original relative spacing as constant along the entire study area.

The smear slide analysis from IODP well U1391 (IODP Expedition 339 Scientists, 2013a) (Figure 3.9) has been used as starting reference for the sediment vertical distribution. The resolution of IODP smear slide analysis varies between 6-7 cm and a maximum of approximately 10 m between each sample. Besides compositional, mineralogical and micropaleontological information, the smear slide analysis provides the percentages of sand, silt and clay down to a depth of 670 m below sea floor (mbsf). We used this information to define each of the 30 sub-units constituting

the model with the same percentage of sand, silt and clay averaged within each sub-layer depth interval (Table 3.6).

Besides the ages of the main discontinuities described by Hernández-Molina et al. (2016), Lofi et al. (2016) provided a higher resolution chronostratigraphic model by identifying a series of 49 gamma ray horizons that have been correlated along five sites drilled by IODP expedition 339 in the Gulf of Cadiz (Figure 3.18). Their study is based on the assumption that the sediments NGR response results from incorporation of particles from igneous rocks, eroded and typically accumulated as clay minerals (Veeken, 2007). Excursions in the NGR log can therefore provide a powerful tool to correlate isochronous intervals with similar grain size at different locations. Gamma ray intervals are proposed as regional isochronous periods of contourite deposition enforcement, expressed with a drop in NGR values. The intervals are dated based on age control points, which have been extrapolated from correlating XRF-derived or benthic foraminifer $\delta^{18}O$ records to regional or global standard chronologies (Figure 3.18) (Abrantes et al., 2017; Bahr et al., 2014; Lofi et al., 2016; Singh et al., 2015; Voelker et al., 2015, 2014). We made use of this chronostratigraphic model to assign ages of deposition to each of the sub-layers constituting Unit II and Unit III (Table 3.6).

The underlying units, which are not included in the chronostratigraphic model (Figure 3.18), have been dated by interpolating the absolute time of deposition of the underlying and overlying reflectors, thus assuming a constant sedimentation rate within each unit. The 10 sub-layers constituting Unit IV have also been dated by considering a constant sedimentation rate between the LQD (0.3 Ma) and the present-day seafloor (Table 3.6).

Finally, porosity data from borehole U1391 (Figure 3.9B) have been plotted to derive a trend for the loss of porosity with depth, at the well location (Figure 3.7 and Figure 3.9B). Even if the porosity measurements show a high degree of scatter, the general trend follows an exponential distribution that we used to groundtruth the model by comparing the final modelled porosity to observed porosity data.

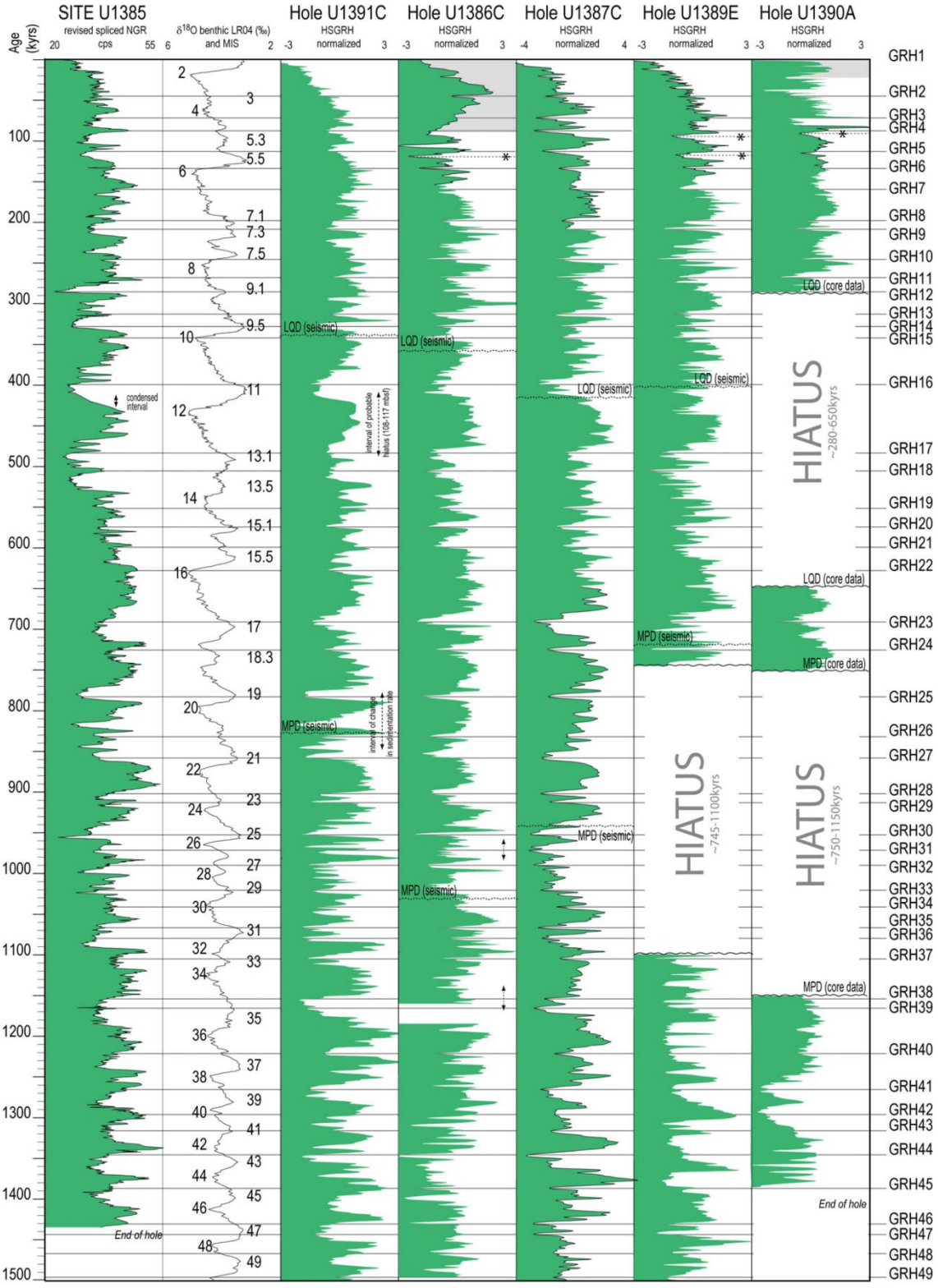

Figure 3.18: Regional scale correlation of gamma ray (HSGR) downhole logs for six sites drilled during IODP 339 expedition in SW Iberia, plotted with respect to geological time. On the right axes the horizon references are indicated. Modified after Lofi et al. (2016).

Table 3.6: Horizons and units constituting the reference stratigraphic model at well 339-U1391 location. Sed. Rate refers to decompacted sedimentation rate.

Boundary horizons	Depth (mbsf)	Age (Ma)	Layer number	Unit name	Thickness (m)	Sed. Rate (cm/kyr)	Sand %	Silt %	Clay %
Seafloor	**0**	**0**							
			29	IV_S10	9	27	13	30	57
UnitIV_Sub9	9	0.034							
			28	IV_S9	9	27	10	25	65
UnitIV_Sub8	18	0.068							
			27	IV_S8	9	27	27	31	42
UnitIV_Sub7	27	0.102							
			26	IV_S7	9	27	12	29	59
UnitIV_Sub6	37	0.136							
			25	IV_S6	9	27	13	30	57
UnitIV_Sub5	46	0.170							
			24	IV_S5	9	27	25	24	51
UnitIV_Sub4	55	0.205							
			23	IV_S4	9	27	14	26	60
UnitIV_Sub3	64	0.239							
			22	IV_S3	9	27	5	25	70
UnitIV_Sub2	73	0.273							
			21	IV_S2	9	27	26	33	41
UnitIV_Sub1	82	0.307							
			20	IV_S1	9	27	16	39	45
LQD	**91**	**0.341**							
			19	III_S3	31	28	14	26	60
UnitIII_Sub2	122	0.451							
			18	III_S2	28	16	9	32	59
UnitIII_Sub1	150	0.632							
			17	III_S1	46	23	25	28	47
MPD	**196**	**0.831**							
			16	II_S7	53	42	10	29	61
UnitII_Sub6	249	0.956							
			15	II_S6	49	33	6	29	65
UnitII_Sub5	298	1.106							
			14	II_S5	54	30	6	26	68
UnitII_Sub4	352	1.282							
			13	II_S4	47	25	7	25	68
UnitII_Sub3	399	1.468							
			12	II_S3	48	22	11	31	58
UnitII_Sub2	447	1.687							
			11	II_S2	55	21	10	29	61
UnitII_Sub1	502	1.949							
			10	II_S1	64	21	9	23	68
EQD	**566**	**2.25**							
			9	I_S2	34	8	10	31	59
UnitI_Sub1	600	2.677							
			8	I_S1	34	8	9	32	59
LPD	**634**	**3.1**							
			7	EP_S3	263	36	7	30	63
EP_Sub2	897	3.833							
			6	EP_S2	262	36	10	50	40
EP_Sub1	1159	4.566							
			5	EP_S1	263	36	10	50	40
M/P	**1422**	**5.3**							
			4	MM_S4	11	0.7	10	50	40
UM_Sub3	1433	6.875							
			3	MM_S3	11	0.7	10	50	40
UM_Sub2	1443	8.45							
			2	MM_S2	11	0.7	10	50	40
UM_Sub1	1454	10.025							
			1	MM_S1	11	0.7	20	50	30
MM	**1465**	**11.6**							

3.4.3.2 Physical properties of different sediment classes

As explained in section 3.4.1, BASIN allows to input physical properties for a maximum of four sediment types, each one defined in terms of porosity, hydraulic conductivity and specific storage. Three of the sediment types in our models are: clay, silt and sand, as these were the three compositional classes resulting from Site U1391 smear slide analysis (Figure 3.9A) that we assumed as the reference stratigraphy for our study area. To define the physical properties of each class, we clustered the results of our geotechnical tests based on the grain size distribution of the tested samples: samples with higher percentages of clay (>30% clay component) provide the physical properties for the "Clay" type. In the same way, sediments that show higher presence of silt (<30% clay) have been clustered as "Silt". The unique values of initial porosity, hydraulic conductivity and specific storage that define each sediment type are the average of each sediment group. Since none of the analysed samples resulted in high presence of sand (e.g., >10%), we defined the "Sand" sediment type with physical properties from the literature. We adopted initial porosity, specific storage and hydraulic conductivity values for sand from Reed et al. (2002).

We introduce a fourth sediment type in the model: the "Mixed System" for practical purposes, with the aim to understand the influence of this deposit in fluid flow pathway evolution and development of overpressure (see stratigraphic interpretation of the area described in section 4.1 and discussed in Chapter 7). This deposit is not present at Site U1391. So, in our models, the Site U1391-derived late Quaternary stratigraphy and physical properties are substituted with this fourth sediment type wherever the model crosses the Marquês de Pombal Plateau. Since all the geotechnical tests from the INSIGHT samples have been performed on sediments collected from this mixed system, the physical properties of this sediment type are calculated by averaging all the values resulting from the tests (Figure 3.20).

3.4.3.3 Models features

3.4.3.3.1 Lateral variations in sediment composition

IODP borehole U1391 provides a detailed stratigraphic description of the uppermost 670 m of sediments in the Alentejo basin (Figure 3.9A). However, the location of the well, in the upper part of the slope and within an area highly affected by the MOW circulation (Figure 2.10), suggests that the facies encountered at the borehole location do not necessarily extend along the Marquês de Pombal Plateau. Even if it has been possible to track the main reflectors along the entire geophysical dataset, it is likely that the high content of sand recovered in the middle slope does not extend to deeper water settings. As explained in section 2.3, depending on the water depth range, the lower slope is dominated by less powerful water currents such as the ML or the NADW (Llave et al., 2006; Rogerson et al., 2012b, 2012a; Schönfeld et al., 2003; Schönfeld and Zahn, 2000). As it is explained more in detail in section 7.1, the transport capacity of these currents is

reduced and sedimentation of coarse sediment is unlikely to take place (McCave, 1984; Miller et al., 1977). Thus, a decrease of sand component within the units at higher water depth is likely.

In absence of other wells drilled in deeper waters within the Alentejo basin, the lateral variation in sand content from shallow to deep waters is inferred from the available gravity cores. As it is mentioned in section 3.3.1, gravity core SdG068-02 (Figure 3.7) is the only core collected within a landslide scar. The scar represents a stratigraphic window of at least some meters within older sediments, even though the sediments collected are most likely still part of the uppermost Unit IV. Grain size measurements performed on gravity core SdG068-02, at 2.07 meters depth, reported a sand content of 8.49%, the higher within all the samples analysed (see Results section 4.2.1 for further details). We correlated this value with the sand content at the closest depth interval in the IODP well U1391 (15% at 2.6 m) and assumed they correspond to the same event. The two sand measurements with the respective water depth (2667 m water depth at core SdG068-02 vs 1073 m at Site U1391) provided a simple relationship for sand fractionation with depth. In absence of stronger evidences, we modelled the decrease in sand content as directly related to the water column at which the deposition happened, with a linear equation expressed by (eq. 14):

$$SandContent = (-0.0041 * WaterDepth) + 19.382 \quad (14)$$

3.4.3.3.2 Canyon erosion

Three out of five models (Line_1, Line_2 and Line_5) (Figure 3.17) end inside the São Vicente Canyon area. As explained in section 2.2.3, the São Vicente Canyon is a relatively recent geomorphological feature, as the upper and middle sector of the canyon (see section 2.2.3) have been eroded starting from the late Quaternary (Serra et al., 2020). Accordingly, the canyon erosion has been modelled starting from the late Quaternary, with a constant rate of erosion distributed between the uppermost 10 sublayers (i.e. erosion equally distributed within the 10 time steps representing the late Quaternary) (Table 3.6). The thickness of eroded sediments have been inferred by connecting the top horizons of the main stratigraphic units on both sides of the canyon and subtracting them from the present-day horizons configuration (Figure 3.19).

The reason why part of the canyon is included in some of our models is to evaluate the possibility for pore water, expelled during the burial history, to laterally flow within permeable pathways and to exit the system through the canyon. This eventuality would reduce the overall overpressure development in the basin. On the other hand, modelling the erosion produced by the São Vicente Canyon generates some perturbation in overpressure results close to the canyon flanks. Each of the ten late Quaternary erosional steps, in fact, must be modelled in BASIN as instantaneous.

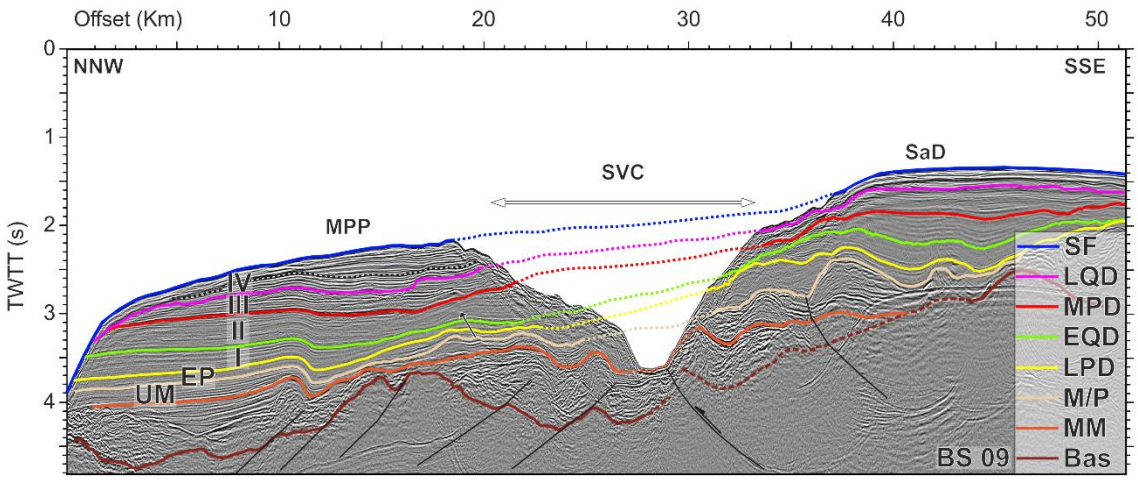

Figure 3.19: MCS profile BS09 showing how the sediment eroded by the SVC have been approximated. LQD: Late Quaternary Discontinuity; MPD: Middle Pleistocene Discontinuity; EQD: Early Quaternary Discontinuity; LPD: Late Pliocene Discontinuity; MP: Miocene/Pliocene horizon; MM: top Middle Miocene; Bas: Basement. I, II, III and IV, EP (Early Pliocene) and UM (Upper Miocene) correspond to the different units defined in between the major discontinuities; MPP: Marquês de Pombal Plateau; SaD: Sagres Drift; SVC: São Vicente Canyon; vertical exaggeration ~ 4x; TWTT : two-way travel time.

According to the overpressure ratio (λ^*) formula presented in section 3.3 (eq. 13), the sudden removal of lithostatic stress (σ) generates an instantaneous increase of λ^*. On the other hand, in reality the late Quaternary erosion of the São Vicente Canyon did not proceeded by instantaneous removal of thick units, but most likely evolved gradually during the entire late Quaternary, providing enough time for pore fluid to escape and overpressure dissipation. With the aim of modelling the influence of the canyon erosion on the overall fluid flow at the basin scale, without considering the artefacts generated at the flank of the canyon itself, we built additional models of Line_1, Line_2 and Line_5 (Figure 3.17) without accounting for the development of the São Vicente Canyon. By subtracting the results from the two types of models (with and without the São Vicente Canyon) it has been possible to detect and isolate areas of unrealistic overpressure development in close proximity of the canyon, yet allowing to evaluate the influence of the canyon erosion in the overall fluid flow and overpressure development in the area (Figure 3.20).

3.4.3.3.3 Fault displacement

Line_1 and Line_5 (Figure 3.17) are two models that cross the Marquês de Pombal Fault perpendicularly. We modelled the fault displacement by distributing the deformation of the NE-SW trending reverse fault constantly from the Early Pliocene to the present day, starting from a regular slope (connecting the NW flank of the canyon with the Infante Don Henrique basin) and evolving into the present-day slope configuration (Figure 3.20).

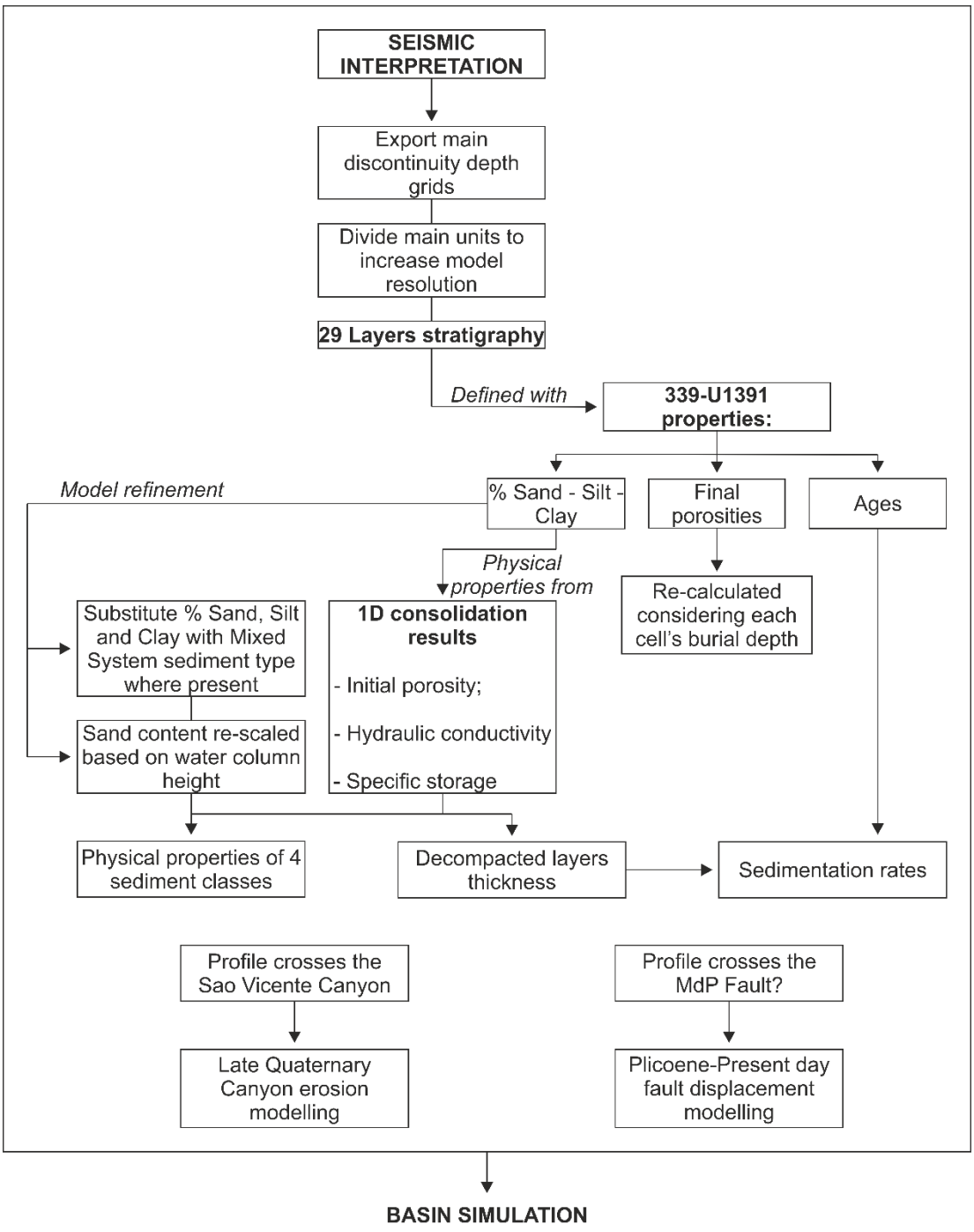

Figure 3.20: Flow chart of the Marquês de Pombal overpressure evolution modelling.

3.4.3.4 Model cross-validation

Finally, the reliability of every model needs to be cross-checked with benchmark points. The only way to measure directly the overpressure in the sediment is through *in-situ* measurements (see section 1.4.3), which have never been performed in the area. However, indirect methods allow us to check at least that the overall sediment distribution and physical properties of the stratigraphic column are correct, reducing the potential range of error of the simulation results.

As explained in this chapter, in BASIN we input the de-compacted thickness of the layers and we let the software calculate their loss in thickness. The loss in thickness depends mainly on specific storage and initial porosity. By comparing the depths of the various horizons at the end of our simulation with the depths determined from the stratigraphic interpretation, we can estimate the error from the degree of difference between the model results and the actual stratigraphic model. Minor differences indicates that the layers' compaction does reproduce a burial history compatible with the present-day bathymetry. This is an indication that the overall definition of the layers' physical properties is correct. Being overpressure generation a direct consequence of sedimentation rate, sediment compressibility and permeability, this simple test returns a proof of the goodness of the first two conditions. The presence of unpredicted layers with different permeability remains, however, an unsolved element of uncertainty in the simulation results.

Another way to quality control the accuracy of physical properties defining the various layers composing the model is to extract, at the end of the simulation, a porosity profile in the proximity of available deep sediment data, represented in our study by the IODP Site U1391 (Figure 3.9). In this case, uncertainties associated with the vertical sediment distribution can be related only with the resolution of the model, which is unable to reproduce the fine stratigraphic details encountered along the well. However, comparing the modelled porosity with the one determined from downhole logs and/or moisture and density measurements provides an indication of the accuracy of the compaction and permeability values used in the model.

3.4.4 Model uncertainties (Monte Carlo analysis)

In order to take into account and understand the role of the uncertainty related to sediment physical properties, a Monte Carlo analysis has been carried out. The software BASIN (Bitzer, 1999) has been adopted for the analysis given its low computational time to perform the simulations and the possibility to test the four sediment types that define our models.

The set of parameters adopted for the Monte Carlo analysis has been picked by using a Simple Random Sampling in between the range of the coefficient of variation for each sediment type and each physical property (Hurtado and Barbat, 1998). A total of 256 models have been created and simulated by combining the four sets of parameters for each of the sediment types randomly.

Where models are made of independent variables, the best approach would be to test the influence of the different sediment physical properties used in the simulation one at a time. In our modelling, however, this approach would not be adequate because the input physical properties of sediments (i.e. specific storage at deposition, porosity at deposition and hydraulic conductivity at deposition) are interdependent parameters. A decrease in porosity, for example, implies a reduction also in specific storage and hydraulic conductivity. Thus, the random generation of the input parameters for the models has taken into account this dependency.

3.5 Slope Stability

To assess the stability of the Alentejo basin, an infinite slope stability approach based on normalized parameters is used. Such approach makes the analysis independent of depth. Despite its simplicity, the infinite slope model is adequate for the purpose of this study because the assumptions of the model approximate the observations from geophysical data (i.e., the shear surface is parallel to the ground surface). In addition, the infinite slope model also lends itself to the spatial assessment of slope stability within GIS. The infinite slope model has been used by numerous authors to assess earthquake slope stability (Collico et al., 2020; Hitchcock et al., 2010; Jibson et al., 2000; Mankelow and Murphy, 1998). Assuming static conditions and cohesionless sediments, the relation between stability of a submarine slope and overpressure can be expressed in terms of the factor of safety (FoS) formulation from Revil et al. (1998) (eq. 15):

$$FoS = \frac{tan\emptyset_f}{sin\theta cos\theta}\ (cos^2\ \theta - \ \lambda^*) \tag{15}$$

where $\emptyset$ is the internal friction angle, θ is the seafloor slope and λ^* is the overpressure ratio (eq. 13). In the FoS formulations failure is expected when FS < 1, and this condition can take place in regions where significant overpressure and/or steep slopes exist.

Pseudo-static analysis are frequently used to evaluate regional landslide hazard assessment under earthquake shaking, and consist in modelling the seismic shaking as a permanent body force added to a conventional, static limit-equilibrium analysis (Jibson, 2011).

The first step of the method consist in deriving the horizontal peak ground acceleration (PGA) attenuation with distance from the earthquake hypocentre. PGA values are typically derived from ground motion attenuation relationship, which are estimated from empirical correlation between the maximum ground acceleration observed during an earthquake and the earthquake magnitude (Collico et al., 2020). In our study, PGA is evaluated using the approach from Ambraseys et al. (2005) that relates to large-magnitude events (Mw > 5) for soft soils (eq. 16):

$$\log(PGA) = 2.6595 - 0.142M_w + (-3.184 + 0.314M_w)\log\sqrt{d^2 + 7.6^2} - 0.084F_N + 0.062F_T - 0.044F_O + \varepsilon_T \tag{16}$$

where $\log(PGA)$ is the logarithm of the horizontal peak ground acceleration (g), M_w is the moment magnitude (7.8 for the Marquês de Pombal Fault), d the hypocentral distance (km), F_N is 1 for normal faulting, 0 otherwise, F_T is 1 for thrust faulting (as in our case), 0 otherwise, F_O is 1 for other styles of faulting, 0 otherwise. ε_T is the transformation uncertainty modeled as~N (0, $\sigma\log_{(PGA)}$), and $\sigma_{\log(PGA)} = \sqrt{(0.666 - 0.065Mw)^2 + (0.222 - 0.022Mw)^2}$.

The PGA relation expressed in eq. 16 involves a dependency of PGA on fault mechanism, introducing the coefficients F_N, F_T and F_O where thrust faults, such as the Marquês de Pombal Fault, provide the most intense shaking.

PGA, slope gradient and overpressure ratio distribution are then computed in order to obtain the pseudo-static factor of safety ($FoS_{p\text{-}stat}$) through the equation (Carlton et al., 2017; Collico et al., 2020) (eq. 17):

$$FoS_{p-stat} = \frac{Cu}{\gamma' z(sin\alpha cos\alpha + k_h \frac{\gamma}{\gamma'} cos^2\alpha)}(1 - \lambda^*) \quad (17)$$

where α is the slope gradient, $\frac{Cu}{\gamma' z}$ is the normalized undrained shear strength, $\frac{\gamma}{\gamma'}$ is the normalized sediment unit weight, $k_h = \eta * PGA$ is the horizontal acceleration coefficient, and λ^* the overpressure ratio.

The value η adopted for the horizontal acceleration coefficient is applied to obtain a performance-based value of k_h and is related with the site condition of soils. Following the approach proposed by Collico et al. (2020) for the Gulf of Cadiz, η values are chosen from the ones proposed by (Rampello et al., 2010) and are those associated to 15 cm permanent Newmark displacement for subsoil conditions described as loose-to-medium soil and/or soft-to-firm cohesive soil.

PART III

RESULTS

Chapter 4: Characterization of the Marquês de Pombal Plateau area: stratigraphy and sediments distribution

The aim of this chapter is to characterize the seismo-stratigraphic architecture, sediment distribution and sediment physical properties of the study area, with special focus on the Marquês de Pombal Plateau area.

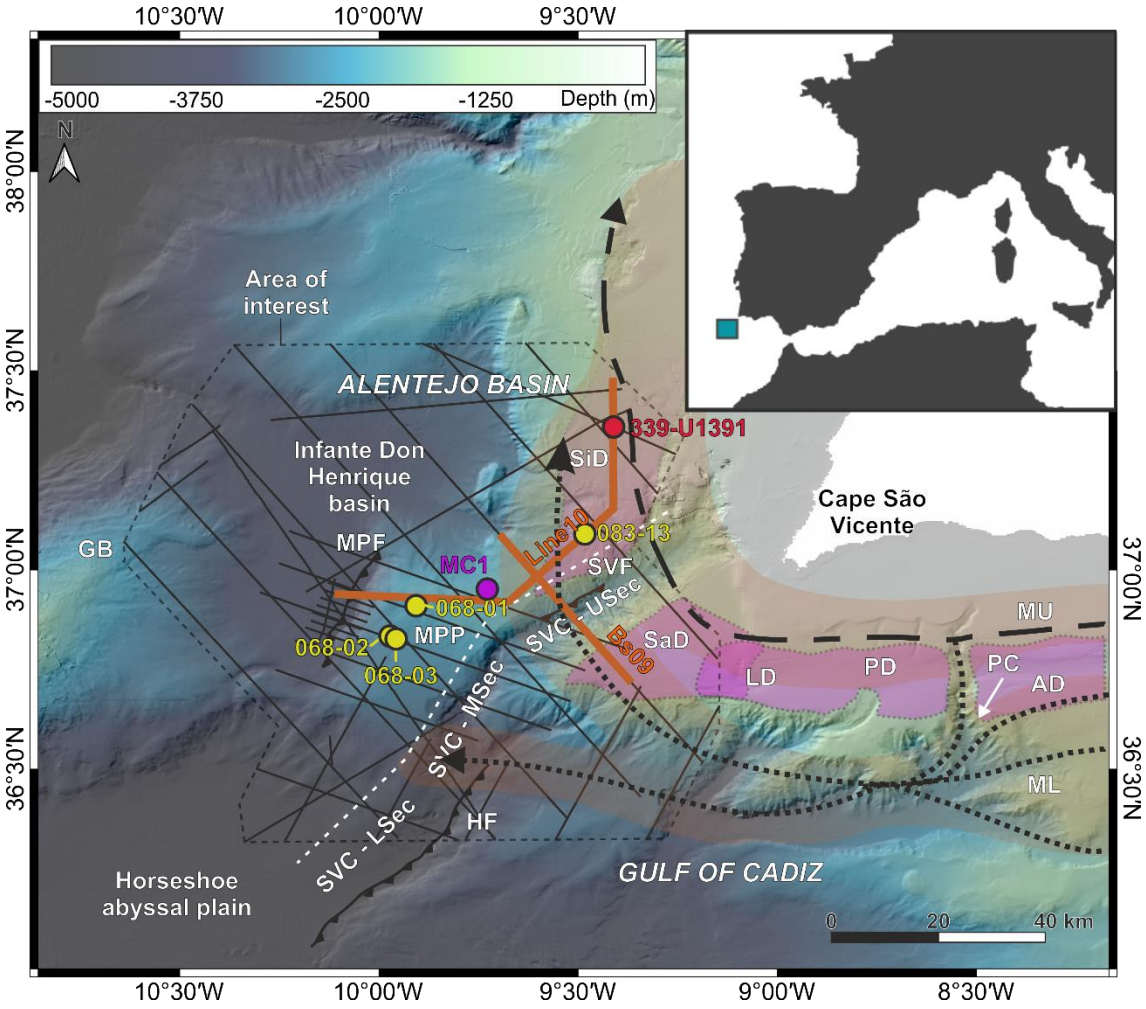

Figure 4.1: Bathymetric map of Alentejo basin and the northern part of the Gulf of Cadiz showing its main geomorphological features. Dashed arrows correspond to the main cores of the Mediterranean Outflow Water (MOW), with areas of influence shaded in orange. Black lines indicate multichannel seismic (MCS) profiles used in this study. The red circle corresponds to the IODP Site U1391. Yellow circles refer to gravity cores collected during the INSIGHT Leg1 and Leg2 cruises: SdG083-13, SdG068-01, SdG068-02 and SdG068-03. The purple circle corresponds to multicore MC1 from Garcia-Orellana et al. (2006). Orange lines show the MCS profiles displayed in this chapter (BS09 and INS2-Line10). Purple areas refer to the estimated drift depositional areas prior to this study. The dashed polygon bounds the area of this study. AD: Albuera Drift; GB: Gorringe Bank; HF: Horseshoe Fault; LD: Lagos Drift; MPF: Marquês de Pombal Fault; MPP: Marquês de Pombal Plateau; MU: MOW upper core (dashed arrow); ML: MOW lower core (dotted arrow); PC: Portimão Canyon; PD: Portimão Drift; SaD: Sagres Drift; SiD: Sines Drift, SVC - LSec: São Vicente Canyon lower section; SVC – Msec: São Vicente Canyon middle section; SVC – USec: São Vicente Canyon upper section; SVF: São Vicente Fault.

Besides increasing the understanding about the depositional systems and sedimentary processes that take place in the area, deriving sediment accumulation rates, thickness and geometric configuration of the various units as well as hydromechanical properties of sediments in the Marquês de Pombal Plateau provide information for fluid flow and overpressure modelling described in Chapter 6. Most of the seismic interpretation and sediment grain size and MSCL analysis reported here have been published in Mencaroni et al. (2021).

4.1 Seismic stratigraphy

The seismo-stratigraphic analysis presented here is mainly based on MCS profiles collected around the canyon system (Figure 4.1). The overall Plio-Quaternary stratigraphy of the area is characterized by a general upward increase in the amplitude of seismic reflections, and a general decrease in the continuity of reflections throughout the entire sequence (Figure 4.2 Figure 4.3**)**. Reflection configurations evolve from parallel, in the deeper part of the study area, to sigmoidal in the shallower segments (Figure 4.2). The sequence contains several discontinuities and hiatuses characterized by truncations and onlap surfaces. A structural high in the upper reaches of the slope immediately north of the São Vicente Canyon (Figure 4.2A) separates the Marquês de Pombal Plateau (Figure 4.2B) from the Sines Drift (Figure 4.2C).

4.1.1 Major discontinuities

In the Sines Drift area, the LPD (see section 2.4 for seismic stratigraphy of the area) appears as a laterally-continuous, clear erosive surface that truncates the underlying units and displays a number of channels (Figure 4.2C). The LPD onlaps the structural high located on the upper reaches of the slope to the west of the São Vicente Canyon ((Figure 4.2A and Figure 4.2C). South-west of the structural high (Figure 4.2B), in the Marquês de Pombal Plateau (Figure 4.1), the LPD does not display the same erosive character as on the location of IODP Site U1391. Here the LPD is conformable with the underlying reflections, except in close proximity of the structural high, where it truncates the older units (Figure 4.2B).

In the Sines Drift area, the EQD is the more prominent erosive surface and appears as a high amplitude reflection that truncates the underlying unit. The EQD also onlaps the structural high south of the Sines Drift (Figure 4.2C). It is also present in the Marquês de Pombal Plateau, where it is conformable with the underlying reflections and onlaps the LPD towards the north-west (Figure 4.2B). On the slope SSE of the São Vicente Canyon, the EQD appears relatively conformable with the underlying reflections while it is truncated by the canyon. In the north-west flank, the EQD onlaps the LPD (Figure 4.3).

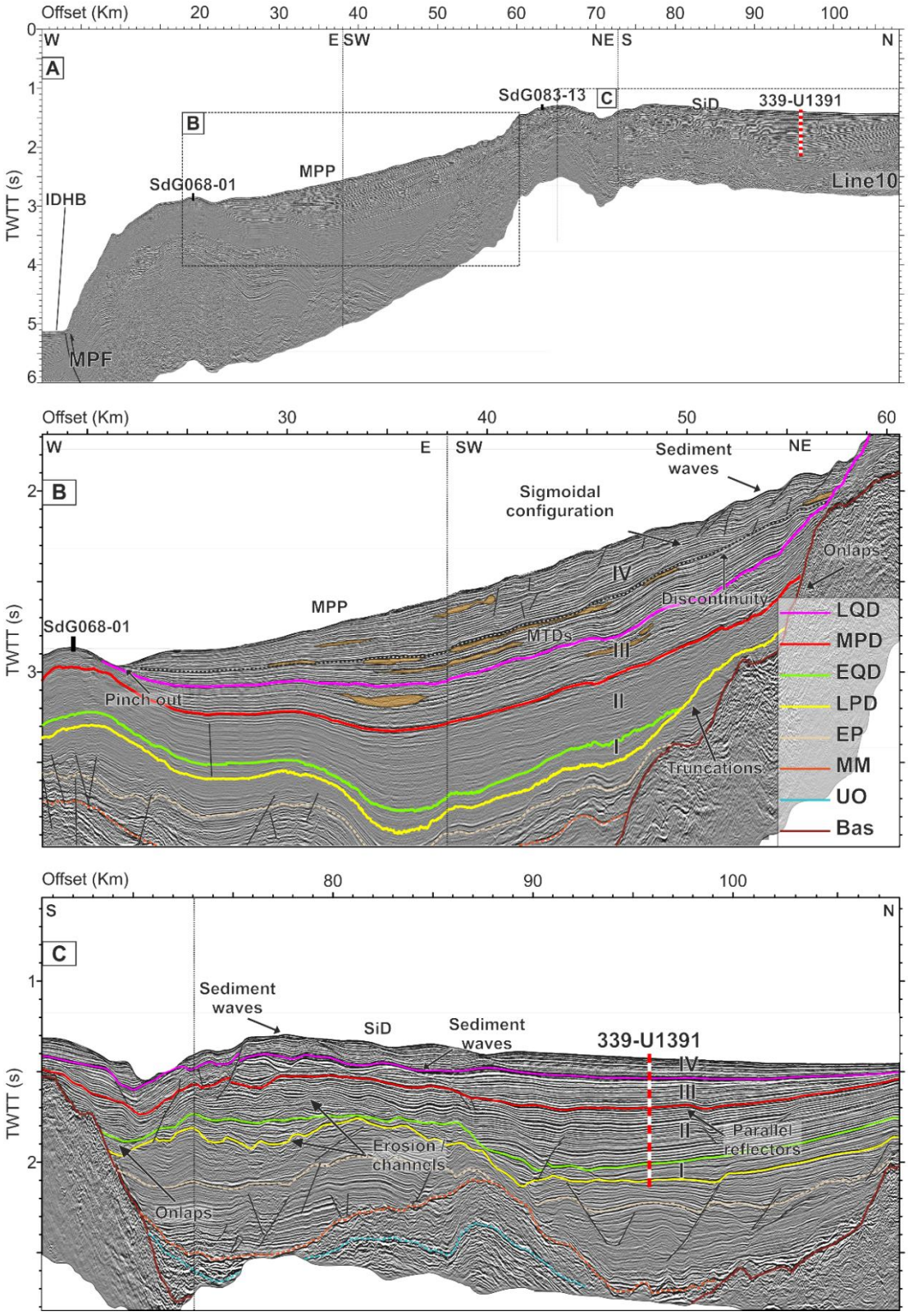

Figure 4.2: (A) Uninterpreted multi-channel seismic profile INS2-Line10 (see location in Figure 4.1). (B) and (C): details of the profile, with interpretation of the main stratigraphic features. Stratigraphic interpretation follows criteria set by Hernández-Molina et al. (2016a) and Serra et al. (2020). LQD: late Quaternary discontinuity (0.4 to 0.3 Ma); MPD: middle Pleistocene discontinuity (0.8 Ma); EQD: early Quaternary discontinuity (2.4 to 2.1 Ma); LPD: late Pliocene discontinuity (3.2 to 3.0 Ma); EP: early Pliocene; MM: middle Miocene; UO: upper Oligocene; Bas: Basement. Orange bodies are MTDs. IDHB: Infante Don Henrique basin; MPF: Marquês de Pombal Fault; MPP: Marquês de Pombal Plateau; SiD: Sines Drift; 339-U1391: IODP Site U1391 location; SdG083-13 and SdG068-01: gravity cores locations; I, II, III and IV correspond to the different units defined in between the major discontinuities; vertical dashed lines correspond to the change in direction of the line (Figure 4.1); vertical exaggeration ~ x7.

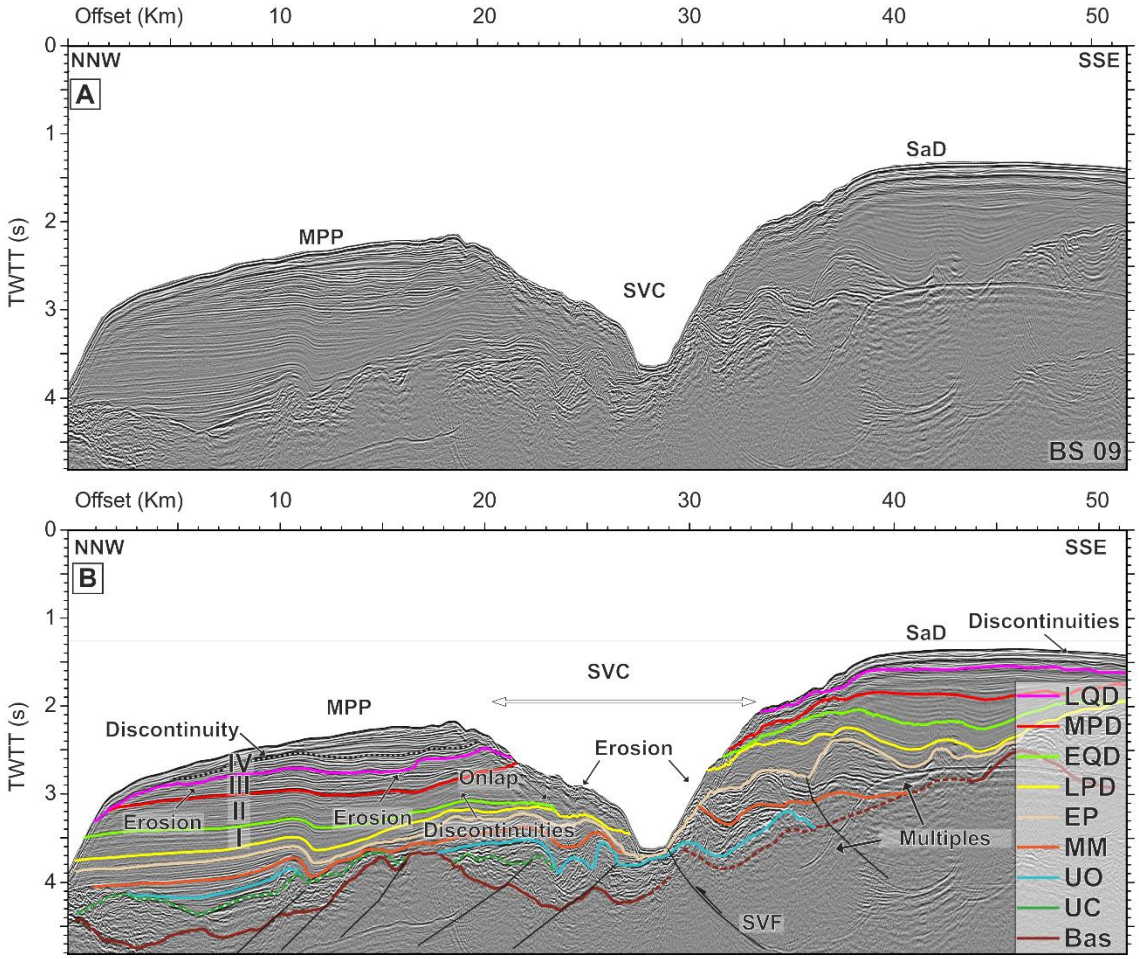

Figure 4.3: Uninterpreted multi-channel seismic (MCS) profile BS09 (see location in Figure 4.1). (B): Interpreted MCS profile. LPD: Stratigraphic interpretation follows criteria set by Hernández-Molina et al. (2016a) and Serra et al., (2020). LQD: late Quaternary Discontinuity (0.4 to 0.3 Ma); MPD: Middle Pleistocene Discontinuity (0.8 Ma); EQD: Early Quaternary Discontinuity (2.4 to 2.1 Ma); LPD: Late Pliocene Discontinuity (3.2 to 3.0 Ma); EP: Early Pliocene; MM: Middle Miocene; UO: Upper Oligocene; UC: Upper Cretaceous; Bas: Basement. I, II, III and IV correspond to the different units defined in between the major discontinuities.; Bas: Basement; MPP: Marquês de Pombal Plateau; SaD: Sagres Drift; SVC: São Vicente Canyon; SVF: São Vicente Fault; vertical exaggeration ~ x4.

As with the previous discontinuities, the MPD also appears as an erosional surface truncating the underlying horizons, especially in the proximity of the structural high on the slope NW of the São Vicente Canyon (Figure 4.2C). On the Marquês de Pombal Plateau, still on the slope north-west of the São Vicente Canyon, the MPD is conformable with the underlying reflections (Figure 4.2B). Unlike the deeper discontinuities, the LQD is not present in the proximity of the Marquês de Pombal thrust fault as it is truncated by the seafloor over a fault related anticline (Figure 4.2B). The LQD is a clearly recognizable discontinuity in the Marquês de Pombal Plateau (Figure 4.2B), where reflections of the topmost unit onlap.

4.1.2 Seismic units

The LPD, EQD, MPD and LQD discontinuities define four seismic units named I to IV from bottom to top, deposited from late Pliocene to the present day (Figure 4.4).

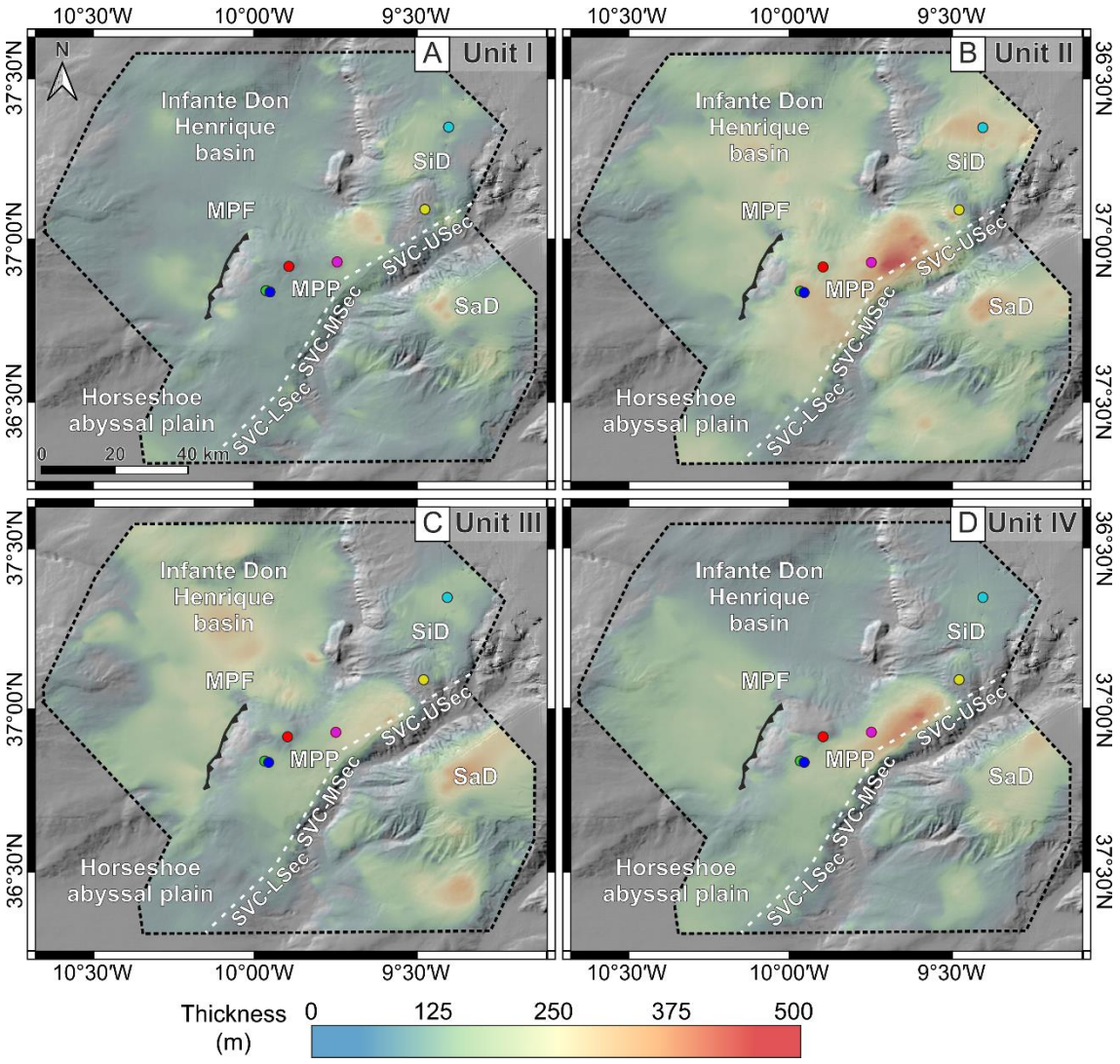

Figure 4.4: Thickness distribution maps. (A) Unit I; (B) Unit II; (C) Unit III; (D) Unit IV. MPF – Marquês de Pombal Fault; MPP – Marquês de Pombal Plateau; SaD – Sagres Drift; SiD – Sines Drift; SVC – LSec: São Vicente Canyon lower section; SVC – Msec: São Vicente Canyon middle section; SVC – USec: São Vicente Canyon upper section; coloured dots indicate the location of IODP Site U1391 (light blue), multicore MC1 (red) and gravity cores SdG083-13 (yellow), SdG068-01 (red) SdG068-03 (blue) and SdG068-02 (green).

Unit I is bounded by the LPD at its base and the EQD at its top. This unit is characterized by middle to high frequency and high-amplitude reflections in the Sines and Sagres Drift areas. It is eroded by the EQD at the top (Figure 4.2 and Figure 4.3). In the shallower parts of the basin, internal erosive features such as truncations and channels characterize the unit. On the other hand, Unit I in the Marquês de Pombal Plateau displays relatively high-frequency, sub-parallel, low-amplitude reflections where internal erosive features are not evident (Figure 4.2B).

Unit II, bounded by EQD at its bottom and the MPD at its top, is characterized by sediment waves and internal erosional surfaces (Figure 4.2C and Figure 4.3B). In the Sines and Sagres Drift areas, Unit II is characterized by high-frequency and continuous internal reflections. The thickness of Unit II (Figure 4.4B**)** is more variable than that of Unit I (Figure 4.4A). The average unit thickness in the Infante Don Henrique basin is between 150 m and 250 m, while in the slope north-west of the São Vicente Canyon (Marquês de Pombal Plateau) it exceeds 500 m. Other depocentres

include the Sines Drift, located close to IODP Site 339-U1391, where the thickness reaches 300 m, and the Sagres Drift, where the thickness reaches 350 m (Figure 4.2C**,** Figure 4.3B and Figure 4.4B). In the Sines Drift, Unit II is the thickest of the four units (Figure 4.4B).

Unit III (Figure 4.4C) is bounded by the MPD and LQD. In the Sines area, the unit shows high amplitude, medium-frequency and parallel internal reflections (Figure 4.2C). Towards the structural high, the unit displays large sediment waves up to 70 m high and 3.5 km in wavelength, which are separated by minor, internal erosional surfaces (Figure 4.2A and C). In the proximity of the structural high, the reflections adopt complex geometries, indicating a higher energy environment, and chaotic and transparent facies associated with MTDs (Figure 4.2). In the Marquês de Pombal Plateau, the reflections show weaker-amplitude close to its base (EQD), changing to stronger reflections in its upper part, where transparent lenses (MTDs) are also present (Figure 4.2B). Unit III is relatively thick (up to 300 m) in the Infante Don Henrique basin and on the slope north-west of the São Vicente Canyon (Figure 4.4C). The main depocentre, however, is present in the Sagres Drift (400 m) and, to a lesser extent, in the Marquês de Pombal Plateau, the slope north-west of the São Vicente Canyon (up to 320 m) (Figure 4.2B, Figure 4.3B and Figure 4.4C).

Unit IV is the latest sedimentary unit, bounded by the LQD at its bottom and the Present seafloor (Figure 4.4D). Similarly to Unit III, in the Sines Drift Unit IV is often characterized by high-amplitude, high-frequency and parallel reflections, changing to long sediment waves (3 km wavelength) and internal unconformities when moving towards the structural high (Figure 4.2C). The maximum thickness reached by Unit IV in the Sines Drift area is less than 100 m (Figure 4.4D). Strong reflections and minor internal erosional surfaces are also visible in the Sagres Drift area, where Unit IV is ~ 250 m thick (Figure 4.3B and Figure 4.4D). In deeper waters, Unit IV is ~ 100 m thick in the northern part of the Infante Don Henrique basin, while it is almost 200 m thick moving towards the footwall of the Marquês de Pombal Fault (Figure 4.4D). The main depocentre in the area is located in the Marquês de Pombal Plateau, on the slope north-west of the São Vicente Canyon, where Unit IV consists of more than 500 m of sediments (Figure 4.2B, Figure 4.3B and Figure 4.4D). In this area, the reflections show higher amplitude compared to the older units. A significant number of seismically chaotic bodies are distributed within this unit in the Marquês de Pombal Plateau between 2 and 3 s TWTT (Figure 4.2B and Figure 4.32C). Unit IV displays an internal unconformity within the Marquês de Pombal Plateau area (Figure 4.3B). Below this surface, the reflections are almost parallel to the underlying LQD, while above the unconformity reflections display onlap to the east and downlap to the west (Figure 4.2B). In agreement with the observed internal geometries, Unit IV thins away from the centre of the Marquês de Pombal Plateau and pinches out over structural highs located in both deep (below 3 s TWTT, Marquês de Pombal Fault hanging wall block) and shallow water settings (above 1.8 s TWTT, structural high south of the Sines Drift) (Figure 4.2B).

4.1.3 Sedimentation rates

Overall, the decompacted sedimentation rates increase in the area through time by a factor of four or five. Unit I deposited in 0.9 Ma and the resulting sedimentation rates for the decompacted unit remain lower than 0.5 m/kyr along the entire study area (Figure 4.5A). Similar sediment accumulation rates characterize Unit II (Figure 4.5B), where sediment deposited during a longer time period (1.3 Ma). Nevertheless, sedimentation on both slopes adjacent to the São Vicente Canyon display comparatively higher accumulation rates than the underlying unit.

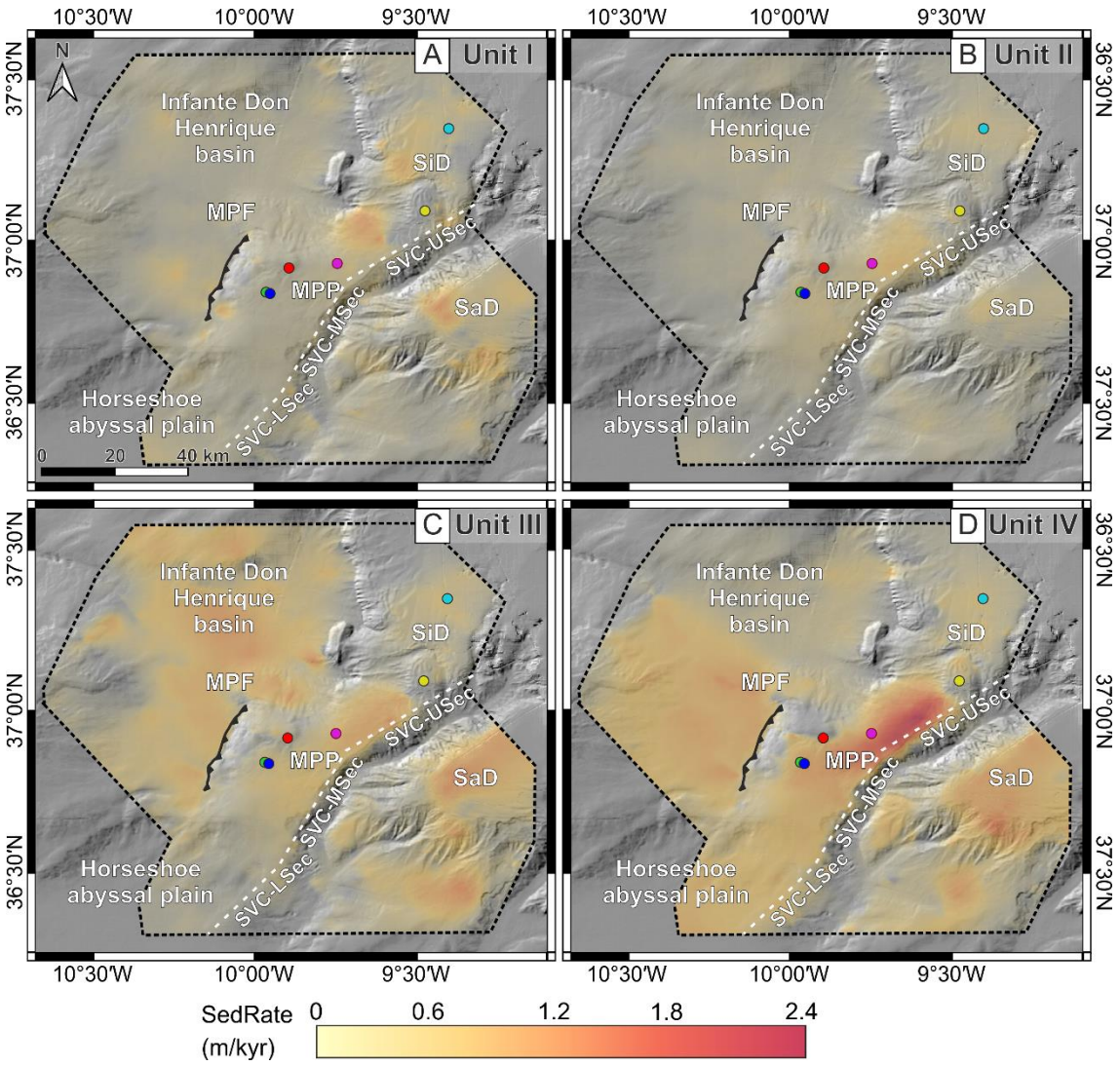

Figure 4.5: Decompacted sedimentation rate maps. (A) Unit I; (B) Unit II; (C) Unit III; (D) Unit IV. MPF – Marquês de Pombal Fault; MPP – Marquês de Pombal Plateau; SaD – Sagres Drift; SiD – Sines Drift; SVC – LSec: São Vicente Canyon lower section; SVC – Msec: São Vicente Canyon middle section; SVC – USec: São Vicente Canyon upper section; coloured dots indicate the location of IODP Site U1391 and gravity cores (see Figure 4.4 caption for key to colors).

Sedimentation rates increase significantly in the two uppermost units. Unit III, which deposited during 0.5 Ma, displays values exceeding 1.0 m/kyr on both sides of the São Vicente Canyon and in the deeper parts of the basin (Figure 4.5C), and approximately 0.5 m/kyr are found in the Sines Drift. The highest decompacted sedimentation rates throughout the studied interval are found in Unit IV (Figure 4.5D), which deposited in only 0.3 Ma. In this unit, sedimentation rates are lower

than 0.3 m/kyr in the Sines Drift and in the northern part of the Infante Don Henrique basin, while values up to 1.0 m/kyr are found at the foot of the Marquês de Pombal Fault and in the Sagres Drift. The highest sedimentation rates are found on the slope north-west of the São Vicente Canyon, where they exceed 2 m/kyr (Figure 4.5D). Near seafloor sedimentation rates determined from multicore MC1 show values of 0.81 ± 0.07 m/kyr (Garcia-Orellana et al., 2006) while the mean sedimentation rates at the same location provided by our stratigraphic interpretations are of 1.1 m/kyr. Both of these sedimentation rates are within similar range and represent a relatively high value for a deep-sea setting.

4.1.4 Occurrence of shallow landslides

Shallow MTDs and landslide scars in the study area have been identified using bathymetric and MCS data (Figure 4.6).

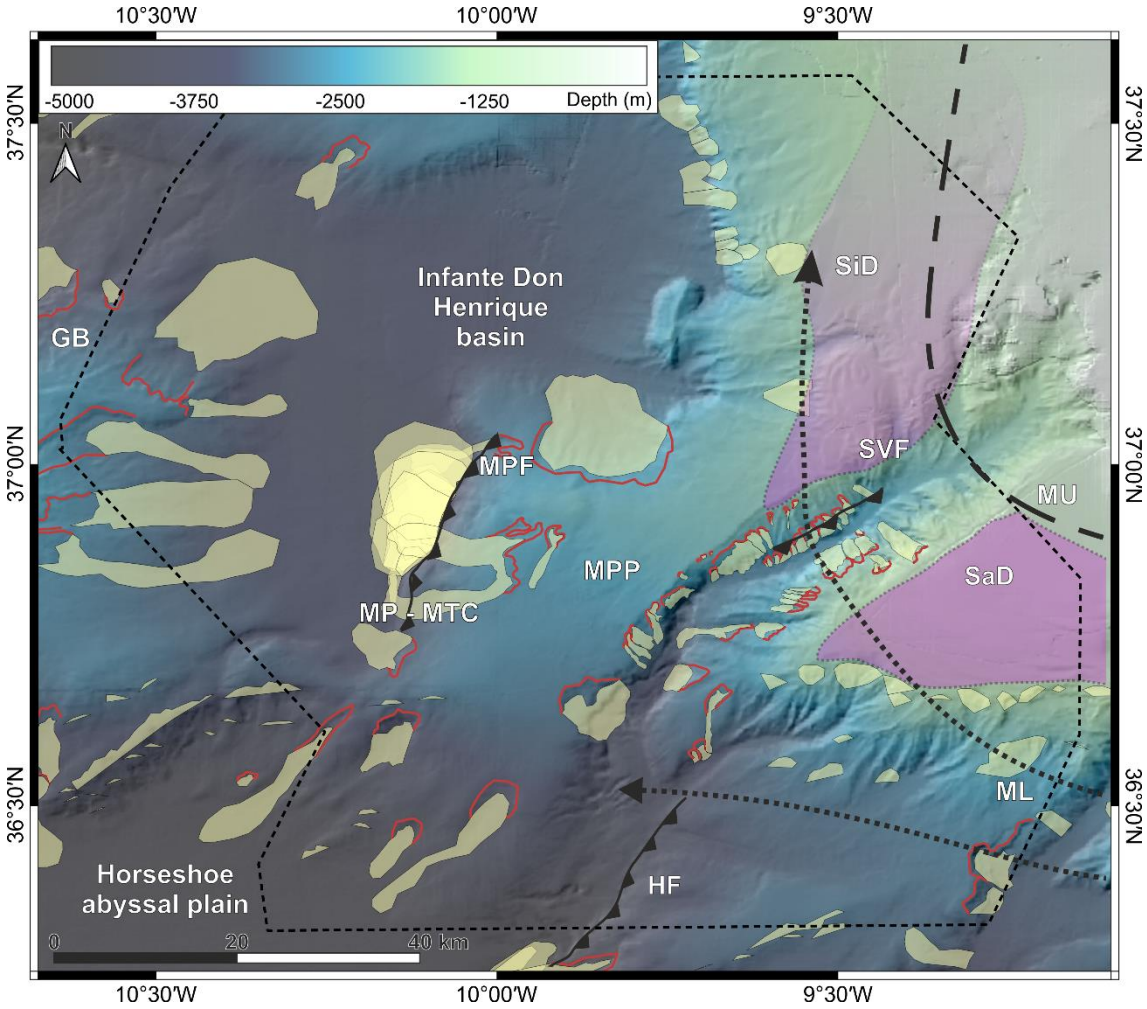

Figure 4.6: Distribution of mass transport deposits (MTDs) (yellow outlines) and scars (red lines) within the area of study (dashed black outline). Dashed lines correspond to the main branches of the Mediterranean Outflow Water (MOW). Purple areas are the estimated drift extensions. GB: Gorringe Bank; HF: Horseshoe Fault; MPF: Marquês de Pombal Fault; MPP: Marquês de Pombal Plateau; MP – MTC: Marquês de Pombal Mass Transport Complex; MU: MOW upper core; ML: MOW lower core; SaD: Sagres Drift; SiD: Sines Drift; SVF: São Vicente Fault.

Results shows that the Infante Don Henrique basin hosts the majority of the MTDs in the Alentejo basin, with mass wasting processes taking place from all the surrounding slopes. Small but frequent MTDs (11 events) took place within the Pereira de Sousa fault, which constitute the western limit of the Sines drift area.

The Gorringe Bank is the source area for the largest MTDs hosted in the Infante Don Henrique basin, with five MTDs displaying a maximum area of 231 km^2 and runout up to 32 km (Figure 4.6). The larger number of landslides deposited in the Infante Don Henrique basin detached from the N-NW borders of the Marquês de Pombal Plateau. Besides a 202 km^2 MTD generated from the north side of the plateau, where a scar in late Quaternary sediments is visible from bathymetric data (Figure 4.4D), the majority of the slope instability took place in the proximity of the Marquês de Pombal Fault. 14 different MTDs have been detected from MCS data on the Marquês de Pombal Fault footwall, constituting the Marquês de Pombal mass transport complex (MTC) (see also Ford et al., 2021). The maximum runout of the deposits constituting the MTC reaches 10 km (Figure 4.6), and according to the stratigraphic analysis of the Infante Don Hernrique basin, the mass wasting deposits are distributed from Unit I, where the thickness reaches 80 m, to Unit IV (Figure 4.7). The location of the Marquês de Pombal MTC, detached from the headwall of the Marquês de Pombal Fault and deposited at its footwall, suggests a relationship between the MTC and the activity of the fault.

Besides the MTDs deposited within the Infante Don Henrique basin, MCS profile Line10 (Figure 4.2B) revealed the presence of mass wasting deposits within the Marquês de Pombal Plateau. Those MTD are distributed between Unit III (3 MTDs) and Unit IV (8) (Figure 4.2B). Multiple, smaller landslides scars are visible within the São Vicente Canyon, both on the Sagres areas (SE flank) and from the Marquês de Pombal Plateau (NW flank). Finally, other MTDs detached from the SW side of the Marquês de Pombal Plateau and deposited in the Horseshoe Abyssal Plain (Figure 4.6).

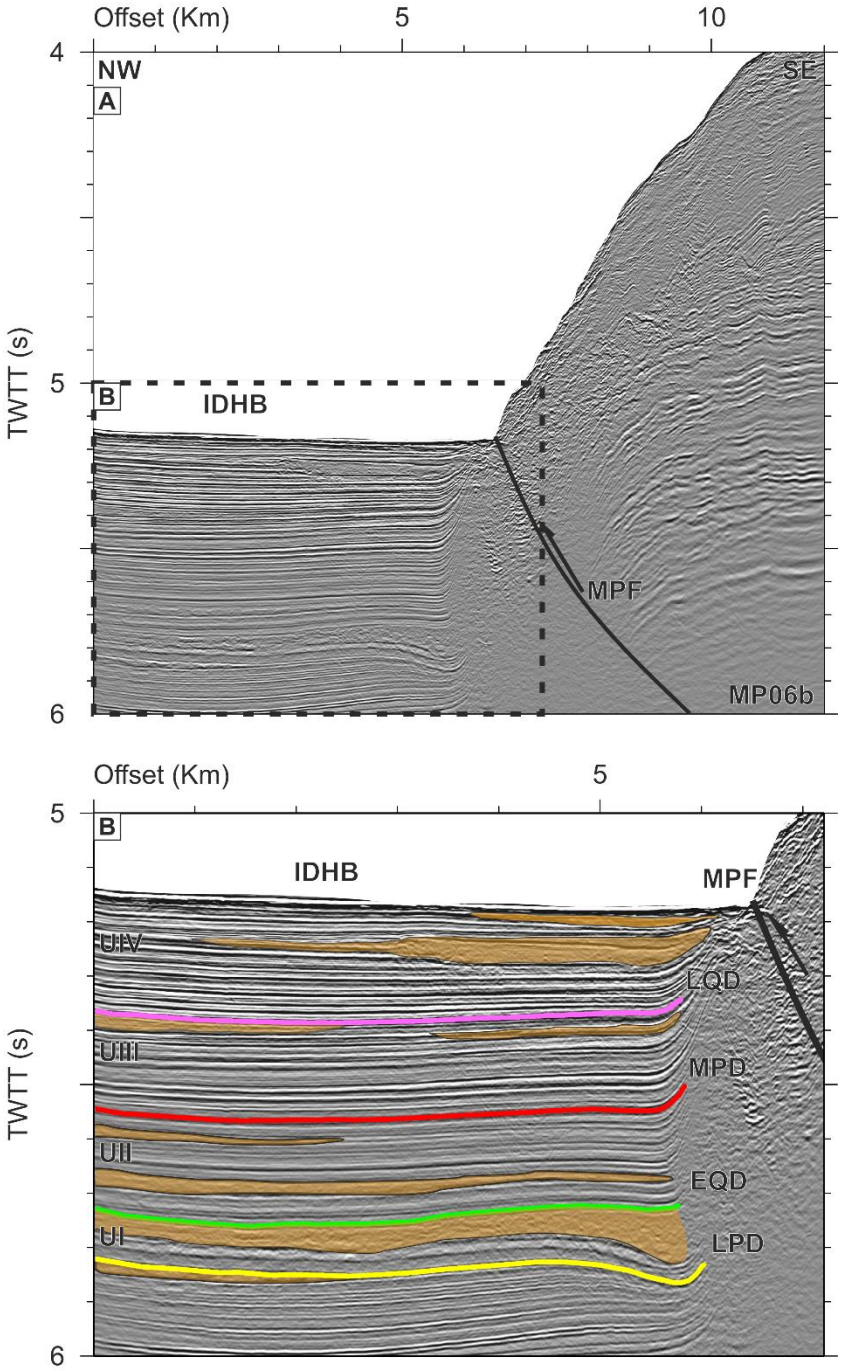

Figure 4.7: Uninterpreted (A) and interpreted (B) MCS profile MP06b showing MTDs (orange bodies) interpreted by Ford et al. (2021) at the footwall of the Marquês de Pombal Fault. LPD: Late Pliocene Discontinuity; MPD: Middle Pleistocene Discontinuity; EQD: Early Quaternary Discontinuity; LQD: Late Quaternary Discontinuity; IDHB: Infante Don Henrique basin; MPF: Marquês de Pombal Fault; vertical exaggeration ~ 4. Modified after Ford et al. (2021).

4.2 Near-seafloor sediment characteristics in the Alentejo basin

Grain size analysis, MSCL measurements, Atterberg limits and water content have been measured at different depths on the gravity cores collected during the INSIGHT-Leg1 (SdG064-01, SdG064-02 and SdG064-03) and INSIGHT-Leg2 (SdG083-13) cruises in the Marquês de Pombal Plateau (Figure 4.8 and Table 3.4). Furthermore, oedometer tests have been carried out

with both Rowe and Barden and CRS cell-types to obtain compressibility (8 samples) and permeability (3 samples) information.

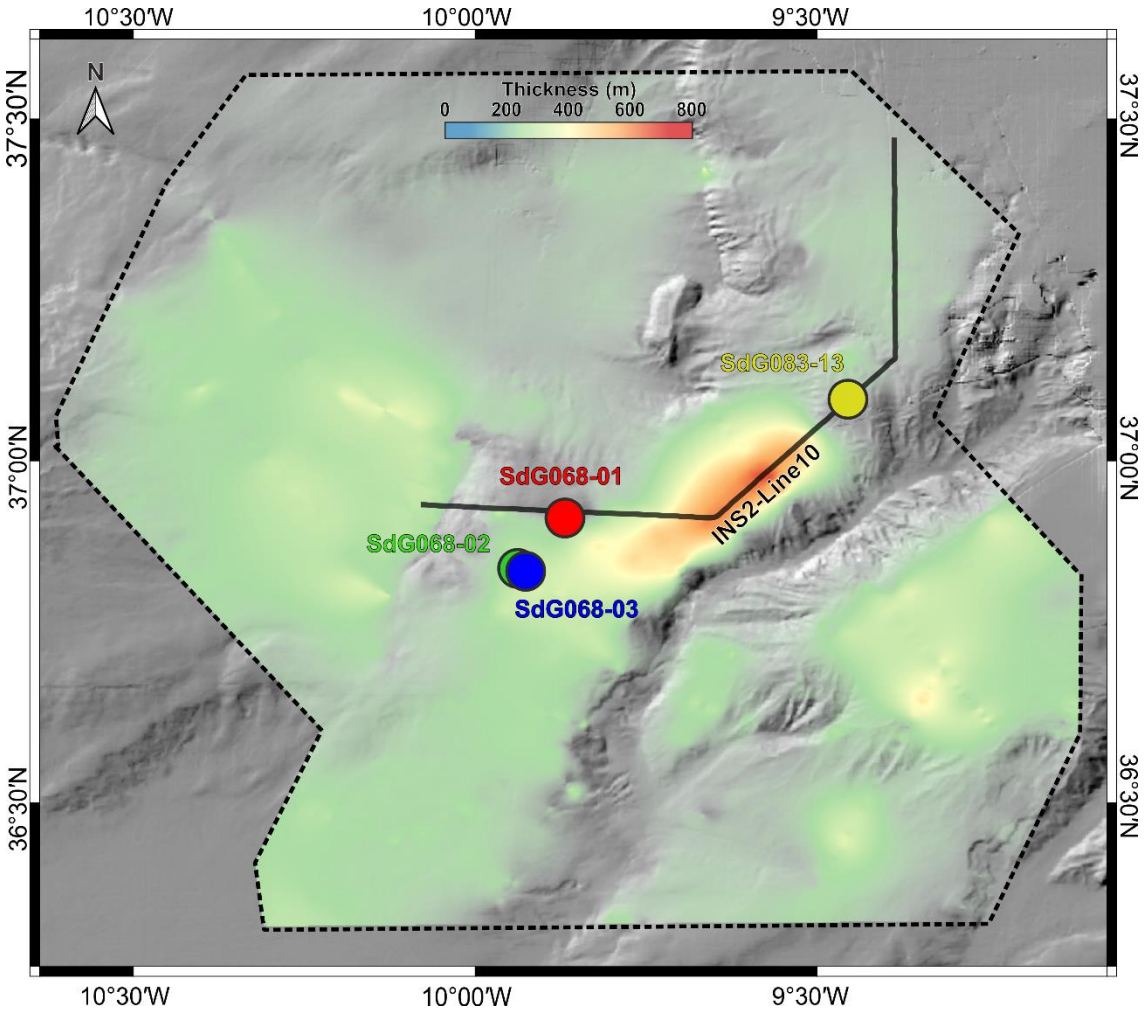

Figure 4.8: Location of gravity cores collected for this study plotted with Unit IV thickness distribution.

4.2.1 Sediment grain size and physical properties

The sediments collected in the Alentejo basin (Figure 4.8) show a relatively homogenous grain size in all cores (Figure 4.9, Table 4.1). MSCL P-wave velocity in core SdG083-13 (236 cm long), located in the shallowest part of the Marquês de Pombal Plateau, on a peripheral position with respect to the depocentre of Unit IV (Figure 4.8) ranges between 1455 ms^{-1} and 1555 ms^{-1}, with a visible increase recorded between 91 cm and 106 cm (Figure 4.10). Density increases from 1.61 g cm^{-3} in the shallower sediments to 2.02 g cm^{-3} in the deeper parts (porosities of 63% to 38% assuming a grain density of 2.65 g cm^{-3}), with an increase of the recorded P-wave velocity in the same interval (Figure 4.10). The anomalous interval does not find an expression in the grain size distribution, which is homogeneous through the core. The core is silt-dominated (4 µm < Ø < 63 µm) along the whole length (between 57.3% and 73.29%), with slightly higher percentages of clay (Ø < 4 µm) in the shallower part (>40% above 70 cm) and more relevant presence of sand (Ø > 63 µm) (between 2.5% and 4.7%) in the interval between 50 cm and 75 cm (Figure 4.10,

Table 4.1). The mean grain size throughout the core is 8.6 µm. Grain size distribution curves reveal a general bimodal, fine-skewed distribtuon of sediment and very poor sorting.

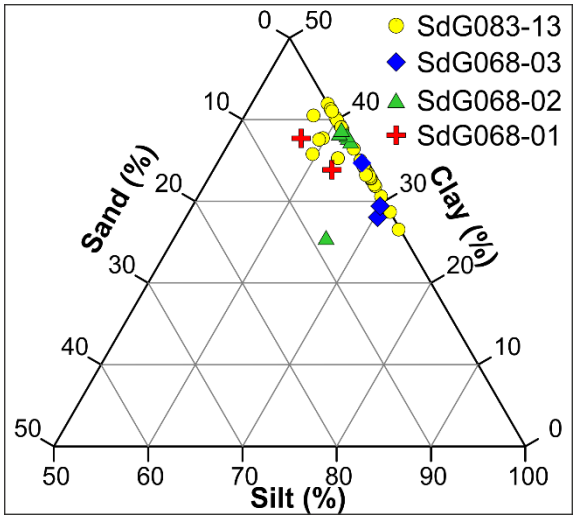

Figure 4.9: Grain-size distribution of the sediments collected during the INSIGHT cruises analysed in this study.

Gravity cores SdG068-01 (243 cm), SdG068-02 (215 cm) and SdG068-03 (248 cm) were collected beyond the pinch-out of Unit IV (Figure 4.2 Figure 4.8). P-wave velocity in core SdG068-01 ranges between 1590 ms^{-1} and 1633 ms^{-1}, while density increases linearly from 1.42 to 1.60 g cm^{-3} (porosity of 75% to 58%) (Figure 4.11). Two grain size measurements from 180 to 195 cm interval record clay percentages between 33.85% and 37.71%, silt between 62.58% and 57.36% and sand between 3.57% and 4.93% (Figure 4.11, Table 4.1). Grain size distribution reveals a bimodal coarse-skewed shape, with higher presence of coarse sediments compared with SdG083-13 and very poor sorting (Figure 4.11). Gravity cores SdG068-02 (Figure 4.12) and SdG068-03 (Figure 4.13) were collected 1.15 km away from one another. Core SdG068-02 was taken from inside a landslide scar (Minning et al., 2006; Vizcaino et al., 2006), while SdG068-03 comes from the undisturbed sediment above the landslide. SdG068-02 shows P-Wave velocity ranging between 1617 ms^{-1} and 1653 ms^{-1}, increasing below 207 cm of depth. Density varies between 1.56 g cm^{-3} (porosity 66%) and 1.73 g cm^{-3} (porosity 56%) (Figure 4.12). Grain size of the shallower interval sampled (78 to 110 cm depth) is mainly silt (61.26 to 62.95%) while in the deeper interval (207 to 217 cm) there is a higher percentage of sand (8.49%) with 66.23% silt and 25.28% clay (Figure 4.12, Table 4.1). The MSCL measurements from core SdG068-03 resulted in P-Wave velocity between 1592 and 1625 ms^{-1}, while density increases linearly from1.40 g cm^{-3} (porosity 75%) to 1.66 g cm^{-3} (porosity 60%) (Figure 4.13). The homogeneous grain-size composition of the core reflects the linear trend of the logs: the uppermost sampled interval (133 to 148 cm) is mainly composed by silt (69.89 to 70.32%), with minor percentage of clay (29.41 to 28.02%) and sand traces (0.70 to 1.66%). The deeper interval (240 cm to 248 cm) shows a similar composition, with 65.46% silt, 34.54% clay and no sand (Figure 4.13, Table 4.1). Grain size distribution from cores SdG068-02 and SdG068-03 displays bimodal, coarse-skewed shape

and very poor sorting, although the higher sand interval between 207 and 217 cm in core SdG068-02 is clearly highlighted by the grain size log (Figure 4.12 and Figure 4.13).

Table 4.1: Grain size distribution of the four gravity cores collected during the INSIGHT cruises considered in this study (see locaiton in Figure 4.8). The grain size classification proposed by Wentworth (1922) has been adopted to derive sand (2 mm - 63 μm), silt (63 μm – 4 μm) and clay (< 4 μm) fractions.

SdG083-13				**SdG068-01**				**SdG068-02**				**SdG068-03**			
Depth (cm)	Sand (%)	Silt (%)	Clay (%)	Depth (cm)	Sand (%)	Silt (%)	Clay (%)	Depth (cm)	Sand (%)	Silt (%)	Clay (%)	Depth (cm)	Sand (%)	Silt (%)	Clay (%)
5	0	61	39	187	4	63	33	78	0	63	37	137	2	70	28
12	0	60	40	190	5	57	38	84	0	63	37	144	1	70	29
18	0	60	40					93	0	62	38	244	0	65	35
24	0	61	39					102	0	61	39				
29	0	60	40					110	1	61	38				
34	0	58	42					207	8	66	26				
39	0	59	41												
45	0	59	41												
50	3	59	38												
55	0	61	39												
60	3	59	38												
65	2	57	41												
70	5	59	36												
75	2	63	35												
80	0	64	36												
85	0	66	34												
90	0	69	31												
95	0	71	29												
100	0	65	35												
105	0	67	33												
110	0	66	34												
115	0	66	34												
120	0	66	34												
125	0	66	34												
130	0	66	34												
135	0	67	33												
145	0	66	34												
150	0	67	33												
155	0	68	32												
160	0	66	34												
165	0	65	35												
170	0	65	35												
175	0	73	27												
180	0	68	32												
185	0	66	34												
190	0	67	33												
195	0	67	33												
200	0	67	33												
205	0	65	35												
210	0	67	33												
215	0	67	33												
220	0	66	34												
225	0	67	33												
230	0	67	33												

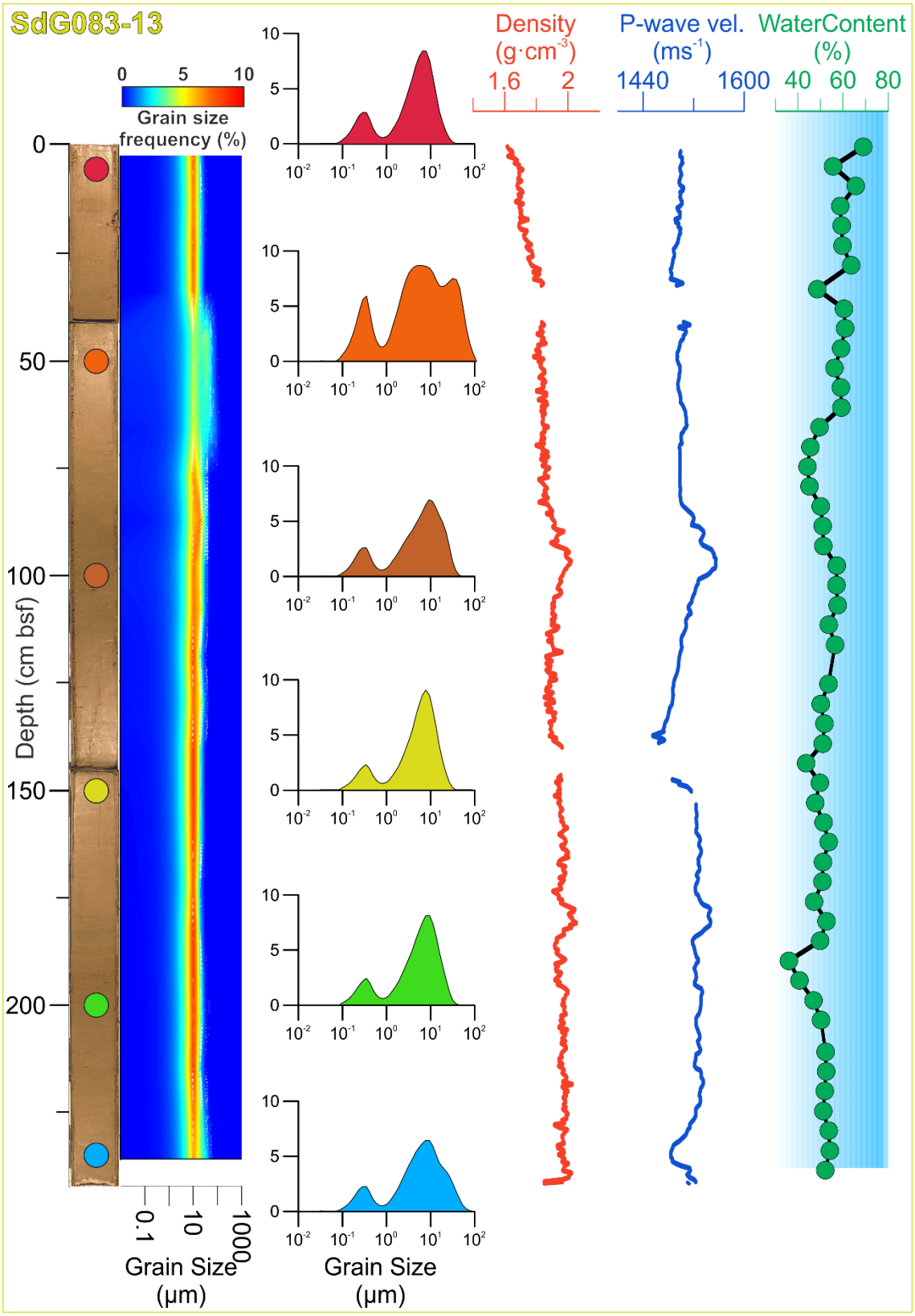

Figure 4.10: Grain size distribution, multi-sensor core logger (MSCL) gamma ray densities (red lines), P-wave velocities (blue lines) and water content (green dots) of gravity core SdG083-13, collected during the INSIGHT-Leg2 cruise (core location in Figure 4.8). Coloured dots represent the location along the core of the samples for which the grain size distribution is shown on the adjacent plot.

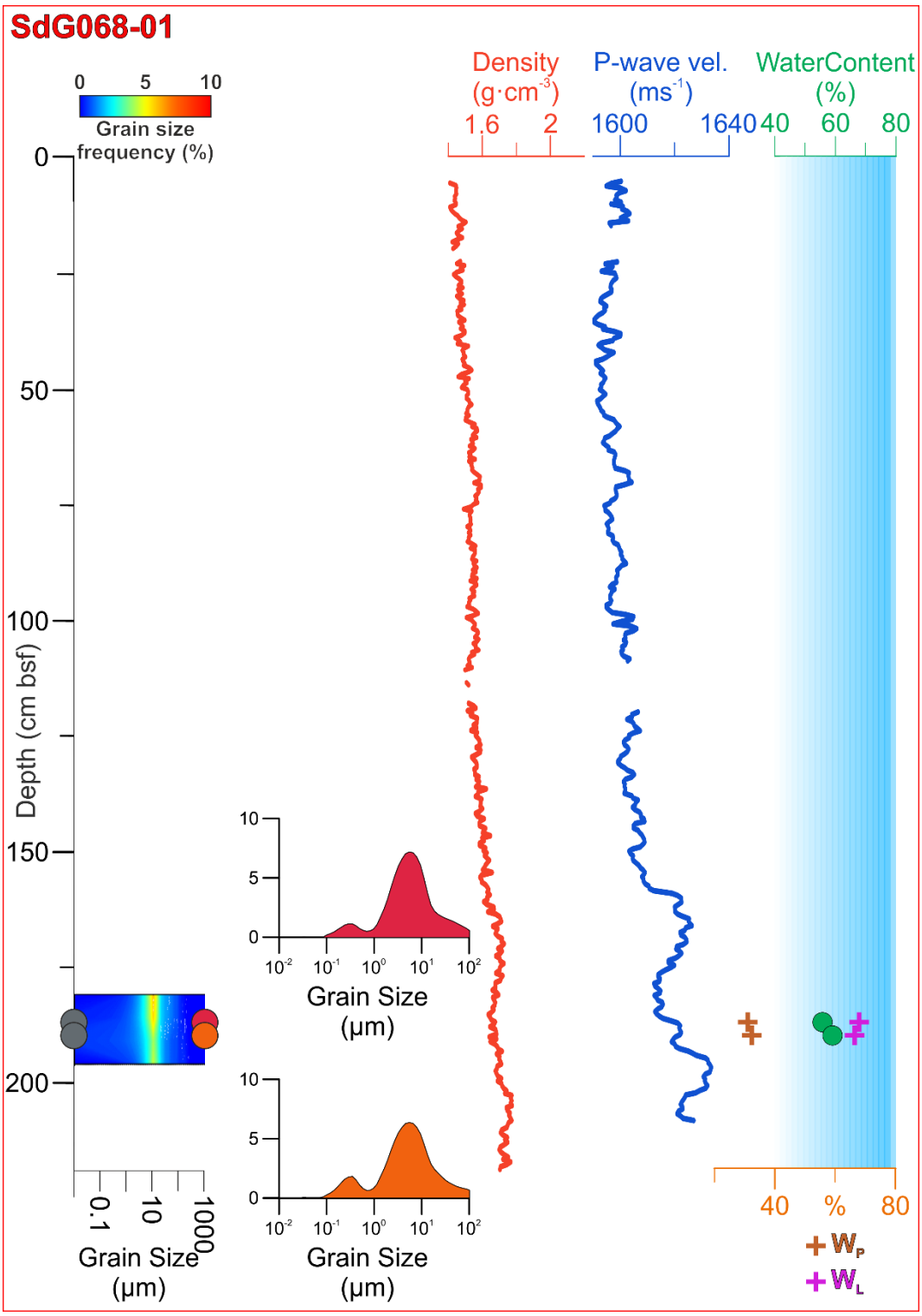

Figure 4.11: Grain size distribution, multi-sensor core logger (MSCL) gamma ray densities (red lines), P-wave velocities (blue lines) and water content (green dots) of gravity core SdG068-01, collected during the INSIGHT-Leg1 cruise (core location in Figure 4.8). Coloured dots represent the sample location along the core of the samples for which the grain size distribution is shown on the adjacent plot. Grey dots indicate where samples for consolidation and permeability testing were collected. Orange and purple crosses indicate measured plastic limit (W_P) and liquid limit (W_L) respectively.

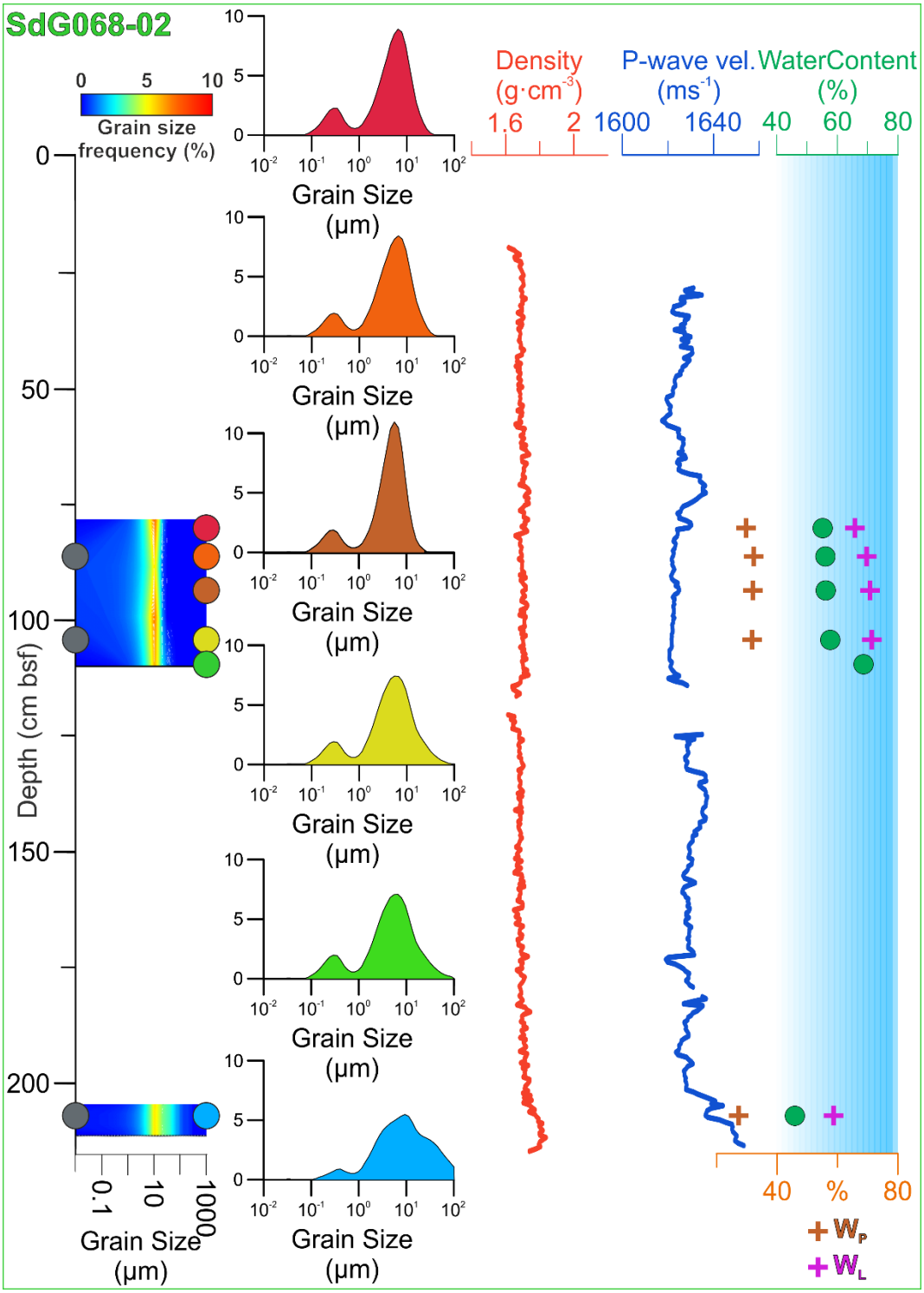

Figure 4.12: Grain size distribution, multi-sensor core logger (MSCL) gamma ray densities (red lines), P-wave velocities (blue lines) and water content (green dots) of gravity core SdG068-02, collected during the INSIGHT-Leg1 cruise (core location in Figure 4.8). Coloured dots represent the sample location along the core of the samples for which the grain size distribution is shown on the adjacent plot.. Grey dots indicates where sample for consolidation and permeability testing were collected from. Orange and purple crosses indicate measured plastic limit (W_P) and liquid limit (W_L) respectively.

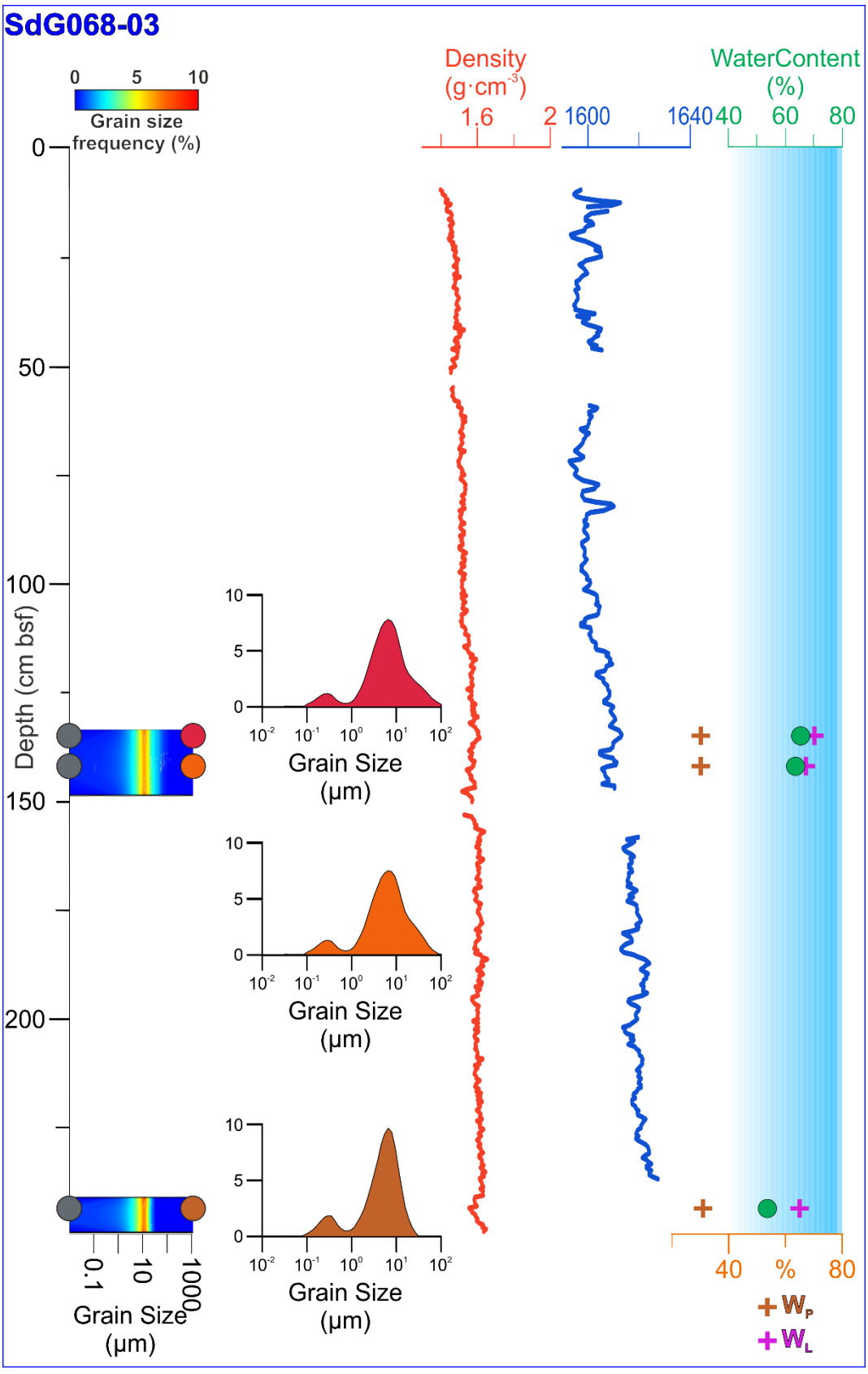

Figure 4.13: Grain size distribution, multi-sensor core logger (MSCL) gamma ray densities (red lines), P-wave velocities (blue lines) and water content (green dots) of gravity core SdG068-03, collected during the INSIGHT-Leg1 cruise (cores location in Figure 4.8). Coloured dots represent the sample location along the core of the samples for which the grain size distribution is shown on the adjacent plot.. Grey dots indicates where sample for consolidation and permeability testing were collected from. Orange and purple crosses indicate measured plastic limit (W_P) and liquid limit (W_L) respectively.

The IODP Site U1391 (Figure 4.1 Figure 4.8) recovered several sand rich intervals within Unit IV (Figure 3.9). Nevertheless, the two uppermost smear slide measurements (at 0.08 m and 0.9 m depth) resulted in clay-dominated sediments (between 65 and 70%) with high percentages of silt (20 to 27%) and sand between 3% and 5%. From 2.6 m depth, the sand fraction increases reaching percentages up to 55% at 50 m depth. Multiple sand-rich layers are also present in Units I-III, with sand beds attaining values of 65 to 70% (Figure 3.9).

Finally, the bulk mineral composition of the 20 cm long multicore MC1 (Figure 3.7, Table 3.4), show that sediment is composed mainly by clay minerals (40 to 65%), and significant amounts of calcite (15 to 30%) and quartz (10 to 20%) (Garcia-Orellana et al., 2006). Feldspar (<5%) and dolomite (<5%) were also present. The fraction coarser than 5 μm resulted in higher amounts of quartz (25 to 45%), feldspars (5 to 20%) and dolomite (<10%).

4.2.2 Sediment mechanical properties

4.2.2.1 Atterberg limits and water content

Atterberg limits have been measured for 10 samples of SdG068-01, SdG068-02 and SdG068-03 cores (Figure 4.8). Although plastic (W_P) and liquid limits (W_L) show some variation in between different samples (W_P between 27.3% and 32.4%, W_L between 58.7% and 71.4%), plasticity index (IP) versus liquidity limit (W_L) plots display that all the samples analysed fit into the high plasticity clays (CH) category (Figure 4.14). High plasticity sediments display high volumetric changes and soil shrinkage capacity in case of cyclic exposure to water (Öser, 2020). The deepest sample collected within SdG-068-02 core (207 cm bsf) is the only sample close to the intermediate plasticity window (CI) in Figure 4.14, showing considerably lower W_P (27.3%) and W_L (58.7%) than the other samples. Sample SdG068-02-207, which has the highest sand fraction of all samples, shows the lower water content (W_i) of all the samples from all cores with a W_i value of 54.53%, while in all other samples W_i ranges between 61.39% and 77.35% (Figure 4.11, Figure 4.12 and Figure 4.13, Table 4.2).

Core SdG083-13 is the only where W_i has been measured continuously along its entire length (Figure 4.10). Besides some local minor perturbations, the general trend shows a general decrease from a maximum of 66% at 9 cm depth to approximately 44% at 230 cm bsf, with a minimum of 27% measured at 215 cm bsf.

Table 4.2: Water content and Atterberg limits for all tested samples.

Core	Depth (mbsf)	*Wi* (%)	W_P (%)	W_L (%)	*IP* (%)	*IL*(%)
SdG068-01	187	55.8	31.0	68.0	37.0	67.03
SdG068-01	190	59.1	32.4	66.5	34.1	78.08
SdG068-02	78	55.1	29.7	65.8	36.0	70.48
SdG068-02	84	56.0	32.3	69.4	37.1	63.83
SdG068-02	93	56.1	32.0	70.8	38.9	62.18
SdG068-02	102	57.6	31.7	71.4	39.6	65.24
SdG068-02	207	45.9	27.3	58.7	31.4	59.09
SdG068-03	137	65.3	30.1	70.2	40.1	87.76
SdG068-03	144	63.5	30.1	67.2	37.8	88.26
SdG068-03	244	53.6	30.9	65.0	34.1	66.54

Wi: water content; W_P: plastic limit; W_L: liquid limit; *IP*: plasticity index; *IL*: liquidity index.

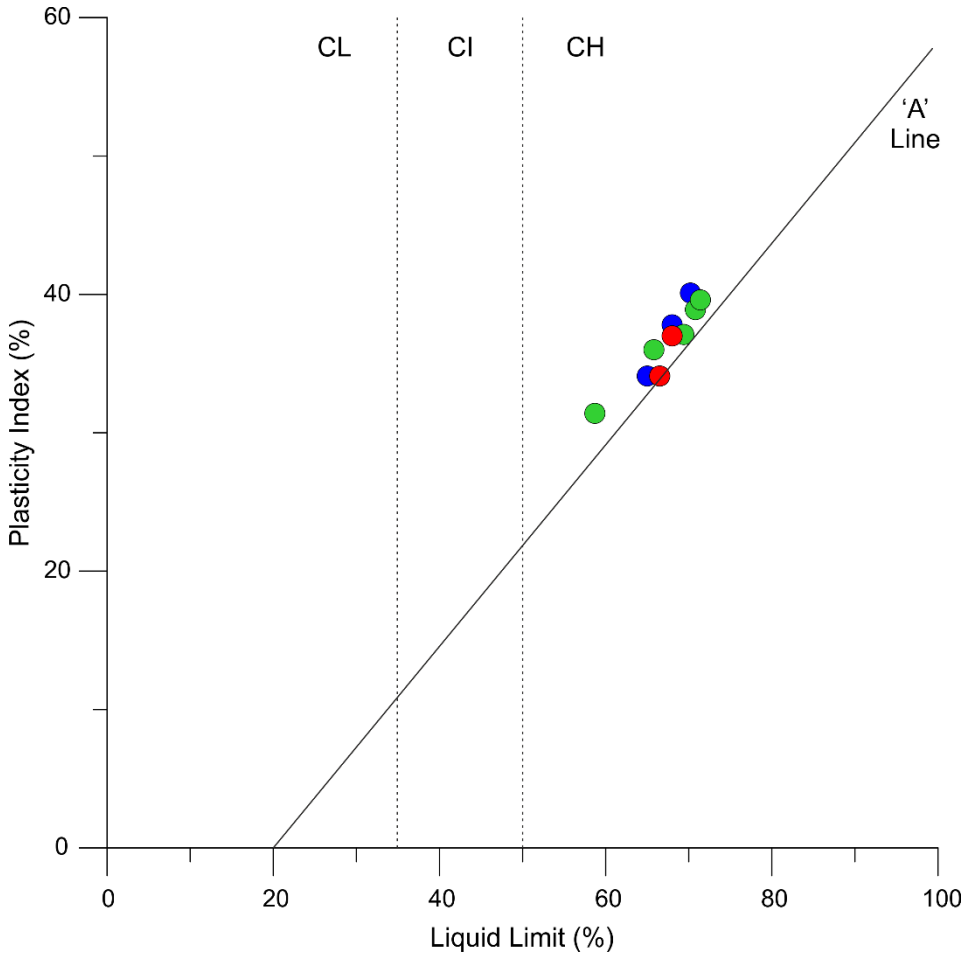

Figure 4.14: Plasticity chart showing the relation between liquid limit and plasticity index. The chart allows to interpret Atterberg limit results in terms of soil engineering properties, distinguishing soil between 3 classes: CL: low plasticity; CI: intermediate plasticity; CH: high plasticity. The empirical 'A' Line separates inorganic clays (above the line) from inorganic silts and organic soils (below).

4.2.2.2 Consolidation and permeability

As explained in section 3.3.6, consolidation (8x) and permeability (3x) tests have been carried out on the sediments collected in the Alentejo basin during the INSIGHT-Leg1 cruise to derive physical properties of sediment at depositional conditions. We conducted CRS tests on 5 samples and R&B tests on 3 samples. Table 4.3 summarizes the details of each test.

Figure 4.15 shows the consolidation curve in the *e*-log (σ'_V) space. From this plot is possible to derive *in-situ* void ratio (e_i), compression index (C_C) and swelling index (C_S). Compression index refers to the slope of the normally consolidated portion of the compression curve in *e*-log (σ'_V) space, while the swelling index refer to the slope of the unloading portion of the compression curve.

In-situ void ratio varies from 1.82 for sample SdG068-02_207 to 2.57 for sample Sdg068-03_137. The variability of *in-situ* void ratio value does not seem be related with the different cores from where sediments have been sampled. C_C varies between 0.45 for sample SdG068-02_207 and 0.65 in SdG068-02_102, while C_S ranges between 0.07 (Sdg068-03_144) and 0.12 (Sdg068-03_137). Also in case of C_C and C_S, a clear correlation between the parameters and the different gravity cores is not visible (Table 4.3).

The geotechnical tests performed on sediments collected in the Alentejo basin aimed to derive the hydromechanical properties that define different sediment types in our numerical models. The three properties defining sediment types are porosity, hydraulic conductivity and specific storage to be input at depositional conditions. Therefore, the three parameters have been determined from extrapolation to 1 kPa loading conditions by using the logarithmic regression of the virgin consolidation line for each sediment sample (Figure 4.15, Table 4.3).

The initial porosity ($Ø_0$) is determined by plotting the variation of void ratio (e_0) vs the effective stress (σ') in logarithmic scale (Figure 4.15). The void ratio (*e*) is related to porosity by the equation (eq. 18):

$$Ø_0 = \frac{e_0}{(1+e_0)} \tag{18}$$

Initial porosity values (estimated at 1 kPa effective stress) vary between 0.69 for sample SdG068-01-GC1-190 and 0.78 for samples SdG068-02_102 and SdG068-03_84, corresponding to 2.23 and 3.55 void ratios respectively, showing little variability and no clear differences between specimens sampled from cores SdG068-01, -02 or -03 (Figure 4.15, Table 4.3). A clear relationship between initial porosities and grain size composition of the samples is also not evident: the higher sand content (8.49% in sample SdG068-02_207) resulted in an average initial porosity value of 0.74 and samples that show the highest clay content (37.1% for SdG068-01_190, 38.51 for SdG068-02_102 and 37.55 for SdG068-03_84) show variable initial porosities (0.69, 0.78 and 0.78 respectively).

Table 4.3: Clay, silt and sand content, intial porosity and specific storage of the sediments that underwent consolidation and permeability tests.

Sample	%Clay	%Silt	%Sand	e_i	C_C	C_S	$Ø_0$	S_0	k_0	Test type
SdG068-01_187	33.85	62.58	3.57	2.08	0.50	0.09	0.77	0.019		CRS
SdG068-01_190	37.71	57.36	4.93	1.99	0.52	0.08	0.69	0.044	1.16E-09	R&B
SdG068-02_84	37.55	62.45	0	2.33	0.63	0.11	0.78	0.016		CRS
SdG068-02_102	38.51	61.25	0.24	2.32	0.65	0.07	0.78	0.033		CRS
SdG068-02_207	25.28	66.23	8.49	1.82	0.45	0.09	0.74	0.014		CRS
SdG068-03_137	28.02	70.32	1.66	2.57	0.62	0.12	0.77	0.034		CRS
SdG068-03_144	29.41	69.89	0.7	2.23	0.48	0.07	0.75	0.044	6.56E-09	R&B
SdG068-03_244	34.54	65.46	0	2.10	0.53	0.09	0.74	0.064	4.75E-09	R&B

e_i: in situ void ratio; C_C, compression index; C_S, swelling index; ϕ_0, initial porosity; S_0, initial specific storage; k_0, initial hydraulic conductivity (m s^{-1}); CRS: Constant Rate of Strain cell; R&B: Rowe&Barden cell.

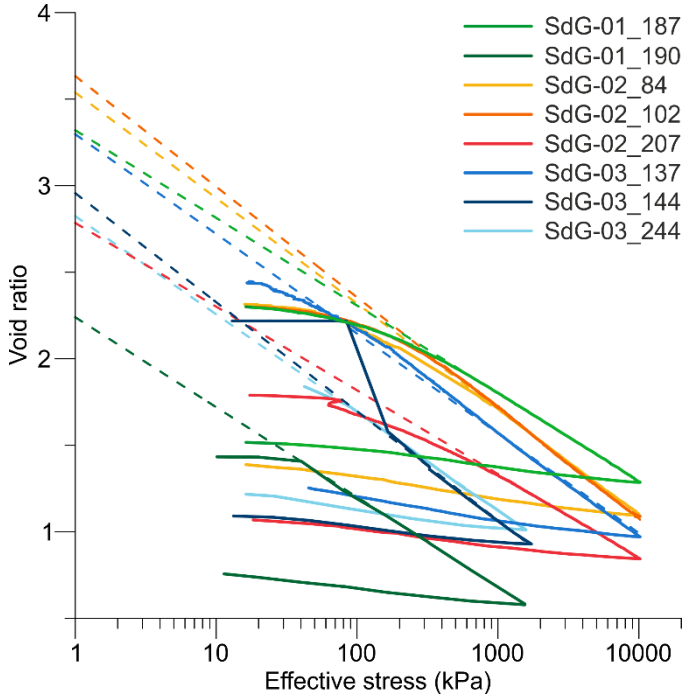

Figure 4.15: Effective stress versus void ratio resulting from the consolidation tests. Dashed lines correspond to extrapolation to 1 kPa used to determine initial (depositional) parameters.

Initial specific storage resulting from consolidation tests varies from 0.014 for sample SdG068-02_207 to 0.064 for SdG068-03_244 (Figure 4.16 and Table 4.3). In this case, the sample with the lower specific storage (i.e., less compressible) corresponds to the sample with the highest sand (8.49%) and lowest clay content (25.28%). However, other measurements resulting in low specific storage (e.g. 0.016 for sample SdG068-03_84 and 0.019 for sample SdG068-01_187) are not associated with the presence of (low amounts) of sand (0% and 3.57%, respectively) or low percentages of clay (37.55% and 33.85%) (Table 4.3). Thus, a clear correlation between initial specific storage and grain size distribution has not been observed either.

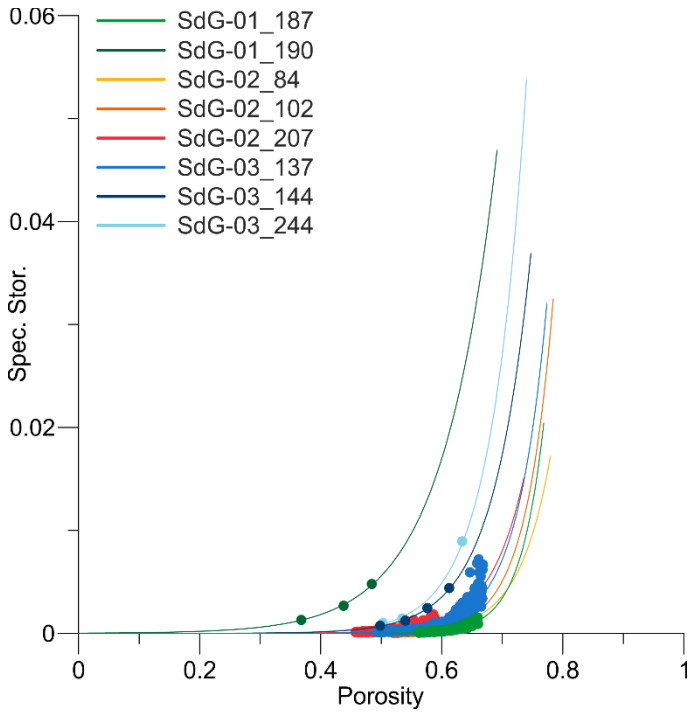

Figure 4.16: Porosity versus specific storage during virgin consolidation.

Initial hydraulic conductivity (k_0) has been measured on three samples by performing direct permeability tests with the constant head method (Figure 4.17 and Table 4.3) (see section 3.3.6). Initial hydraulic conductivity varies from 1.16E-09 for sample SdG068-01_190 to 6.56E-09 for sample SdG068-03_144 (Table 4.3).

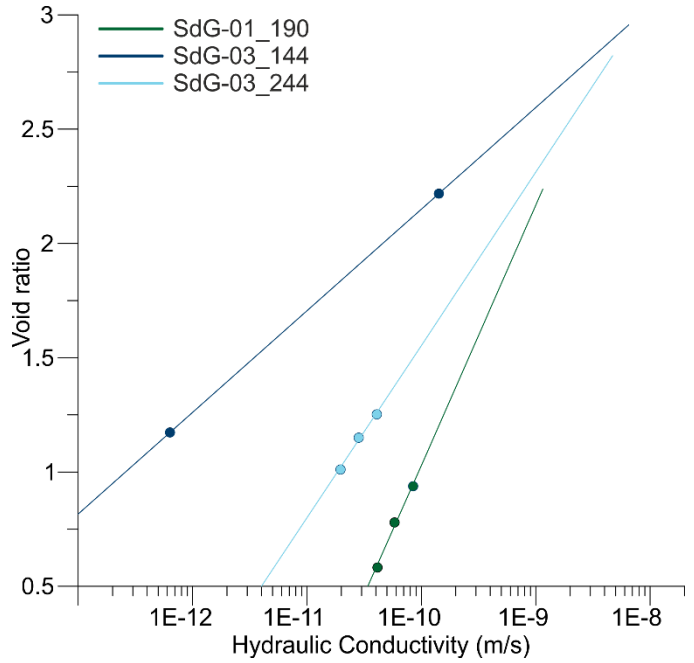

Figure 4.17: Flow-through hydraulic conductivity versus void ratio mesurements determined during virgin consolidation.

Chapter 5: Influence of measured physical properties in finite-element overpressure models

This chapter describes the results from a sensitivity analysis that aims to quantify the influence of defining hydrogeological models with physical properties of sediments measured on purpose for a specific area compared to using general literature data (see motivations and workflow in section 3.4.2). The first part of this chapter describes the geotechnical properties and grain size distribution from sediments collected in the Alentejo basin (see also section 4.2), Grenada basin (Lafuerza et al., 2014) and Ursa basin (Urgeles et al., 2010). The second part focuses on the results from the different modelling scenarios. The results showed in this chapter have been published in Mencaroni et al. (2020).

5.1 Alentejo, Grenada and Ursa basins: sediment properties comparison

The grain size distribution of sediments collected in each study area (Alentejo, Grenada and Ursa basins) are relatively homogeneous, although each location has a distinctly different composition. Whilst all samples collected during the INSIGHT cruises in the Alentejo basin are silt dominated, silt percentages vary significantly between 57.36% and 83.1% (Figure 5.1, Table 5.1). Clay contents also ranged between 11.1% and 42.2%, and sand sized grains comprised the lowest fraction at each site (0% to 10.5%) (Figure 5.1, Table 5.1). Ursa basin sediments show the lowest sand content, with 8 out of 9 samples corresponding to the "E" class of Flemming's classification (sand < 5%) (Figure 5.1). Within the Grenada basin, 2 out of 3 samples tested show a sand content greater than 5% and a clay content less than 25%. Sediments from the Alentejo basin are similar to the Ursa basin: sand content is less than 5% for 5 out of 6 samples, with clay values between 25% and 35%. Therefore, group D-II in Flemming's classification is only represented by two samples from the Grenada basin (Table 5.1).

We used ternary contour diagrams to visualize different textural composition of sediment in relation with their initial porosities (Figure 5.2A), compression index (Figure 5.2B) and initial hydraulic conductivity (Figure 5.2C). Results show a broadly heterogeneous relationship between grain size and physical properties. Compression index (Figure 5.2B) ranges between 0.22 and 0.92. The highest C_c values are related to an increase in silt percentage and tend to decrease in sediments with some sand content.

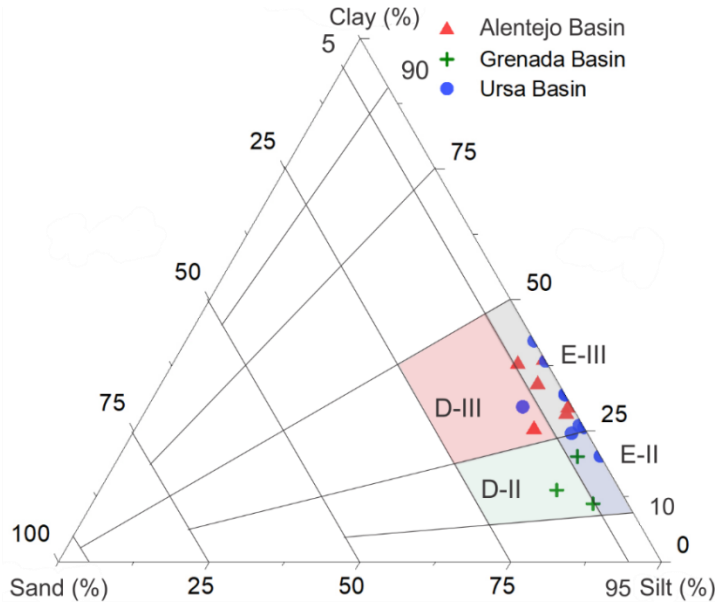

Figure 5.1: Grain size distribution of the sediments analyzed in the Alentejo, Grenada and Ursa basins. The internal subdivision refers to the classification for muddy marine sediments proposed by Flemming (2000).

Table 5.1: Compiled physical and grain-size data from the Gulf of Cadiz, off Martinique and the Gulf of Mexico.

Area	Sample	Original depth (mbsf)	Sand (%)	Silt (%)	Clay (%)	Texture class*	ϕ_0	C_c	k_0
Alentejo basin	SdG-01_190	1.9	4.93	57.36	37.71	E-III	0.69	0.52	1.16×10^{-9}
	SdG-01_187	1.8	3.57	62.58	33.85	E-III	0.77	0.50	
	SdG-03_144	1.4	0.7	69.89	29.41	E-III	0.75	0.48	6.56×10^{-9}
	SdG-03_137	1.3	1.66	70.32	28.28	E-III	0.77	0.62	
	SdG-02_207	2.0	8.49	66.23	25.28	D-III	0.74	0.45	
	SdG-02_102	1.0	0.24	61.25	38.51	E-III	0.78	0.65	
Ursa basin	308_1322_B2_H3	8.0	0	57.8	42.2	E-III	0.77	0.92	5.70×10^{-10}
	308_1322_B4_H1	24.0	0	68	32	E-III	0.71	0.57	1.12×10^{-8}
	308_1322_B7_H2	54.0	8.2	62.2	29.6	D-III	0.66	0.41	3.48×10^{-8}
	308_1322_B13_H2	111.0	0	68.1	31.9	E-III	0.56	0.23	1.06×10^{-8}
	308_1322_B17_H2	144.0	0	61.69	38.4	E-III	0.59	0.25	3.08×10^{-8}
	308_1322_B26_H2	212.0	0.63	73.37	26	E-III	0.52	0.22	4.41×10^{-8}
	308_1324_B2_H3	8.0	2.65	72.4	24.4	E-II	0.71	0.58	2.32×10^{-8}
	308_1324_C1_H5	57.0	0	74.3	25.7	E-III	0.63	0.35	8.87×10^{-9}
	308_1324_C2_H2	103.0	0	79.8	20.2	E-II	0.61	0.28	5.70×10^{-10}
Grenada basin	340-1399B_4H4	30.5	10.5	75.8	13.7	D-II	0.78	0.69	1.55×10^{-9}
	340-1399B_6H3	46.5	3.9	76.1	20.1	E-II	0.79	0.75	1.32×10^{-9}
	340-1399B_19H3	138.9	5.8	83.1	11.1	D-II	0.77	0.67	1.41×10^{-9}

ϕ_0, initial porosity; C_c, compression index; k_0, initial hydraulic conductivity (m s^{-1}). *Flemming (2000).

Samples from the Grenada basin, with higher silt content, show a compression index ranging between 0.67 and 0.75, while the lowest values are found in sediments from the Ursa basin, where most of the samples show C_c values below 0.65 (Figure 5.3, Table 5.1). An exception is represented by sample 308-1322B_H08, which has higher clay content (42.2%) and compression index (0.92). A similar trend is illustrated in the initial porosity diagram (Figure 5.2A), with porosity values ranging between 0.52 and 0.79. The highest porosity values are reached in sediments with higher silt content while the lower values are linked to higher sand content.

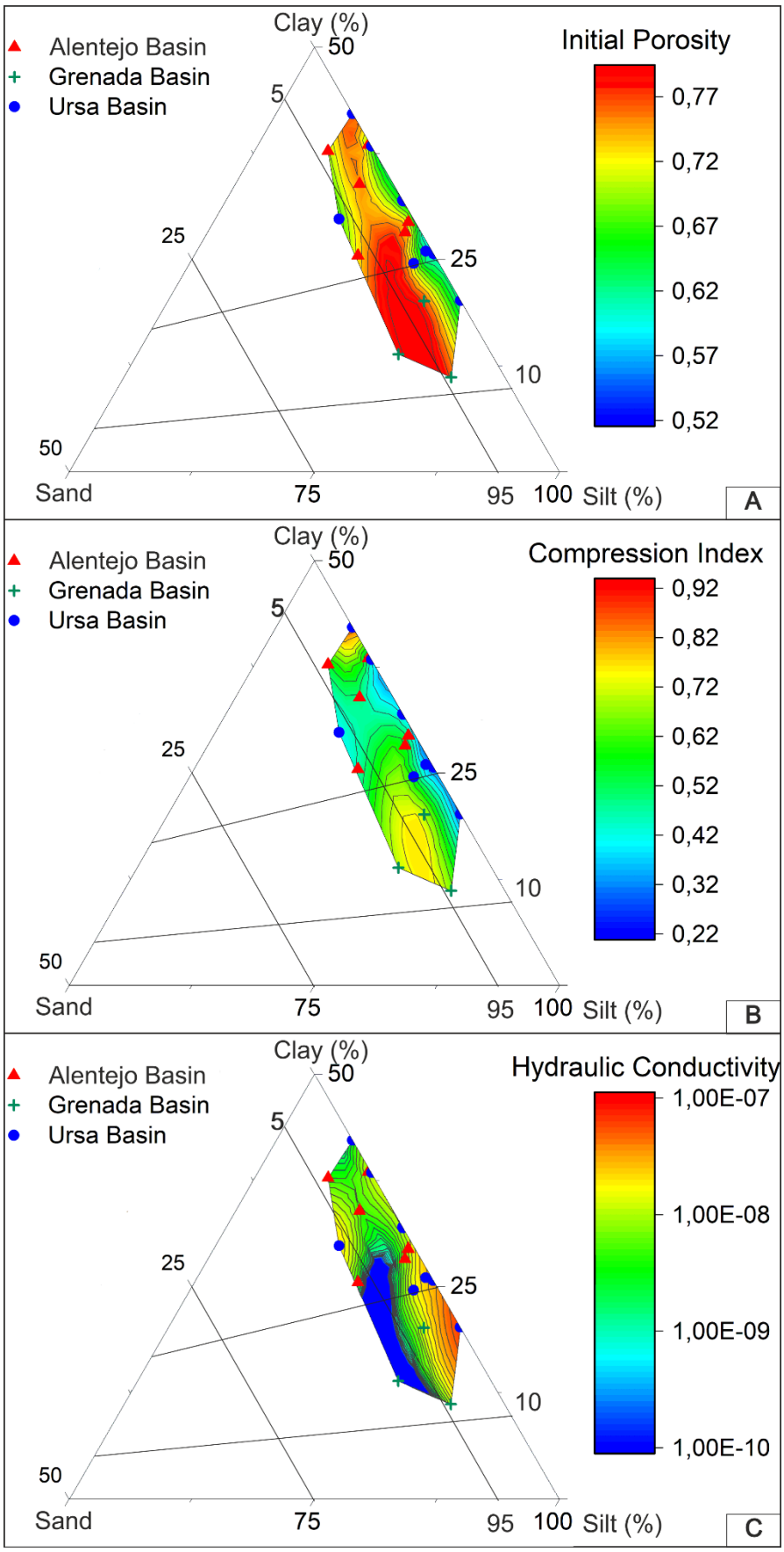

Figure 5.2: Ternary contour diagrams comparing sediment composition (% sand, silt and clay) with (a) initial porosity, (b) compression index and (c) hydraulic conductivity. Sand axes have been reduced to the range 50–100% to facilitate visualization.

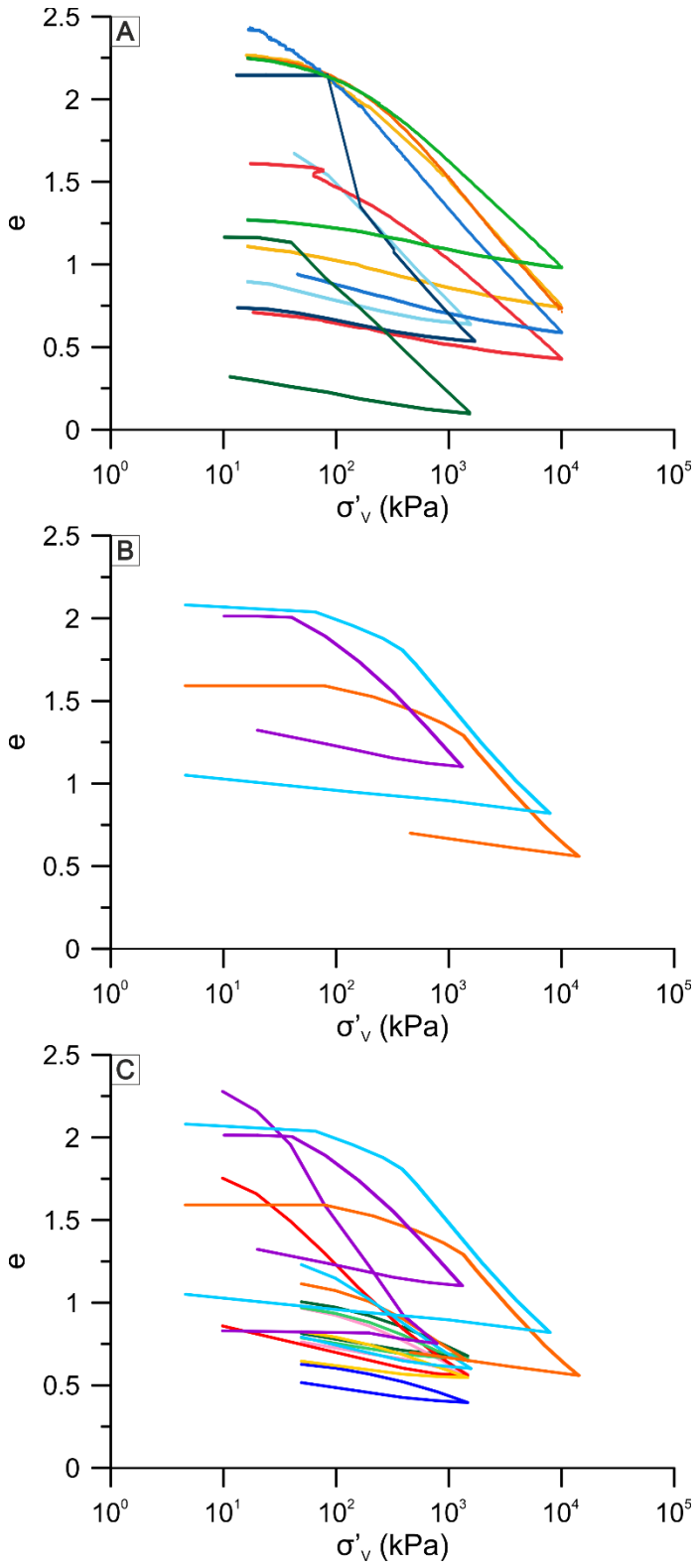

Figure 5.3: Consolidation curves showing void ratio *e* reduction while increasing uniaxial loading σ'_v. Each plot refers to one of the analyzed areas.. (**A**) Alentejo basin; (B) Grenada basin (Lafuerza et al., 2014). (**C**) Ursa basin (Urgeles et al., 2010).

However, sample SdG_02_102 differs from this trend showing a high initial porosity (0.78) despite a relatively low silt content (61%).

Values of hydraulic conductivity at deposition (1 kPa) vary within two orders of magnitude (10^{-8} to 10^{-10} m/s). The Ursa basin samples produce the highest values while the lowest hydraulic conductivity values correspond to samples from the Grenada basin (Figure 5.2C).

5.2 Modelling results

Our first modelling stage (Scenario A) (Figure 5.4) consisted in three separate models, where physical properties of the hemipelagic layer described above have been averaged for each study area (Table 5.2).

Table 5.2: Physical properties of sediments used for the simulations described in this chapter.

	Samples	$Ø_0$	S_0 (m^{-1})	k_0 (m/s)
Turbidite Layer	(Urgeles et al. 2010)	0.5	0.001	1×10^{-6}
Hemipelagic Scenario A - Areas	Alentejo basin	0.74	0.025	3.86×10^{-8}
	Grenada basin	0.78	0.005	1.43×10^{-9}
	Ursa basin	0.64	0.023	2.71×10^{-8}
Hemipelagic Scenario B – Classes	D - II	0.77	0.003	1.48×10^{-9}
	D – III	0.69	0.014	2.90×10^{-8}
	E – II	0.70	0.017	1.04×10^{-7}
	E – III	0.69	0.027	3.09×10^{-8}

$Ø_0$: initial porosity at 1kPa; k_0: initial hydraulic conductivity at $Ø_0$; S_0: initial specific storage at $Ø_0$.

Fine-grained sediments from the Alentejo basin and from the Ursa basin show a comparable range of overpressure development, reaching a maximum overpressure ratio (λ) of 0.18 at 343 mbsf for the model using Alentejo basin sediment characteristics and 0.25 at 341 mbsf for the model using Ursa basin sediment characteristics (i.e., immediately below the turbidite unit). The computed overpressure ratio for the model using Grenada basin sediment characteristics shows higher values with λ up to 0.56 at 329 mbsf (Figure 5.4A).

The second modelling scenario (Scenario B) consisted in defining the hemipelagic units with physical properties averaged from their grain size distribution classes (Figure 5.4B). The minimum peak value (λ ~0.06) is observed in the model defined with properties from the group E-II (sand<5%, clay < 25%). Models from groups E-III and D-III show comparable maximum overpressure ratios (0.24 and 0.19), while the maximum values (λ ~0.53) are reached by the model defined with the properties averaged from the samples in the group D-II (Sand > 5%, Clay < 25%) (Figure 5.1 and Figure 5.4B).

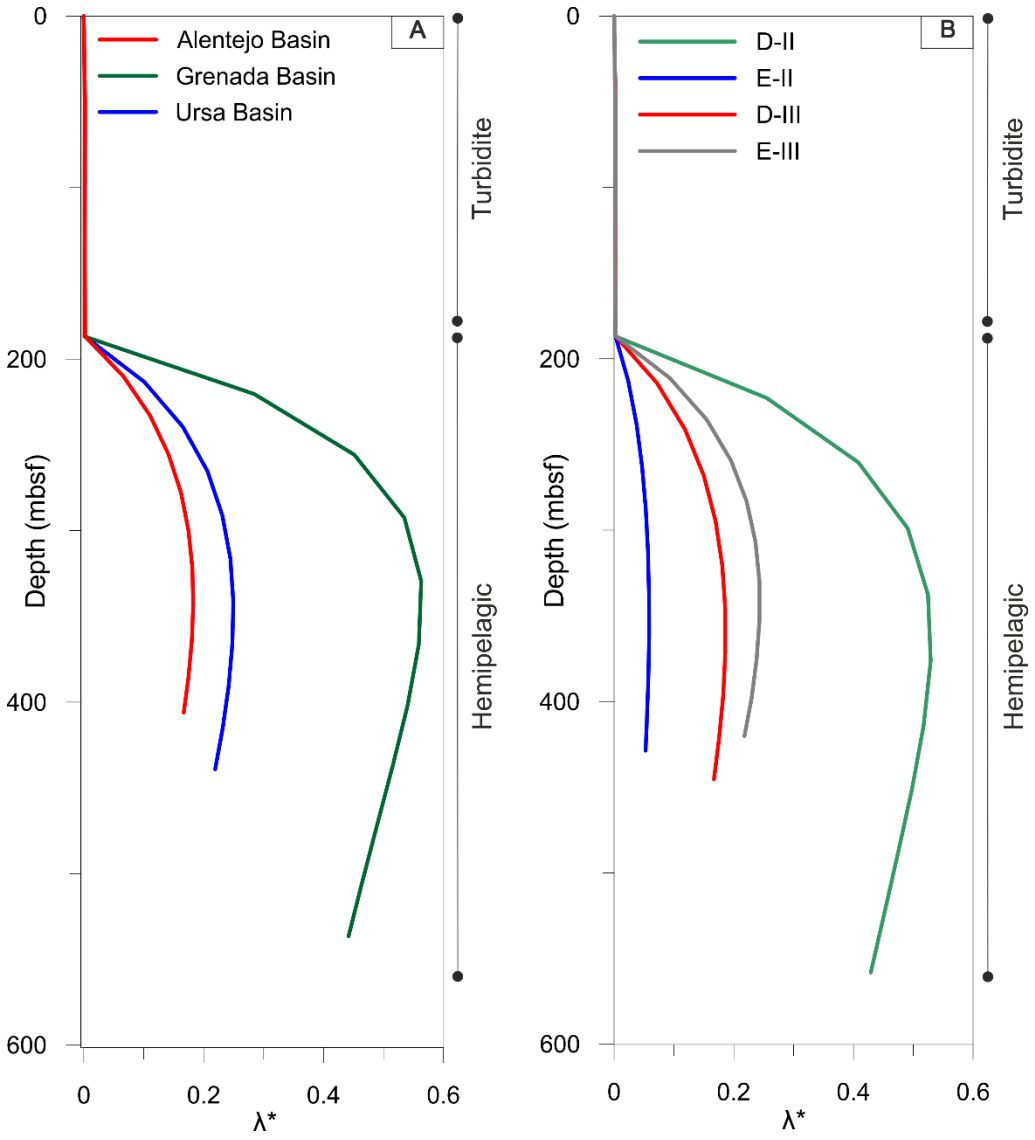

Figure 5.4: Overpressure generated at the end of the simulations vs computed final depths. The plots refer to (A) Scenario A, where physical properties of the hemipelagic units are averaged from each study area and (B) Scenario B, where the properties of the hemipelagic layer are averaged from each of the four represented textural classes.

Figure 5.5 shows the present-day overpressure resulting at IODP Site U1324 in the Ursa basin from the 1D simulations in this study (see section 3.4.2 for experimental setup). Changes in the physical properties of the hemipelagic unit, at the top of the stratigraphy, did not allow any of our scenarios to fit perfectly neither the reference 1D model (Urgeles et al. 2010) nor the *in-situ* overpressure measurements (Flemings et al. 2008). The model defined with hydraulic conductivity, specific storage and initial porosity from the Alentejo basin underestimates the overpressure within the hemipelagic layer, mainly because of its higher permeability compared with the hemipelagic sediment from the Ursa basin (Table 5.2). The model defined with physical properties from the Grenada basin provides a very different output compared with the other models (Figure 5.5). Even if it reproduces better the measured *in-situ* overpressures from the hemipelagic layer, the hydrodynamics of the model is split in two separate systems: in the lower part of the stratigraphy the overpressure increases constantly from the bottom to the top, reaching

a maximum overpressure value of 1 at the base of the muddy sediments. Above this point, the overpressure drops, keeping a constant value of 0.7 up to the seafloor.

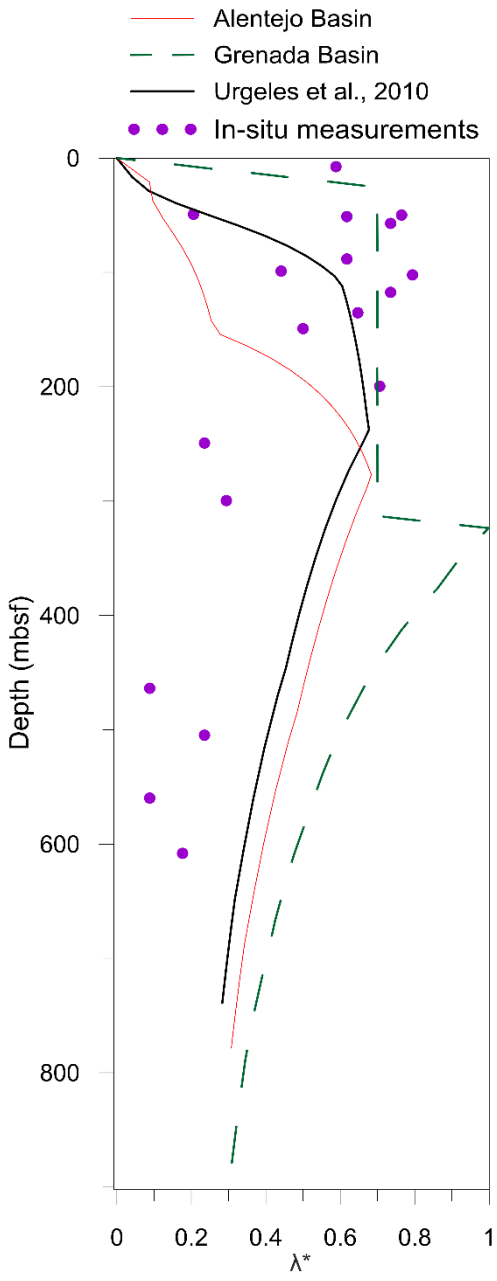

Figure 5.5: Overpressure generated at IODP Site U1324 in the Ursa basin vs computed final depth for the *in-situ* piezometer measurements (purple dots); reference overpressure modelled at the same site by Urgeles et al. (2010) (black line); overpressure resulting by defining the hemipelagic units with properties collected from the other study areas (red and green lines).

Chapter 6: Modelling overpressure in the Marquês de Pombal Plateau area

This chapter shows the results from FEM models of joint stratigraphic, physical properties and resulting fluid flow and pore pressure development in the Marquês de Pombal area using the software BASIN. As explained in section 3.4.1, BASIN allows to define the physical properties of maximum 4 sediment types and the ones adopted in this study are "Clay", "Silt", "Sand" and, for practical purposes, "Mixed System", where "mixed" refers to a sedimentary system built by the interaction between along-slope and down-slope sedimentary processes (see section 1.7.3). Initial porosity, specific storage and hydraulic conductivity are the three physical properties to input for each of the sediment types in BASIN, which have been derived from the consolidation and permeability tests performed on the sediments collected during the INSIGHT cruises and described in section 4.2. As explained in detail in section 3.4.3, "Clay" and "Silt" types have been grouped based on the mean grain size of the tested sediments. For the "Sand" class we used the initial porosity, specific storage and hydraulic conductivity values adopted by Reed et al. (2002), since none of the samples from the near surface tested showed considerable percentages of sand, which on the other hand seem to be present from IODP Site U1391 (Figure 3.9). Finally, physical properties for the "Mixed System" sediment class are calculated by averaging all the values resulting from all geotechnical tests (Table 6.1).

In section 4.2.2.2 we showed how the analysed samples resulted in relatively homogeneous compressibility and permeability values (Table 4.3) reflecting the similar grain size distribution of the sediments (Figure 4.9). Accordingly, the physical properties of the sediment types used for the models are characterized by little variability. Initial porosity varies from 0.75 for the "Mixed System" and "Clay" sediment types to 0.77 for "Silt". Initial specific storage ranges between 0.033 for the "Mixed System" lithology to 0.037 for the "Silt". The minimum initial hydraulic conductivity value is associated with "Clay" (2.95×10^{-9} m/s), while "Silt" shows the highest (6.56×10^{-9} m/s) (except for the "Sand" sediment type, 1×10^{-6} m/s) (Table 6.1).

As explained in section 3.4.3.1, the relative percentage of Clay, Silt and Sand vary in between the layers according to the reference stratigraphy revealed by IODP Site U1391, but also the percentage of sand decreases linearly with water depth. Where the 2D models cross the major Quaternary depocenter in the Marquês de Pombal Plateau (Figure 4.4D), the uppermost 10 layers (representing Unit IV) are entirely composed by the "Mixed System" sediment type. This sediment type is otherwise absent from the pre-LQD sedimentary units. Geometry of the layers and times of deposition of the units are the other two key information used as input in BASIN to run the simulation: the workflow adopted to derive that information is reported in section 3.4.3.

Table 6.1: Initial porosity, initial specific storage and initial hydraulic conductivity assigned to each of the sediment types adopted in the models. "Samples" column indicates the samples from which physical properties have been averaged (see section 4.2.2.2).

Sediment type	Samples	$Ø_0$	S_0 (m^{-1})	k_0 (m/s)
Clay	SdG068-01_187 SdG068-01_190 SdG068-02_102 SdG068-03_84 SdG068-03_244	0.75	0.035	2.95×10^{-9}
Silt	SdG068-02_207 SdG068-03_137 SdG068-03_144	0.77	0.037	6.56×10^{-9}
Mixed System	All samples	0.75	0.033	4.15×10^{-9}
Sand	(Reed et al., 2002)	0.5	0.001	1×10^{-6}

$Ø_0$: initial porosity at 1kPa; k_0: initial hydraulic conductivity at $Ø_0$; S_0: initial specific storage at $Ø_0$.

As it was explained in Methods section 3.4.3, five 2D models have been built in this study with the aim of representing all the possible stratigraphic and morphological influences on the overall fluid-flow and overpressure development in the Marquês de Pombal Plateau area. The São Vicente Canyon represents one of the elements with largest potential for flow perturbation, and in order to investigate the influence of the canyon in the overall hydrogeology in the area, three of the models (Line_1, Line_2 and Line_5) cross it on their SW end (Figure 6.1). Line_1 and Line_5 also cross the Marquês de Pombal Fault on their NE side. As the fault displacement has been modelled from the Pliocene to the present day, those two models will also provide an overview about potential influence of the fault movement in the overpressure development in the area. Finally, Line_3 and Line_4 models cross the Marquês de Pombal Plateau following a NE-SW orientation (Figure 6.1). These 2D models allow a direct visualization of the influence of sediment deposition over the Marquês de Pombal Plateau on the overall overpressure development in the area, without being affected by potential features allowing overpressure dissipation such as the São Vicente Canyon erosion. Line_4 is the model located closer to depocenter of Unit IV, while the NE end of Line_3 is located in the external part of the Unit IV depocenter and allows to follow the transition towards deeper areas of the plateau (Figure 6.1).

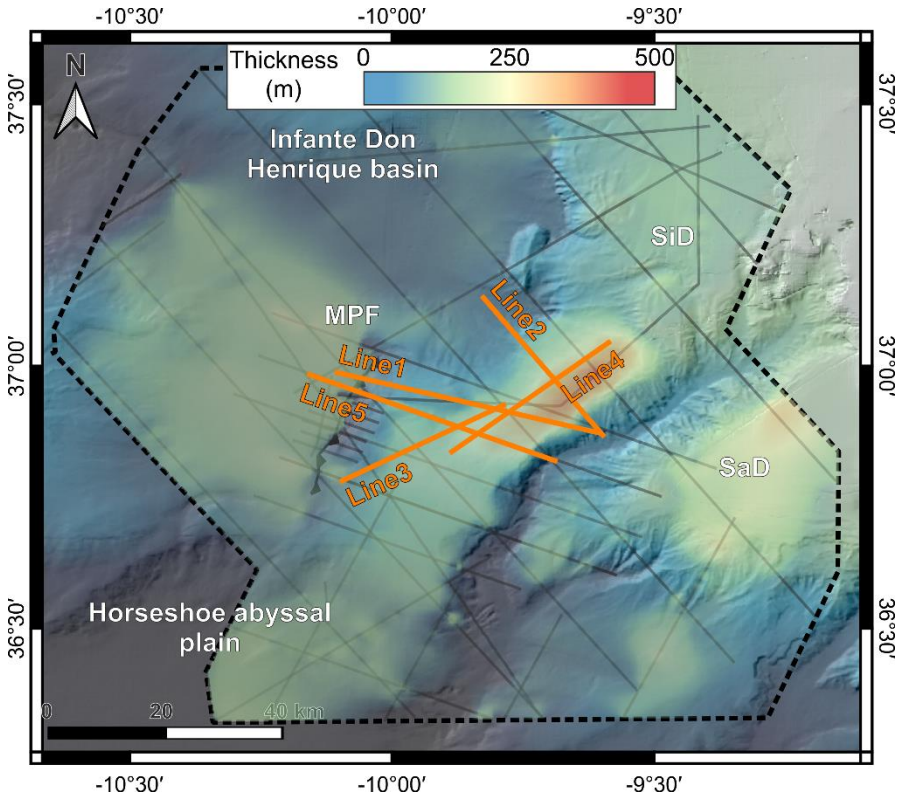

Figure 6.1: Location of the models plotted over the thickness map of Unit IV, which allows to see the location of the depocenter on the Marquês de Pombal Plateau. MPF: Marquês de Pombal Fault; SaD: Sagres drift; SiD: Sines drift.

6.1 Line_1

Line_1 model extends from the northern edge of the Marquês de Pombal Fault to the São Vicente Canyon, following a ESE-WNW orientation and crossing the Marquês de Pombal Plateau area not far from the depocenter of Unit IV (Figure 6.1).

At the end of the simulation, thickness of the Early Pliocene unit, Unit I, Unit II and Unit III remain relatively constant throughout the model. Unit IV reaches the maximum thickness in the proximity of the São Vicente Canyon (up to 380 m) and thins out progressively towards the Marquês de Pombal Fault area and more abruptly towards the São Vicente Canyon (Figure 6.2A). Within the Marquês de Pombal Plateau, Unit IV is composed by the "Mixed System" sediment type. At the footwall of the Marquês de Pombal Fault Unit IV transitions towards a mixed "Clay" and "Silt" alternation in the Infante Don Henrique basin (Figure 6.2B).

Present-day porosity values along Line_1 model vary from 0.75 at the seafloor to 0.2 within the deepest sediments of the Marquês de Pombal Plateau (Figure 6.3A). Although porosity decreases linearly with burial depth through the model, at the headwall of the Marquês de Pombal Fault (between 15 km and 25 km offset) porosities decrease slower with depth than in the central part of the Marquês de Pombal Plateau (-0.04 vs -0.06 Ø / 100 m). Furthermore, in the Marquês de Pombal Plateau a localized low porosity interval (~0.35) is visible within Unit IV from 2400 to 2700 mbsf (Figure 6.3A).

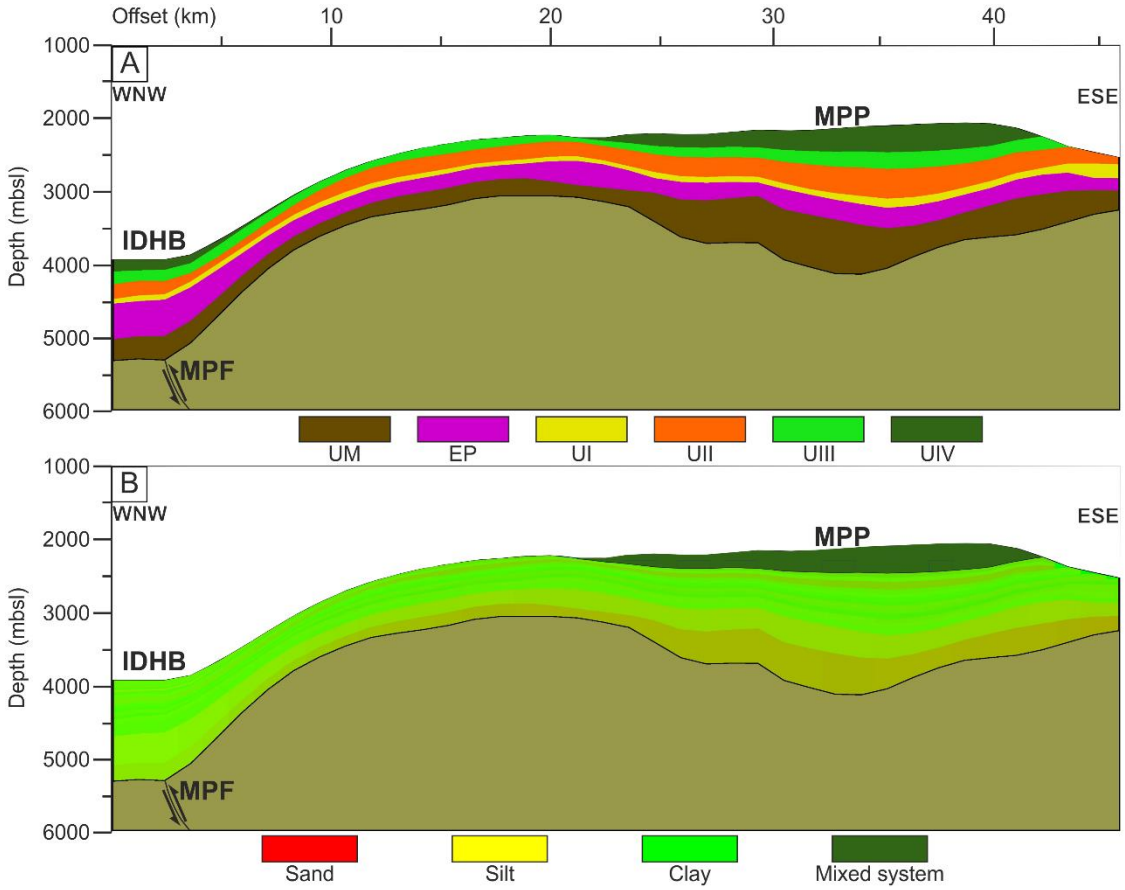

Figure 6.2: Present day stratigraphy (A) and sediment distribution (B) along the model of Line_1. MPF: Marquês de Pombal Fault; MPP: Marquês de Pombal Plateau; IDHB: Infante Don Henrique basin.

The hydraulic conductivity of the model varies between orders of magnitude of 10^{-8} and 10^{-11} m/s (Figure 6.3B). In general, hydraulic conductivity in the model follows the porosity trend. The slope and headwall generated by the Marquês de Pombal Fault (between 5 and 25 km offset) show higher hydraulic conductivity (10^{-9} m/s) than the central part of the Marquês de Pombal Plateau (10^{-11} m/s) within Early Pliocene, Unit I and Unit II (Figure 6.3B). In the deeper part of the Marquês de Pombal Plateau, however, hydraulic conductivity increases to values up to 10^{-10} m/s reflecting the more sandy lithology that defines the lowermost layer (Upper Miocene). The combination of these deep higher permeability and the low permeability region above them allow lateral transfer of fluid from the deeper parts of the Marquês de Pombal Plateau area towards both the Marquês de Pombal Fault headwall and towards the São Vicente Canyon. In this profile, the canyon erosion affects Units II and III, developing during the 10 timestep representing the late Quaternary and proceed with a constant erosion rate of 1.31 m/kyr. In areas of lower permeability contrast the flow is primarily vertical (Figure 6.3B). Low porosity and hydraulic conductivity values in the central part of the Marquês de Pombal Plateau area are also associated with slight overpressure ratio development, up to 0.15 (Figure 6.3C). However, overpressure does not develop only within the low permeability intervals (Early Pliocene, Unit I and Unit II), but expands also to the shallower part of the model (Units III and IV). Overpressure is mainly associated with areas of vertical fluid flow and does not develop along the anticline associated

with the Marquês de Pombal Fault nor in the proximity of the São Vicente Canyon, where the flow is mainly horizontal (Figure 6.3C).

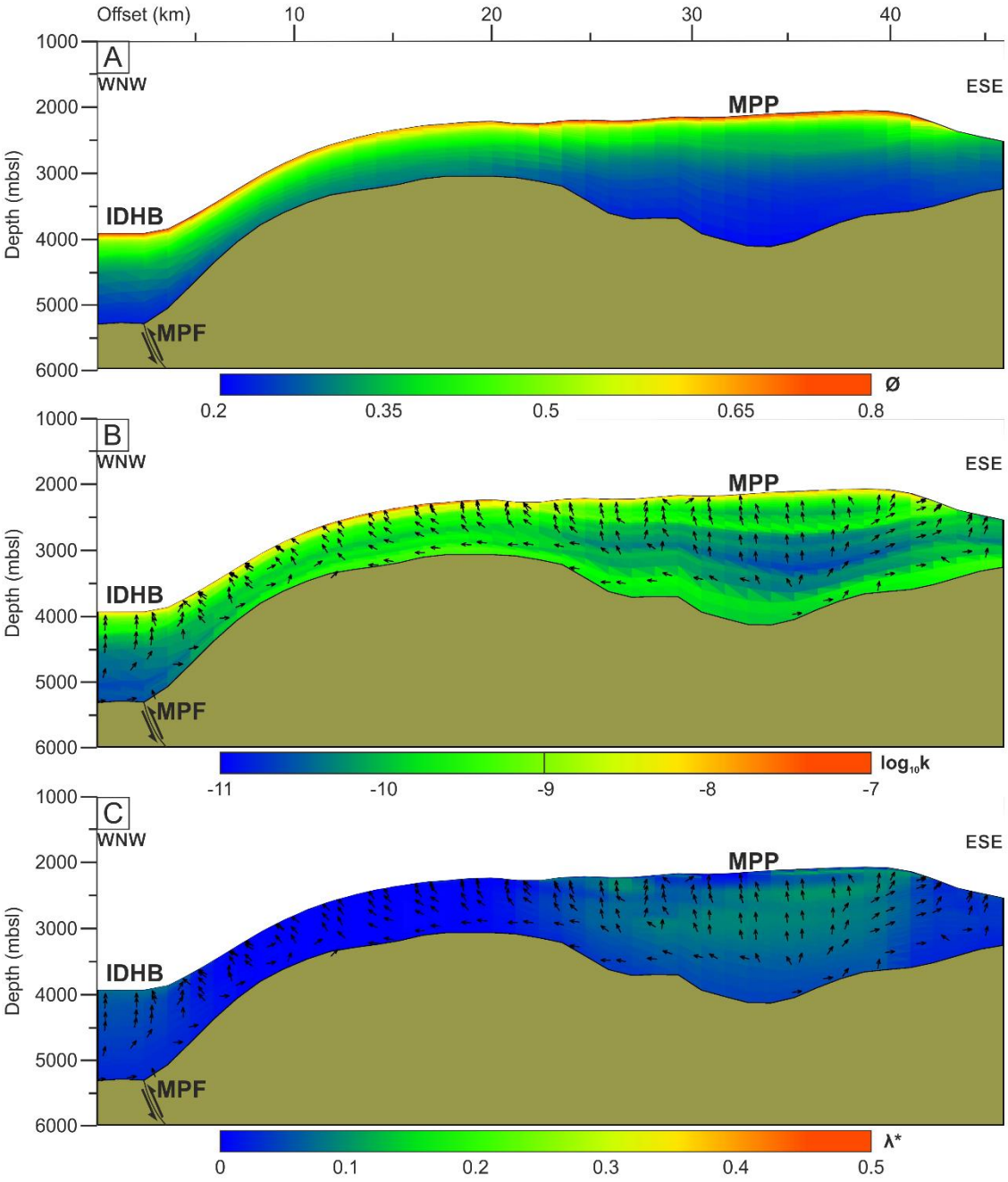

Figure 6.3: Present day (A) porosity, (B) hydraulic conductivity and (C) overpressure ratio of Line_1 model. MPF: Marquês de Pombal Fault; MPP: Marquês de Pombal Plateau; IDHB: Infante Don Henrique basin.

6.2 Line_2

The 2D model Line_2 follows a NNW-SSE direction, extending from the São Vicente Canyon to the Infante Don Henrique basin (Figure 6.1). Since the model does not cross the steep slope generated by the Marquês de Pombal Fault, the transition from the Marquês de Pombal Plateau area towards the deep part of the basin in the NNW appears smoother than in Line_1. Thus, the transition from the "Mixed System" sediment type in in proximity of the depocenter of Unit IV

to the "Silt"/"Clay" alternation in the Infante Don Henrique basin is distributed over a couple of kilometres following the thickness distribution of Unit IV (Figure 6.1 and Figure 6.4).

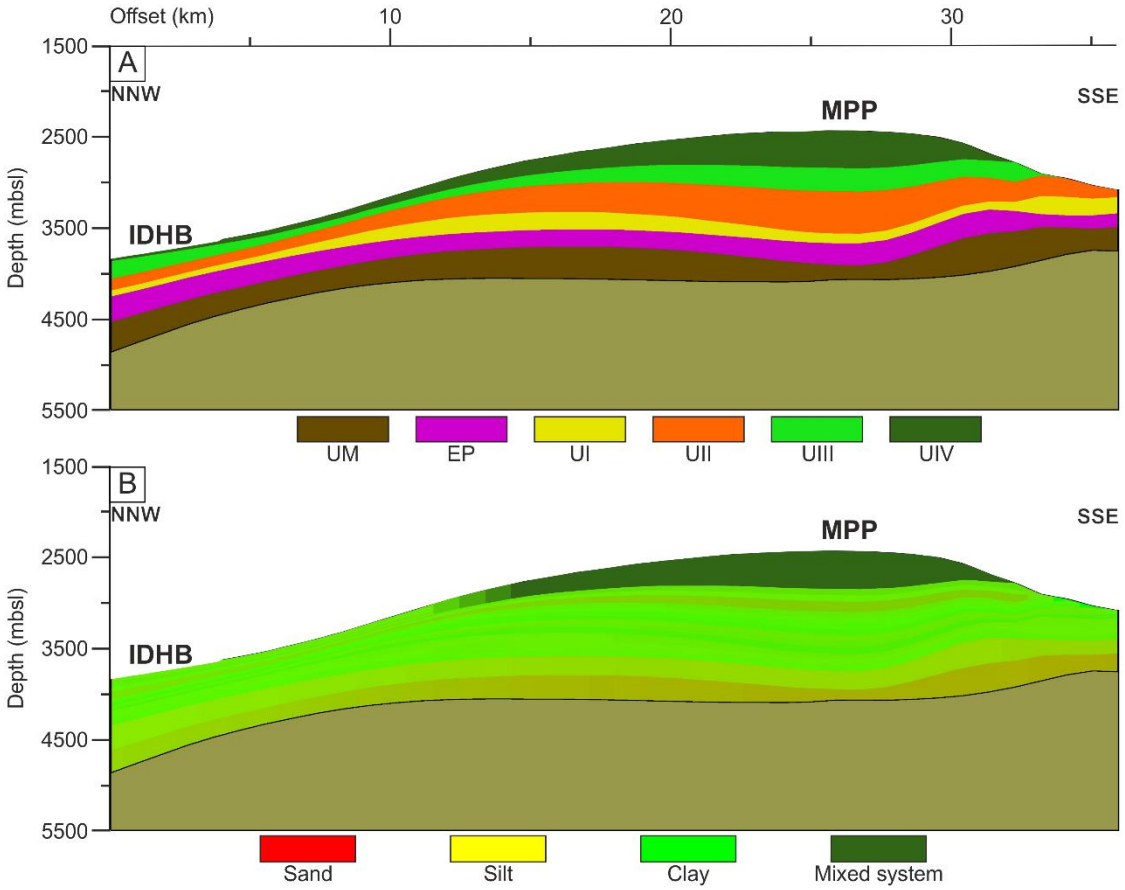

Figure 6.4: Present day stratigraphy (A) and sediment distribution (B) along the model of Line_2. MPP: Marquês de Pombal Plateau; IDHB: Infante Don Henrique basin.

Unit IV in Line_2 reaches a maximum thickness of ~400 m close to the São Vicente Canyon. The São Vicente Canyon erodes Units III and part of Unit II in the SSE flank of the Marquês de Pombal Plateau (Figure 6.4). The erosion is distributed during the late Quaternary timesteps, with a constant rate of erosion reaching 1.42 m/kyr.

Porosities along Line_2 model vary between 0.75 and 0.22, with lowest values attained in the deeper units within the Marquês de Pombal Plateau. In this area, porosity remains relatively constant with depth within Units IV and III (~0.4), after which a sharp transition at the top of Unit II occurs with the porosity decreasing to <0.3 (Figure 6.5A). This transition is also visible in the hydraulic conductivity results, where the limit between Units III and II is marked by a change from ~10^{-9} to ~10^{-11} m/s (Figure 6.5B). Higher hydraulic conductivity values in the deeper units (~10^{-10} m/s) promote lateral fluid flow, transferring interstitial fluids towards both the São Vicente Canyon and the slope to the NNW. These two areas are characterized by higher porosity and hydraulic conductivity values due to the lower burial load (Figure 6.5B).

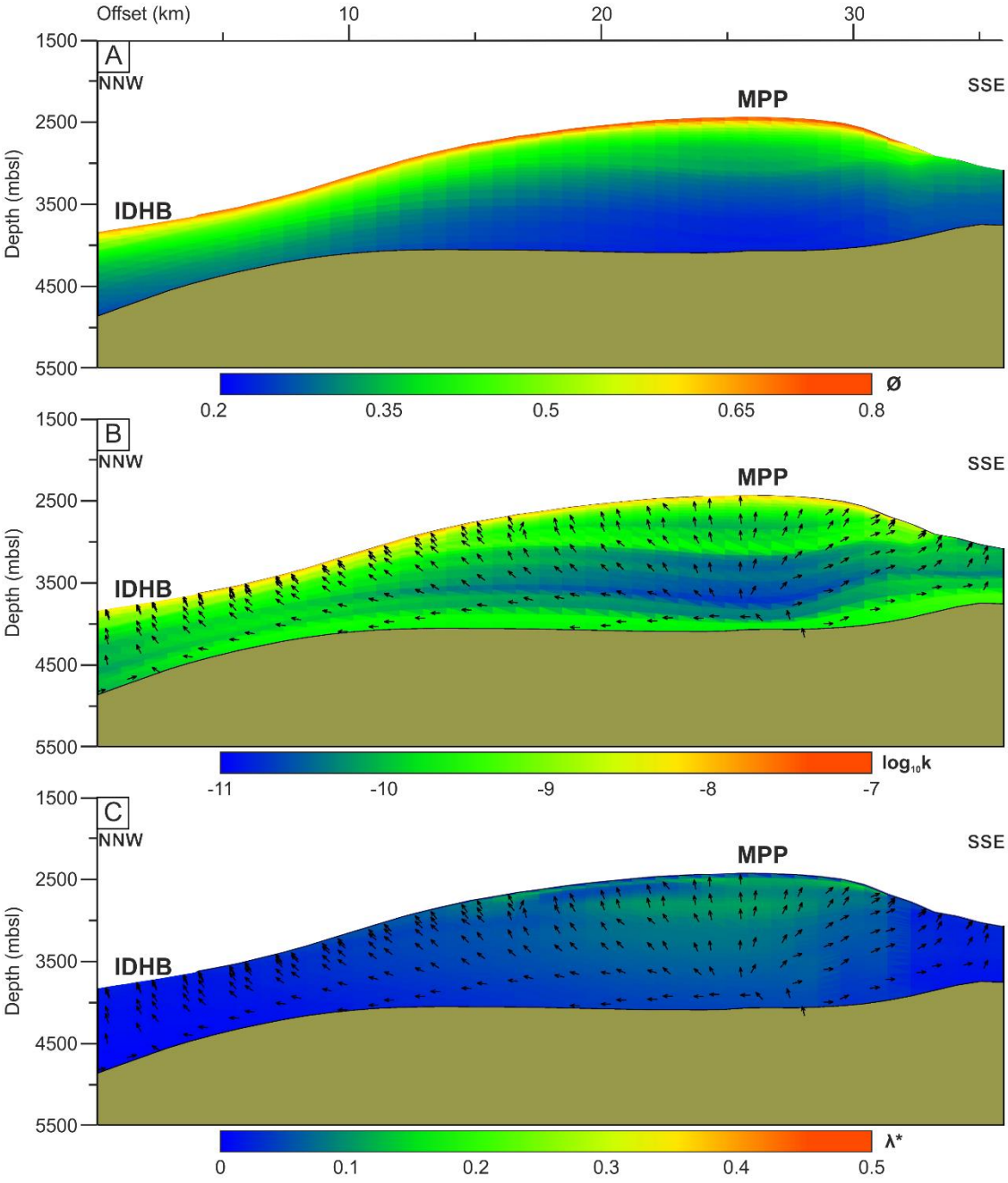

Figure 6.5: Present day (A) porosity, (B) hydraulic conductivity and (C) overpressure ratio along the model of Line_2. MPP: Marquês de Pombal Plateau; IDHB: Infante Don Henrique basin.

Build up of overpressure is rather low in Units III and IV in the Marquês de Pombal Plateau, with overpressure ratio up to ~0.15 within Unit IV (Figure 6.5C). As it was noticed for Line_1, overpressure develops in areas of the model where the flow is primarily vertical, while in areas of lateral fluid flow the build up of overpressure is minimum (Figure 6.5C).

6.3 Line_3

The model of Line_3 crosses the Marquês de Pombal Plateau following an ENE-WSW orientation (Figure 6.1). The seafloor along the profile is characterized by a gentle slope ranging from ~1º to ~9º towards the WSW (Figure 6.6A). The model does cross neither the São Vicente Canyon nor the Marquês de Pombal Fault scarp. The ENE edge of the model is located close to the depocenter

of Unit IV (Figure 6.1), with the unit maintaining a constant thickness (190 to 170 m) before thinning out towards the WSW end of the model (down to 5m in the thinnest part) (Figure 6.6A). Near the WSW end of Line_3, the sediment type within Unit IV transitions from the "Mixed System" to a "Silt"/"Clay" mixed composition (Figure 6.6B).

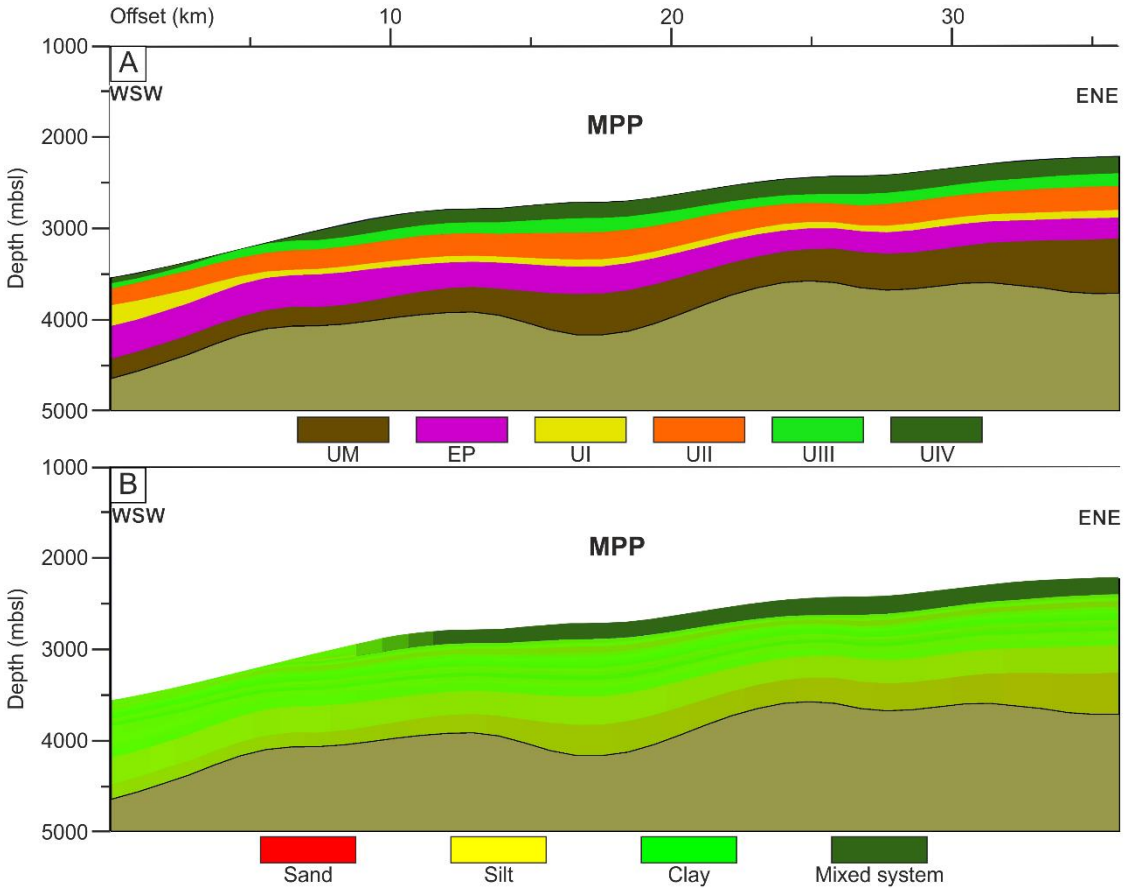

Figure 6.6: Present day stratigraphy (A) and sediment distribution (B) along the model of Line_3. MPP: Marquês de Pombal Plateau.

Unlike the models of Line_1 and Line_2, porosity in Line_3 decreases regularly from 0.75 in the surface to 0.2 in the deeper part at ~1500 m burial depth (Figure 6.7A). The regular porosity trend reflects also in the hydraulic conductivity values that range between ~ 10^{-9} to ~ 10^{-10} m/s in most of the model and decrease down to ~ 10^{-11} m /s only in localized layers within Unit II and Early Pliocene (Figure 6.7B). The overall higher hydraulic conductivity at the end of the simulation in Line_3 compared with Line_1 and Line_2, prevent overpressure generation, that results in maximum overpressure ratio ~0.1 only in the shallower parts of Unit IV, while in the deeper units λ^* never rises above 0.05 (Figure 6.7C). Apart from some lateral flow in the deeper part of the model promoted by the topography of the basement, water flow is mainly vertical.

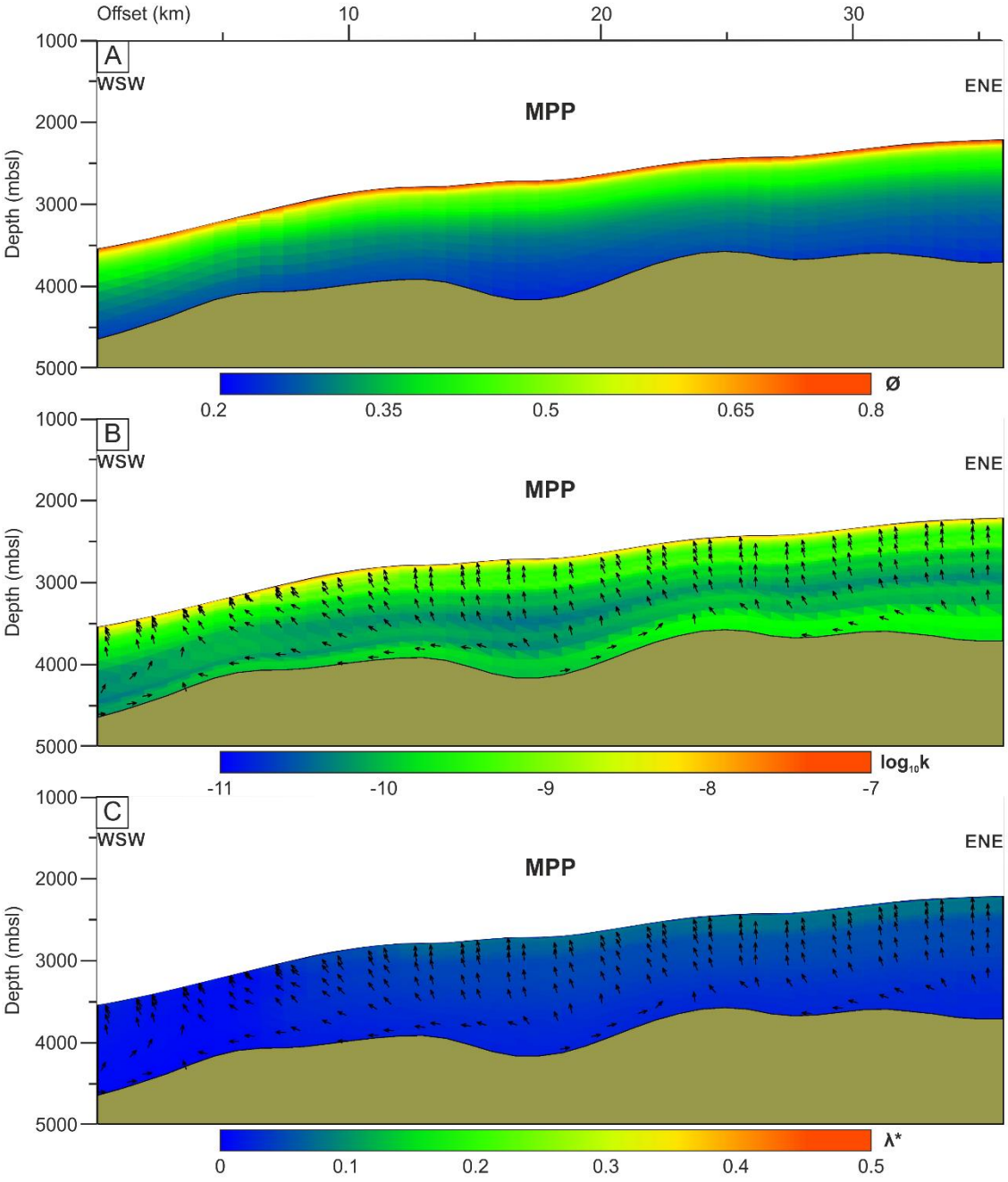

Figure 6.7: Present day (A) porosity, (B) hydraulic conductivity and (C) overpressure ratio of the model along Line_3. MPP: Marquês de Pombal Plateau.

6.4 Line_4

The model of Line_4 crosses the Marquês de Pombal Plateau along a NE-SW trend parallel to the São Vicente Canyon axis orientation (Figure 6.1). The model is located very close to the depocenter where Unit IV is composed entirely by the "Mixed System" sediment type (Figure 6.8B). Unit IV maintains a rather constant thickness between 200 and 320 m through the entire 2D profile (Figure 6.8A). On the other hand, the Upper Miocene Unit increases its thickness from 73 m in the NE to 524 m in the central part of the profile and slightly decreases towards the SW. Line_4 is characterized by a gentle slope (~2º along most of the line, increasing up ~ 6º in the SW end), where seafloor depth varies from 1650 m in the NW edge of the model to 2600 in the SE,

making it the overall shallower model (Figure 6.8A). Since the relative presence of "Sand" sediment type within the various units is modelled as a function of water depth (see also section 3.4.3.3.1), the little variations in water depth imply a more constant presence of sand within the various units compared to previous models (Figure 6.8B).

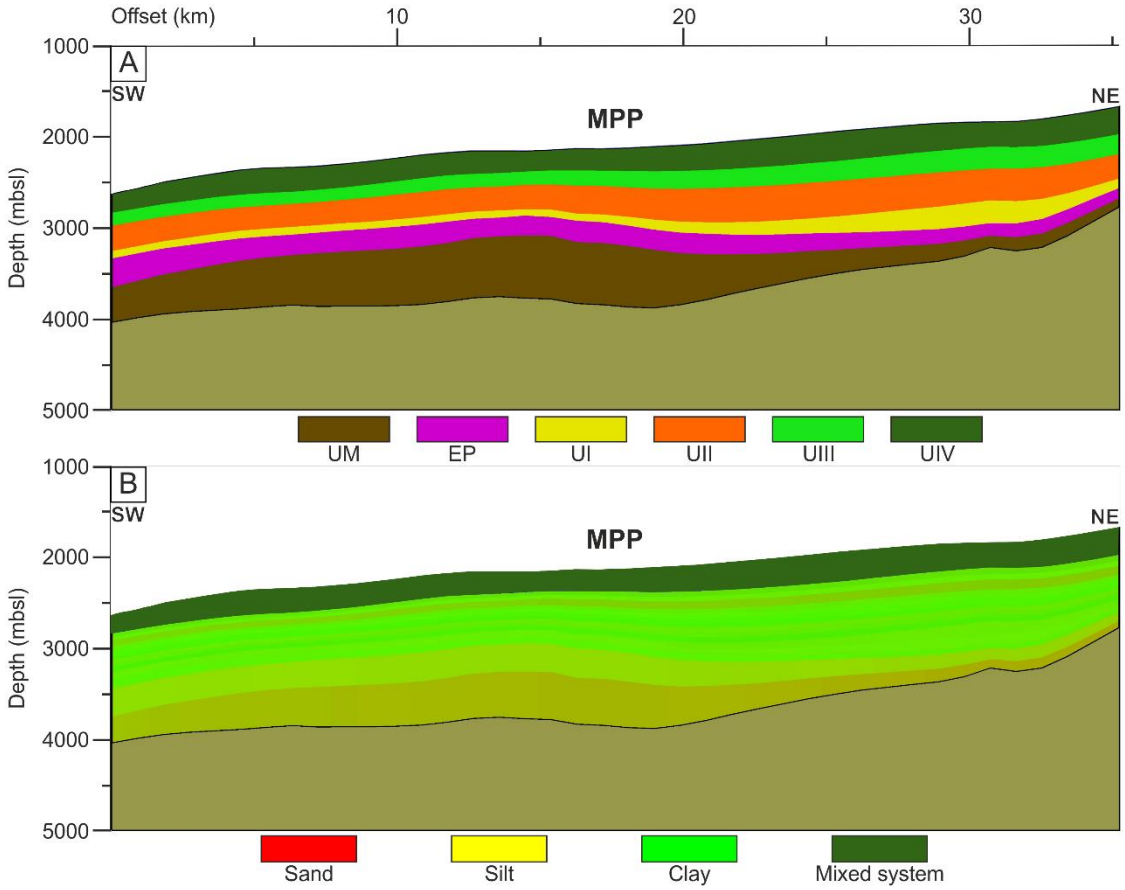

Figure 6.8: Present day stratigraphy (A) and sediment distribution (B) along the model of Line_4. MPP: Marquês de Pombal Plateau.

Similarly to what it has been observed in the model of Line_3, porosity in Line_4 decreases regularly with burial depth (from 0.75 to 0.22) along the entire model, mainly due to the relatively constant thickness that characterizes the units (Figure 6.9A). Hydraulic conductivity ranges between ~ 10^{-9} and ~ 10^{-10} m/s in Unit IV and within Upper Miocene, while the lower values are found in the central part of the sedimentary sequence where it decreases to ~ 10^{-11} m/s, especially within Units I and II. Except for lateral fluid flow taking place along the Upper Miocene unit, the fluid flow is mainly vertical. Overpressure ratio within Units IV and III reaches values up to 0.15 at 18-29 km offset. The same overpressure ratio values are also reached in the shallower-most layers both from 5 to 13 km offset and from 27 to 31 km offset (Figure 6.9C).

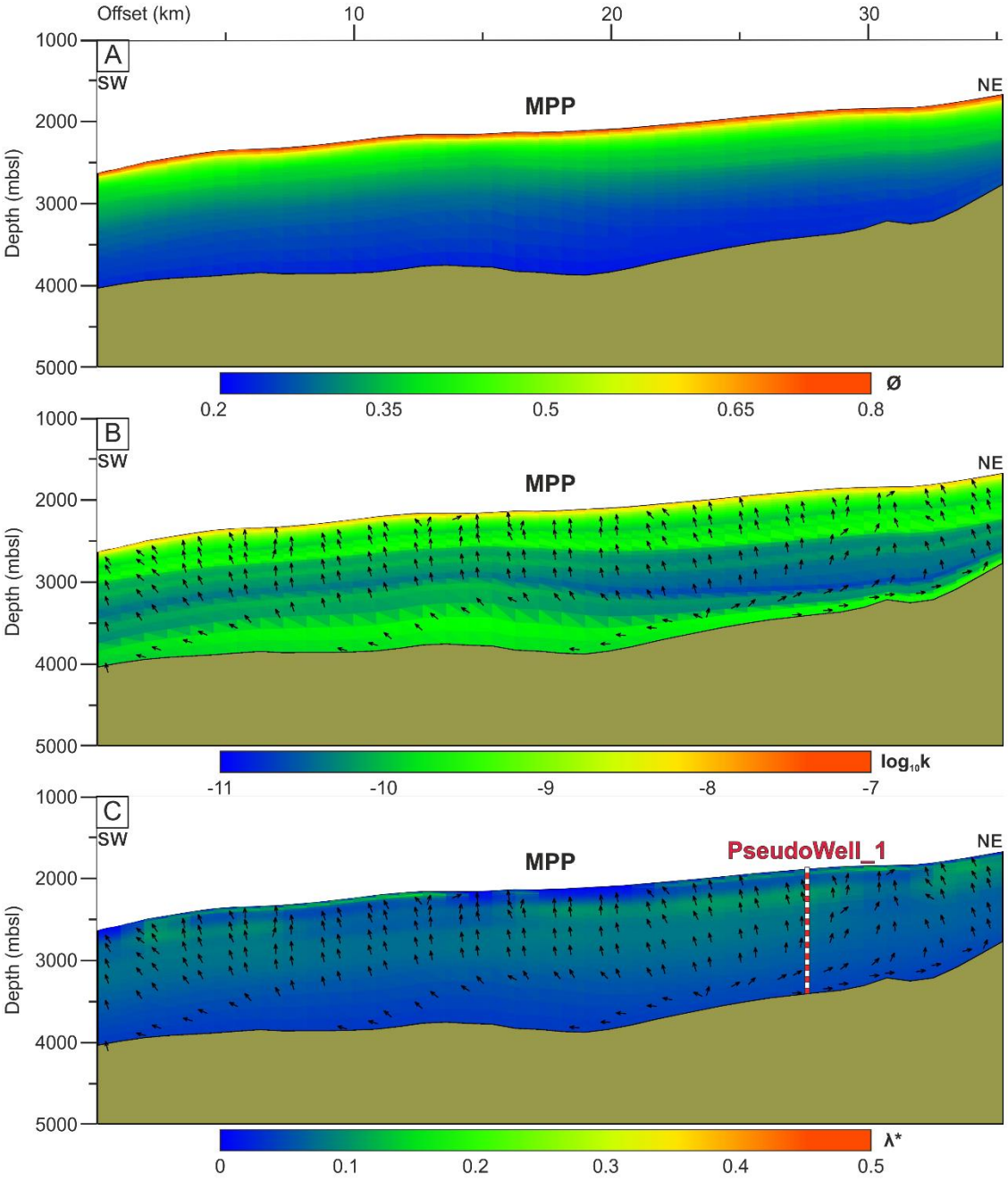

Figure 6.9: Present day (A) porosity, (B) hydraulic conductivity and (C) overpressure ratio along the model of Line_4. PseudoWell_1 location is reported. MPP: Marquês de Pombal Plateau.

Between all the considered models, Line_4 is the one located closer to the depocenter of Unit IV (Figure 6.1), where sedimentation rates reach values of 1.95 m/kyr (Figure 6.10A). A pseudo-well (PseudoWell_1) located in the proximity of the depocenter is used to analyse the influence of Unit IV maximum deposition in the overpressure development (Figure 6.10) (see PseudoWell_1 location in Figure 6.1 and Figure 6.9C). Figure 6.10B shows the burial history of the Marquês de Pombal Plateau at the location of PseudoWell_1 together with the overpressure ratio evolution. The first signs of overpressure development ($\lambda^* < 0.1$) are visible between EQD and MPD (i.e., during deposition of Unit II), when sedimentation rates boost from 0.62 m/kyr to 1.15 m/kyr (decompacted) (Figure 6.10A). A decrease in sedimentation rate taking place during deposition of Unit III is followed by pore pressure dissipation, before increasing again up to the

maximum values (λ* ~ 0.15) reached during Unit IV deposition (Figure 6.10B). This transition is marked by a spike in sedimentation rate that increases to ~ 2 m/kyr decompacted (Figure 6.10A). Figure 6.10C provide a more detailed overview of the overpressure ratio evolution during deposition of Unit IV, showing that overpressure ratio maintains fairly stable values between 0.1 and 0.15 during the last 341 kyr (Figure 6.10C).

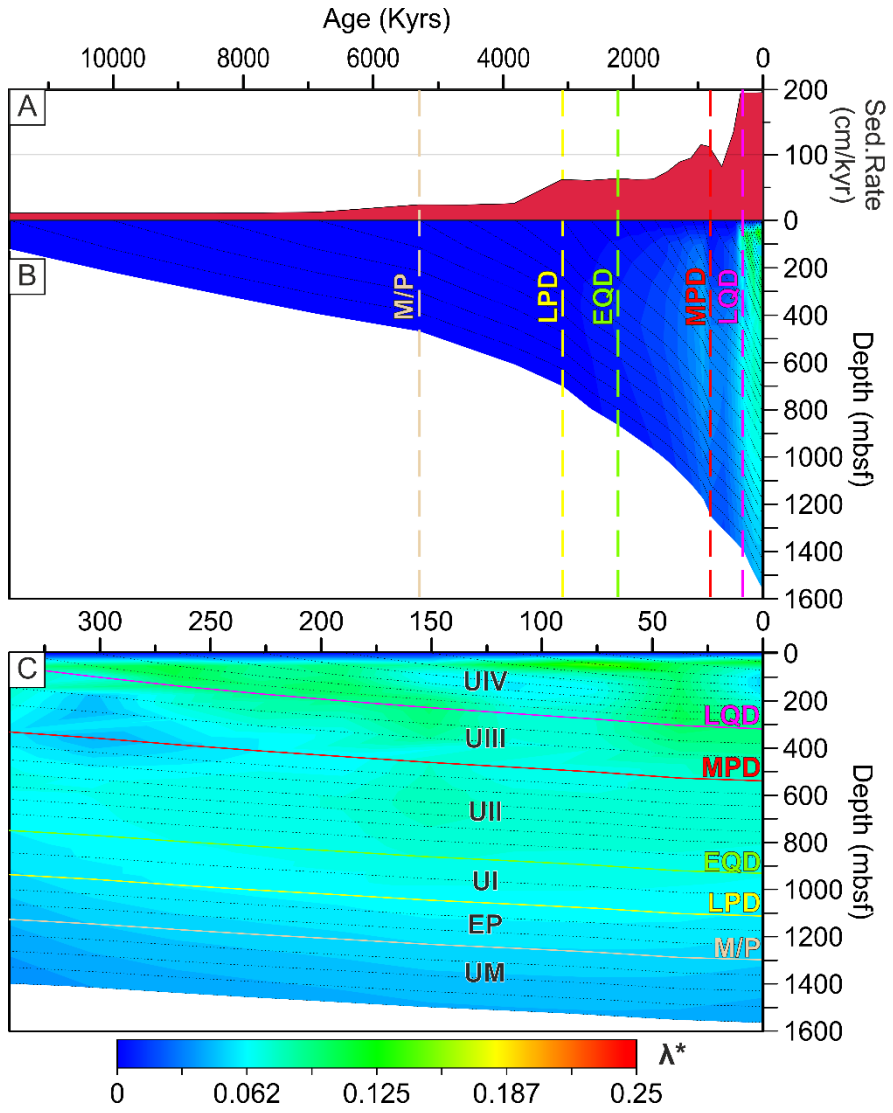

Figure 6.10: (A) Decompacted sedimentation rate at the location of PseudoWell_1 (see locaiton in Figure 6.1 and Figure 6.9C) based on Line_4 model results. (B) Burial history chart plotted together with overpressure ratio evolution through time at the location of PseudoWell_1. (C) Zoom in the burial history and overpressure ratio evolution during deposition of Unit IV (last 341 kyr). M/P: Miocene/Pliocene; LPD: Late Pliocene Discontinuity; EQD: Early Quaternary Discontinuity; MPD: Middle Pleistocene Discontinuity; LQD: Late Quaternary Discontinuity. UIV to UI: Unit IV to Unit I; EP: Early Pliocene Unit; UM: Upper Miocene.

6.5 Line_5

Between all the 2D models adopted in this study, Line_5 is the one that better represents the morphological and structural complexities of the study area. Built following the MCS profile BS21, Line_5 crosses the Marquês de Pombal Plateau following a NW-SE direction, entering the

São Vicente Canyon almost perpendicular to its axis and crossing the Marquês de Pombal Fault perpendicular to its orientation (Figure 6.1).

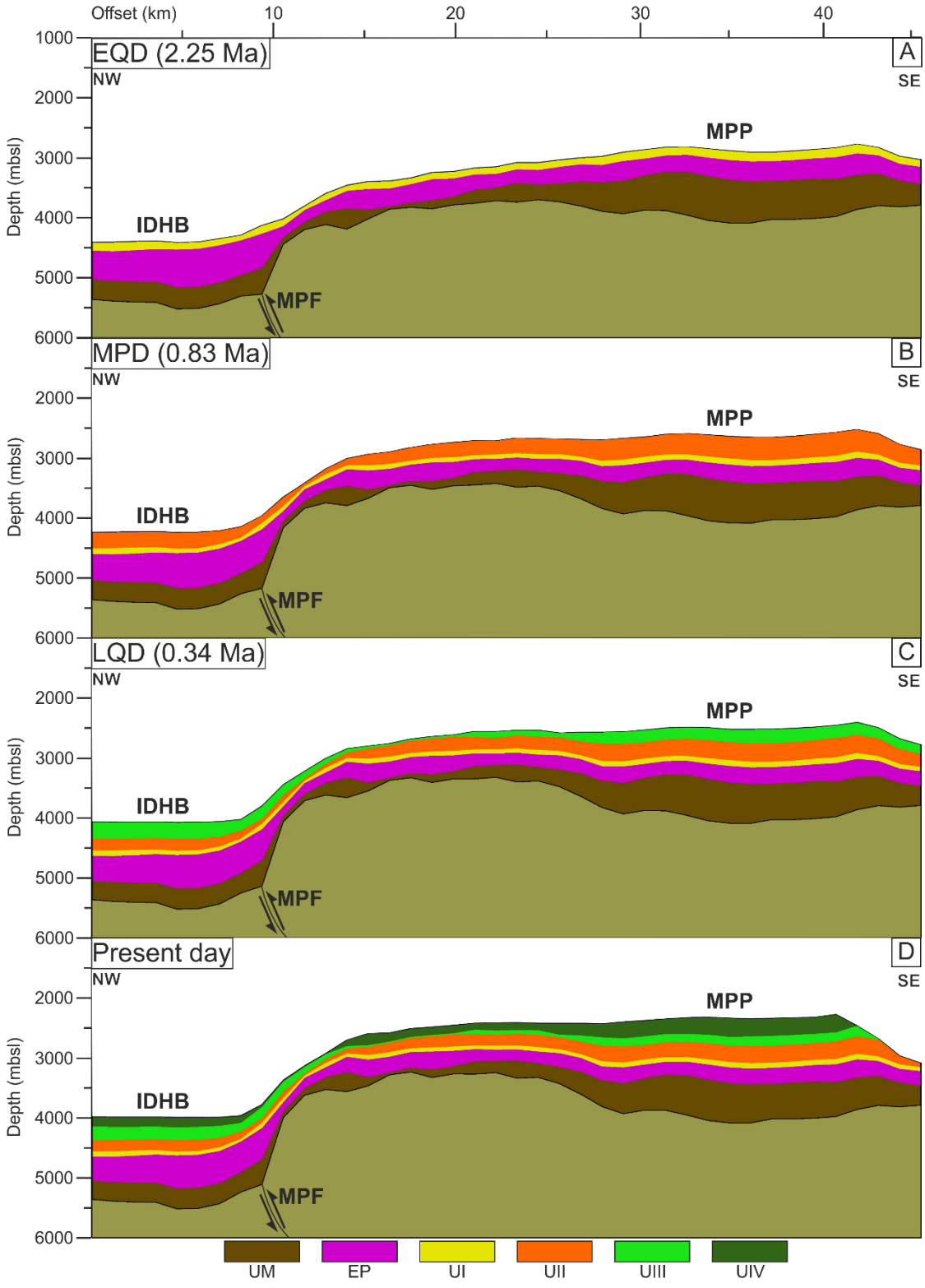

Figure 6.11: Stratigraphic evolution of the model of Line_5 where displacement along the MPF is simulated. MPF: Marquês de Pombal Fault; MPP: Marquês de Pombal Plateau; IDHB: Infante Don Henrique basin. EQD: Early Quaternary Discontinuity; MPD: Middle Pleistocene Discontinuity; LQD: Late Quaternary Discontinuity.

Figure 6.11 shows four stratigraphic evolution steps of the model (corresponding with EQD, MPD, LQD and present day) during the last 2.25 Ma of simulation. As it was explained for Line_1 model in section 6.1, the fault movement in BASIN is modelled as a simple displacement of the basement, while the fault plain displacement of overlying strata is taken into account by the input stratigraphic pattern. Line_5 crosses the Marquês de Pombal Fault perpendicular to its axes, and it allows the best visualization of the deformation. The displacement of the Marquês de Pombal thrust, which started in the Pliocene, is modelled with a constant slip rate of 0.33 mm/yr. The erosion on the São Vicente Canyon is assumed constant through time, and in this profile shows an average rate of erosion of 2.10 m/kyr within the 10 timesteps composing Unit IV. At the end of the simulation, erosion affects Units II and III, while deposition of Unit IV in the canyon area does not take place (Figure 6.11D). The shallower area of the model is represented by the northwest flank of the São Vicente Canyon (~2300 mbsl), while at the foot of the Marquês de Pombal Fault the water depth reaches almost 4000 m. The model crosses a peripheral part of the depocenter associated with Unit IV (Figure 6.1), where the maximum thickness of the unit reaches 315 m (Figure 6.11). In the proximity of the Marquês de Pombal Fault the sediment type within Unit IV shifts from the "Mixed System" type to a blend dominated by the "Clay" and "Silt" sediment types (Figure 6.12). All the units undergo thinning moving from the Marquês de Pombal Plateau towards the Marquês de Pombal Fault (Figure 6.11).

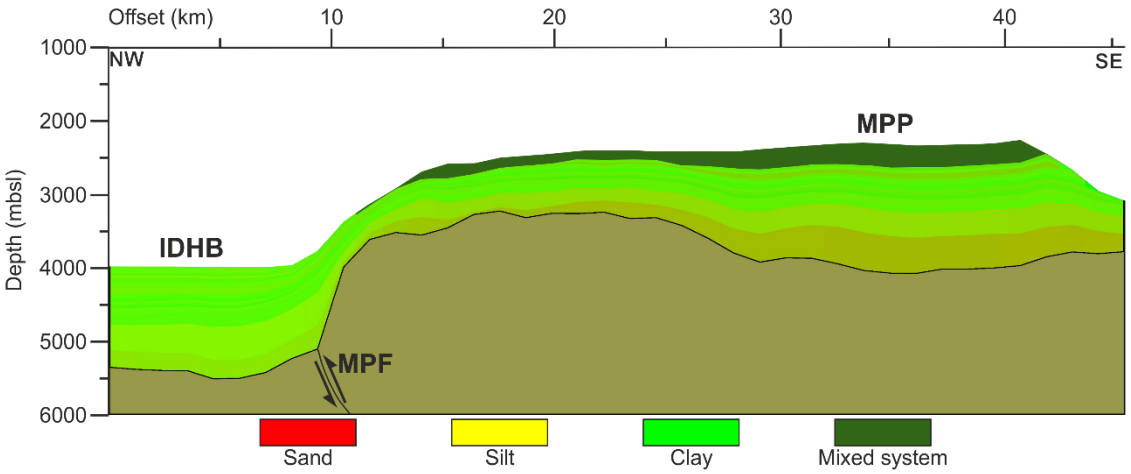

Figure 6.12: Present day sediment distribution of the model along Line_5. MPF: Marquês de Pombal Fault; MPP: Marquês de Pombal Plateau; IDHB: Infante Don Henrique basin.

Porosity at the end of simulation along Line_5 varies from 0.75 at the seafloor to 0.21 in the deepest layers (Figure 6.13A). Compared with the model of Line_1, that shows a similar geometry and orientation, the decrease in porosity with increasing burial depth appears smoother. In both models, however, porosity values are higher close to the Marquês de Pombal Fault (Figure 6.13A). Analogies between the models of Line_1 and Line_5 can also be found in the final hydraulic conductivity distribution, showing values between 10^{-8} to 10^{-10} m/s when moving from the shallower Unit IV to Upper Miocene (Figure 6.13B). Only in the first tens of meters below sea floor, hydraulic conductivity values reach ~10^{-8} m/s because of the little overburden and lack

of consolidation. In both models, a low permeability area (k~10^{-11} m/s) is present within Unit II, Unit I and the uppermost part of Early Pliocene in the Marquês de Pombal Plateau, although this lower hydraulic conductivity area appears thicker in Line_1 than in Line_5 (Figure 6.3B and Figure 6.13B).

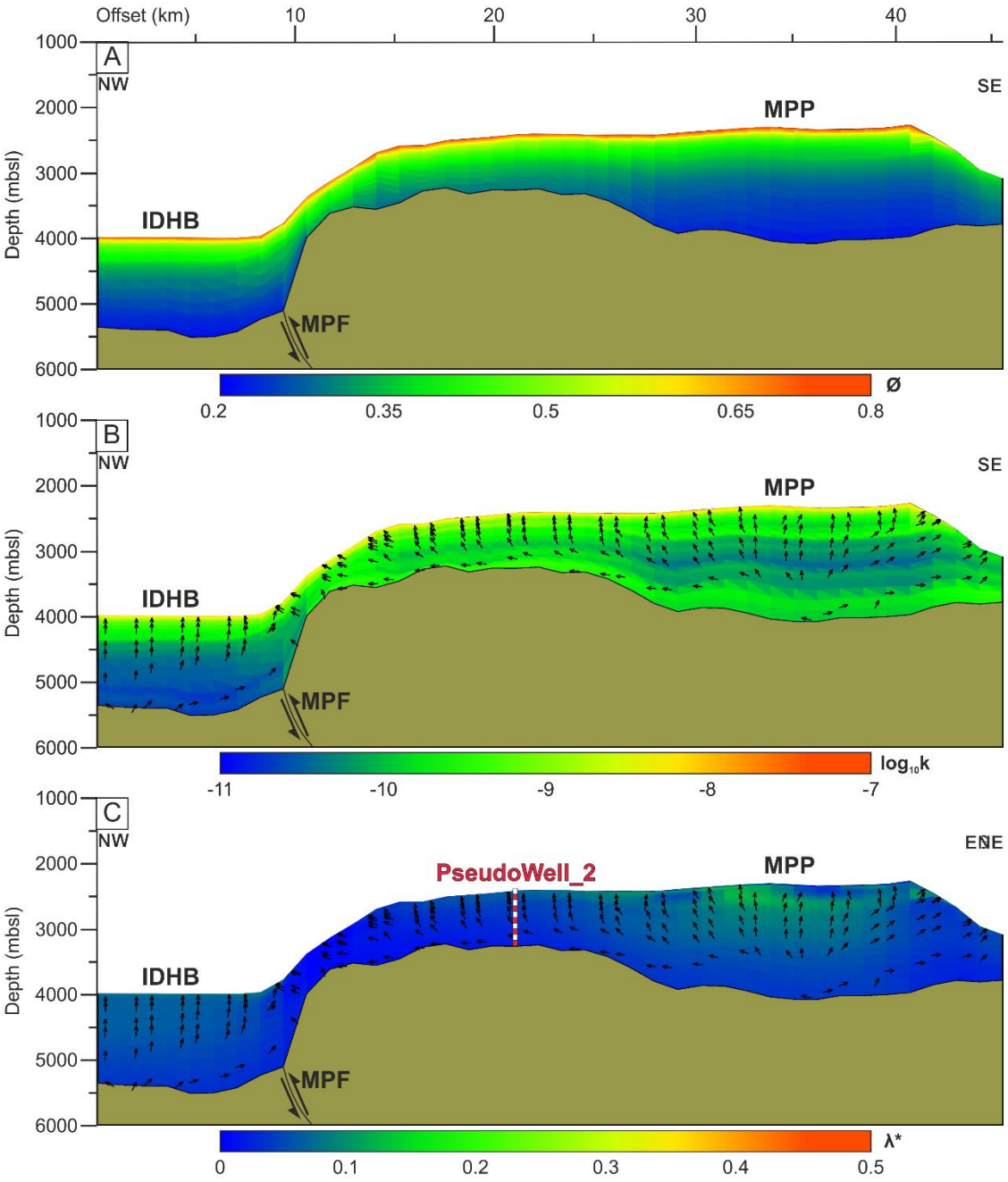

Figure 6.13: Present day (A) porosity, (B) hydraulic conductivity and (C) overpressure ratio along the model of Line_5 . PseudoWell_2 location is reported. MPF: Marquês de Pombal Fault; MPP: Marquês de Pombal Plateau; IDHB: Infante Don Henrique basin.

Simulation results indicate that an overpressure ratio of about 0.1 is estimated in the shallower parts of the Marquês de Pombal Plateau sediments, especially within Units IV and III (Figure 6.13C). Since Line_5 crosses the Marquês de Pombal Fault, a pseudo-well located close to the fault scarp (Figure 6.1 and Figure 6.13) allows to visualize how and if overpressure evolved in the proximity of the fault scarp, from where the Marquês de Pombal MTC, and likely other MTCs,

originated (Figure 4.6 and Figure 4.7) (see section 4.1.4). Unlike what has been observed in PseudoWell_1, located close to the depocenter of Unit IV (Figure 6.10), overpressure does not appear to develop in the sediments close to the Marquês de Pombal Fault until the late Quaternary (Figure 6.14). Sedimentation rate at PseudoWell_2 location increases from 0.27 m/kyr to 0.47 m/kyr with the beginning of Unit II deposition. The increment in sedimentation rate is not followed by overpressure development, which started only with the deposition of Unit IV when it reached λ* = 0.07. During this period, sedimentation rate reaches its maximum values of 0.61 m/kyr (Figure 6.14C).

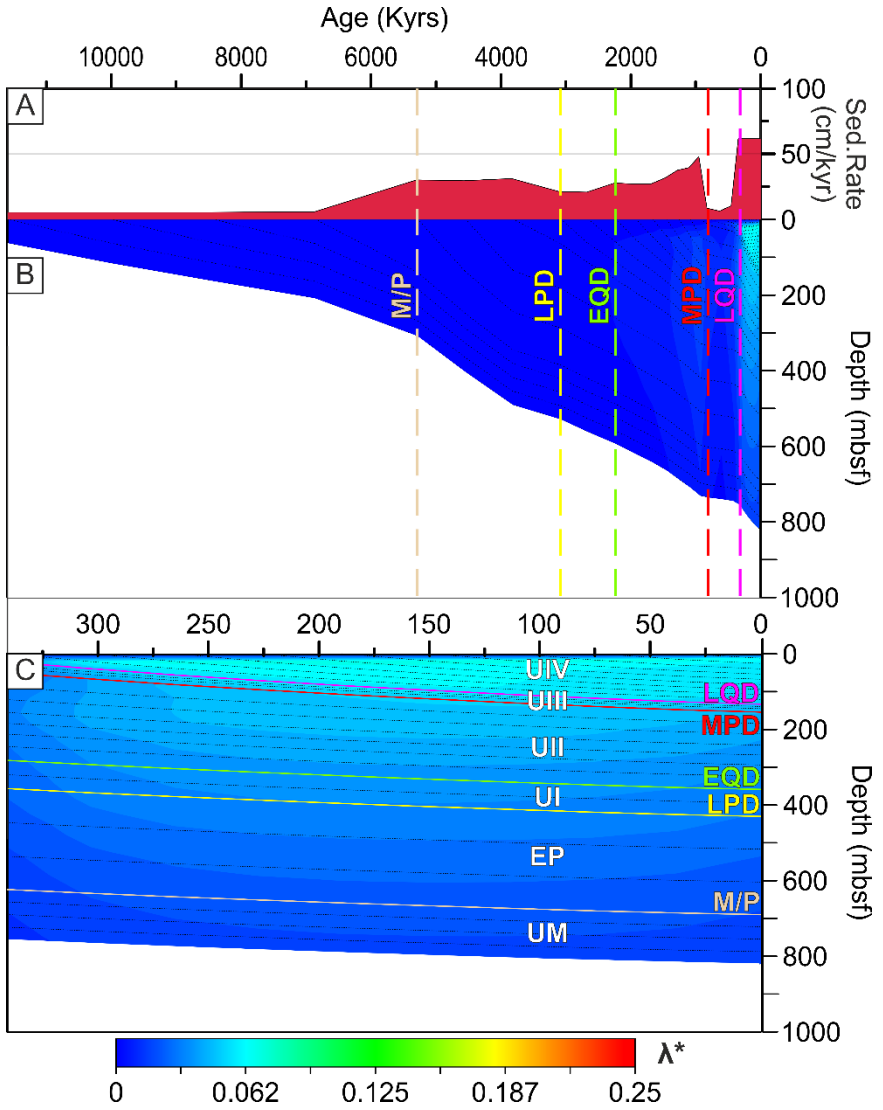

Figure 6.14: (A) Decompacted sedimentation rate at the location of PseudoWell_2 (see location in Figure 6.1 and Figure 6.13C). (B) Burial history chart plotted together with overpressure ratio evolution through time at the location of PseudoWell_2. (C) Zoom in the burial history and overpressure ratio evolution during deposition of Unit IV (last 341 kyr). M/P: Miocene/Pliocene; LPD: Late Pliocene Discontinuity; EQD: Early Quaternary Discontinuity; MPD: Middle Pleistocene Discontinuity; LQD: Late Quaternary Discontinuity. UIV to UI: Unit IV to Unit I; EP: Early Pliocene Unit; UM: Upper Miocene.

PART IV

DISCUSSION

Chapter 7: A mixed turbidite – contourite system related to a major submarine canyon: The Marquês de Pombal Drift

7.1 Down-slope versus along-slope processes in the Marquês de Pombal Plateau: significance of units I to IV

Internal geometries and reflections characteristics of units I to IV described in section 4.1 are interpreted as the result of the interplay between the predominant sedimentary processes in the area and their relative importance through time.

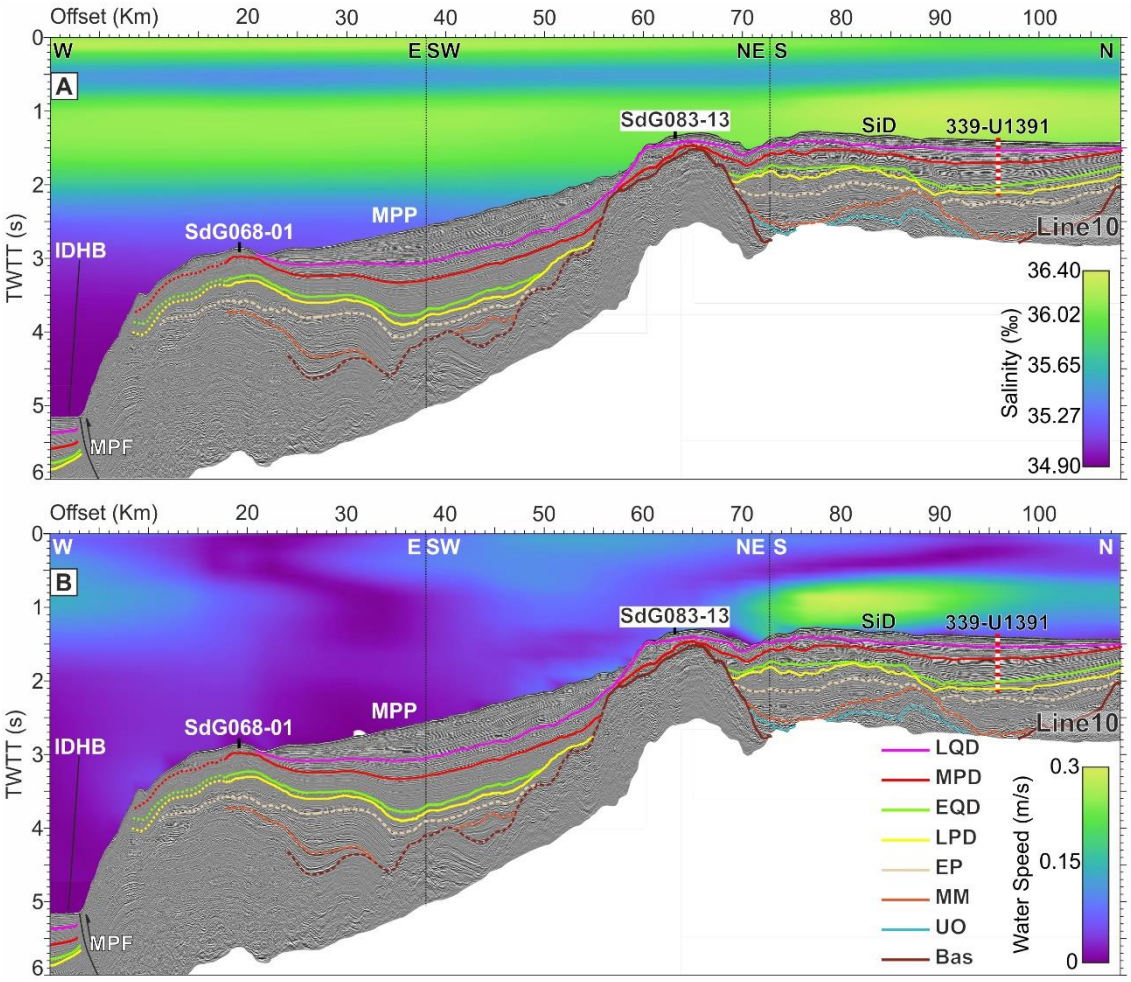

Figure 7.1: Interpreted multi-channel seismic profile INS2-Line10 (see location in Figure 4.1) with (A) water salinity and (B) speed plotted from (Sotillo et al.,2015; Amo et al., 2020). Stratigraphic interpretation follows criteria set by Hernández-Molina et al. (2016a) and Serra et al. (2020). LQD: Late Quaternary Discontinuity (0.4 to 0.3 Ma); MPD: Middle Pleistocene Discontinuity (0.8 Ma); EQD: Early Quaternary Discontinuity (2.4 to 2.1 Ma); LPD: Late Pliocene Discontinuity (3.2 to 3.0 Ma); EP: Early Pliocene; MM: Middle Miocene; UO: Upper Oligocene; Bas: Basement. IDHB: Infante Don Henrique basin; MPF: Marquês de Pombal Fault; MPP: Marquês de Pombal Plateau; SiD: Sines Drift; 339-U1391: IODP Site U1391 location; SdG083-13 and SdG068-01: gravity cores locations; vertical dashed lines correspond to the change in direction of the line (Figure 4.1); vertical exaggeration ~ x7.

In shallow areas, such as the Sines and Sagres drifts (Figure 4.2C and Figure 4.3B), all four Plio-Quaternary units are the expression of contourite sedimentation controlled by the MOW hydrodynamics. Relatively high amplitude reflections are associated with multiple channels, truncation and sediment waves, indicating high-contour current energy conditions (Figure 4.2C and Figure 4.3B). This observation agrees with multiple sand layers, hiatuses and erosional features identified at IODP Site U1391 (Figure 3.9), which have been interpreted as variations in the MOW hydrodynamic regime (Brackenridge et al., 2013; Hernández-Molina et al., 2002; Llave et al., 2007a, 2006; Lofi et al., 2016; Stow et al., 2013b). Present-day water velocity data in these shallow areas (up to 0.3 ms^{-1}) (Figure 7.1B and Figure 7.2B**)**, indicate relatively strong bottom currents that would be able to transport the sediments found over the deeper Marquês de Pombal Plateau (57 to 73% silt dominance) (McCave, 1984; Miller et al., 1977) (Figure 4.9, Figure 4.10, Figure 4.11, Figure 4.12 and Figure 4.13).

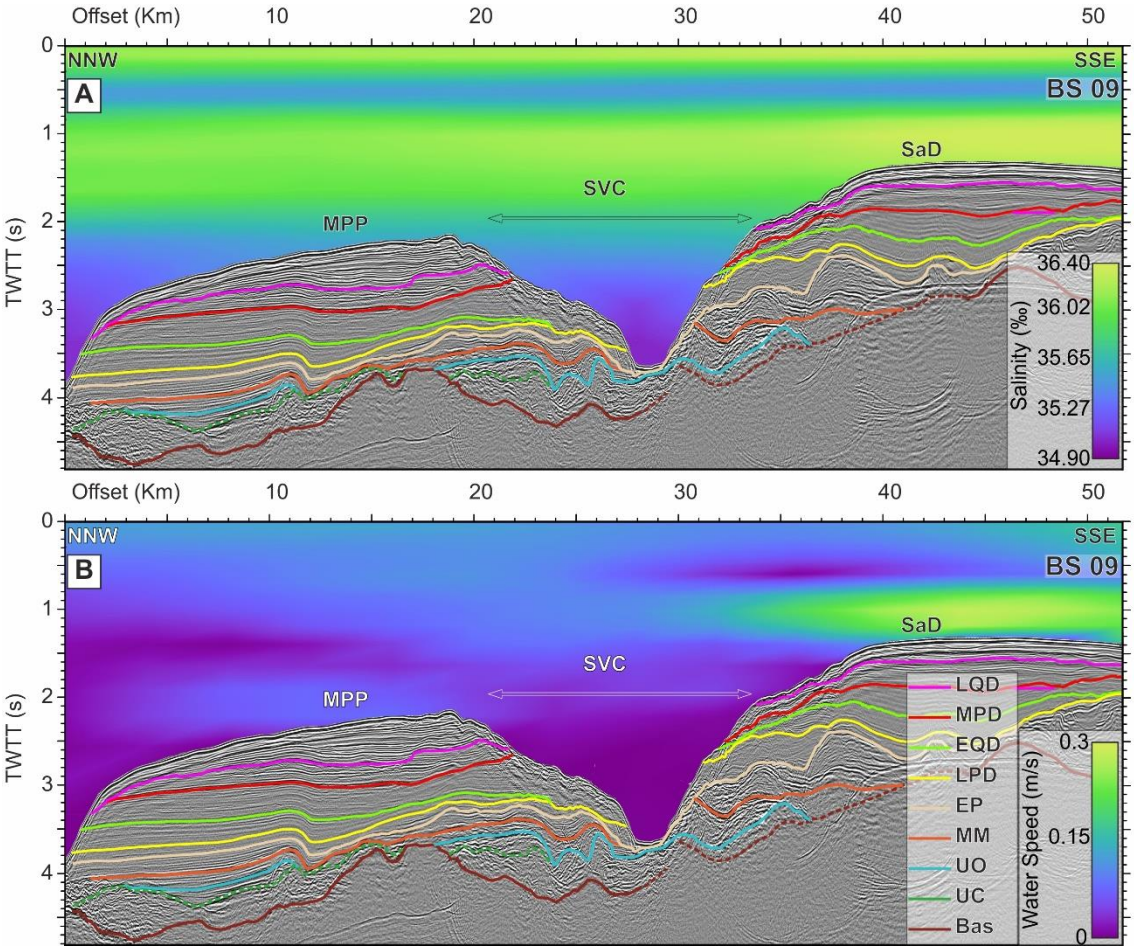

Figure 7.2: Interpreted multi-channel seismic profile BS09 (see location in Figure 4.1) with (A) water salinity and (B) speed plotted from (Sotillo et al.,2015; Amo et al., 2020). Stratigraphic interpretation follows criteria set by Hernández-Molina et al. (2016a) and Serra et al. (2020). LQD: Late Quaternary Discontinuity (0.4 to 0.3 Ma); MPD: Middle Pleistocene Discontinuity (0.8 Ma); EQD: Early Quaternary Discontinuity (2.4 to 2.1 Ma); LPD: Late Pliocene Discontinuity (3.2 to 3.0 Ma); EP: Early Pliocene; MM: Middle Miocene; UO: Upper Oligocene; Bas: Basement. IDHB: Infante Don Henrique basin; MPF: Marquês de Pombal Fault; MPP: Marquês de Pombal Plateau; SiD: Sines Drift; 339-U1391: IODP Site U1391 location; SdG083-13 and SdG068-01: gravity cores locations; vertical dashed lines correspond to the change in direction of the line (Figure 4.1); vertical exaggeration ~ x7.

The transition from contourite sedimentation in the middle slope to that of deeper waters is, however, not so well understood. Beyond 1500 m water depth bottom currents are relatively weak (~ 0.05 ms^{-1}) but thick sedimentary bodies with characteristics compatible with sediment transport by bottom currents are present (Figure 7.1 and Figure 7.2). In this regard, the MCS profiles here presented (Figure 7.1 and Figure 7.2) offer a unique opportunity to image this transition and the interaction of the bottom current with a major sediment pathway such as the São Vicente Canyon. In the Marquês de Pombal Plateau, there is an overall upward increase in amplitude of seismic reflections and a change in seismic facies, which likely indicates the passage from a relatively homogeneous hemipelagic dominated sedimentation into a more energetic environment with increasing abundance of sandier and silty beds (Figure 4.2 and Figure 7.1). This passage is concomitant with development of the São Vicente Canyon, which is mainly Quaternary (Serra et al., 2020).

Units I, II and III show parallel configuration of the reflections, without the clear erosive features that characterize the shallower part of the slope (Figure 4.2 and Figure 7.1). Minor discontinuities are only visible within Units II and III from the perspective provided by profile BS09 (Figure 4.3 and Figure 7.2). This change in stratal architecture is interpreted as the transition from a basinal lower-energy environment to a MOW-dominated deposition. Unit IV displays pinch-out both upslope and downslope accompanied by downlap (at 2.9 to 3 s TWTT; ~ 2200 mbsl) (Figure 4.2B) and onlap of internal reflections (at ~ 2.5 s TWTT; ~ 1800 m water depth), respectively. The sediments collected in water-depths ranging from 2600 to 1000 m (within and outside the present depth range of the MOW) all show homogeneous poorly sorted clayey silts (Figure 4.9, Figure 4.10, Figure 4.11, Figure 4.12 and Figure 4.13). All of these features are diagnostic of contour current-related sedimentation (Faugères and Stow, 2008; Nichols et al., 2020; Nielsen et al., 2008). Further to that, Unit IV hosts the main depocentre in the study area, reaching ~ 500 m in thickness in its central part and a decompacted sedimentation rate of 2 m/kyr (Figure 4.4D, Figure 4.5D, Figure 7.1 and Figure 7.2), which is interpreted as the result of boosted sediment supply and significant turbidity current activity along the São Vicente Canyon. In the Sagres Drift, south-east side of the canyon, Unit IV is ~ 250 m thick, approximately half of the thickness in the Marquês de Pombal Plateau, resulting in an asymmetrical build-up of the slopes adjacent to the canyon (Figure 4.4 and Figure 7.2).

Contour currents are well known to interact with turbidity currents and deposit their finer fraction downstream from the current (Edwards et al., 2018; Fuhrmann et al., 2020; Gong et al., 2013; Lucchi and Rebesco, 2007; Rasmussen et al., 2003; Rebesco et al., 1996). Accordingly, this sedimentary body is interpreted as a mixed turbidite–contourite deep water drift, that has been named Marquês de Pombal Drift. Nevertheless, it should be noted here that the canyon is incised ~ 1.5 km in the continental slope and that turbidity currents therefore travel deeply entrenched,

making the interaction with contour currents more complex (see following section 7.2 for mechanisms facilitating interaction).

In shallow areas of the Marquês de Pombal Plateau, Units III and IV display sediment waves and stratal pinch-out features (Figure 4.2B). These sediment waves extend in water depths between 950 m and 1650 m. A slightly undulated seafloor can be found down to water depths of 1850 m (Figure 4.2B). The slope-parallel orientation of the wave crest suggests sediment mobilization perpendicular to the slope (Ribó et al., 2016; Wynn and Stow, 2002). Similar features in 300 to 500 m water depth have been mapped some kilometres eastward (Mestdagh et al., 2020) and have been interpreted to result from internal waves energy propagating at the interface between the MOW and the AIW. Because of the depth at which sediment waves develop within Unit IV in the Marquês de Pombal Drift, those have most likely developed by internal waves propagating in between the base of the MOW and the underlying NADW (Figure 7.3 and Figure 7.4). Faster sediment accumulation upsequence translates in a number of slope failures within Units III and IV in the Marquês de Pombal Drift, which display as chaotic lenses, interpreted as MTDs (Figure 4.2B). Distribution of MTDs indicates that mass-wasting activity has been particularly intense during periods of erosion/non-deposition linked to enhancement and deepening of the MOW. A similar pattern of occurrence of MTDs has been reported in drifts of the eastern Gulf of Cadiz, such as the Lagos, Portimão and Faro drifts (Marchès et al., 2010; Mulder et al., 2006, 2003) (Figure 4.1).

Multiple studies suggest that the main MOW core flows, at present, above 1500 m water depth along the northern part of the Gulf of Cadiz (Hanquiez et al., 2010; Hernández-Molina et al., 2014b; Llave et al., 2011, 2007b; Lofi et al., 2016; Mulder et al., 2003; Stow et al., 1986). Present day water velocity data (Figure 7.1 and Figure 7.2) show that, at depths greater than 1900 m (2.4 s TWTT), the water current speed is as low as 0.03 ms^{-1}, which is only one tenth of the speed reached in the shallower Sines or Sagres Drift areas (Figure 7.1 and Figure 7.2). The transport capacity of such slow bottom currents is not enough to transport the type of sediments found in the Marquês de Pombal Plateau (Figure 4.9, Figure 4.10, Figure 4.11, Figure 4.12 and Figure 4.13). However, the ML is estimated to settle in 2000 m water depth during glacial periods (Rogerson et al., 2012a, 2012b; Schönfeld et al., 2003; Schönfeld and Zahn, 2000) (Figure 7.4), resulting in enhancement of bottom currents over the Marquês de Pombal Plateau. Under these conditions, the MOW is capable of transporting sediment along most of the Marquês de Pombal Plateau. Enhancement and deepening of the ML also resulted in increasing number of erosion/non-deposition events and changes in reflections configuration (parallel to slightly wavy and onlaps) (Figure 4.2B and Figure 4.3B). This trend is probably linked to the longer duration and increased amplitude of sea-level oscillations after the Mid-Pleistocene Transition (Clark et al., 2006; Miller et al., 2005; Zachos et al., 2001). The erosion/non-deposition horizons indicate

that current velocities could intermittently exceed the value of 0.2 m/s, that marks the switch from depositional to erosional behaviour of the ML (Stow et al., 2009).

7.2 Mechanisms of interaction between the Mediterranean Outflow Water and sediment gravity flows along the São Vicente Canyon

The position of the late Quaternary deposit right on the slope north-west of the São Vicente Canyon, downstream from the MOW current orientation, suggests that interaction between sediment gravity flows within the canyon and the MOW could be responsible for its deposition. The retrogressive erosion that led to the incision of the São Vicente Canyon upper sector (Figure 4.1) is also coeval with deposition of Unit IV (Serra et al., 2020). Such retrogressive erosion triggered intense turbidity current activity that discharged sediments from the shallower part downslope, as confirmed by compositional analysis of piston cores collected in the Horseshoe Abyssal Plain (Lebreiro et al., 1997). This activity continues to present, as sand and gravel deposits imaged in TOBI sidescan sonar data along the canyon thalweg (Serra et al., 2020; Vizcaino et al., 2006) indicate active sediment transport. Turbidity current activity within the canyon is also demonstrated by erosive bedforms such as grooves and scours, implying a minimum current speed between 1.0 and 2.5 ms^{-1} (Serra et al., 2020).

The question that remains is nevertheless how the MOW can incorporate sediment from turbidity currents that travel within a canyon such as the São Vicente Canyon incised up to 1.5 km within the continental slope. The height of the canyon flanks clearly exceeds the maximum height of sediments brought to suspension by any observed turbidity current (Azpiroz-Zabala et al., 2017; Liu et al., 2012; Paull et al., 2018), which typically do not exceed a few hundred metres. In the absence of hydrographic transects with measurements of suspended sediment concentration and/or time-series of moored sensors, several mechanisms by which sediment travelling along the São Vicente Canyon could be incorporated in the ML and Marquês de Pombal Drift afterwards are envisioned. All of these mechanisms require a density contrast in between water masses, here namely the MOW and NADW, along which a nepheloid layer can form with the finer sediment fraction detaching from the bottom of the canyon (de Stigter et al., 2011; Ribó et al., 2013) (Figure 7.3 and Figure 7.4).

First is the occurrence of classical turbidity currents within the canyon, where the most dilute part of the flow, upon encountering the density contrast in between the MOW and NADW, would form a nepheloid layer spreading out of the canyon and incorporated in the ML (Figure 7.3A and Figure 7.4). Evidence of nepheloid layers associated with the MOW has been found further north on the Lisbon-Setúbal Canyon.

Second, the strong density gradients at the boundaries of the MOW are thought to favour internal wave activity and sediment resuspension (McCave and Hall, 2002). It is well-known that submarine canyons trap internal wave energy, which drives elevated turbulence and mixing (e.g.

Kunze et al., 2002; Puig et al., 2004). Re-suspended sediment could be temporarily incorporated in the ML and redeposited in the Marquês de Pombal Drift (Figure 7.3B and Figure 7.4).

Third, most works assume that the MU is geostrophically balanced at present. However, Ochoa & Bray (1991) and Marchès et al. (2007) report that several branches flow down small local canyons and eventually re-join the main branch halfway to Cape São Vicente. Schönfeld & Zahn (2000) report increased MOW density during glacial maxima and periods of intensified MU extending to 1200 m water depth. If the flow (or the lower part of it) had (or still has) some density-driven component near the São Vicente Canyon, ageostrophic effects could be important. Hence, part of the MU (likely the denser lower part) could sink in the canyon and re-join the lower core at its neutral buoyancy level (Figure 7.3C and Figure 7.4).

Fourth, if the MU is primarily geostrophic, but is able to entrain enough sediment in suspension, the potential exists for the near-bed water column to gain density and sink in the canyon. Given the lack of major fluvial inputs around Cape São Vicente, sediment supply to the MU mostly results from processes in the benthic boundary layer and have a significant seasonal component (Figure 7.3D and Figure 7.4). As the head of the São Vicente Canyon is located a mere 10 km from the coast and 200 m below sea level, on the MOW pathway (Figure 4.1), it is likely that the MU could be trapped in the canyon given the last two hypotheses (Figure 7.4). Fonnesu et al. (2020), Fuhrmann et al. (2020) and Miramontes et al. (2020) show that contour currents can winnow the finer part of a turbidity suspension cloud. In the model presented here, the interaction between turbidity currents travelling along the São Vicente Canyon and the MOW is mediated by a nepheloid layer, with the suspended sediment being deflected towards the north-west side of the canyon, downstream from the MOW, and ultimately deposited at the top of the Marquês de Pombal Drift (Figure 7.4 and Figure 7.5).

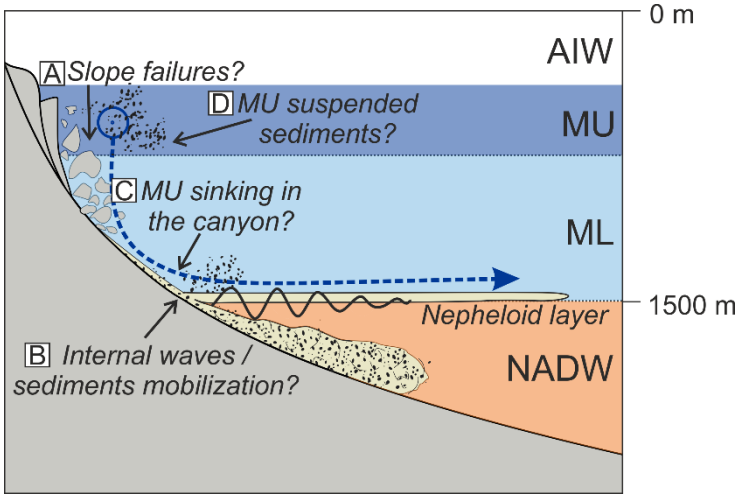

Figure 7.3: Schematic 2D representation of the potential processes contributing to feed nepheloid layer within the São Vicente Canyon. (A) sediment suspended by retrogressive erosion processes and feeding turbidity currents; (B) Sediments mobilized by internal waves activity; (C) partial MU capturing processes and interaction with the seafloor; (D) Sediment suspended within the MU.

Evidence linking the turbidity currents travelling along the São Vicente Canyon and the Marquês de Pombal Drift is provided by the dolomite present in the terrigenous fraction of the sediments collected from the drift (Garcia-Orellana et al., 2006) (Figure 4.1). At IODP Site U1391, dolomite rich sediments were recovered from Units I and II, as dolomite diagenesis was associated with depositional hiatuses during the LPD and EQD (Hernández-Molina et al., 2016a; IODP Expedition 339 Scientists, 2013c; Stow et al., 2013a). The stratigraphic interpretation of the area reveals that Unit I and II in the Alentejo basin are exposed only at the head and flanks of the São Vicente Canyon, where erosion reaches the early Pliocene (Figure 4.3B). Thus, mineral composition indicates that the sediments at the top of the late Quaternary Marquês de Pombal Drift belong to older stratigraphic units (Unit I and II), eroded during the canyon formation.

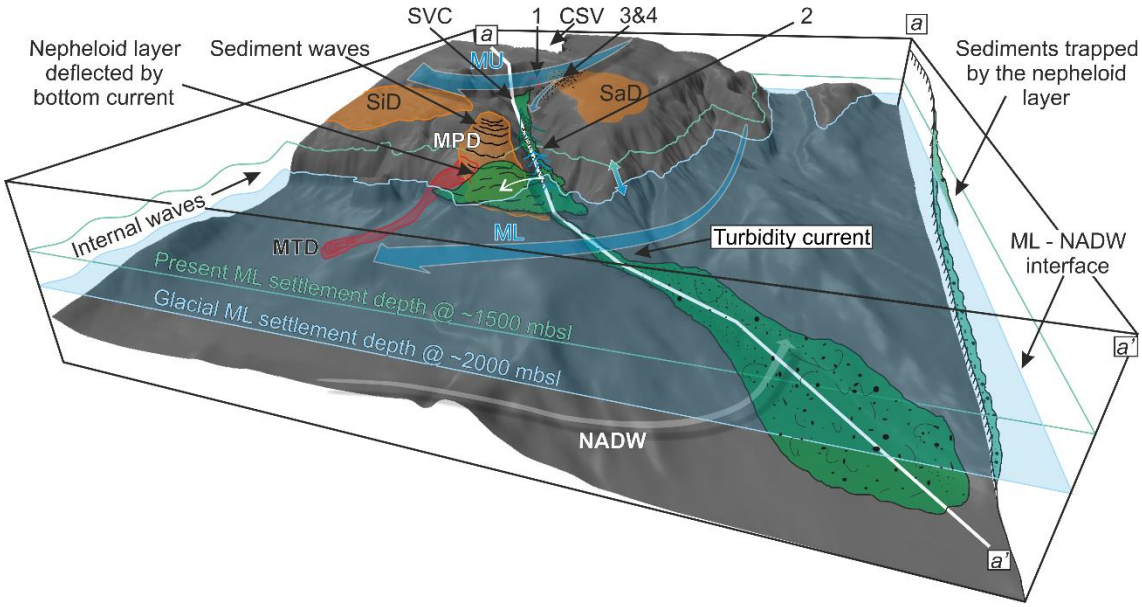

Figure 7.4: Schematic representation of potential types of indirect interaction between the MOW and the sediment travelling along the São Vicente Canyon displayed during a glacial period. 1: Classical turbidity currents; 2: internal waves trapped in the canyon inducing sediment resuspension; 3: the denser lower part of the MOW upper core (MU) sinks in the canyon and rejoins ML at its neutral buoyancy level; 4: the MU entrains sediment in suspension, the near-bed water column gains density and sinks in the canyon. All of the scenarios require the formation of a nepheloid layer between the MOW and NADW along which the sediment finer fraction detached from the bottom of the canyon is incorporated in the MOW lower core (ML). White line along a-a' displays 2D section of sediment gravity flow and intermediate nepheloid layer on the side of the block diagram. CSV: Cape São Vicente; MPD: Marquês de Pombal Drift; SaD: Sagres Drift; SiD: Sines Drift; SVC: São Vicente Canyon; MU: MOW upper core; ML: MOW lower core; NADW: North Atlantic Deep Waters.

Features diagnostic of mixed turbidite–contourite systems such as regular uni-directional, low-angle, offset stacking of channels and lobe complexes (Fonnesu et al., 2020; Fuhrmann et al., 2020) and smooth slopes upstream of the bottom current (Rebesco et al., 1996) are not found in the mixed turbidite – contourite system of the Marquês de Pombal Drift. The steep slope of the northern flank of the São Vicente Canyon (Figure 4.3B) is rather a result of intense erosional processes along the canyon, while its position is locked within a syncline between two major thrust faults (Serra et al., 2020). Mixed turbidite – contourite depositional systems developing in channel–levée systems have been widely recognized (Fonnesu et al., 2020; Gong et al., 2013; He

et al., 2013; Hernández-Molina et al., 2016b; Michels et al., 2001; Rebesco et al., 1996; Sansom, 2018). However, in all previous cases, direct interaction between turbidity currents and contour currents was made possible because the incision was not deep, allowing turbidity current overbanking with consequent migration of the channels upstream from the contour current (e.g. Gong et al., 2013; Fuhrmann et al., 2020).

The morphological and depositional differences found in between the Marquês de Pombal Drift and those of previous studies might require introducing a new mixed turbidite – contourite depositional model. While previously mentioned studies refer to syn-depositional interaction within the turbidity currents, this case is better described as a syn-erosional to syn-depositional interaction between turbidity currents affecting submarine canyons and contour currents. In this model, contour currents capture the finer-grained component of turbidity currents within submarine canyons via nepheloid layers and deposit this sediment on the slope adjacent to the canyon downstream from the contour current (Figure 7.4 and Figure 7.5).

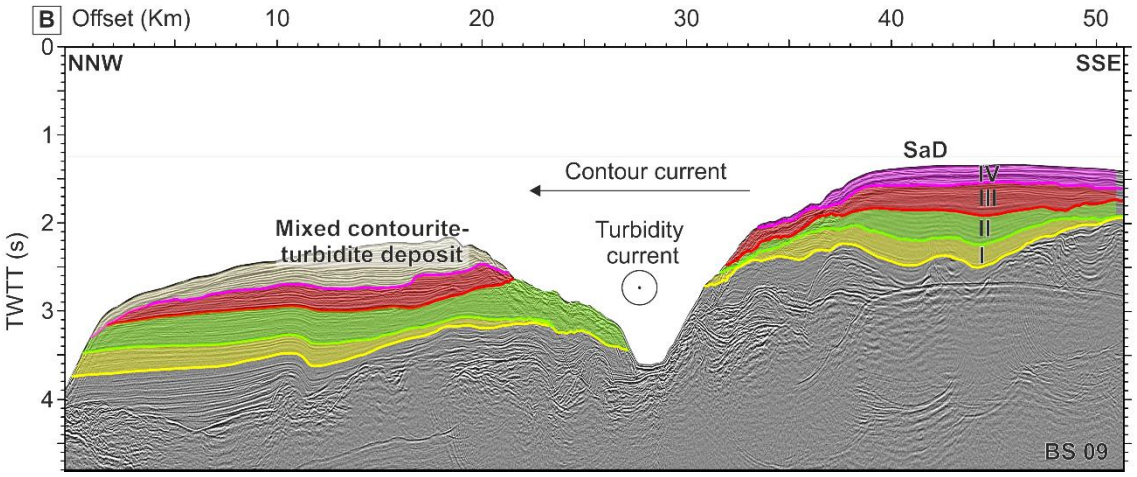

Figure 7.5: Interpreted cross section of the São Vicente Canyon from multi-channel seismic profile BS09 (see location in Figure 4.1) showing position and size of the drift deposit generated by the mixed turbidite - contourite system. I, II, III and IV correspond to the different units defined in this study; SaD: Sagres Drift; SVC: São Vicente Canyon; vertical exaggeration ~ 4.

Flume tank experiments (e.g. Cossu et al., 2010, 2015) and direct observations (e.g. Peakall et al., 2012) show that the Coriolis force may also have a significant influence in asymmetrical deposition within levées in channel–levée systems, especially at high latitudes. Asymmetrical deposition in these levées departs from the assumption that the levée height provides an indication of the flow depth (Bowen et al., 1984). However, given that the São Vicente Canyon is incised to a depth of between 1000 m and 1500 m in the depth range of the Marquês de Pombal Drift, turbidity currents along the canyon are likely to be fully contained within the canyon. Therefore, it seems unlikely that the Coriolis force alone could have a significant role in the development of the Marquês de Pombal Drift.

Although mixed turbidite-contourite depositional systems developing in channel-levée systems have been extensively documented (e.g. Rebesco et al., 1996; Michels et al., 2001; He et al., 2013;

Sansom, 2018; Fonnesu et al., 2020; Fuhrmann et al., 2020), in this study we demonstrate that they can also develop in deeply incised canyons if the interaction is mediated by the presence of a nepheloid layer. Bottom currents worldwide are linked to water masses that offer density contrasts along which nepheloid layers can form. Therefore, the depositional dynamics described in this study could potentially take place in other canyons crossing the path of a contour current. Also, because submarine canyons are the major sediment pathway in most continental margins, such sedimentary dynamics could have a significant role not only in along-slope sediment transport worldwide, but also in the stability of nearby slopes.

7.3 Mass wasting events in the Alentejo basin Significance for submarine slope instability

The Alentejo basin is an area subject to multiple mass failures (Collico et al., 2020; Ford et al., 2021; Gràcia et al., 2010; Minning et al., 2006; Neves et al., 2016; Teixeira et al., 2019; Urgeles and Camerlenghi, 2013). Figure 7.6 shows that a number of these failures detached from the outer flanks of the Sines and the Marquês de Pombal drifts. The smaller landslides from the Sines Drift evolve towards the São Vicente Canyon (Serra et al., 2020), but a majority of the larger failures evolve from the W outer edge of the Marquês de Pombal Drift in the hanging wall block of the Marquês de Pombal Fault, towards the Infante Don Henrique basin (Figure 7.6). Within this basin, at the foot of the Marquês de Pombal Fault, multiple overlapping MTDs have accumulated since the LPD (Figure 4.7). The most recent event is the Marquês de Pombal mass transport complex, which extends from the hanging wall to the footwall of the Marquês de Pombal Fault (Gràcia et al., 2010, 2003b, 2003a; Minning et al., 2006; Vizcaino et al., 2006) (Figure 7.6). The fact that thickness and sedimentation rate maps display high accumulation rates in the Infante Don Henrique basin, especially in Units III and IV (Figure 4.4C and D, Figure 4.5C and D), might indicate that MTDs are abundant in the basin, within the time frame of deposition of these units (831 ka to Present). An additional 202 km^2 MTD originating from the NW edge of this drift has been mapped in the western part of the Infante Don Henrique basin (Figure 7.6). Further to the landslides originating in the drift, the Infante Don Henrique basin also records slope failures from the NE flank of Gorringe Bank (Figure 7.6**)**.

The fact that this area displays relatively high seismicity (Martínez-Loriente et al., 2018, 2013; Silva et al., 2017; Stich et al., 2005) and the spatial relationship between recurrent slope failures and the Marquês de Pombal Fault implies that earthquakes likely played a major role in the observed slope failures (Figure 2.1). Nevertheless, there is also a spatial relationship between the base of the Marquês de Pombal Drift and many of the observed landslides (Figure 7.6). We suggest that the sedimentation rates of up to 2 m/kyr along this body during the late Quaternary played a role in the stability of the sediments in the area (Figure 7.6). The Marquês de Pombal mixed contourite-turbidite system is dominated by fine-grained sediments, which are usually associated with low permeability. Rapidly-deposited, localized sediment bodies constituted by

low-permeability sediments may have a dramatic influence in overpressure build up of the underlying units, particularly if permeable pathways exist in these underlying units along which fluids can be laterally transferred (Llopart et al., 2019; Mencaroni et al., 2020; Revil et al., 1998; Sammartini et al., 2019; Urgeles et al., 2010). As such, we see the build up of overpressure due to the high sedimentation rates as the most straightforward pre-conditioning factor for mass failure in the area (Figure 7.6**)**. The modelling results presented in Chapter 6 have been used to test this hypothesis.

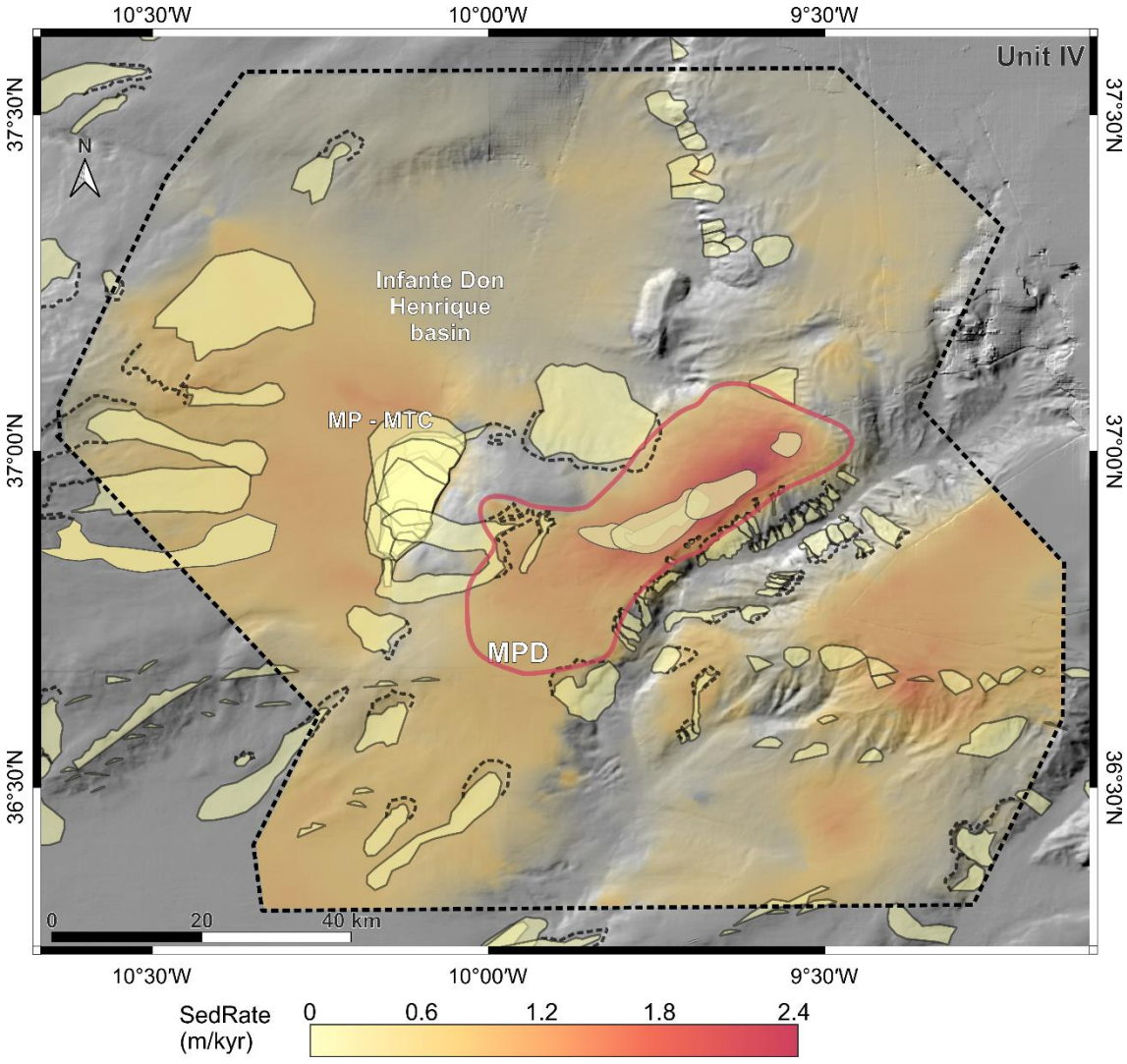

Figure 7.6: Location and extent of MTDs (yellow polygons) and scars (black dashed lines) within the area of interest plotted together with sedimentation rates of the late Quaternary Unit IV. MP – MTC: Marquês de Pombal Mass Transport Complex. Red outline shows the approximate areal distribution of the Marquês de Pombal Drift (MPD).

Chapter 8: Factors influencing overpressure development in the Alentejo basin

The late Quaternary Marquês de Pombal Drift increased the decompacted sedimentation rate in the Marquês de Pombal Plateau up to 2 m/kyr. Given the fine-grained sediment nature of the Marquês de Pombal Drift some amount of overpressure could develop in the area (Gibson, 1958), implying potentially favourable conditions for slope instability, particularly during the late Quaternary. Such hypothesis was already suggested by Neves et al. (2016) and Teixeira et al. (2019) for the shallower part of the Alentejo basin. However, none of the previous work tried to quantify the magnitude of overpressure development, especially considering the increased sedimentation rates induced by deposition of the Marquês de Pombal Drift.

As it has been explained in section 3.4, depending on the aim of the study and on the depositional scenario, overpressure modelling can be performed in 1D, 2D or, ideally, 3D. 1D hydrogeological models are adopted to reproduce the overpressure development in flat areas with a stratigraphy characterized by horizontal units maintaining their relative thicknesses and sediment distribution over long distances (Figure 8.1A). Although this is an unrealistic scenario in real world depositional settings, 1D overpressure simulation are adequate for synthetic models aiming to evaluate how physical properties and sedimentation rates influence the development of overpressures (Dugan and Flemings, 2000; Mencaroni et al., 2020; Revil et al., 1999).

2D hydrogeological models can be adopted to calculate the fluid flow along continental margins where changes in unit thicknesses or properties take place along a slope and the geometry and composition of the units remains relatively constant perpendicularly to the model direction (Figure 8.1B) (Hustoft et al., 2009; Kvalstad et al., 2005; Llopart et al., 2021, 2019; Orange et al., 2003; Urgeles et al., 2010; Urlaub et al., 2013, 2012). If the geometry of the continental margin is relatively complex and/or the subsurface stratigraphy has considerable variations in thickness in both X and Y space dimensions and/or significant compositional changes occur in these two dimensions, a 3D hydrogeological model should be considered. Such models are computationally demanding and difficult to set up. In the Marquês de Pombal Plateau, the presence of morphological elements such as the São Vicente Canyon or the Marquês de Pombal Fault, lateral heterogeneities in the units and different slope gradients, would ideally require 3D hydrogeological modelling to tackle those potential flow perturbations and achieve reliable overpressure estimations (Figure 8.1C). However, as explained in section 3.4, 3D overpressure modelling at the scale of a large marine basin has been performed to study overpressure only within deep, consolidated rock formations (Borge and Sylta, 1998; Broichhausen et al., 2005). Coupling compaction and fluid flow in unconsolidated sediments at the basin scale, in fact,

implies computational limitations that cannot be overcome on regular desktop computers at present.

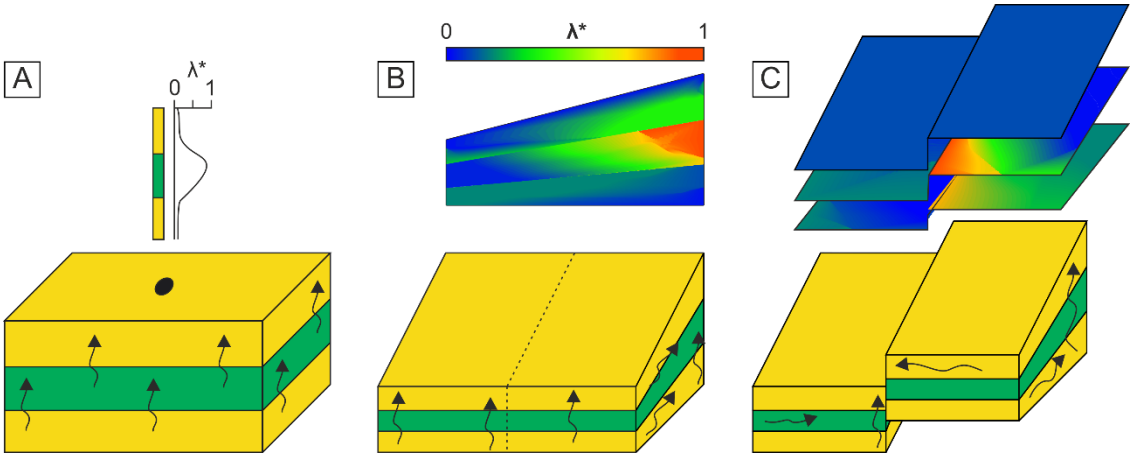

Figure 8.1: Conceptual fluid flow scenarios that could be modeled by adopting (A) 1D models, (B) 2D models and (C) 3D models.

In order to circumvent these computational limitations, the 5 FEM hydrogeological models presented in Chapter 6 have been adopted to reproduce different elements that could affect fluid flow within and around the Marquês de Pombal Plateau and to visualize their influence on overpressure development through time. We use the results from these models to also assess whether the 2D assumption is valid or 3D hydrogeological models are required.

8.1 Influence of stratigraphic and morphological elements in the overpressure development

8.1.1 How does the Marquês de Pombal Drift deposition influence overpressure development?

Line_2 and Line_4 are the two models located closer to Unit IV depocenter, allowing the best visualization of the influence of the Marquês de Pombal Drift deposition on the overall fluid flow and overpressure development in the Marquês de Pombal Plateau. The maximum overpressure ratio values in the models (~0.2) are found in the proximity of the depocenter of Unit IV and develop within the shallowest units (Unit IV and Unit III), progressively decreasing towards deeper sediments (Figure 6.7C and Figure 6.13C). The overpressure generating within the two uppermost units is associated with vertical fluid flow, while in deeper units higher permeability associated with greater sand presence allows horizontal flow and overpressure do not develop.

The lateral distribution of overpressure within the two uppermost units is not regular: in some areas, overpressures developed within the deeper part of Unit IV and Unit III, while in other sectors they are focused in very shallow depths below the seafloor. The distribution of overpressure areas is also variable in time, changing their relative position at different timesteps of the late Quaternary (Figure 8.2).

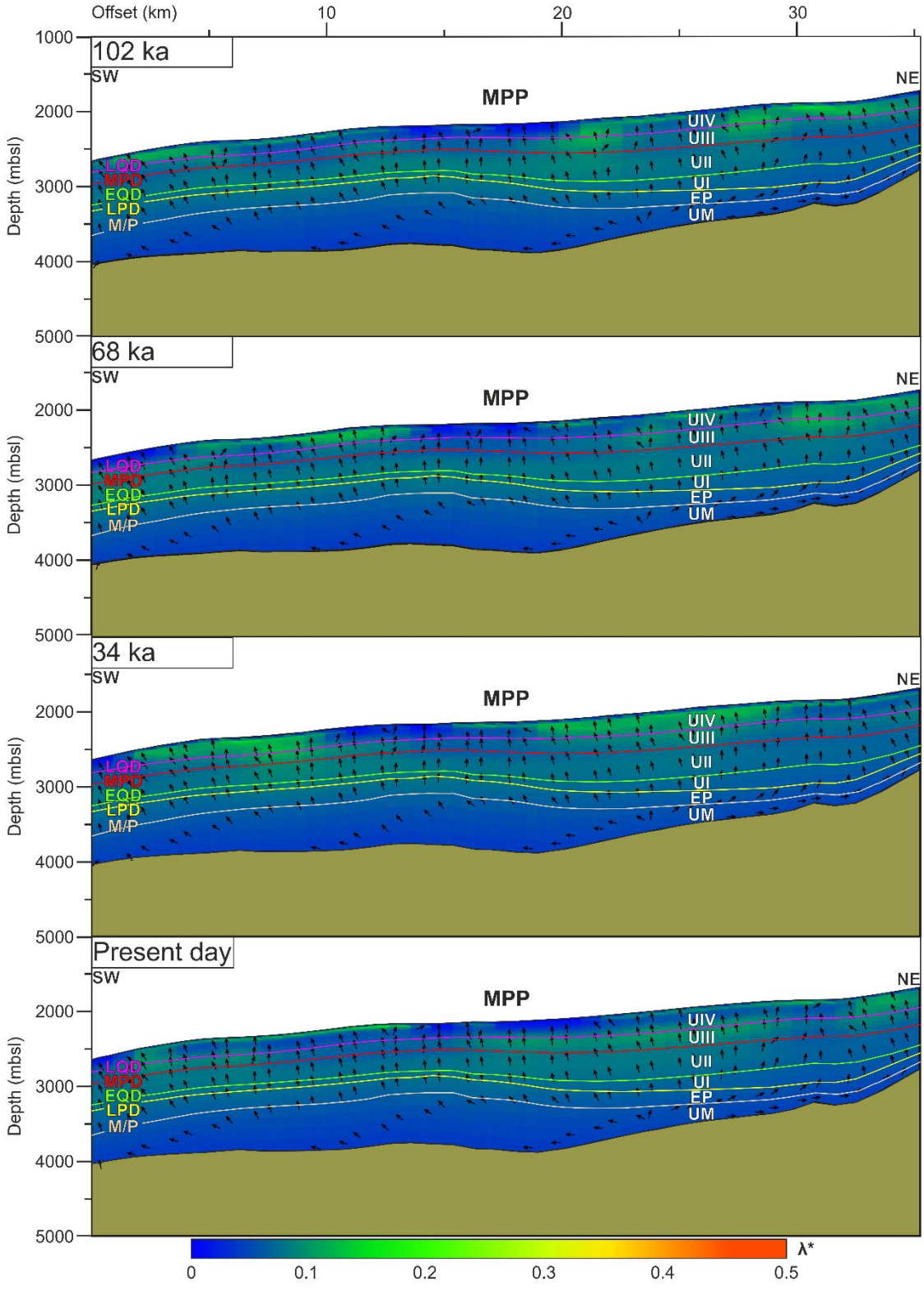

Figure 8.2: Late Quaternary overpressure ratio evolution along Line_4. This profile shows how through deposition of Unit IV the maximum overpressure ratio does not exceed ~0.2, but the location of overpressure areas close to the seafloor changes. M/P: Miocene/Pliocene transition; LPD: Late Pliocene Discontinuity; EQD: Early Quaternary Discontinuity; MPD: Middle Pleistocene Discontinuity; LQD: Late Quaternary Discontinuity. UIV to UI: Unit IV to Unit I; EP: Early Pliocene Unit; UM: Upper Miocene. MPP: Marquês de Pombal Plateau.

The relatively homogeneous distribution of lithostatic load by the Marquês de Pombal Drift along Line_4 maintains porosity and permeability values continuous along the profile (Figure 6.13A and B), resulting in continuous areas of vertical fluid flow and overpressure development, especially within Unit IV and Unit III (Figure 6.13C and Figure 8.2).

The modelling results show that overpressure generated after the Marquês de Pombal Drift deposition reaches ~20% of the lithostatic load. The influence of the increased sedimentation rates characterizing the Marquês de Pombal Drift is shown at PseudoWell_1, where the vast majority of the overpressure started to develop since deposition of Unit IV and is sustained along the entire late Quaternary (Figure 6.14). Given the direct relationship between deposition of the Marquês de Pombal Drift and overpressure development, the lateral and temporal variability that characterize the location of overpressure areas within Unit IV and Unit III is somehow unexpected, especially considering the homogeneous distribution of porosity and permeability within the mixed-system deposit (Figure 6.13A and B).

The modelling results show that overpressure ratio does not exceed the value of 0.2. The inhomogeneous lateral distribution of overpressure within Units III and IV indicates that, in areas where overpressure reaches 20% of the lithostatic load at a given timestep, pore pressure dissipates generating a local hydraulic gradient that involves lateral fluid flow to the adjacent areas (Figure 8.2). Lateral flow of pore water in shallow sediments is responsible for the alternation of overpressure towards adjacent areas during consecutive timesteps.

When considering the reasons behind the modelled overpressure of 0.2, different mechanism driving excess pore pressure generation and dissipation can be considered as reported in chapter 1.4. In our modelling approach, overpressure development is constrained by the sedimentation history of the basin coupled to the sediment physical properties. Other potential factors influencing pore pressure development or dissipation, such as changes in pore fluid volumes, chemical and diagenetic processes, osmosis or cycling loading, are not taken into account. However, in the SW Iberian margin development of overpressure can only be related with the depositional history of the basin given the shallow burial depths and sediment composition (e.g. Mencaroni et al., 2021; Neves et al., 2016; Teixeira et al., 2019). Additional considerations are required for cyclic loading, which will be dealt when analysing slope stability in Chapter 9. Based on this assumption, the factors that will be analysed to assess the degree of overpressure development resulting from our simulations are the sedimentation rate, hydromechanical properties of sediments and lateral fluid flow.

As reported in section 1.3, development of overpressure in marine sediments takes place when sediment deposition increases above the consolidation rate, preventing the dissipation of pore water and maintaining sediment in an underconsolidation state (Gibson, 1958). In order to understand if the overpressure value of 0.2 could be exceeded by a faster rate of sediment

deposition, we reproduced the model of Line_4 with a sedimentation rate of the Marquês de Pombal Drift increased x1.5 times by changing the time of deposition of the unit (~ 3 m/kyr maximum decompacted sedimentation rate instead of ~ 2 m/kyr). The simulation results show that, under these conditions, the overpressure would develop continuously through most of the stratigraphic units. However, also in this case the overpressure ratio would not increase above 0.2 (Figure 8.3).

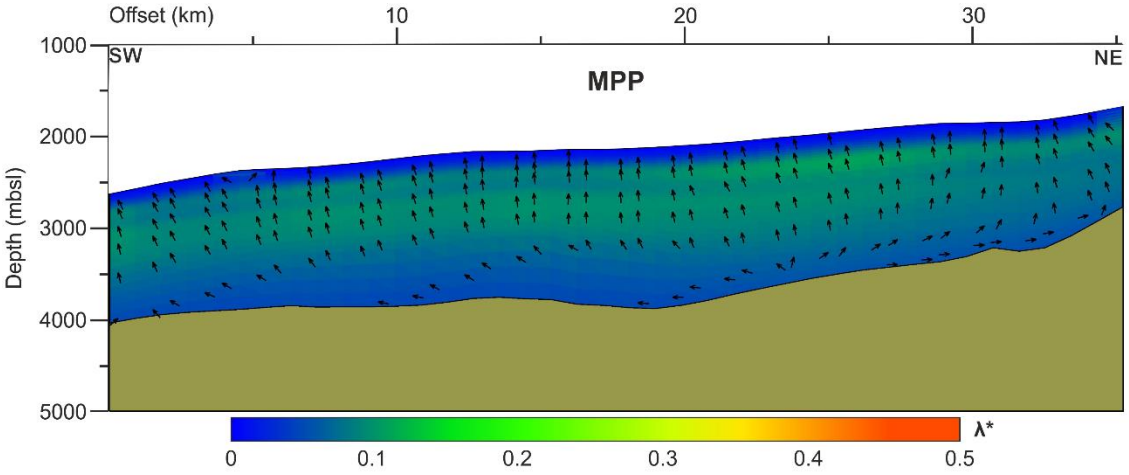

Figure 8.3: Present day overpressure ratio in Line_4 model when Unit IV sedimentation rate is increased x1.5 times. In this scenario, overpressure develop within most of the units, although the overpressure ratio threshold of ~0.2 is not bypassed.

This modelling scenario suggests that, in presence of permeability and compressibility values defining the "Mixed System" sediment type, a much higher sedimentation rate is needed in order to exceed the overpressure of 0.2. In order to understand the role of hydromechanical properties in overpressure generation, we compared initial porosity ($Ø_0$), initial specific storage (S_0) and initial hydraulic conductivity (k_0) that defines the "Mixed System" sediment type with the same values adopted for fine-grained sediments (hemipelagic) in previous overpressure modelling studies from Urgeles et al. (2010), Urlaub et al. (2015) and Llopart et al. (2019) (Table 8.1).

Table 8.1: Comparison between physical properties input for fine-grained hemipelagic sediments in this and previous pore pressure development models.

	$Ø_0$	S_0 (m^{-1})	k_0 (m/s)
Urgeles et al., 2010	0.80	0.09	3×10^{-9}
Urlaub et al., 2015	0.75	0.064	4×10^{-9}
Llopart et al., 2019	0.77	0.044	3×10^{-9}
This study	**0.75**	**0.033**	**4.15×10^{-9}**

$Ø_0$: initial porosity at 1kPa; S_0: initial specific storage at $Ø_0$; k_0: initial hydraulic conductivity at $Ø_0$.

The comparison shows that, although all the parameters fit within the same order of magnitude, the specific storage defining the "Mixed System" sediment type is lower compared with the previous studies, while the hydraulic conductivity is higher. In our interpretation, the combined effect of relatively low compressibility and high permeability at deposition prevent sediments in

the model from undergoing high loss of permeability and porosity with increasing burial depth in the two uppermost units. The final hydraulic conductivity and porosity resulting from the model of Line_4 (Figure 6.9A and Figure 6.9B), in fact, show that porosity and hydraulic conductivity undergo only a minor decrease within the uppermost stratigraphic unit.

In order to validate the hypothesis by which the high hydraulic conductivity value assigned to the "Mixed System" sediment type prevents overpressure generation above 0.2, we created a third copy of Line_4 model with original sedimentation rates (~2 m/kyr decompacted), but decreasing the hydraulic conductivity of the "Mixed System" sediment type from 4.15 x 10^{-9} m/s to 1 x 10^{-9} m/s. Also in this case, overpressure develops along the entire model. However, by decreasing the hydraulic conductivity of the "Mixed System" sediment type the overpressure ratio within Units III and IV reaches values of 0.3 (Figure 8.4).

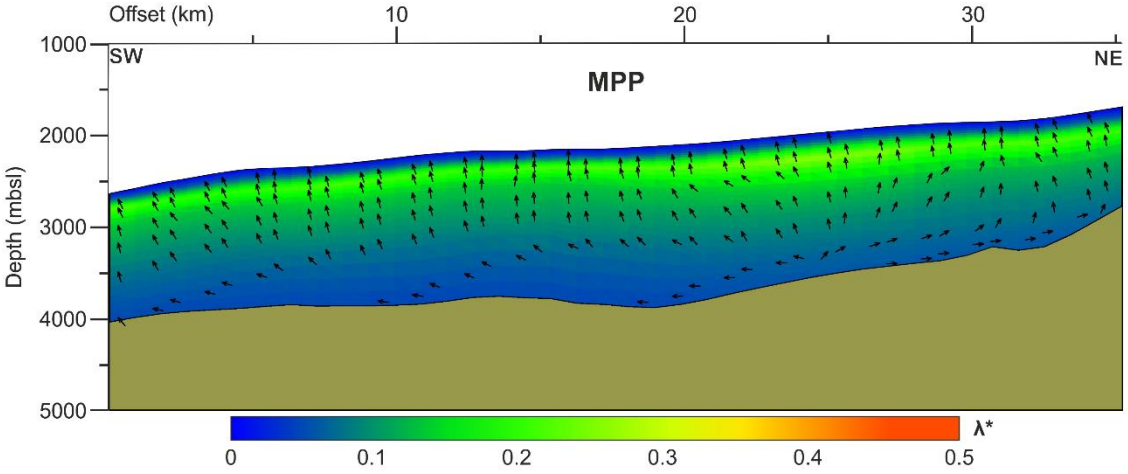

Figure 8.4: Present day overpressure ratio in Line_4 model when "Mixed System" sediment type is defined with k_0 = 1 x 10^{-9} instead of 4.15 x 10^{-9}. Similarly to what it is visible in Figure 8.3, overpressure develop along the entire stratigraphy, but the maximum overpressure ratio in shallow units reaches 0.3.

The results shown in Figure 8.4 indicate that by decreasing the permeability of Unit IV from 4.15 x 10^{-9} to 1 x 10^{-9}, the Marquês de Pombal Drift would increase considerably their pore water retention capacity. This would allow overpressure buildup above the value of ~ 0.2. Figure 8.5 shows the present-day porosity (Figure 8.5A) and hydraulic conductivity (Figure 8.5B) resulting at PseudoWell_1 location (see position in Figure 6.9) for the three Line_4 modelling scenarios analysed in this section: Line_4 base model (Figure 8.2), Line_4 model with increased Unit IV sedimentation rate (Figure 8.3) and Line_4 model with decreased initial hydraulic conductivity for the "Mixed System" sediment type (Figure 8.4).

The profiles indicate that porosities follow a similar trend for all the three models, decreasing from 0.75 at the seafloor to 0.37/0.35 at the base of Unit IV, located at 310/320 mbsf. Deeper than this stratigraphic level, porosities decrease down to 0.22 at 1552/1562 for all the models (Figure 8.5A). The hydraulic conductivity within Unit IV for Line_4 base model and the one with enhanced Unit IV sedimentation rate decreases from -8.38 to -10.11/-10.18 $\log_{10}$k.

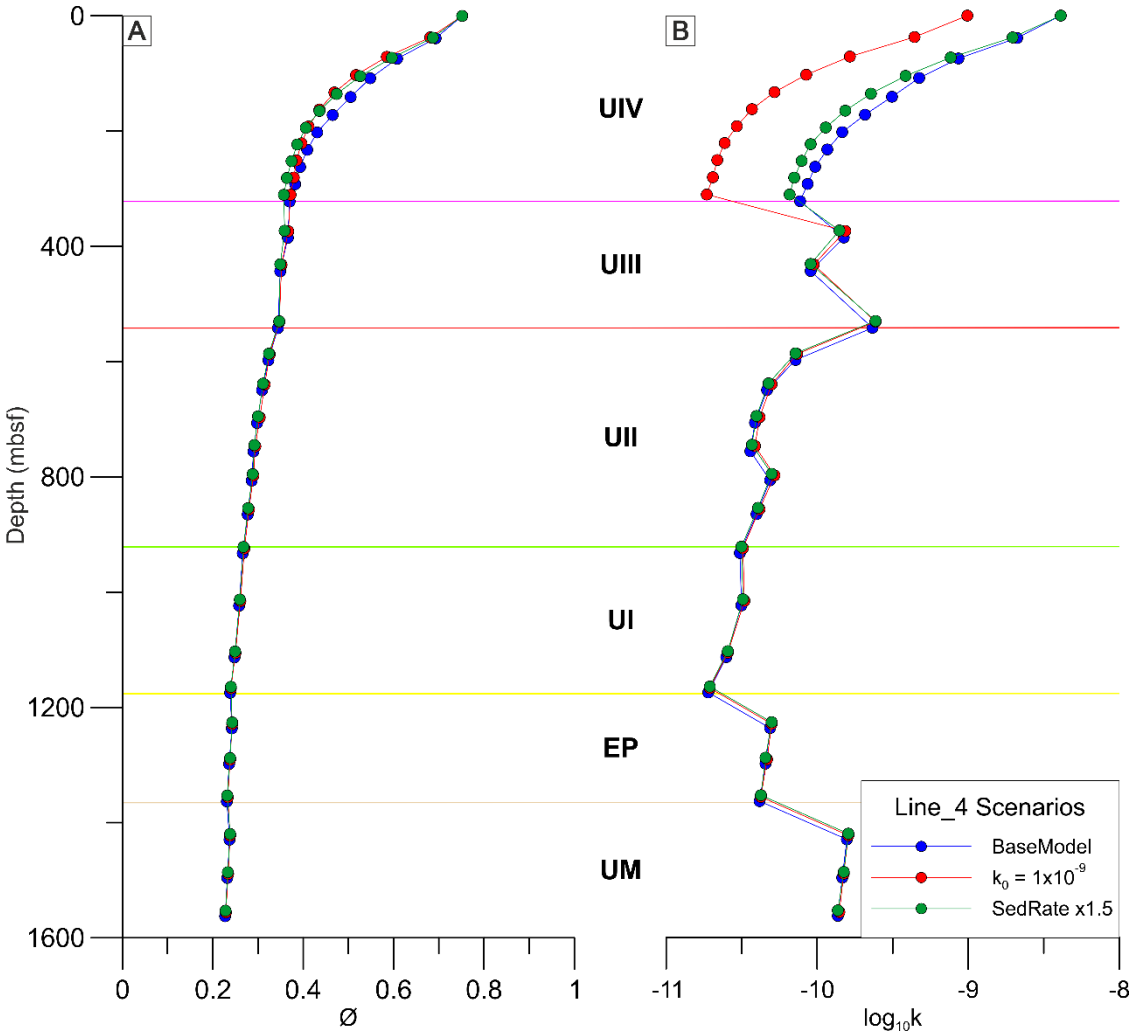

Figure 8.5: Porosity (Ø) and hydraulic conductivity ($log_{10}k$) profiles resulting at the end of the simulation at PseudoWell_1 (see location in Figure 6.9) for the three Line_4 model scenarios analyzed in this section. Each dot represents one of the layers composing the stragraphy. EP: Early Pliocene Unit; UM: Upper Miocene.

A similar trend of reduction is visible in the model of Line_4 where the "Mixed System" hydraulic conductivity is lower, although due to the lower input value the hydraulic conductivity decreases from -9 $log_{10}k$ at the seafloor to -10.73 $log_{10}k$ at the base of Unit IV (Figure 8.5A). Starting from Unit III, the three hydraulic conductivity curves follow a similar trend, with an alternation of lower and higher permeability values depending on the sediment composition of the underlying units.

The results shown in Figure 8.5 confirm that sediment hydromechanical properties have the main role in overpressure dissipation in the model of Line_4. The decrease in initial hydraulic conductivity defining the "Mixed System" sediment type has a more significant effect compared to the model with enhanced sedimentation rate. The slightly lower compressibility and higher permeability defining the Marquês de Pombal Drift deposit compared to that of other regions (Table 8.1) could explain the prevalence of vertical fluid flow.

Line_3 model follows a similar orientation to Line_4. Being located a bit more distant respect to the area of maximum deposition of Unit IV, the late Quaternary unit is thinner (Figure 6.9) and, consequently, the sedimentation rate is lower. The lower lithostatic load from deposition of Unit IV results in lower overpressure in the shallower part of Unit IV (< 0.1) (Figure 6.10C) compared with Line_4 (~0.2) (Figure 6.14). On the other hand, the shallow overpressure zone in Line_3 appears more continuous than in Line_4 (Figure 8.2). Overpressure results in Line_3 model confirm that, in the Marquês de Pombal Plateau, the development of overpressure is controlled by the rate of deposition of the Marquês de Pombal Drift. However, while the sedimentation rate has a key role in triggering overpressure generation, in the Marquês de Pombal Plateau the magnitude of overpressure is limited by the small loss of permeability with increasing burial depth, especially within the two uppermost units. This is due to the combined effect of high hydraulic conductivity at deposition and the low degree of compressibility of the sediments, which prevent sediments to undergo a significant loss in porosity and permeability within the uppermost part of the sedimentary column. This is in accordance with the results from Urlaub et al. (2015), where it has been demonstrated how exceptionally low permeability values (10^{-11} at depositional conditions) and high compressibility of sediments are required to generate significant overpressure in presence of low sedimentation rates. If these two conditions are not satisfied, sedimentation rates much higher than the ~ 2 m/kyr observed in the Marquês de Pombal Drift are required to generate higher overpressure. This is also confirmed by known examples of continental margins where high overpressure has been proven to exist. For example, at the Storegga slide headwall overpressure development is associated with sedimentation rates up to 36 m/ka at the end of the last glaciation (Leynaud et al., 2007), and the well-documented overpressure in the Ursa basin is due to the sedimentation rates up to 25 m/kyr from sediment entering the basin from the Mississippi River (Flemings et al., 2008).

8.1.2 Assessing the influence of major stratal discontinuities in overpressure development: erosion along the São Vicente Canyon and Marquês de Pombal Fault

The role of the São Vicente Canyon and Marquês de Pombal Fault scarp as potential source of lateral fluid flow and overpressure dissipation remains to be assessed. In the upper sector of the São Vicente Canyon (Figure 6.1), erosion takes place entirely during the late Quaternary (see also section 2.2.3). The erosion affects Units II and III, while Unit IV does not deposit in the canyon, as reproduced in the models (Figure 6.2, Figure 6.4 and Figure 6.11). In principle, incision of the canyon could favour the dissipation of overpressure by creating a hydraulic gradient between the eroded area (at hydrostatic conditions) and adjacent areas with excess pore pressure. However, in order to allow the lateral transfer of pore pressure, a continuous and relatively permeable layer is needed (Behrmann et al., 2006; Osborne and Swarbrick, 1997; Urlaub, 2013).

The occurrence of lateral flow has been evaluated by analysing the flow pathways in the hydrological models. As expected, the flow is directed from higher lithostatic load areas located below the Marquês de Pombal Drift depocenter (especially within Unit I, II and Early Pliocene) towards the SE side of the models, where the São Vicente Canyon is present (Figure 6.3C, Figure 6.5C and Figure 6.13C). The highest overpressure takes place below the areas of maximum deposition of Unit IV, indicating that the sedimentation rates of ~ 2 m/kyr related with the Marquês de Pombal Drift produce a load that cannot be compensated by pore fluid expulsion and consequent pore pressure dissipation. The water expelled from deeper stratigraphic units, which have slightly higher sand content than the shallower ones, is able to flow laterally towards areas of lower lithostatic stress located in the slope areas and in the proximity of the São Vicente Canyon. This lateral fluid flow process might allow pore pressure dissipation not only in the deeper stratigraphic units, where lateral fluid flow does directly take place (Figure 6.3C, Figure 6.5 and Figure 6.13C), but also within Units III and IV despite the fluid flow within these shallower units is mostly vertical. Lateral fluid flow from the deeper units might decrease the overall water volume in the uppermost units, thus erosion along the canyon could have played a fundamental role in the overall overpressure evolution of the system.

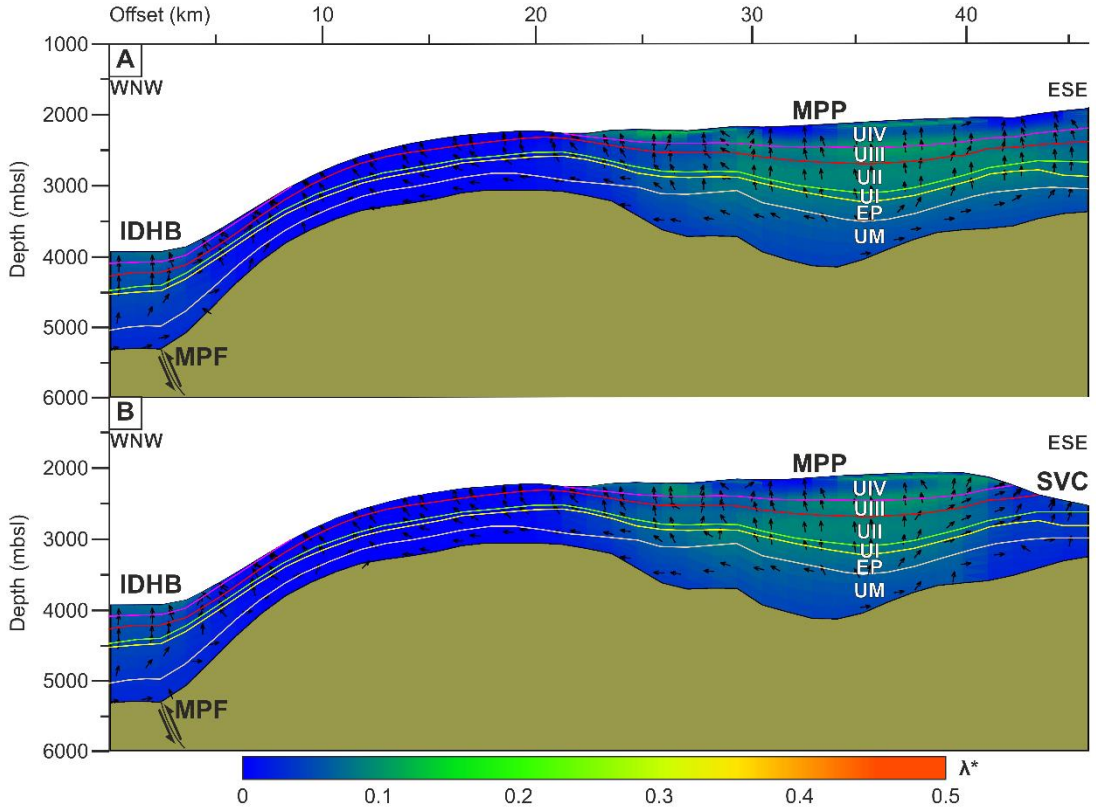

Figure 8.6: Present day overpressure ratio along the model of Line_1 (A) without erosion by the São Vicente Canyon and (B) with the erosion induced by the São Vicente Canyon during the late Quaternary. EP: Early Pliocene Unit; UM: Upper Miocene. MPP: Marquês de Pombal Plateau; IDHB: Infante Don Henrique basin.

In order to test the actual contribution of the canyon erosion in the dissipation of overpressure, we built models in a hypothetical scenario where the São Vicente Canyon erosion did not take

place (along Line_1, Line_2 and Line_5; more information about the models configuration in Methods section 3.4.3.3.2) (Figure 8.6). By subtracting the overpressure at the different finite element mesh nodes resulting from the two models (i.e., the model accounting for canyon erosion from the one where the canyon is not present), it is possible to quantify the excess pore pressure dissipation due to the late Quaternary canyon incision (Figure 8.7).

The comparison between the two models shows significant differences in flow pathways near the area of the canyon, to the ESE of the modelled section. Here, the flow has a strong ESE lateral component in the scenario where the São Vicente Canyon erosion is taken into account (Figure 8.6B), while it is vertical in the one not affected by the erosion (Figure 8.6A). The flow in the rest of the model remains largely unchanged.

Differences in overpressure for the two models at the end of the simulation and during the time steps corresponding to the canyon erosion are mainly visible in the São Vicente Canyon area (Figure 8.7). Where erosion is not modelled, overpressure associated with vertical fluid flow develops throughout the entire Marquês de Pombal Plateau (Figure 8.6A), including the SE model boundary, resulting in positive overpressure differences within the canyon's area (Figure 8.7). Such overpressure pattern results from the non-equilibrium consolidation induced by deposition of Unit IV extending to the SE end of the model. The lateral fluid flow towards the São Vicente Canyon does not affect the overpressure buildup in the Marquês de Pombal Plateau within Units III and IV (Figure 8.7), suggesting that the overpressure development within these units is a direct consequence of the sedimentation rate and load generated by deposition of the Marquês de Pombal Drift.

It should be noted, however, that the software BASIN models erosion as instantaneous in each time step (10 for erosion of the São Vicente Canyon upper sector during the late Quaternary) and that the removal does not produce an instantaneous and proportional dissipation of the pore pressure, which in a fully saturated environment is not in agreement with Terzaghi's principle of effective stress and may lead to some inaccuracies. Also, due to the combination of horizontal resolution and thickness of the uppermost layers, stretched triangles in the mesh could lead to slightly diverging results (spots in Figure 8.7).

Another major element to consider as a potential influence in the overpressure development in the Marquês de Pombal Plateau is the Marquês de Pombal Fault displacement and the associated changes in slope and stratal configuration. According to our stratigraphic interpretation, the slope corresponding to the Marquês de Pombal Fault scarp is located at the western edge of the Marquês de Pombal Drift depositional area (Figure 7.1).

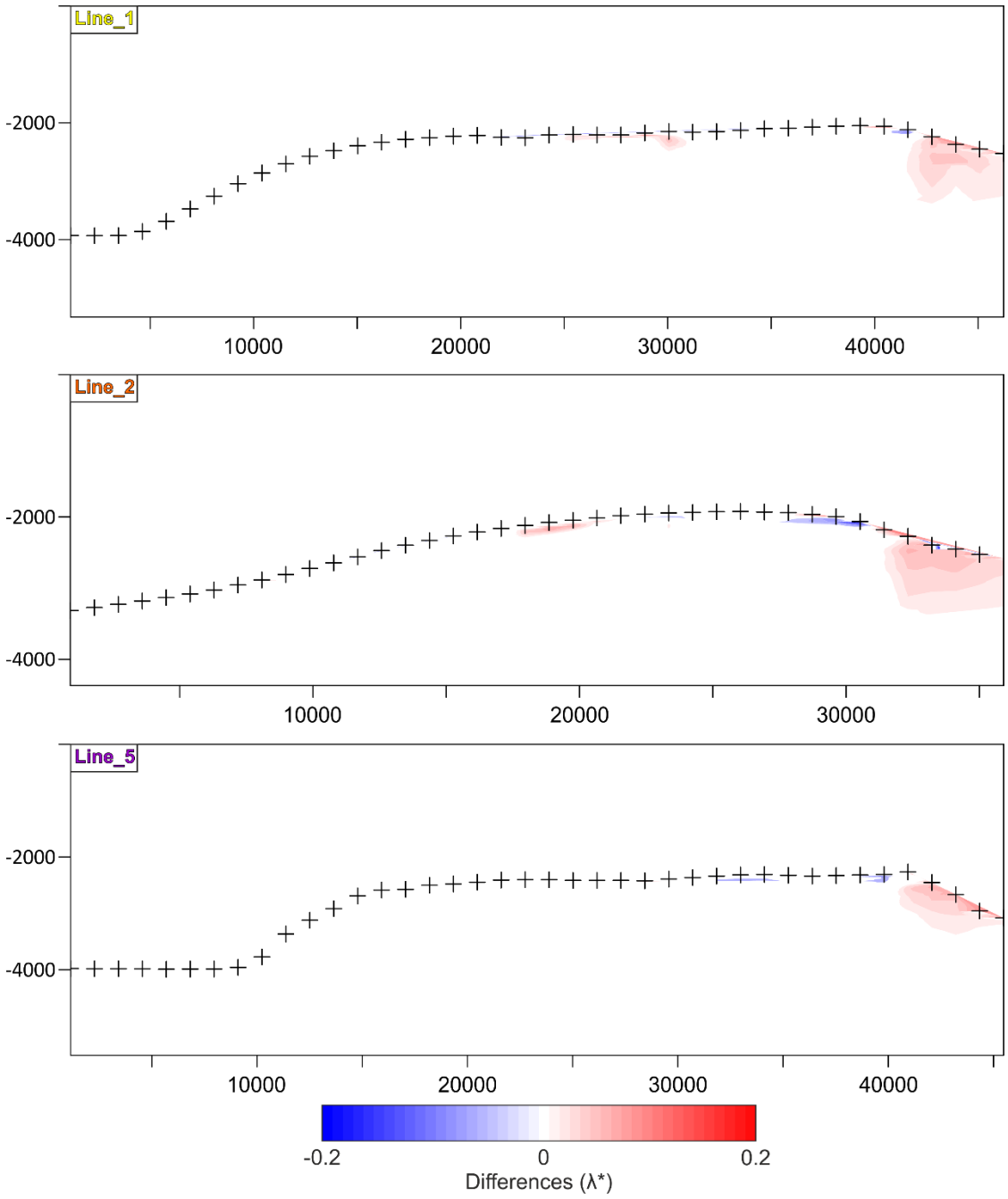

Figure 8.7: Differences generated by subtracting the overpressure ratio resulting from the models where the São Vicente Canyon erosion has not been modelled from the same models where the canyon erosion is represented.

The lower lithostatic load due to the thinner Unit IV over this slope area results in lower consolidation of the underlying sediments, resulting in higher porosity, higher hydraulic conductivity and no overpressure development in the proximity of the Marquês de Pombal Fault (Figure 6.1, Figure 6.3 and Figure 6.13). Similarly to what has been noticed with regards to the São Vicente Canyon, the lower lithostatic load in the proximity of the Marquês de Pombal Fault generates an hydraulic gradient that favours lateral flow towards the Marquês de Pombal Fault area within the deeper stratigraphic units (i.e. Early Pliocene and Upper Miocene) (Figure 6.3C and Figure 6.13C).

The overpressure resulting at PseudoWell_2, in the proximity of the slope (Figure 6.13C), shows that maximum overpressure values <0.1 only develop after deposition of Unit IV during the late Quaternary and are associated with sedimentation rate values of ~ 0.7 m/kyr (Figure 6.14). The lower overpressure generation at PseudoWell_2 (<0.1) compared with PseudoWell_1 (~ 0.15), located closer to the depocenter of Unit IV, confirm the direct influence of the Marquês de Pombal Drift on the development of overpressure, as it has been extensively explained in section 8.1.1.

Despite BASIN allows to model fault planes with different orientations and to assign specific permeability values to the fault, we had no elements to realistically assess the permeability of the fault. Therefore, the only role of the fault assessed in this study is to modify the morphology of the margin. Depending especially on the type of faulting and the sediment properties, fault planes can act like high permeability conduits where fluid flows are facilitated, while in other cases permeability along faulted sediments (or rocks) drops, generating impermeable barrier for the flow (Borge and Sylta, 1998). The correct characterization of fault permeability is key in the field of petroleum exploration, as they can act as preferential pathways for hydrocarbon migration or generate structural traps. In the same way, permeable or impermeable fault planes can be key element in overpressure evolution. In this study, high permeability related with the Marquês de Pombal Fault could act as a drainage path for water flow and transfer fluids from the deeper to the shallower parts of the stratigraphy, dissipating pore pressure or transferring them to other stratigraphic levels. On the other hand, an impermeable fault plane could have acted as a barrier, preventing flow transfer from the Marquês de Pombal Plateau towards the slope and potentially promoting overpressure buildup. Since no previous studies have focused on the permeability of the Marquês de Pombal Fault plane, however, introducing the fault and its permeability in the models would only increase further elements of uncertainties in the results.

In summary, overpressure development in the Marquês de Pombal Plateau is largely related with the late Quaternary deposition of Unit IV, and in particular with the increased sedimentation rates associated with development of the Marquês de Pombal Drift. Before the mixed system emplaced, minimum overpressure generated in the area and is not until the late Quaternary to present day that overpressure ratio values rise up to 0.2.

Lateral fluid flow develops especially within the Upper Miocene and Early Pliocene, following a hydraulic gradient from the areas below the depocenter of Unit IV towards the São Vicente Canyon and the Marquês de Pombal Fault. The influence of lateral fluid flow on the overall overpressure development is minimum and areas of overpressure development in our models are associated with vertical fluid flow. The reduced impact of lateral fluid flow on dissipating overpressures in the area testify that the water flow contribution from deeper units is not critical in the overpressure development within Units III and IV.

8.2 Influence of sedimentary environment on physical properties and development of overpressure

As explained in Chapter 5, 1D models have been adopted to assess the influence of sedimentary environment on physical properties and development of overpressure. Two different scenarios have been used to analyse the role of grain size composition of hemipelagic sediments in overpressure development. In scenario (A), the hemipelagic layer is defined using physical properties collected from different study areas (two siliciclastic settings, the Ursa basin and Gulf of Cadiz, and one volcanoclastic setting, the Grenada basin). The results show that, considering the same burial history, the sediments of the Grenada basin develop much higher overpressure compared to those of the other two areas considered. In Scenario (B), the samples are selected according to their represented textural class, and those with relatively high silt, low clay content and sand content higher than 5% (sediment class D-II, including only samples from the Grenada basin) generated the highest overpressure. These results therefore indicate that overpressure generation is also related with sediment composition and depositional setting, not only with grain size distribution. This is in agreement with previous studies showing that there is no direct correlation between grain size distribution and sediment physical properties (Lafuerza et al., 2014) in marine muddy sediments.

However, when considering each depositional environment (e.g. river vs volcanically influenced), the grain size distribution has a major influence on overpressure development. Thus, sediments with low clay content and very low (E-II) to low sand content (D-III) generated lower overpressure (Figure 5.1 and Figure 5.4A). Nonetheless, factors not considered in this study such as sorting and particle rounding might have played a significant role that should be investigated in future works.

Comparing the overpressure results with the physical properties used for the simulations indicates that the development of overpressure is associated with low initial hydraulic conductivities and specific storages (Table 5.1). Such differences in physical properties between the Grenada basin and the other two areas could reflect substantial diversity in sediment composition and mineralogy. This may in turn be directly linked to the depositional environment: a) the hemipelagic sediments in the Alentejo and Ursa basins are largely fluvially derived from the Guadalquivir and Mississippi rivers, respectively; b) sediments from the Grenada basin are influenced by deposition of volcanic ashes released in the Lesser Antilles volcanic arc (Wiemer and Kopf, 2015).

Comparing the 1D consolidation behaviour for volcanically influenced hemipelagic sediments to the river-fed samples, it is possible to make assumptions about the reasons for such notable differences in physical properties (Figure 5.3). The Grenada basin sediments show lower compressibility at low consolidation stress and a transition to high compressibility at higher vertical stress (Figure 5.3B). Similar behaviour known as structuration has been documented

especially for fossiliferous, cemented or highly bioturbated sediments (Locat et al., 2003; Spinelli et al., 2007). In these instances, sediments are capable of holding water in rigid structures, preventing compaction during the early stages of consolidation or, in case of high degrees of cementation, also at high burial depths. Physical properties of the sediments from the Grenada basin, with higher compression index and lower specific storage and hydraulic conductivity, suggest that a similar mechanism could occur in the volcanic ash-rich hemipelagic sediments from the Lesser Antilles volcanic arc. Volcanic ashes, in fact, may generate the same type of structures preventing pore water to be released in the system at low consolidation stresses.

Structuration in the Grenada basin sediments retains the water in the pore space, reducing the specific storage (which is, by definition, the volume of water removed from a unit volume of a confined aquifer) and decreasing the permeability, since the pore water gets trapped into rigid structures. Those physical properties represent the ideal conditions for the development of overpressure in marine sediments, and this could explain why the Grenada basin sediments (scenario A) develop higher overpressure (near lithostatic), which leads to a lower vertical deformation in the model.

It must also be mentioned that defining hydrogeological models with marine sediments that show structuration might question the hydrogeological model results. “Delayed consolidation” (Locat et al., 2003), as it is visible for the Grenada basin hemipelagic sediments (Figure 5.3B), implies two different consolidation responses within the same sediment sample. Considering that the compression index is usually input as one representative value for each lithology, modelling such variation can represent a challenge. This is the reason why it is important to recognize structuration phenomena in the analysed samples and to consider its consequences while evaluating simulation results.

This behaviour is well exemplified when modelling the Ursa basin sedimentation history with physical properties from the Grenada basin (Figure 5.5). The lower hydraulic conductivity and specific storage of the sediments from the Grenada basin, mainly due to the structuring phenomena previously discussed, makes the hemipelagic unit act as a perfectly impermeable seal in case of the very high sedimentation rates of the Ursa basin. The pore water from deeper formations, characterized by coarser grain size and higher permeability, flow upwards and accumulates at the base of the seal, reaching extreme overpressure values up to 1 (Figure 5.5). Nonetheless, this trend does not find correspondence in the *in-situ* measurement, where overpressure reaches its maximum within the hemipelagic layer and decreases constantly with depth, indicating a continuity between the pore water flow in the lower part of the stratigraphy and in the uppermost hemipelagic layer.

8.3 Models validation and quality of results

Numerical models aiming to simulate any type of variables should ideally be groundtruthed with *in-situ* measurements, performed at strategic locations, in order to test the accuracy of results. In the field of marine geosciences, however, the acquisition of calibration data to test the accuracy of simulation aiming to reproduce any processes taking place in the subsurface is challenging, since it always involves the organization of expensive and logistically complicated offshore cruises. In an ideal scenario, the overpressure modelling results should be calibrated by testing the Marquês de Pombal sediment properties with one of the *in-situ* measurement methods described in section 1.5. The best way to calibrate overpressure results would be by using penetrometers to groundtruth overpressure, as it was already done, for example, by Orange et al. (2003) and Flemings et al., (2008) in the Gulf of Mexico. The occurrence of overpressure could also be tested by acquiring log data or recovering deep sediment cores (e.g., Hart et al., 1995; Revil et al., 1998; Dugan & Flemings, 2002; Saffer, 2003). However, although these measurements are commonly performed for oil and gas exploration purposes, their application in the frame of geohazard assessment are often too expensive to be performed for academic purposes and represent exceptions more than routine analysis.

Many elements of uncertainty are inevitably involved with the project described in this thesis. As it has been explained in the previous chapters, most of the deep stratigraphic data adopted in our seismic interpretation and overpressure modelling come from the drilling of IODP well U1391 (Stow et al., 2013a) and from studies that made use of the core and log data revealed after IODP 339 expedition (e.g. Hernández-Molina et al., 2016a; Lofi et al., 2016; Rodrigues et al., 2020). Nevertheless, IODP Site U1391 is located in the Sines drift area, approximately 60 km away from the Marquês de Pombal Plateau, and at ~ 1000 m shallower water depth (Figure 4.1). The first element of uncertainty is the sediment composition and variations in this composition along the model. Many studies document the primary role of the MOW hydrodynamics in the depositional evolution in Alentejo basin middle slope (750 m to 1800 m) (e.g., Hernández-Molina et al., 2016a; Lofi et al., 2016; Neves et al., 2016; Rodrigues et al., 2020; Teixeira et al., 2020) (see section 2.3 and 2.4.2), but the transition of contourite facies towards deeper parts of the basin has never been studied in detail. In our stratigraphic interpretation, we have been able to track the horizons related with the main stratigraphic discontinuities (LPD, EQD, MPD and LQD) along the entire study area, allowing to derive a chronostatigraphic frame for the Alentejo basin that also integrates older seismic units (down to the Middle Miocene) (Martínez-Loriente et al., 2018, 2013). By interpreting new MCS data and sediment properties from the Marquês de Pombal Plateau, we demonstrated the emplacement of a previously unknown mixed contour current – turbidity current deposit: the Marquês de Pombal Drift. Nevertheless, the vertical sediment variability of the model strongly rely on the information revealed by the drilling of IODP Site U1391. Only a second well drilled in the Marquês de Pombal Plateau area could reveal which correlation exists between the

sediment distribution in the Sines drift area (middle slope) and the Marquês de Pombal Plateau area (lower slope) before the incision of the São Vicente Canyon in the late Quaternary. In the Methods section 3.4.3.3.1 we explain that grain size variation with depth has been modelled as a linear reduction of sand content with increasing water column. The sand reduction curve has been derived from the sand content measured in the gravity cores collected for this study, based on the simple assumption that the transport capacity of the MOW is higher in the middle slope, where the bottom current core is located, compared with deeper water settings (Stow et al., 2009). The assumption that sand content decreases when moving away from the MOW cores is justified by the fact that the Alentejo basin is located away from the main river inputs (i.e. the Guadalquivir and Guadiana rivers), thus the siliciclastic sediments present in the area have mostly been transported by the bottom current (Mulder et al., 2003; Nelson et al., 1999). This simple relation between sand content and water depth likely does not reproduce accurately the facies transitions from IODP Site U1391 towards the Marquês de Pombal Plateau, or at least it cannot be checked without drilling a second well in the study area. However, in absence of calibration points, a rough estimation of the overall accuracy of the stratigraphy and physical properties of the sediments composing our models can be achieved by comparing the simulation results at the present day with seismic interpretation and IODP downhole log results. As described in the next two sections (8.3.1 and 8.3.2), we can also derive an overall error in the models by comparing the depth of the seafloor and that of the interfaces in between the main units with the ones from the depth grid that constituted the starting geometry of the models (see Methods section 3.4.3.1), determined from the seismic data. Finally, we compared the final porosity trend resulting from the models with the porosity measured at IODP Site U1391.

8.3.1 Computed depths of seafloor and units

In order to simulate porosity and permeability reduction from sediment self-weight, and their role in the development of overpressure, the various units have to be input using de-compacted thicknesses as BASIN derives the degree of compaction for each unit based on the physical properties from each sediment type (see section 3.4.1 for more details about the workflow adopted). The loss of thickness of sediments under a vertical load is a function of their initial porosity and compressibility (Long et al., 2011). The latter is expressed in BASIN with the specific storage at depositional conditions (see section 3.4.1). At the end of the simulations, each of the 29 layers composing the models has undergone a reduction in thickness, and the final thickness values should ideally match the ones observed from the seismic interpretation. Therefore, by comparing the modelled depths of the seafloor at the end of the simulation with the seafloor depth derived from seismic interpretation, it is possible to obtain a first order assessment of how the model fits the observations. The error associated with each model in Figure 8.8 refers to the difference between computed and seismic seafloor depth with respect to the overall stratigraphic thicknesses (eq. 19):

$$Error\ (\%) = \left|\frac{z_S - z_C}{h_{strat}}\right| \quad (19)$$

Where z_S and z_C are the seismic and computed seafloor depths and h_{strat} is the total stratigraphic thickness measured at the same location.

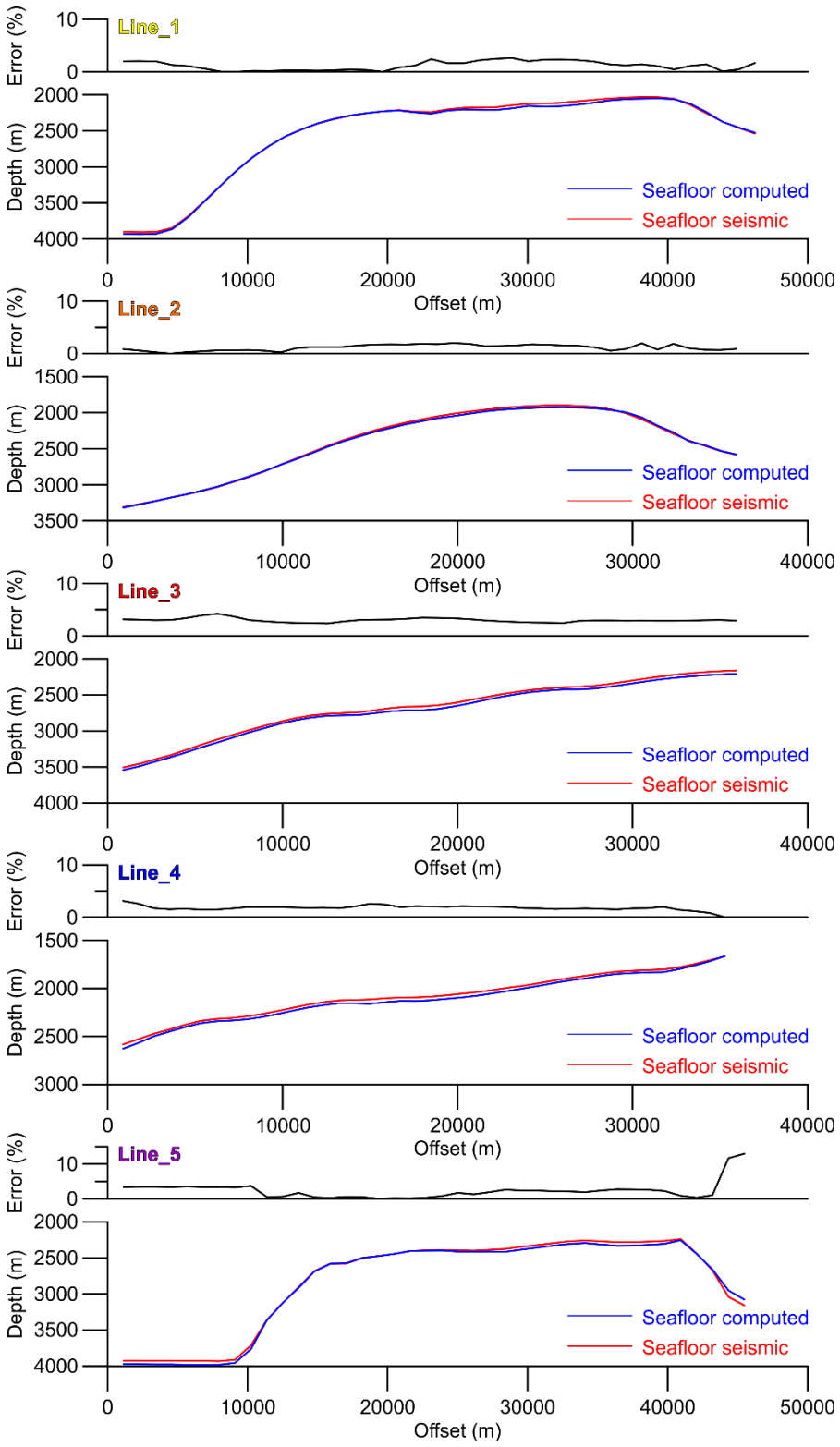

Figure 8.8: Visual comparison beween seafloor depth resulting from our simulation (blue lines) and the one measured from seismic interpretation after time to depth converiosn following the relationsip proposed in section 3.2.2 (red lines) for the five considered models. Relative errors (%) are reported on top of each graph.

This evaluation provides information on the accuracy of the sediment properties assigned to the different sediment classes, and the relative abundance of each of the sediment class within the strata composing the models. It should be noted however that different combinations of physical properties and relative abundance of the different sediment classes could yield similar results. Therefore, the source of the uncertainty cannot be clearly identified. Figure 8.8 provides a visual comparison of the differences in the seafloor depths, showing that in most of the models the match between computed and actual depth-converted seafloor depths as measured from seismic data returns a relatively good match with errors < 10%. In the steeper slopes area discrepancies are almost absent, while in the central part of the models of Line_1, Line_2 and Line_5, as well as for the entire length of Line_3 and Line_4, errors do not exceed 4%. The largest discrepancy of ~ 13% is found in the São Vicente Canyon area associated with Line_5.

The plot in Figure 8.9 shows the error generated by the difference in depth of the seafloor between computed models and seismic data (eq. 19) versus the total stratigraphic thickness, for all 40 nodes constituting the seafloor at the final stage of each model.

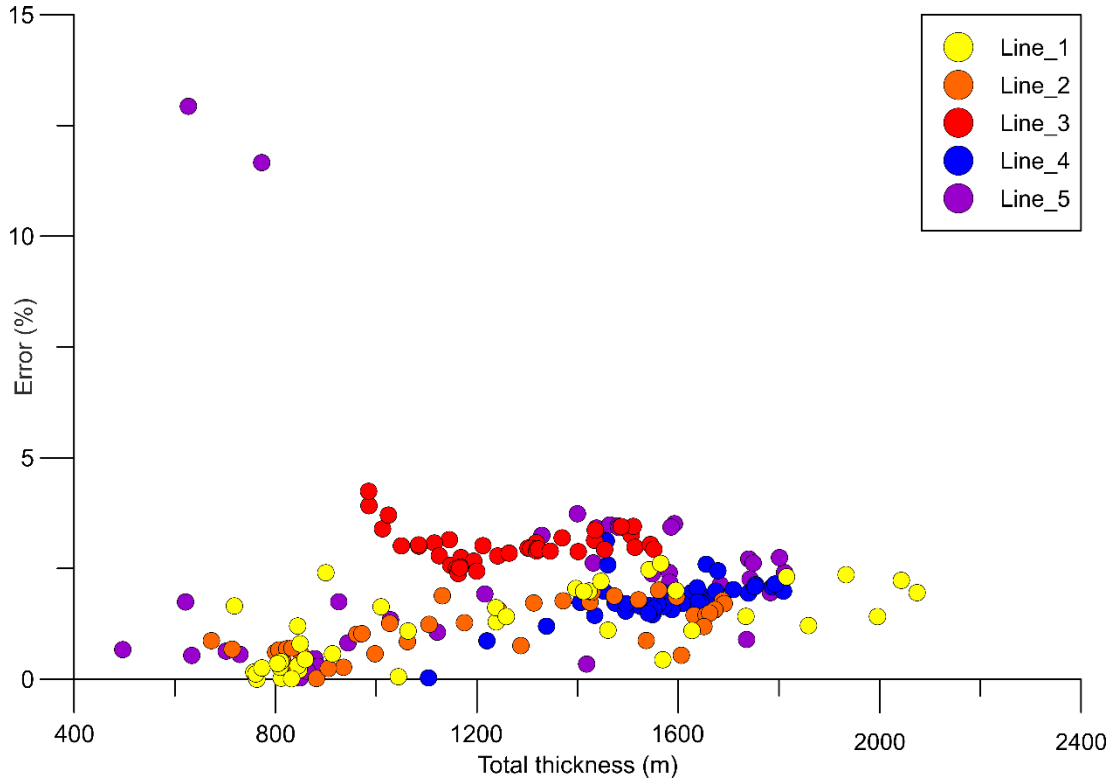

Figure 8.9: Error (%) derived from differences in depth of the seafloor between computed models and that picked from seismic data for all 40 nodes constituting the seafloor at the final stage in each model (Figure 8.8).

In most instances, the error is < 5%, except for two cells in Line_5 contained in the São Vicente Canyon area, where the error is ~12%. The not-so-accurate reproduction of the modelled seafloor depths within the eroded areas is due to computational problems as BASIN distributes the erosion

of thick sedimentary packages in only a few timesteps (hundreds of meters distributed in 10 time steps in the São Vicente Canyon).

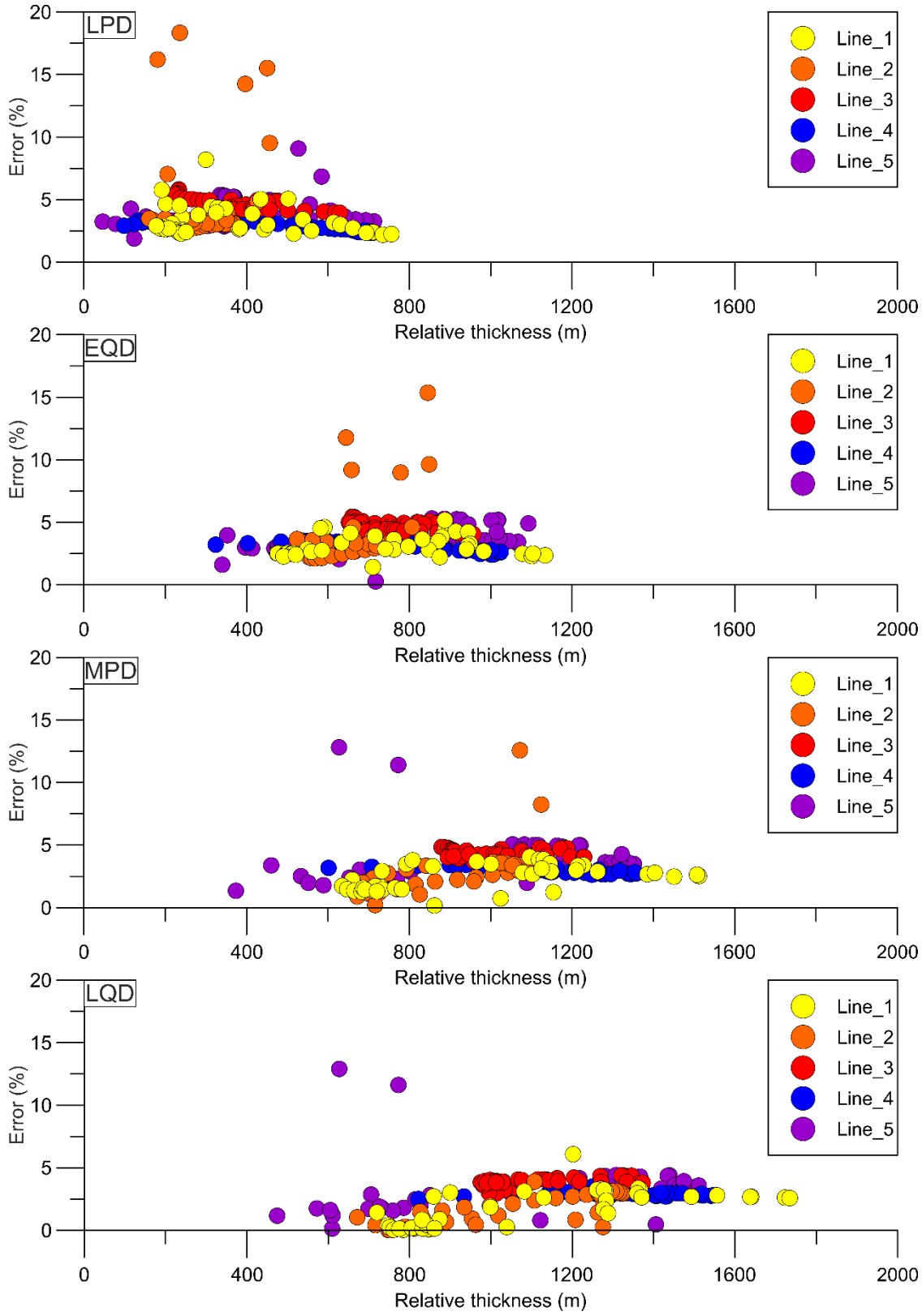

Figure 8.10: Error (%) derived from differences in depth of the interfaces separating the major seismic units between computed models and those picked from seismic data for all 40 nodes constituting the interfaces at the final stage in each model (Figure 8.8).

Figure 8.10 shows how potential errors related to the input physical properties and initial sedimentary thicknesses propagate after sediment compaction to the depth of the main stratigraphic discontinuities considered in this study (LPD, EQD, MPD and LQD) at the end of the simulation. In this case, the error plotted against their relative thickness remains around 5% for most of the cells, except for Line_2 where the error associated with LPD is close to 20%, while progressively decreasing to <5% for the shallower LQD discontinuity. The higher errors in Line_2 and Line_5 (Figure 8.10) correspond to the nodes of the ESE part of the models where the erosion by the São Vicente Canyon is simulated. As commented above, these high values are due to simulation issues during erosion.

In general, the error associated with the computed depth of the seafloor and the main discontinuities in our models compared with that measured in depth-converted seismic data is low, indicating that the compressibility/permeability characteristics of the sediment and the decompaction of the different units are overall correct. Despite actual sediment properties could only be tested by drilling a borehole, the relatively low error in the depth of the various interfaces provides an indication that the physical properties defined for the various sediment classes is able to reproduce correctly the stratigraphy of the Marquês de Pombal Plateau and Infante Don Henrique basin.

8.3.2 Measured vs computed porosities

Another way to test the overall reliability of the physical properties that define the sediments of our models is by comparing the final porosities resulting from our simulations with *in-situ* measurements from the IODP Site U1391, located closer to the modelled transects. However, none of the models considered in this study crosses the borehole location, which was drilled in shallower waters in the pathway of the present MOW. To overcome this problem, we built a 1D model defined with sand, silt and clay content compositions as measured from smear slide analysis of the borehole samples (IODP Expedition 339 Scientists, 2013b) (Figure 3.9). For the decompaction operations (eq. 12) the thickness of the units observed in the well has been taken into account. Physical properties assigned to the different sediment types are the same as the ones used for the main 2D models (Table 6.1), as well as the number of sub-layers.

The shallowest porosity value for the measured and computed curves are equal (0.70), while at depths greater than 100 mbsf the exponential trend for the two curves starts differing (Figure 8.11). Measured porosities show a rapid decrease to ~0.5 in the first 20 mbsf of sediments. Similar porosity values are found in the modelling results at ~ 150 m depth. Both measured and computed porosity values range between 0.50 and 0.43 between 200 and 360 mbsf. Deeper than that, the loss in porosity is higher in the computed values compared with the measured ones: the last porosity measurement at Site U1391 (495 mbsf) records a value of 0.42, while at the same depth the computed porosity is 0.35 showing a difference of ~ 20% (Figure 8.11).

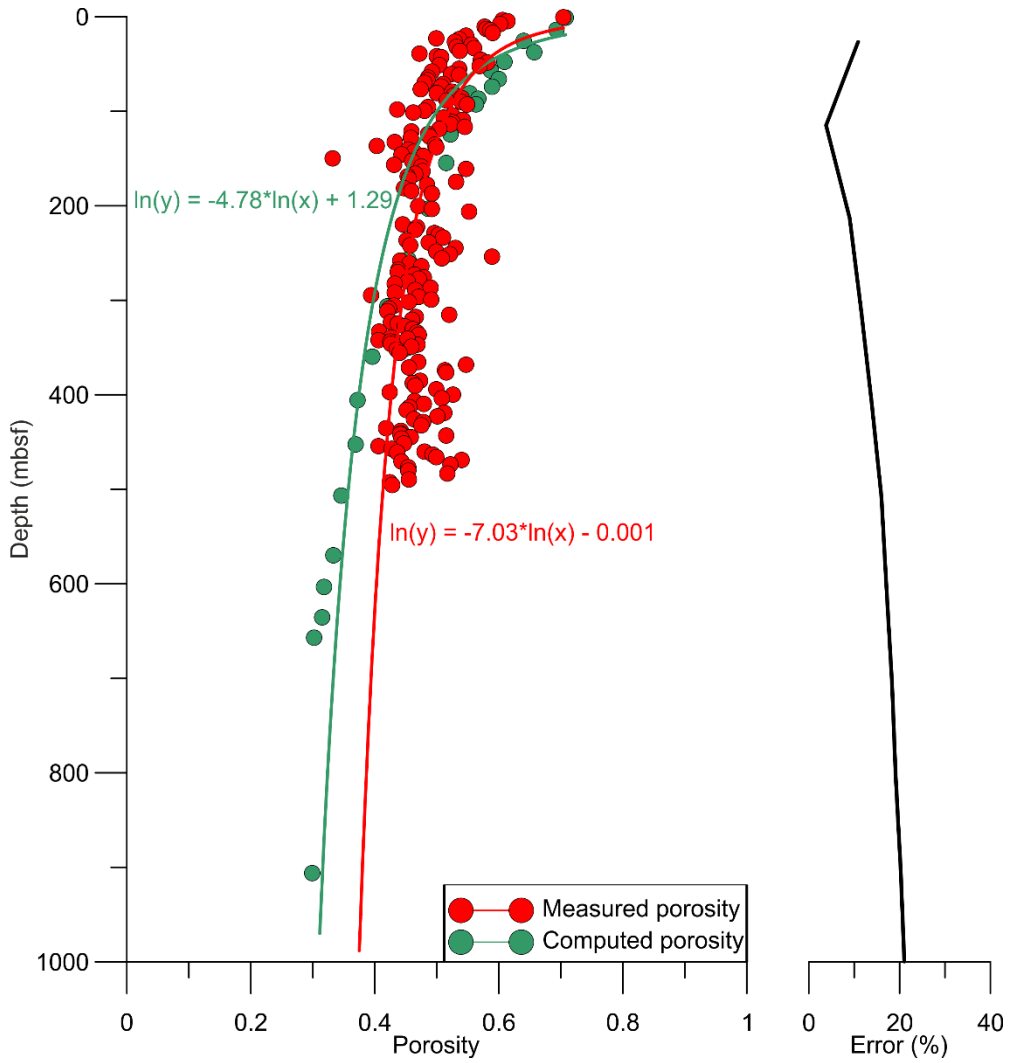

Figure 8.11: Porosity measured at IODP Site U1391 (red points and trend line) vs porosity resulting from 1D model simulating the deposition at Site U1391 (green points and trend line). The plot on the right indicates the differences (%) between the two trend lines.

Comparing the computed vs measured porosity curves at IODP Site U1391, differences are visible both in shallow and deeper stratigraphic levels. The rapid loss in porosity recorded in the first tens of meters in measured values indicates that sand content within Unit IV might have been overestimated in the simulation. This could be related with the different resolution of the two porosity measurements, since in our numerical models Unit IV is composed by only 10 layers while there are multiple measurements performed *in-situ*. The late Quaternary unit at IODP Site U1391 revealed the presence of multiple sand-rich intervals where sand reaches 45% according to smear slide analyses (IODP Expedition 339 Scientists, 2013b). Those intervals are alternated with others where sand content does not exceed 5% (Figure 3.9, Table 3.6), following the changes in MOW hydrodynamic conditions in the middle slope (Hernández-Molina et al., 2016a; Rodrigues et al., 2020). As explained in section 3.4.3.1, our approach consisted in averaging the grain size content within 10 equally spaced intervals composing Unit IV. The resulting values show high sand content for almost all layers deposited after the LQD, where sand content ranges between 10% and 26%.

Considering that approximations and limitations in resolution are inevitable in basin scale models, those differences in resolution might have played a critical role in keeping clay intervals underrepresented in the model. Furthermore, changes in the MOW hydrodynamics in the middle slope generate an alternation between periods of deposition and erosion responsible for the regional discontinuities described in section 2.4.2.

Minor MOW enforcement periods related, for example, with seasonal cycles (Bahr et al., 2015; Sánchez-Leal et al., 2020) might have triggered small-scale, local erosional stages, promoting overconsolidation in the sediments deposited during the Sines drift maintenance stage (Rodrigues et al., 2020). The ~0.07 porosity mismatch in Unit IV should not represent a major issue in the modelled transects as, following our interpretation in Chapter 7, Unit IV in the Marquês de Pombal Plateau is the result of mixed contour current – turbidity current deposition which is not present at Site U1391. In the modelled transects, the "Sand" sediment group is absent in Unit IV since the entire unit is defined with a dedicated "Mixed System" sediment type (Table 5.2), characterized with physical properties collected directly from the deposit (see section 4.2).

Differences in vertical resolution could be responsible also for the greater loss in porosity resulting from our 1D simulation compared with what it has been measured in the IODP Site U1391 below 360 mbsf. In Units I and II, the sand deposition associated with the Sines drift growth stage (Hernández-Molina et al., 2016a; Rodrigues et al., 2020) might be unrepresented in the models due to the lower vertical resolution of these deeper units, resulting in a generalized higher clay content (Table 3.6) and higher porosity loss than what it has been measured *in-situ*. However, as it is explained above, it is very unlikely that the sand in the Sines drift that is deposited under the influence of the MOW could also be found in deeper water settings. Therefore, the sand intervals likely do not play a major role in porosity loss in the lower slope.

8.3.3 Identifying 3D fluid flow issues: overpressures at model intersections

In section 8.1, we show that the lateral fluid flow towards the São Vicente Canyon and the slope areas in the NE side of the Marquês de Pombal Plateau does not have a clear impact on the overpressure development in the study area. Thus, we infer that fluid flow responsible for increasing overpressure within Unit III and IV is mainly vertical. If this assumption is correct, overpressure in the area should be driven mainly by the different sediment accumulation rates that characterize different areas of the Marquês de Pombal Plateau. Those will be higher in the proximity of Unit IV depocenter and decrease moving towards the external parts of the mixed depositional system. Since flow is mainly 1D, overpressure generated at the interceptions between modelled profiles should return similar values, regardless of their orientations.

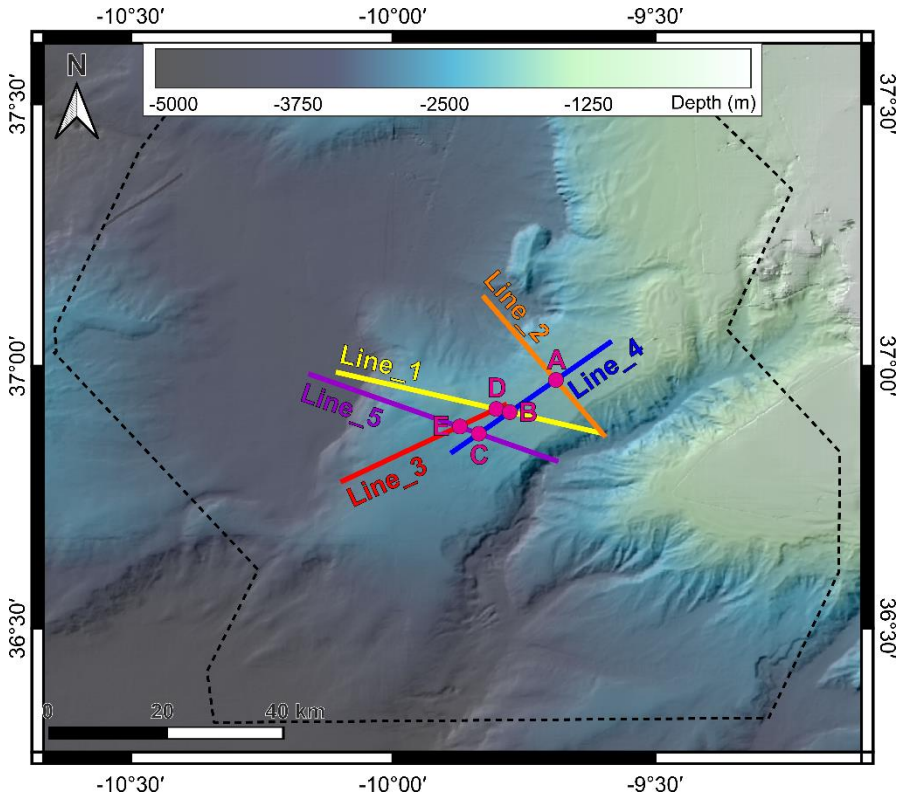

Figure 8.12: Location of the points of interception between the different models. Comparison between the resulting overpressures is shown in Figure 8.13.

Overpressure results at the end of the simulations have been extracted at the 5 interception points of the various models, located within the Marquês de Pombal Plateau. Points A, B and C are located at the interception between the NE-SW oriented models Line_2, Line_1 and Line_5, crossing both slope areas and the São Vicente Canyon, with Line_4. Points D and E represent the interceptions between Line_1 and Line_5 with Line_3 (Figure 8.12).

The resulting computed overpressure (Figure 8.13) indicates a high degree of consistency at all interceptions points. All the curves show similar overpressure trends with depth, with maximum build-up in the swallower sediments, decreasing in the uppermost tens of meters of the stratigraphy before undergoing a slight increase at the base of Unit IV. Below Unit IV, overpressure decreases almost linearly until reaching values between 0.03 and 0.05 at the bottom of the stratigraphy. All intersections show differences in overpressure ratio between 0 and 0.03, with the smaller differences found at Point A and the largest at Point E (Figure 8.13).

Besides almost inevitable small differences, the results shown in Figure 8.13 indicate good match in the overpressure modelled from 2D sections at the different intersections of profiles oriented along different directions and crossing different morphological elements (e.g., the slopes and the São Vicente Canyon). These results indicate that in the Marquês de Pombal Plateau overpressure development is independent from the orientation of the 2D models, meaning that the pore pressure build up is mostly associated with vertical fluid flow, while the effect of lateral flow is responsible only for minor discrepancies in overpressure development at the interception points. Since the

flow is primarily 1D it is not necessary to take into account the 3D orientation of the pore water flow.

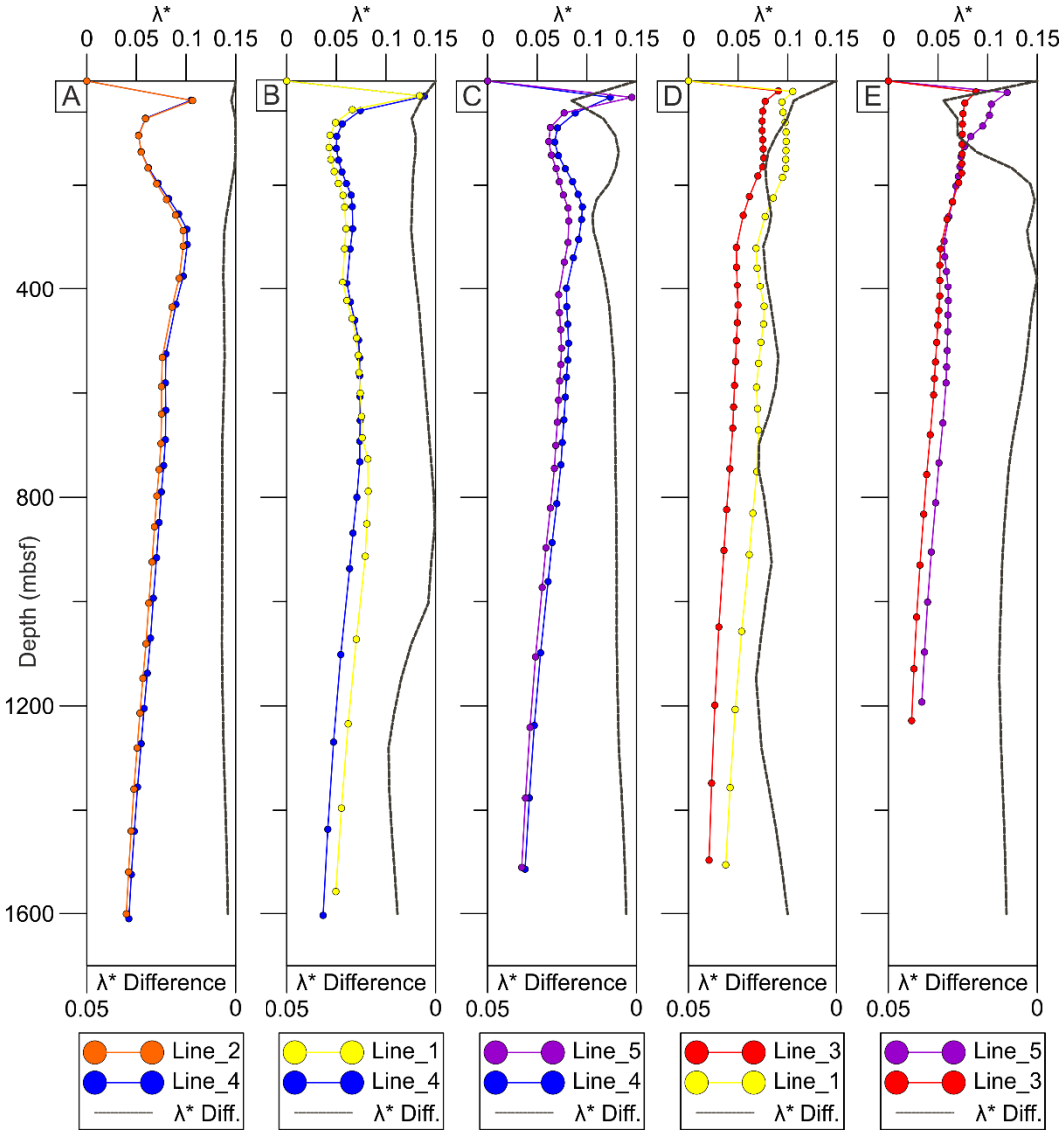

Figure 8.13: Vertical distribution of overpressure ratios at different interceptions between modeled profiles.

8.3.4 Monte Carlo simulations

Without direct pore pressure measurements (such as those provided by penetrometers) it is not possible to evaluate if the models reproduce correctly the development of overpressure in the Marquês de Pombal Plateau. The potential variability in our modelling results can, however, be tested using the expected variation in input parameters in Montecarlo-type analyses.

Modelling studies such as the ones described in this thesis involve inevitable sources of errors, mostly related with transformation and parameter uncertainties that determine the uncertainty of output results (Llopart et al., 2019; Nadim, 2015). Transformation uncertainties are those related with the approximations and simplifications inevitably inherent to the models, and adopted to relate model inputs to model outputs (Nadim, 2015). Parameter uncertainty is related with the

model structure (e.g., seismic data resolution issues, inaccuracies related with time to depth conversion, accuracy of sound speed determination, facies attribution and/or heterogeneity within units) and variability in physical properties (Llopart et al., 2019). A Monte Carlo analysis is here used to test the influence of the variability in sediment physical properties on output uncertainty. The uncertainty related with mechanical and hydraulic properties of the sediments is mostly due to possible inaccuracy during laboratory operations, and to how representative the input physical properties are of sediments in deeper units (see also Methods section 3.4.4 for specific information about the approach adopted).

Given the limited number of geotechnical tests performed in this study, a set of coefficients of variation (C_V) for each physical property and sediment type has been adopted as input for the Monte Carlo analysis instead of the standard deviation (Table 8.2). The set of physical properties created for the Monte Carlo runs has been obtained by using a Simple Random Sampling (SRL) approach in between the range of the confidence interval level of 98%. The Monte Carlo analysis has been performed on Line_4 model, which is located close to the depocenter of Unit IV (Figure 4.1), thus where the maximum overpressure develops (Figure 6.9C). The overpressure resulting from the Monte Carlo runs have been averaged and the standard deviation to the reference model has been calculated (Table 8.2).

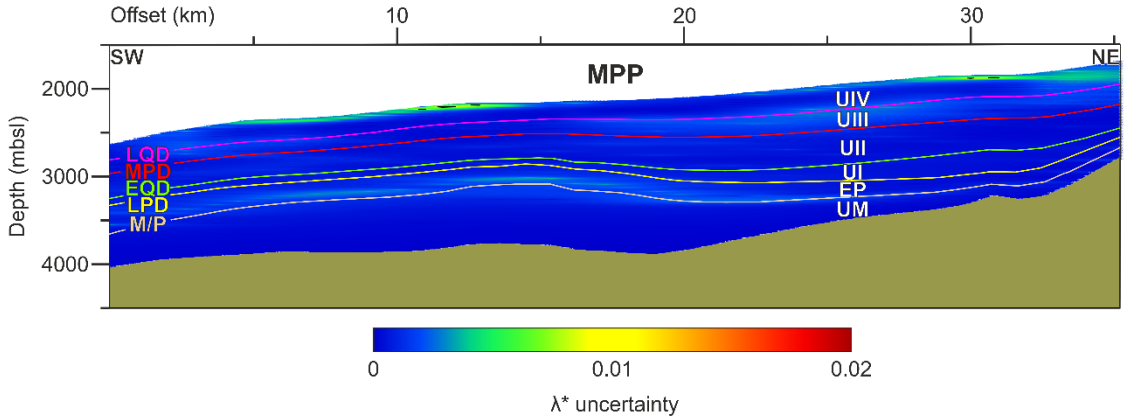

Figure 8.14: Overpressure uncertainty along the model of Line_4 derived from variability in input physical properties using a Monte Carlo analysis over BASIN. EP: Early Pliocene Unit; UM: Upper Miocene. MPP: Marquês de Pombal Plateau.

The Monte Carlo analysis resulted in a mean value of uncertainty for the whole model of ~1%, with maximum uncertainty reaching 2% in the shallowest sediments. The overall low degree of uncertainty of the model indicates that the overpressure resulting from the simulation is not very sensible to the random variation in the physical properties defining the various sediment classes (Clay, Silt, Sand, Mixed System) (Table 6.1) that dominate the models, reflecting their overall homogeneity in physical properties. Only in one of the 64 models of the Montecarlo analysis where all the sediment physical properties correspond to the low members (i.e. minimum specific storages and minimum hydraulic conductivities) the maximum overpressure ratio reached values of ~0.38. The uncertainty reached in the shallower sediments reflects the lateral variability in

Table 8.2: Parameters derived from geotechnical tests in this study, mean values, standard deviation and coefficient of variation range for each physical property and sediment type. Coefficient of variation has been used in the Monte Carlo analysis.

	SdG068-01 190	SdG068-01 187	SdG068-02 102	SdG068-03 244	SdG068-03 84	SdG068-03 144	SdG068-03 137	SdG068-02 207	Literature	All Samples
Sediment type	Clay	Clay	Clay	Clay	Clay	Silt	Silt	Silt	Sand	Mixed System
$Ø_0$	0.69	0.77	0.78	0.74	0.78	0.75	0.77	0.78	0.5	0.75
μ			0.75				0.76		0.5	0.075
σ			0.04				0.02		0.04	0.04
C_v			0.66 / 0.84				0.72 / 0.80		0.41 / 0.59	0.66 / 0.84
Log_{10} (k_0)	-8.94	-	-	-8.32	-	-8.18	-	-	-6	-8.38
μ			-8.63				-8.18		-6	-8.38
σ			0.43				0.434		0.434	0.434
C_v			-9.64 / -7.62				-9.19 / -7.18		-7.01 / -4.99	-9.39 / -7.37
S_0	0.044	0.193	0.033	0.064	0.016	0.044	0.034	0.033	0.001	0.033
μ			0.0352				0.0392		0.001	0.044
σ			0.008				0.007		0.007	0.007
C_v			0.017 / 0.054				0.022 / 0.056		0.0007/0.0013	0.027/0.061

$Ø_0$: initial porosity at 1kPa; k_0: initial hydraulic conductivity at $Ø_0$; S_0: initial specific storage at $Ø_0$; μ: mean; σ: standard deviation; C_v: coefficient of variation range.

maximum overpressure areas as explained in section 8.1, highlighting the influence of small variations in physical properties in the overpressure distribution close to the seafloor.

Higher uncertainty areas (0.2-0.5%) are visible in the transition between the Upper Miocene, characterized by higher sand content, and the Early Pliocene units (Figure 8.15). As explained in section 3.4.3.2, in absence of sand-rich samples from the Alentejo basin to test, "Sand" sediment type is the only sediment class defined with mechanical and hydraulic properties obtained from the literature (Reed et al., 2002), thus with the higher degree of uncertainty.

To test the influence of different properties associated with the "Sand" sediment type on the modelling results, we performed a second Monte Carlo analysis where we tested the variability of physical properties only for the "Sand" lithology, leaving the other sediment types unvaried (Table 8.2). Areas of maximum uncertainty (~1%) are found in the shallower part of the stratigraphy, confirming the sensitivity of shallow overpressure distribution to small changes in physical properties, and within the Upper Miocene and Early Pliocene units. Due to the relatively low sand content within the various units, however, the uncertainty remains low, indicating that changes in physical properties of sand do not involve important changes in the final modelled overpressure (Table 8.2).

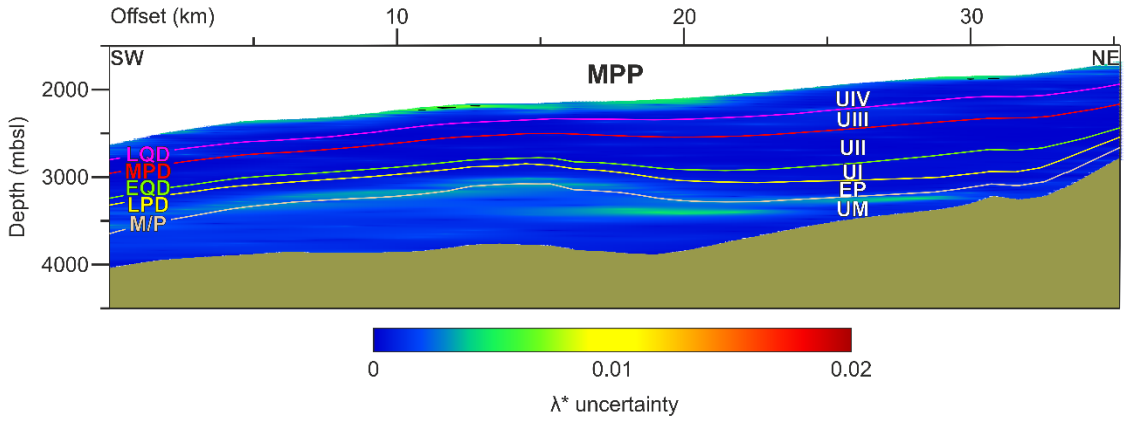

Figure 8.15: Overpressure uncertainty along the model of Line_4 derived from variability in input physical properties only for the "Sand" sediment class, using a Monte Carlo analysis over BASIN. EP: Early Pliocene Unit; UM: Upper Miocene. MPP: Marquês de Pombal Plateau.

8.4 From 2D models to areal distribution of overpressure

In sections 8.2 and 8.1, we showed that the lithostatic load imposed by the Marquês de Pombal Drift deposition is the main driver for the development of overpressure in the Marquês de Pombal Plateau. Lateral fluid flow towards the São Vicente Canyon and the slope areas adjacent to the Marquês de Pombal Fault takes place within the Upper Miocene and Early Pliocene units, but the contribution from such lateral flow to the overall fluid migration and its influence in the development/dissipation of overpressure is minimum, particularly in the shallower stratigraphic units. The role of the Marquês de Pombal Drift deposition in overpressure development appears

clear in Figure 6.10 and Figure 6.14, where the overpressure significantly increases with deposition of Unit IV. Figure 8.13 further indicates that fluid flow is mainly 1D, vertical and largely related to the deposition of Unit IV. The values of overpressure generated at the intersection of the models located farther from the depocenter of Unit IV (e.g., Points D and E in Figure 8.13), in fact, show lower overpressure than those closer to the depocenter (Points A, B, C).

Given the similar compressibility and permeability values of the different sedimentary units (Table 6.1), the main contribution to overpressure build-up is the variation in Marquês de Pombal Drift sedimentation rates. The relationship between the decompacted sedimentation rates of the Marquês de Pombal Drift and overpressure development for the different models (Figure 8.16) allows to make a first order estimate of the overpressure in areas within the Marquês de Pombal Plateau not covered by the 2D simulations. The data reported in Figure 8.16 refers to the maximum present-day overpressure developed at the end of the simulations within Unit IV (the "Mixed System" sediment type, representing the Marquês de Pombal Drift), for the 10 layers composing Unit IV and for all 5 models analysed. Despite the distribution of data in the decompacted sedimentation rate vs overpressure ratio plot shows a considerable amount of scattering, as expected it is possible to see a general increase in maximum overpressure as the sedimentation rate increases (Figure 8.16).

The simplified relationship between decompacted sedimentation rate in Unit IV and overpressure development is expressed by the linear trend (eq. 20):

$$\lambda^* = 0.078 * \ Sed.Rate \qquad (20)$$

The linear trendline is forced to the origin because, in this simplified approach, the overpressure development is only related to the sedimentation rate; thus, we assume that if no sediments are deposited, no overpressure can develop.

Although a clear relationship between Unit IV sedimentation rate and overpressure development is visible in Figure 8.16, a considerable amount of data scatter is also present. This is because the models contain a series of other variables that have an influence in the final overpressure results. First, the models are characterized by different geometries and variable thickness of Unit IV and underlying units. The pore water expelled during compaction of Units I, II and III most likely contributes to the total water volume in the system, which is transferred towards Unit IV, potentially enhancing overpressure build-up in this uppermost unit. Secondly, the maximum overpressure values in most of the models is biased by the occurrence of localized areas of higher overpressure within the uppermost sedimentary sequence that anticipate fluid escape phenomena and vary laterally, as it was documented in section 8.1.

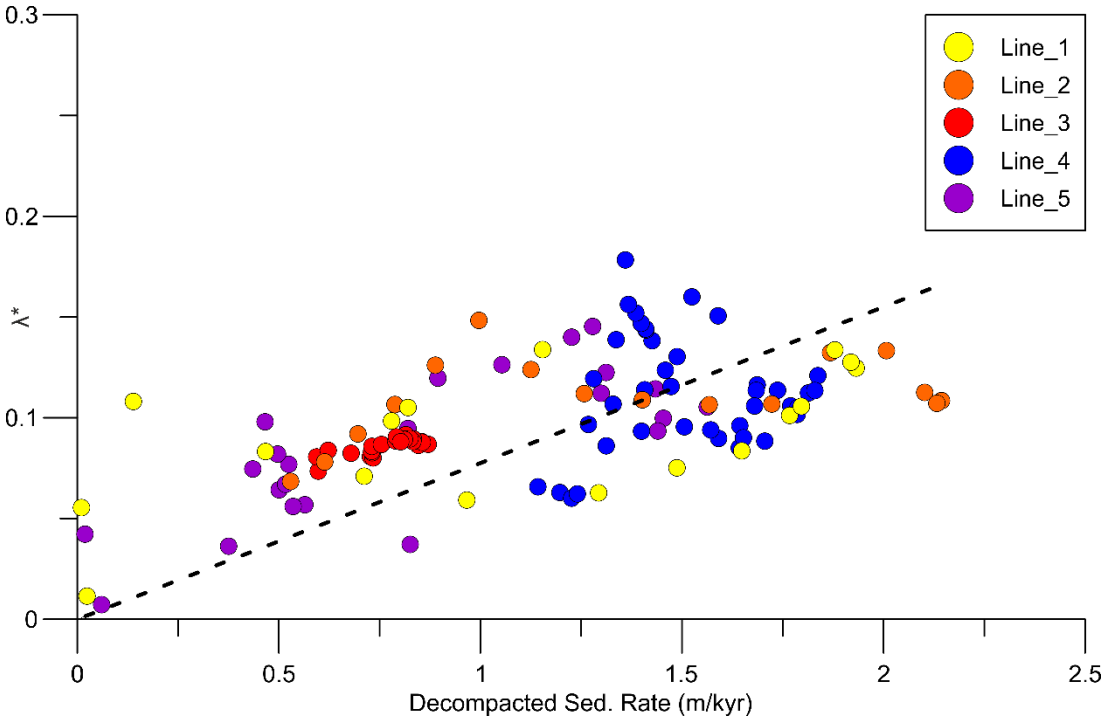

Figure 8.16: Relation between decompacted sedimentation rate and maximum overpressure ratio in Unit IV. The maximum overpressure ratio is calculated from the 10 layers composing Unit IV, where the unit is constituted by the "Mixed System" sediment type. As explained in methods section 3.4.1, in BASIN the lateral resolution is limited to 40 cells; thus, Line_4 is the only model represented by 40 maximum overpressure values since the "Mixed System" sediment type is distributed along the entire length of the model (Figure 6.8A). For the other models, the maximum overpressure values in Unit IV have been extracted only within the range of distribution of this unit ("Mixed System" sediment type).

The position of those localized areas of high overpressure is variable through time (Figure 8.2). Due to the data scatter visible in Figure 8.16, the linear relation adopted to reproduce the increase in overpressure with increasing sedimentation rate in Unit IV (eq. 20) is questionable, thus an additional test has been performed to define the most adequate trend reproducing overpressure development at various sedimentation rates in BASIN. The tests consisted in creating a series of 1D models aiming to reproduce the overpressure buildup only within the Marquês de Pombal Drift, in order to simulate the overpressure generated by the mixed-system deposit self-compaction and exclude the influence of eventual lateral fluid flow or water flow from underlying units. We created a series of 21 1D models composed by 10 sublayers (Table 3.6) and defined with "Mixed System" sediment type physical properties (Table 6.1), in the same way the Marquês de Pombal Drift deposit is defined in the other 2D models considered. The only variable for the different models was the sedimentation rate that increases from 0.01 m/kyr to 10 m/kyr. The resulting maximum overpressure development within the mixed system deposit is shown in Figure 8.17, and indicates that overpressure development increases linearly with sedimentation rate. Accordingly, the relation indicated in eq. 20 is considered valid despite the considerable scatter.

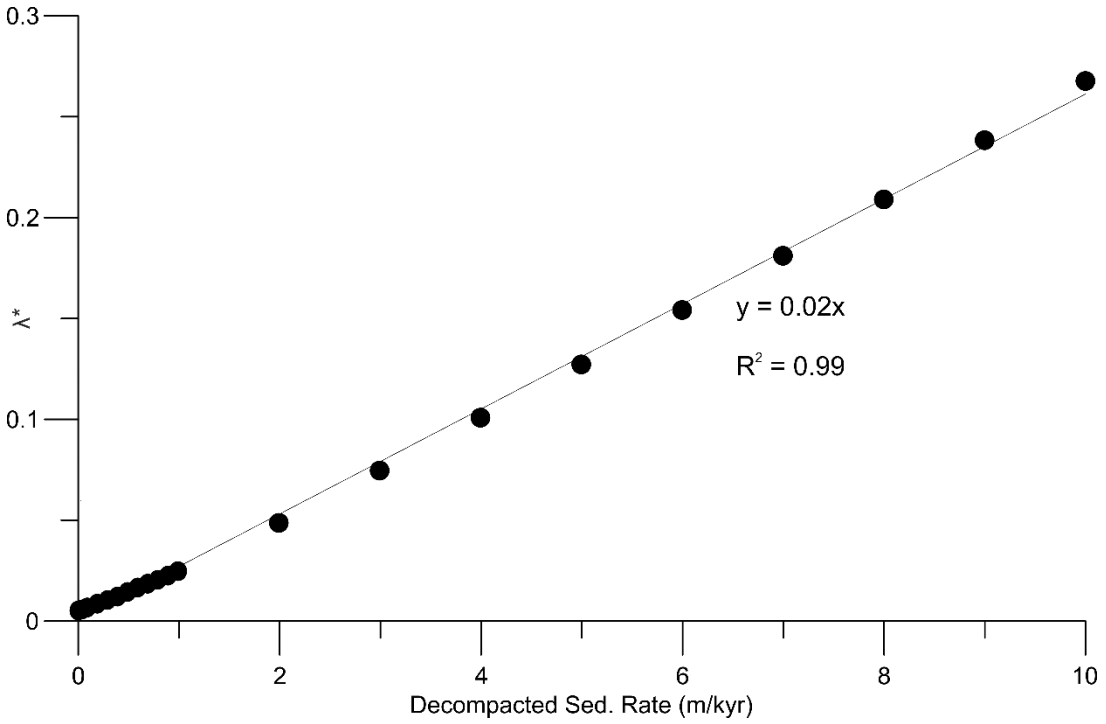

Figure 8.17: Maximum overpressure ratio and decompacted sedimentation rate resulting from 1D modelling test. Each of the 21 models taken in consideration for these tests is composed by 10 layers defined with the "Mixed System" sediment type physical properties (Table 3.6).

By simulating the overpressure development for the Marquês de Pombal Drift at different sedimentation rate conditions, we aim to visualize the relationship between maximum overpressure development and sedimentation rate without being influenced by lateral fluid flow or pore water contribution from underlying units. The relationship in eq. 20 can be used to extend the overpressure results from 2D sections in space throughout Unit IV, using the sedimentation rate map of Figure 4.5D as input. Maximum overpressure values reach ~0.2 in the depocenter of Unit IV, where the decompacted sedimentation rate approaches ~2.5 m/kyr (Figure 8.18). According to the relationship in eq. 20, the overpressure in the Marquês de Pombal Plateau decreases when moving towards the edges of the Marquês de Pombal Drift (Figure 4.5D and Figure 8.18). The relationship between sedimentation rate and overpressure development derived from the Marquês de Pombal Plateau cannot be applied for middle slope areas, such as the Sines drift. The very different depositional conditions generated by the MOW do not allow assuming that development of overpressure could eventually be linked to the sedimentation rate with a similar relationship, since the presence of sand-rich layers in shallower areas could substantially modify the fluid flow conditions. In this regard, the 1D model created to define the porosity trend at the location of Site U1391 (Figure 8.11) resulted in hydrostatic pore water pressure during the entire depositional history. This is not surprising considering the lower sedimentation rate (0.3 m/kyr compacted), lower compressibility and higher permeability associated with the sand-rich contourite sediments of the Sines drift compared with those of the Marquês de Pombal Plateau. In these areas, absence of 1D overpressure build-up implies no potential for lateral transfer of overpressure towards other areas of the slope, in spite of the high permeability sand-rich intervals

bounded by fine-grained sediment units resulting from variations in MOW hydrodynamic and transport capacity.

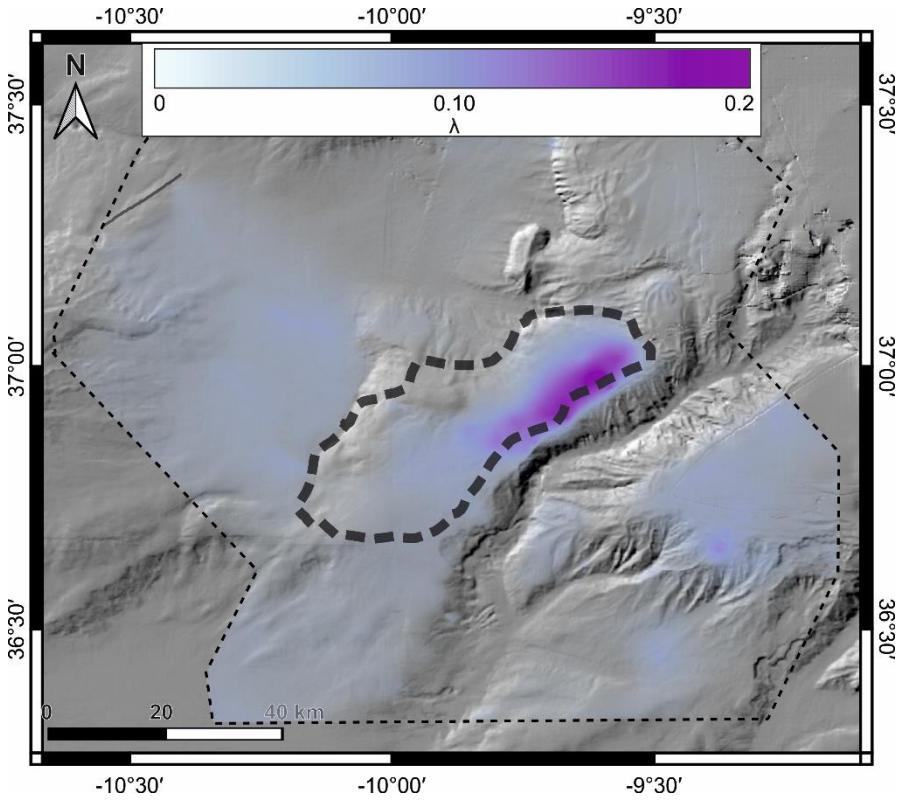

Figure 8.18: Overpressure in the study area as inferred from the relationship between sedimentation rate and overpressure in eq. 20. Dashed outline shows the approximate areal distribution of the Marquês de Pombal Drift (MPD).

Chapter 9: Slope instability in mixed contour current – turbidity current systems: balance between pre-conditioning factors and trigger mechanisms

Overpressure development is often assumed as a likely pre-conditioning factor for submarine slope instability (e.g., only in the Alentejo basin, Neves et al., 2016; Teixeira et al., 2019; Mencaroni et al., 2021). This study and previous ones (i.e., Dugan & Flemings, 2000; Leynaud et al., 2007; Urgeles et al., 2010; Urlaub et al., 2013, 2015; Llopart et al., 2019; Mencaroni et al., 2020), on the other hand, demonstrate that given the characteristics of most marine sediments exceptionally high sedimentation rates are needed to rise pore pressure significantly above hydrostatic to trigger submarine slope failure without invoking additional external factors.

In Chapter 8, we documented how the deposition of the Marquês de Pombal Drift created the conditions for overpressure build-up in the Marquês de Pombal Plateau. The development of excess pore pressure is strictly related with the increased sedimentation rate associated with the mixed turbidity-contourite system. The maximum overpressure ratio values do not exceed 0.2 and are found in the proximity of the Marquês de Pombal Drift depocenter, far from slope areas. In this chapter, we assess the influence of the overpressure in slope stability in the Marquês de Pombal Plateau compared to the effect of major seismic ground motions and some final considerations and conclusions about the modelling results are drawn, discussing the wider implications that can be derived from our study.

9.1 Role of overpressure in slope stability in the Alentejo basin

A preliminary quantification of the influence of the overpressure generated by the Marquês de Pombal Drift deposition on the stability of the slope can be obtained by adopting the simplified static factor of safety (FoS) analysis proposed by Flemings et al. (2008) and already introduced in section 1.6. We used eq. 15 to calculate the FoS (Figure 9.2) associated to overpressure (λ^*) developed from deposition of Unit IV. We adopted the surface slope of the area (Figure 9.1), the overpressure ratio distribution map calculated for Unit IV, described in section 8.4 and shown in Figure 8.18, and a friction angle of 32.5º averaged from the measurements performed by Lee & Baraza (1999) on continental slope sediments of the Gulf of Cadiz. A FoS greater than 1 indicates stable slope, while values lower than 1 are associated with slope instability conditions. Given the uncertainties of adopting a single friction angle for the entire slope system, slopes with resulting FoS values in between 1 and 2 can also be considered in metastable conditions.

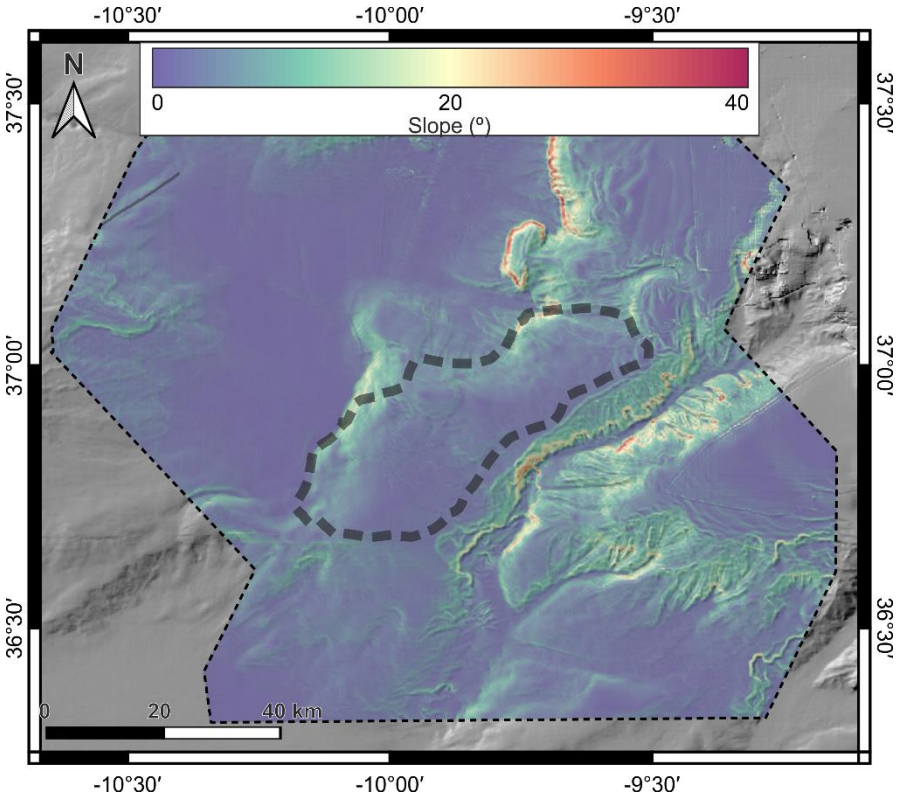

Figure 9.1: Slope gradient distribution in the study area. Dashed outline shows the approximate areal distribution of the Marquês de Pombal Drift (MPD).

Comparison of the slope map (Figure 9.1) with the FoS map (Figure 9.2) reveals that the areas where the FoS < 1 are found where the slope gradient exceeds 30º. This is the case along the Pereira de Sousa Fault scarp (corresponding to the east Sines drift boundary), a restricted slope sector in the north part of the Marquês de Pombal Plateau and multiple areas within the São Vicente Canyon. The slope gradient of the Marquês de Pombal Fault scarp varies between 10º and 15º, and the resulting FoS of the slope reaches minimum values of ~1.5 (Figure 9.2). The slope bounding the Marquês de Pombal Plateau northern part (east from the Marquês de Pombal Fault) shows a lower gradient, not exceeding 5º, associated with a FoS always higher than 4. Within the Marquês de Pombal Plateau, the FoS is mostly > 20, indicating present-day stability of the sediments deposited in the area. The high FoS is associated with the very mild slope within the plateau, where gradient never exceed 4º (Figure 9.1 and Figure 9.2).

It must be pointed out, however, that sediments associated with FoS < 1 under static conditions, likely result from the simplification of omitting sediment cohesion (and its spatial variability) in eq. 15 as well as the lack of spatial variability in friction angle. The fact that our stratigraphic interpretation reveals sedimentary coverage over the steep areas characterized by FoS < 1 indicates that the shear strength of the sediments in these relatively steep areas is underestimated. Additional sources of inaccuracy originate from, first, the fact that we did not perform shear strength tests directly on the sediments collected in the study area, and the friction angle of 32.5º adopted for this calculation has been measured from sediments collected in the internal part of the Gulf of Cadiz (Lee and Baraza, 1999). Given the different depositional conditions of this area

compared with the Alentejo basin (e.g. higher influence of the MOW flow, closer proximity to direct sediment inputs such as the Guadalquivir River and/or potentially higher presence of coarse-grained sediments), the friction angle adopted from the literature might not be representative of the sediments in the study area. Secondly, the FoS map shown in Figure 9.2 refers to sediments not affected by erosion, and therefore the analysis does not take into account different degrees of consolidation of the sediments. As the sediments exposed within the São Vicente Canyon belong to older stratigraphic units, they are most likely characterized by a greater degree of consolidation and thus higher cohesion. Older units likely outcrop in the steeper slopes of the Marquês de Pombal and Pereira de Sousa Fault scarps. In this sense, the FoS map shown in Figure 9.2 must be considered an approximation aiming to provide a general overview of the stability conditions for the sediment in the area and cannot be considered as an accurate estimation of the degree of slope stability.

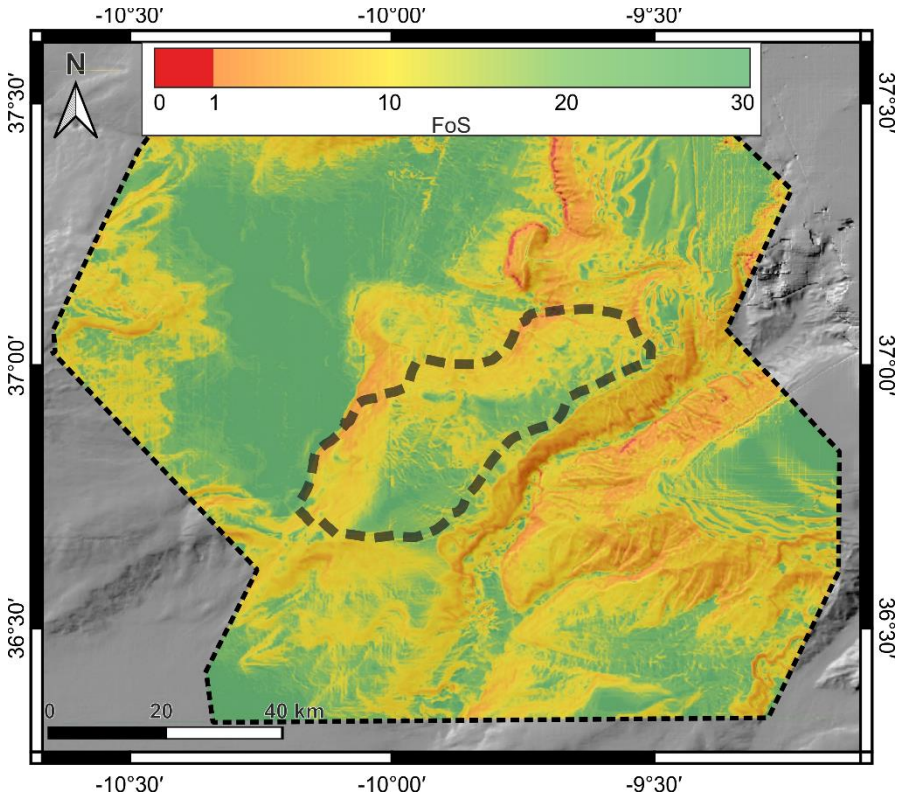

Figure 9.2: FoS distribution in the study area under static conditions by using eq. 15. Dashed outline shows the approximate areal distribution of the Marquês de Pombal Drift (MPD).

In order to quantify the influence of overpressure development within Unit IV as pre-conditioning factor for slope instability in the Alentejo basin, we compared the FoS results shown in Figure 9.2 with an hypothetical scenario where the overpressure is hydrostatic (λ^* in eq. 13 equal to 0). The spatial pattern of the FoS difference between the two maps is that of the overpressure distribution (Figure 8.18). Accordingly, the highest differences between the FoS map considering overpressure development in Unit IV vs the one assuming hydrostatic pore water conditions are found in correspondence of the Marquês de Pombal Drift depocenter. In this area, the differences

in FoS reach 18%, while moving towards areas of lower Unit IV sedimentation rates (Figure 4.5D) the difference becomes null (Figure 9.3).

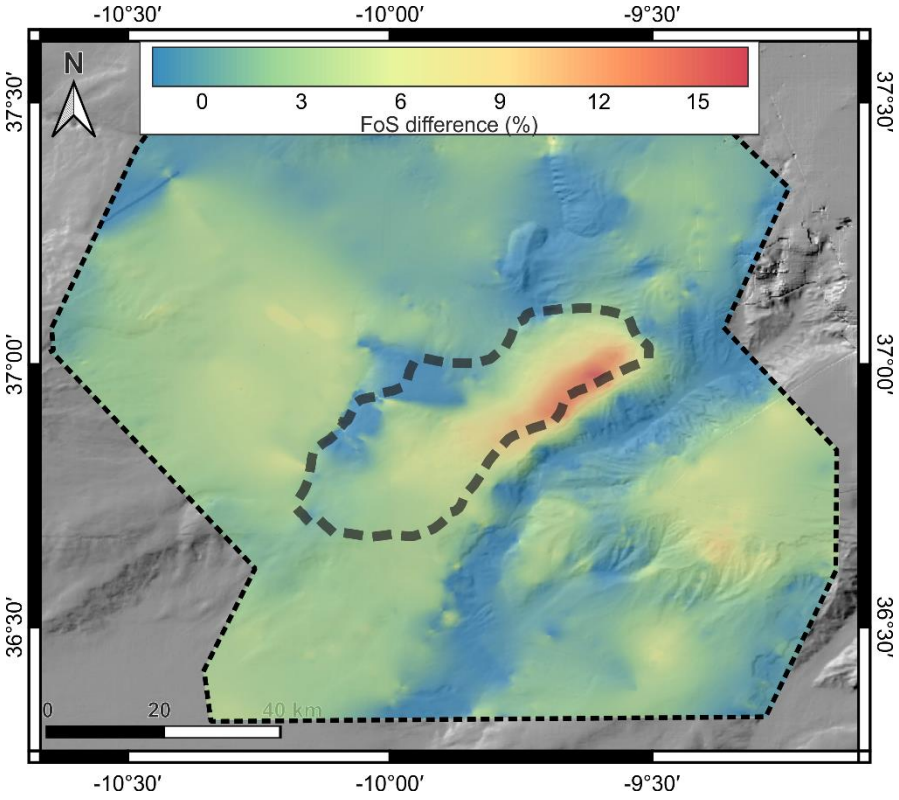

Figure 9.3: Differences (%) in computed FoS resulitng from considering overpressure development from deposition of Unit IV vs that assuming hydrostatic pore water conditions. Dashed outline shows the approximate areal distribution of the Marquês de Pombal Drift (MPD).

Since the area of maximum Marquês de Pombal Drift deposition is associated with mild slope gradients (Figure 8.18), the 18% decrease in the FoS in the Marquês de Pombal Plateau area related with overpressure development does not involve a significant reduction in the FoS, which remains high (> 20) (Figure 9.2 and Figure 9.3). The areas located in the external part of the Marquês de Pombal Drift deposit are associated with low FoS because of their steep slope gradients, despite overpressure is relatively low. In those areas, differences between the FoS accounting for the overpressure vs those under hydrostatic conditions are 0-10% in the Pereira de Sousa Fault scarp area, 0-7% in the Marquês de Pombal Fault scarp and 0-5% within the São Vicente Canyon (Figure 9.3). Despite differences in FoS are smaller, the relatively low overpressure in those areas contributes to decrease the FoS to values close to instability conditions (FoS < 1), thus a small contribution from overpressure should be carefully evaluated too.

Overpressure development has been proposed as one potential key element favouring the emplacement of multiple MTDs in the Alentejo basin (Mencaroni et al., 2021; Neves et al., 2016; Teixeira et al., 2019). Our results show that overpressure contributes to decrease the FoS up to 18 % only in gentle slope areas within the Marquês de Pombal Plateau, where the slope is the most

stable. On the other hand, FoS close to 1 associated with steep normally-consolidated sediments indicates that the slope gradients play a more important role as pre-conditioning factor even where overpressure development is minimum. The influence of slope gradient compared with that of overpressure development is highlighted by Figure 9.4, where MTDs and landslide scars in the area are plotted together with the FoS. Landslide scars, from which the MTDs originate, are found within high slope gradient areas where the FoS is close to 1. In particular, most of the scars are found within the steep flanks of the São Vicente Canyon (Figure 9.4). It should be remarked that the consideration on slope angle applies only where normally consolidated sediments are present, as those areas are likely to display erosional processes and past mass-wasting activity, which likely produced overconsolidated sediments. For those sediments the strength input parameters used in eq. 15 are likely underestimated, if not invalid.

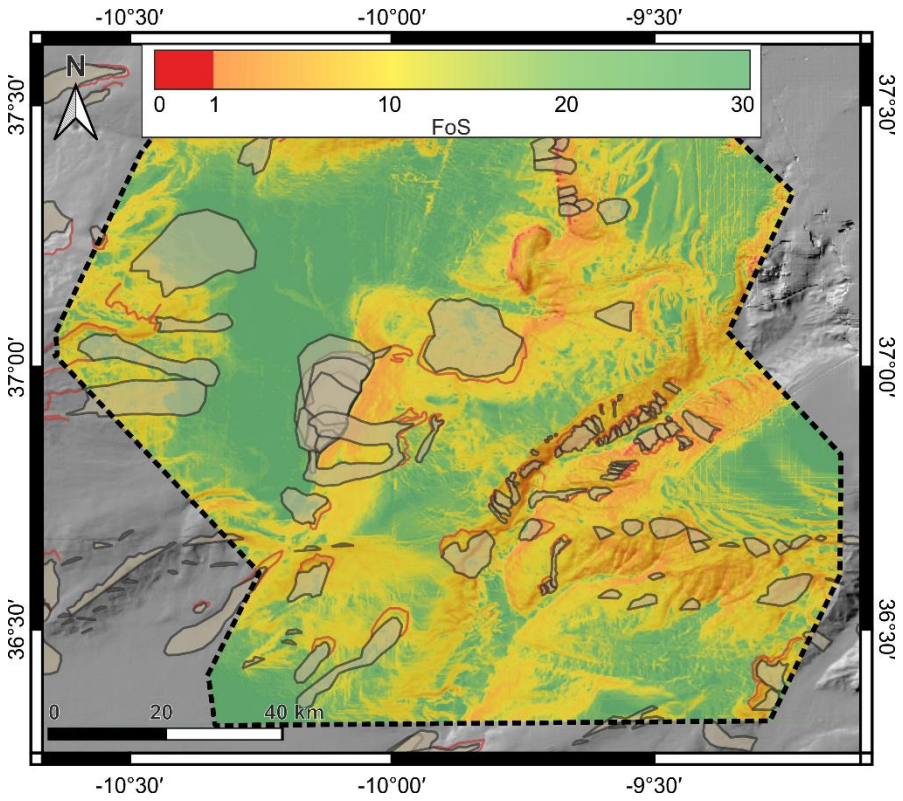

Figure 9.4: FoS distribution in the study area plotted together with landslides scars (yellow lines) and MTDs (blue polygons).

The primordial role of slope gradient on landslide occurrence has also been shown by Teixeira et al. (2019), especially for the Sines drift. This pattern of slope failure distribution occurs in spite of the generalized vertical fluid flow, as shown from our simulations, implying little transfer of overpressure to areas of lower Unit IV overburden. The hypothetical presence of a higher permeability unit, however, could potentially contribute to lateral fluid flow and transfer overpressure towards the slope area, decreasing slope stability in the same way that it has been observed in the Ursa basin (Flemings et al., 2008). In absence of further information about the grain size distribution of the units in the Marquês de Pombal Plateau area, this is an element of uncertainty in the analysis. In the same way, it must be remembered that the physical properties

have been tested on gravity cores collected in the first few meters of the sediment column, and sediment classes to the deeper units have been assigned based on expected sediment distribution. Figure 8.4 shows that the overpressure models are very sensitive to the input permeability, thus the inevitable uncertainty about the physical properties of deeper units adds uncertainty to the results.

As final consideration, Figure 9.4 shows that most of the MTDs and scars in the study area are located in the proximity and within the areas where the FoS approaches 1, although only in localized, very high gradient slopes the FoS is <1. This indicates that an external trigger needs to be invoked to justify the mass wasting processes. Previous studies (Collico et al., 2020; Garcia-Orellana et al., 2006; Gràcia et al., 2010; Lo Iacono et al., 2012; Minning et al., 2006; Sallarès et al., 2010; Vizcaino et al., 2006) suggest that earthquake shaking induced by the multiple active faults in the area of interest is the most likely triggering mechanism for the slope failures. Attempts have also been made to correlate ages and sizes of mass transport deposits with faults dislocation to derive information about earthquake rate of recurrence and magnitudes (Gràcia et al., 2010; Minning et al., 2006; Vizcaino et al., 2006). Because most of the MTDs in the area originate from steep (> 15º) slopes that are close to instability (Figure 9.4), the minimum earthquake magnitude required to generate the failures observed in the area is probably small. In the next section, we analyse how earthquake-induced accelerations possibly generated by the nearby Marquês de Pombal Fault could influence the slope stability.

9.2 Pseudo-static analysis of slope stability under earthquake-induced acceleration

The static FoS analysis described in section 9.1 allowed to visualize the overall stability condition of the slopes, and to evaluate the role of pre-conditioning factors such as overpressure development and slope gradient for the emplacement of MTDs. In this section, we want to provide an overview of how a transient event such as an earthquake could affect the stability in the Alentejo basin. The aim is to compare the impact of pre-conditioning factors analysed in section 9.1 vs triggering events in decreasing the stability of the slopes.

As explained in section 2.2 and 7.3, the moderate-to-high seismic activity in the SW Iberian margin (Martínez-Loriente et al., 2018, 2013; Silva et al., 2017; Stich et al., 2005) indicates seismic shaking as the most obvious triggering mechanism for the multitude of MTDs and scars detected in the area (Figure 9.4). The Marquês de Pombal Fault is the seismogenic structure located closest to the Marquês de Pombal Plateau, thus to the area of maximum overpressure development in the study area. We adopted the pseudo-static approach proposed by Collico et al. (2020) to analyse the effect of earthquake acceleration induced by the Marquês de Pombal Fault on the FoS of the area (see section 3.5).

The earthquake hypocenter is assumed to be located at the centre of the Marquês de Pombal Fault plane, at 9.5 km depth. Fault plane polygon and information have been collected from the European Database of Seismogenic Faults (EDSF) (Basili et al., 2013; García-Mayordomo et al., 2012). The maximum earthquake magnitude for the Marquês de Pombal Fault reported in the EDSF database is 7.8 assuming full-length fault activation (see also Gràcia et al., 2003a; Terrinha et al., 2003), which is plausible considering the Quaternary time-frame. Maximum PGA values of 0.82 g are expected in the vertical projection of the fault plane centre given the ground motion attenuation relationship of eq. 16, while minimum values in the more external parts reach 0.12 g (Figure 9.5). Nevertheless, Serra et al. (2021), using the empirical scaling relations proposed by Leonard (2014), propose that given the length and width of the fault the maximum earthquake magnitude that can be delivered by the Marquês de Pombal Fault is 7.15. Those would result in significant reduction of the estimated PGA.

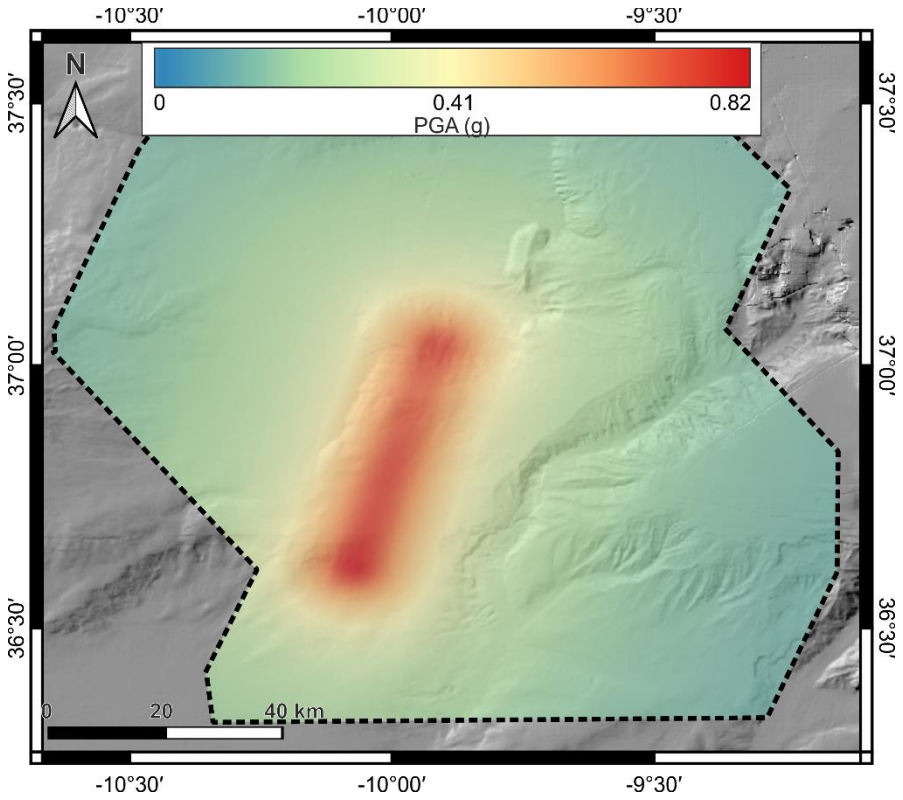

Figure 9.5: Maximum PGA (eq. 16) expected for the study area in case the Marquês de Pombal Fault activates at full length. In absence of direct measurement, the normalized undrained shear strength adopted in our formulation is 0.41, as determined from Bayesian statistics by Collico et al. (2020) on sediments collected in the Gulf of Cadiz (Lee and Baraza, 1999; Minning et al., 2006).

The factor of safety calculation resulting from the pseudo-static analysis (eq. 17) and shown in Figure 9.6 indicates that, in case of a 7.8 M_W earthquake generated from the Marquês de Pombal Fault, the FoS along the entire study area would be considerably reduced compared to the static conditions. The entire Marquês de Pombal Plateau area records FoS values < 1, as well as the majority of the steeper slopes (e.g., the flanks of the São Vicente Canyon and the Pereira de Sousa Fault scarp) and the part of the Infante Don Hernrique basin closer to the epicentre. Most of the middle slope areas (e.g., Sines and Sagres drifts) are characterized by FoS ranging between 1.5

and 3, in a similar way to the most epicentre-distal part of the Infante Don Henrique basin. Thus, in case of an earthquakes triggered by full-length rupture of the Marquês de Pombal Fault, failures could involve significant parts of the Marquês de Pombal Plateau and from the steepest slopes in the study area (> 5º) while, despite a radical reduction in FoS (from > 20 to < 3, see Figure 9.2), the middle slope areas would not fail.

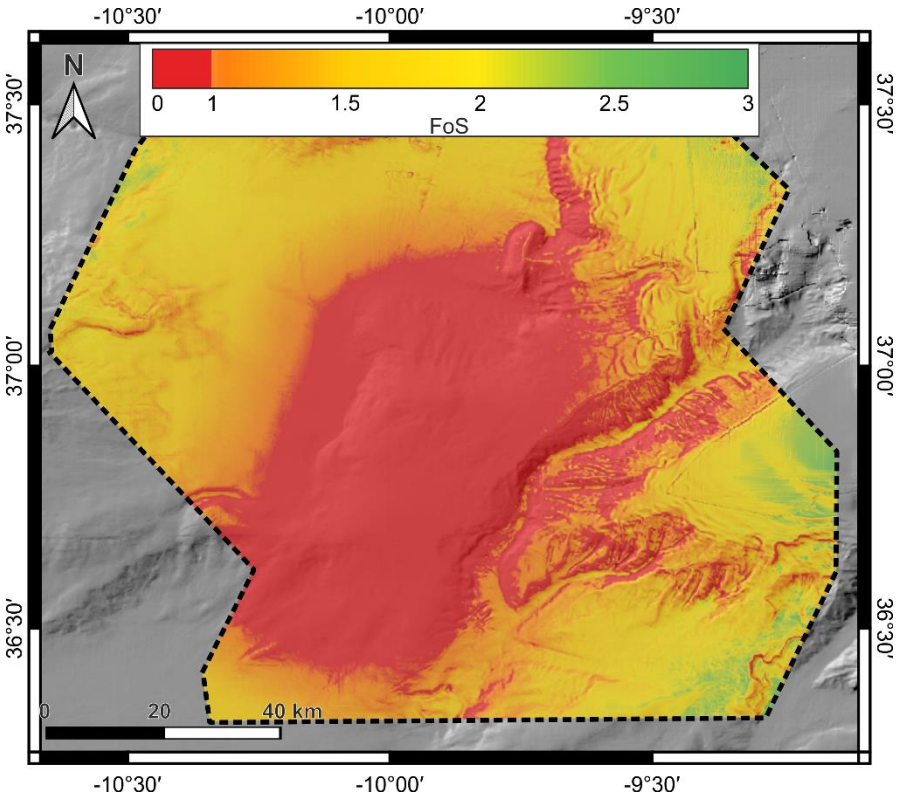

Figure 9.6: FoS resulting from pseudo-satic analysis (eq. 17) of earthquake acceleration induced by the Marquês de Pombal Fault activated at full length.

The results from the pseudo-static FoS analysis provide a rough estimation of the effect that the worst-case earthquake scenario generated from the Marquês de Pombal Fault would have on the stability of the slope. Although earthquake shaking in the study area could be triggered by dislocation of other more distant faults, thus the PGA in the area could be considerably lower, this test allows to compare the effect of pre-conditioning factors vs triggering mechanisms on reducing the slope stability in the Alentejo basin. The static FoS analysis described in section 9.1 demonstrate how the stability of the slopes in the Alentejo basin is mostly driven by the slope gradients rather than overpressure development. The areas of maximum overpressure, generated by the Marquês de Pombal Drift deposition, is the mild slope area associated with the Marquês de Pombal Plateau where maximum overpressure ratios of 0.2 are not able to induce slope instability. On the other hand, large magnitude earthquakes originating at the Marquês de Pombal Fault would heavily affect the stability of the whole study area, decreasing dramatically the FoS even in mild slopes.

9.3 Assessing overpressure with translocated data: significance for submarine slope instability

The development of overpressure in a submarine slope affects the magnitude of the events that can trigger a failure (e.g., earthquakes) or, in case of very high values and/or steep slopes, can lead to slope instability without external trigger (Stigall and Dugan, 2010; Urlaub et al., 2015). By adopting the simplified FoS equation (eq. 15) (Flemings et al., 2008), we can assess the consequences of overpressure resulting from the 1D models at Site U1324 (Figure 5.5 in Chapter 5) on an hypothetical 2º slope using physical properties from sediments in different sedimentary environments. In this case, a single friction angle θ_f of 28º, as measured on hemipelagic sediments of the Ursa basin by Urgeles et al., (2007) is adopted, despite such value could also change depending on sedimentary environment.

The FoS has been calculated on the surface corresponding to the horizon deposited 40 kyrs ago, corresponding to the beginning of the mud dominated channel levee assemblage, for the time interval comprised between its deposition and present day (Figure 9.7). As the FoS decreases with increasing overpressure, the model generated defining the hemipelagic units with the physical properties from the Alentejo and the original Ursa basin reference model, show a decrease in the factor of safety until ~20 ka. At this point, the lower sedimentation rate associated with hemipelagic sediment deposition dissipates overpressure (Figure 9.7). The FoS for these two models reaches a minimum FoS of around 3, increasing up to five towards present. On the contrary, the model where the hemipelagic layer is defined with the physical properties from the Grenada basin shows an increase in overpressure values also after 20ky. This is because the deposition and compaction of the already low permeability (at depositional conditions) hemipelagic sediments creates a seal, which prevents the water from the lower part of the stratigraphy to flow upwards. In this case, the FoS reaches values of around 2 which remain almost constant from 20 ka to present-day (Figure 9.7).

At the end of the simulations, none of the models result in a FoS low enough to induce the slope to fail (<1) in the considered stratigraphic level. Nevertheless, 1D sedimentation models at Site U1324 show a completely different overpressure development history when the model is defined with the hemipelagic sediments from the Grenada basin, resulting in a considerable underestimation of the factor of safety at the base of the first-deposited fine-grained sedimentary unit. The results therefore show that physical properties derived only from the lithological characterization or the grain size distribution may produce inaccurate overpressure models, with consequent misleading slope stability estimations.

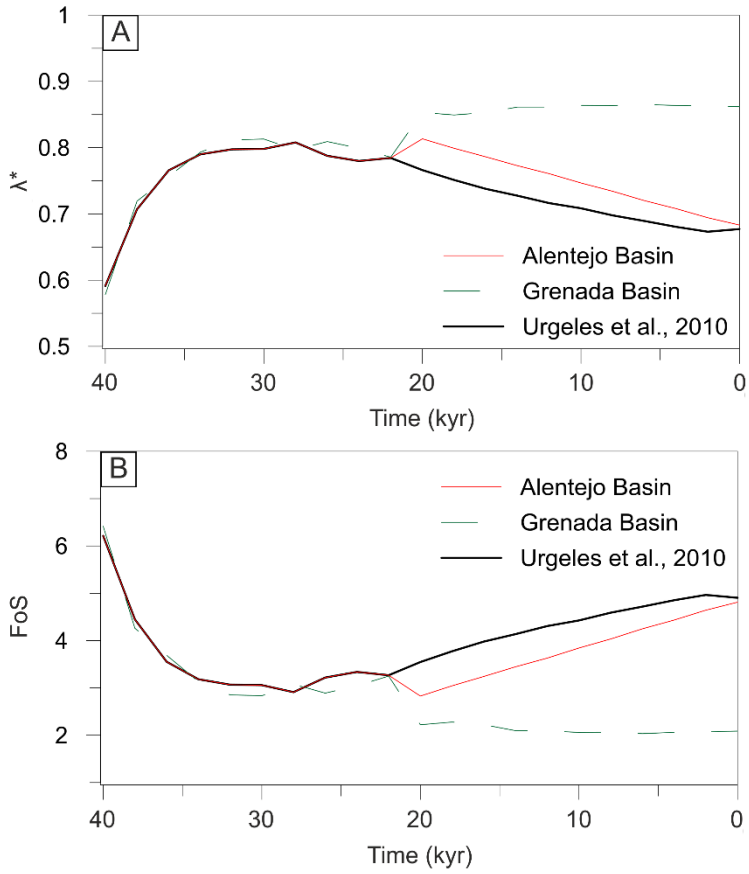

Figure 9.7: Overpressure evolution during the last 40 kyrs (a) and computed factor of safety (b) for all models at location of IODP Site U1324. The graph refers to the base of the fine-grained channel levee assemblage unit, which started depositing ~40 kyrs ago.

On the other hand, models based on physical properties derived from similar grain size, depositional environment and expected compositional nature of sediments provide similar overpressure development results. This indicates that, in absence of direct measurements, literature derived physical properties based not only on grain size characteristics, but also on depositional setting, are expected to produce more accurate overpressure development for stability analysis of submarine slopes. Special care should be taken in settings where presence of microfossils such as diatoms, initial cementation or volcanic glass particles could provide sediment structuration.

PART V

CONCLUSIONS AND FORWARD LOOK

Chapter 10: Conclusions

The combined analysis of the geophysical dataset, core data, geotechnical tests and 2D hydrogeological models allowed to improve our knowledge about the depositional processes taking place in the Alentejo basin, and to understand their influence on the slope instabilities in the area. With regard to the main hypothesis put forward in section 1.1, we will now briefly elaborate to approve it or refute it.

Seismic data and sediment cores presented in section 4.1 and discussed in Chapter 7 reveal the existence of a previously unknown, ~ 500 m thick, silt-dominated sedimentary body on the slope north-west of the São Vicente Canyon, which was largely deposited during the late Quaternary in concurrent development with the canyon. Sedimentation rate in this deposit increased 10-fold from the late Pliocene to the late Quaternary, from values not exceeding 0.2 m/kyr to values up to 2 m/kyr. The sedimentary body is interpreted as the result of a mixed downslope-alongslope sedimentary system generated from the interaction between the MOW and turbidity currents travelling along the São Vicente Canyon and has been named "Marquês de Pombal Drift". The deeper parts of the drift are likely active only during glacial periods when the MOW settles deeper, as present conditions are not favourable for transport of the grain-size fraction present over the drift. The peculiarity of this mixed turbidite-contourite system, with respect to the previously reported mixed systems, is that it develops adjacent to a canyon the incision of which (up to 1.5 km) exceeds the height of turbidity currents by several hundreds of meters, thus direct interaction between down-slope and along-slope currents is unlikely to take place. The mechanism by which sediment traveling along the São Vicente Canyon is incorporated in the MOW is likely related to the density contrast in between water masses, here namely the MOW and North Atlantic Deep Water (NADW), along which a nepheloid layer can form. The coarser particle fraction within gravity flows would settle in the canyon, while the finer sediments in the intermediate nepheloid layer would be incorporated in the deeper MOW core (ML). These finer sediments are finally deposited on the north-west slope of the canyon, originating the mixed turbidite–contourite sedimentary body.

The hydrogeological modelling results presented in Chapter 6 and discussed in Chapter 8 suggest that maximum overpressure ratio in the Alentejo basin reaches ~0.2. Fluid flow and overpressure evolution show that excess pore pressure development is strictly associated with the deposition of the Marquês de Pombal Drift, since almost no overpressure develop before the LQD, when the mixed contour current – turbidity current started depositing. Overpressure is distributed especially within the two uppermost units (Unit III and IV) and the lateral distribution of overpressure zones varies as a consequence of localized lateral fluid flow and overpressure dissipation processes.

Tests performed on models defined with different hydraulic conductivity and sedimentation rates suggest that permeability and compressibility values defining the Marquês de Pombal Drift deposit do not generate the conditions needed to develop overpressure ratios higher than 0.2. Under the resulting overpressure conditions, the static factor of safety calculation suggests that the contribution of overpressure development as pre-conditioning factor for the emplacement of MTDs in the Alentejo basin is rather low, while the areas displaying the lower FoS (i.e. lower slope stability) are associated with steep slopes. Thus, slope gradients represent the most relevant pre-conditioning factor favouring slope instability under static conditions in the area.

The modelling effort described in this thesis allows to infer that, the MTDs distributed around the Marquês de Pombal Drift have been mostly facilitated by the presence of steep slopes, while triggering events (i.e., earthquake shaking) are needed to generate the observed slope failures. Factor of safety values lower or close to 1, indicating slope areas prone to failure, are associated with slope angles > 15º. Slope gradients have thus a much stronger control over slope instabilities than overpressure development given the physical properties and sedimentation accumulation rates identified in the Alentejo basin.

Overpressure development is typically invoked as a likely pre-conditioning factor to justify the emplacement of mass transport deposits in marine geohazard studies. In this thesis we found that even in presence of sedimentation rates ~2 m/kyr and hydromechanical properties (permeability and compressibility) of sediments in line with typical values for fine marine sediments, high overpressure values able to affect the stability of a mild submarine slope are hard to reach.

Having analysed the main hypothesis of this study, the scientific objectives introduced at the beginning of this thesis (section 1.2) are resolved as follows:

1. ***Identify mechanisms of interaction between bottom current and sediment travelling within deeply incised submarine canyons.***
    a. *What type of interaction take place between the Mediterranean Outflow Water (MOW) and the deeply incised São Vicente Canyon?*

The depth of incision of the São Vicente Canyon does not allow direct interaction between bottom currents and downslope sediment transfer within the canyon. We infer that the finer fraction of sediment gravity flows within the canyon is incorporated in the MU bottom current with the mediation of nepheloid layers that detach at the interface between major water masses.

    b. *How does contourite deposition and São Vicente Canyon erosion influence the sedimentation in deeper areas of the Alentejo basin, such as the Marquês de Pombal Plateau?*

The stratigraphic analysis, combined with oceanographic and core data, confirms that a contourite depositional system in the Alentejo basin emplaces in the middle slope, approximately between

800 and 1400 m water depth. This depth interval corresponds to the present-day MU depth of flow. However, our study shows that influence of the MOW in the sediment distribution in the area is not limited to the middle slope, since the Marquês de Pombal Drift deposited down to ~ 2000 m water depth. This is due to the action of the lower MOW core (ML), which is capable, especially during glacial periods, of transporting the suspended fine-grain sediments incorporated in nepheloid layers out of the canyon, depositing them in the Marquês de Pombal Plateau. Erosion along the São Vicente Canyon, which developed since the Quaternary almost concomitant with the Marquês de Pombal Drift, acts as the main direct source of sediments to the drift.

2. ***Understand how does sediment physical properties and sedimentation rates of mixed contour current – turbidity current systems affect the development of pore pressure.***
    a. *How does fine-grain sediments and high sedimentation rate associated with the Marquês de Pombal Drift deposition influence the development of overpressure in the Marquês de Pombal Plateau?*

Physical properties and sediment accumulation rates of the fine-grained Marquês de Pombal Drift sediments do not allow the development of overpressure in the Alentejo basin exceeding values of ~ 0.2. Despite the physical properties of the sediments collected in the Alentejo basin are in line with what has been measured on similar fine-grained sediments in other marine basins, the results show that sediment accumulation rates resulting from development of the Marquês de Pombal Drift (~ 2 m/kyr decompacted at depocenter) are too low, given the permeability of the sediments, to develop enough overpressure to impact the stability of the slopes.

    b. *How does lateral fluid flow towards the São Vicente Canyon and the Marquês de Pombal Fault influence the development of pore pressure?*

The hydrogeological models show that lateral fluid flow towards the São Vicente Canyon and the Marquês de Pombal Fault has a minimum impact in overpressure development. This is mainly related to the fact that lateral flow takes place within deep stratigraphic units (Upper Miocene and Early Pliocene), from which the fluid flow and pore water volumes contribution towards shallower units is minimum. The largest uncertainty related with the influence of the São Vicente Canyon as potential element for overpressure dissipation remains, however, the possible presence of one or more high permeability layers within Units III and IV. If undetected coarse-grained layers were present within these units, they would most likely play an important role in connecting areas of high overpressure with the canyon, potentially reducing the overpressure in the centre of the Marquês de Pombal Plateau, but likely increasing it along the shallow subsurface of the canyon.

3. ***Evaluate the suitability of hydrogeological models based on literature-derived physical properties of sediments collected from similar depositional environments and with comparable grain size distributions.***

a. *How does the definition of hydrogeological model with physical properties (porosity, permeability and compressibility) measured from sediment collected in the study area affect the reliability of resulting overpressure?*

We demonstrate that fine-grained marine sediments collected from different sedimentary environments (volcanic-influenced vs. river-dominated) can result in differences in overpressure in excess of one order of magnitude. Phenomena such as structuration of marine sediments need to be carefully considered when carrying out basin hydrogeological models. Our results support the idea that, to achieve accurate results, besides accurate stratigraphic architecture and ages of units, hydrogeological models should be defined with physical properties measured from samples collected in the study area. In instances where such an approach is not feasible, assigning an initial void ratio, hydraulic conductivity and specific storage extracted from the literature for samples with similar expected lithologies, composition and depositional settings are likely to provide the most accurate estimates.

4. ***Assess the significance of pre-conditioning factors versus trigger mechanisms in a seismically active area.***

a. *What is the contribution of pore pressure development generated by the mixed contour current – turbidity current on the emplacement of MTDs in the Alentejo basin?*

Overpressure development does not seem to represent a primary pre-conditioning factor for the emplacement of MTDs in the Alentejo basin. Static factor of safety calculations indicate that values lower or close to 1, indicating conditions of slope instability, develop in correspondence of the steepest slopes in the Alentejo basin (> 15º) where overpressure development is almost absent (e.g., Pereira de Sousa Fault scarp, Marquês de Pombal Fault scarp). However, in the Marquês de Pombal Plateau, where maximum overpressure ratios of 0.2 develop associated with the Marquês de Pombal Drift depocenter, is characterized by slope gradients of ~3º. In presence of such gentle slope, much higher overpressure would be required to create the conditions for sediment instability. Slope gradient is considered to have a stronger control as pre-conditioning factor for slope instability than overpressure development in the Alentejo basin.

b. *What is the influence of pre-conditioning factors (i.e. overpressure development, slope gradient) compared with triggering mechanisms (i.e. earthquake shaking) in decreasing the slope stability in the area?*

A pseudo-static slope stability analysis under earthquake-induced acceleration shows that, in case of hypothetical full-length rupture of the Marquês de Pombal Fault (M_W 7.8 earthquake), the FoS would decrease below 1 within the entire Marquês de Pombal Plateau area and other sectors of the Alentejo basin, indicating widespread slope instability conditions. These results indicate that earthquake shaking, often assumed as the most likely triggering event for slope instabilities, has

a much stronger influence for the emplacement of the MTDs found in the Alentejo basin compared with pre-conditioning factors such as overpressure or slope gradient, particularly considering the frequent seismic activity in the area.

Chapter 11: Forward look

In this thesis we document the existence of a mixed contour-current turbidity current system that develops by the interaction of downslope sediment transport taking place within the São Vicente Canyon and alongslope MOW flow. To support these results, we made use of published and newly collected MCS profiles, core data and oceanographic profiles obtained from publicly available databases. In a second stage of the study, we quantified the potential development of overpressures related with the mixed system deposition by making use of numerical models, and quantified their impact as pre-conditioning factor for the slope instability in the study area.

In this last chapter, we introduce some ideas about data, methods and analysis that might improve the reliability of our stratigraphic interpretation and modelling results, as well as potential next steps to improve the understanding about the effect of mixed contour/turbidity current system deposition for slope instabilities.

11.1 *In-situ* and laboratory measurements and calibration points

As explained in chapter 3.4.3.4 and 8.3, many elements of uncertainty are inevitably related with this study. The most important follow up of this project would be the acquisition of *in-situ* data that could prove the assumptions that have been put forward for the proposed depositional models and the following hydrogeological models. Within other aspects, three type of *in-situ* and laboratory measurements would allow to strengthen the reliability of our results:

a. Stratigraphic distribution:

One of the most significant elements of uncertainty related with this thesis is the lack of deep stratigraphic information for the lower slope in the Alentejo basin. In absence of other data, the reference stratigraphy adopted has been the one derived from the IODP Site U1391, drilled in the middle slope with the aim of understanding the influence of the MOW hydrodynamics in the development of the contourite depositional system. After the presence of the mixed contourite-turbidite system has been detected from seismic interpretation, the stratigraphic model has been updated with the introduction of the late Quaternary Marquês de Pombal Drift sediment type in the Marquês de Pombal Plateau. Besides this difference, the sand content measured from Site U1391 has been decreased linearly with water depth. However, as explained in section 3.4.3.3.1, the IODP Site is located ~ 60 km away from the Marquês de Pombal Plateau area, thus sediment transition from the middle slope to deeper areas represent an important element of uncertainty of this study.

The recovery of piston cores from the Marquês de Pombal Plateau area would allow to confirm or deny our stratigraphic interpretation. Furthermore, performing additional geotechnical tests on sediments recovered from deeper stratigraphic levels would improve the reliability of the input physical properties that define deeper stratigraphic units in our hydrogeological models. Ideally, two piston cores should be collected: the first one would be located in the proximity of the Marquês de Pombal Drift depocenter. If our interpretation is correct, this core should be entirely composed by the mixed-system lithology, showing homogeneous, fine-grained sediment distribution with minor grain size variations related to small changes in the MOW hydrodynamic and transport capacity during glacial/interglacial cycles. By recovering few tens of meters of sediments in this area, it would be possible to derive information about the evolution of porosity with depth, and the collected sediment could be tested to derive more accurate physical properties of the mixed contourite - turbidite deposits allowing a better definition of the finite-element models.

A second piston core should be located at the edge of the mixed deposit (ideally, at SdG068-01 location, Figure 3.7). This core would provide information about the lateral distribution of pre-LQD units, allowing to visualize the transition of sediments from borehole U1391 towards the Marquês de Pombal Plateau. In this way, it would be possible to understand if the MOW hydrodynamics affected also deeper parts of the basin at some point in the past. This core could also detect eventual sand-rich intervals that would have important effects in promoting lateral fluid flow and dissipating pore pressures.

b. Long-term instrumented mooring deployments:

The role of the MOW hydrodynamics in transporting suspended sediments is a key point in our interpretation of the Marquês de Pombal Drift deposition. Our depositional model, in fact, strongly rely on the effect of the lower MOW branch (ML) in transporting sediment out of the São Vicente Canyon and depositing it over the Marquês de Pombal Plateau. The São Vicente Canyon is also assumed to capture part of the MOW upper branch (MU) and transported sediments. In our conceptual model, those sediments would contribute to the formation of a nepheloid layer at the interface of major water masses, which exports the fine grained suspended sediments that are transported and ultimately deposited over the Marquês de Pombal Drift. Although partial capture phenomena and high presence of suspended particulate matter have been measured in nearby canyons (Portimão Canyon in the East and Setubal Canyon in the North), mooring stations within the São Vicente Canyon would provide important *in-situ* measurements to confirm our model. CTD measurements, turbidity sensors and currentimeters would be able to assess whether or not part of the MU is trapped into the canyon, the concentration of suspended particulate matter related with nepheloid layers and the currents that could capture the sediments in the nepheloid layer.

c. Pore pressure measurement

The lack of calibration points for the overpressure results of our model represents a limit of this study that could only be fixed by collecting *in-situ* pore pressure measurements. Ideally these measurements should be performed in the proximity of the Marquês de Pombal Drift depocenter, where the maximum overpressure development is expected to take place, by performing piezometer measurements as described in section 1.5. Acquiring *in-situ* pore pressure data would allow to test the accuracy of the modelling results described in this thesis, and to adopt a stochastic approach that could take into account a number of different scenarios able to match the pore pressure measured *in-situ*.

11.2 Slope stability analysis

The influence of overpressure development on the slope stability in the area has been evaluated in section 9.1 and 9.2 by making use of simplified static and pseudo-static factor of safety calculations that take into account, among other variables, internal friction angle and undrained shear strength of sediments (eq. 15 and 17). As no triaxial/simple shear tests have been performed for this study, either static or dynamic, those values have been taken from the literature. However, a much more detailed analysis of the effect of overpressure development on the slope stability in the area and the relationship between slope failure and earthquake shaking could be achieved by performing dynamic shear strength tests on the available sediments from the area. By adopting a geotechnical finite-element software, it could be possible to integrate the stratigraphy of the area, overpressure evolution and sediment response to earthquake shaking in a truly dynamic analysis. In this way, it would be possible to perform more accurate estimations about the earthquake magnitude needed to trigger slope failures in the area.

References

Abrantes, F., Santos, C., Ventura, C., Voelker, A., Röhl, U., 2017. Data report: IODP Expedition 339 Site U1391: an improved splice and preliminary age model on the basis of XRF data 339. https://doi.org/10.2204/iodp.proc.339.203.2017

Akhurst, M.C., Stow, D.A.V., Stoker, M.S., 2002. Late Quaternary glacigenic contourite, debris flow and turbidite process interaction in the Faroe-Shetland Channel, NW European continental margin. Geol. Soc. Mem. 22, 73–84. https://doi.org/10.1144/GSL.MEM.2002.022.01.07

Alonso, B., Ercilla, G., Casas, D., Stow, D.A.V., Rodríguez-Tovar, F.J., Dorador, J., Hernández-Molina, F.J., 2016. Contourite vs gravity-flow deposits of the Pleistocene Faro Drift (Gulf of Cadiz): Sedimentological and mineralogical approaches. Mar. Geol. 377, 77–94. https://doi.org/10.1016/j.margeo.2015.12.016

Alves, T., Gawthorpe, R., Hunt, D., Monteiro, J., 2000. Tertiary evolution of the Sao Vicente and Setubal submarine canyons, Southwest Portugal: insights from seismic stratigraphy. Ciências da Terra 14, 243–256.

Alves, T.M., Gawthorpe, R.L., Hunt, D.W., Monteiro, J.H., 2003. Cenozoic tectono-sedimentary evolution of the western Iberian margin. Mar. Geol. 195, 75–108. https://doi.org/10.1016/S0025-3227(02)00683-7

Alves, T.M., Moita, C., Cunha, T., Ullnaess, M., Myklebust, R., Monteiro, J.H., Manuppella, G., 2009. Diachronous evolution of late jurassic-cretaceous continental rifting in the northeast atlantic (west iberian margin). Tectonics 28, 1–32. https://doi.org/10.1029/2008TC002337

Ambar, I., Howe, M.R., 1979. Observations of the Mediterranean outflow-I mixing in the Mediterranean outflow. Deep Sea Res. Part A, Oceanogr. Res. Pap. 26, 535–554. https://doi.org/10.1016/0198-0149(79)90095-5

Ambar, I., Howe, M.R., I., A.M., 1976. A Physical and Chemical Description of the Mediterranean Outflow in the Gulf of Cadiz. Dtsch. Hydrogr. Z. 29, 58–68.

Ambraseys, N.N., Douglas, J., Sarma, S.K., Smit, P.M., 2005. Equations for the estimation of strong ground motions from shallow crustal earthquakes using data from Europe and the middle east: Horizontal peak ground acceleration and spectral acceleration, Bulletin of Earthquake Engineering. https://doi.org/10.1007/s10518-005-0183-0

ASTM, 2012. D4186/D4186M-12. Standard test method for one-dimensional consolidation properties of saturated cohesive soils using controlled-strain loading. ASTM Int. 2458000, 1–18. https://doi.org/10.1520/D4186

Athy, L.F., 1930. Density, Porosity, and Compaction of Sedimentary Rocks1. Am. Assoc. Pet. Geol. Bull. 14, 1–24. https://doi.org/10.1306/3D93289E-16B1-11D7-8645000102C1865D

Azerêdo, A.C., Wright, V.P., Ramalho, M.M., 2002. The Middle-Late Jurassic forced regression and disconformity in central Portugal: Eustatic, tectonic and climatic effects on a carbonate ramp system. Sedimentology 49, 1339–1370. https://doi.org/10.1046/j.1365-3091.2002.00501.x

Azpiroz-Zabala, M., Cartigny, M.J.B., Talling, P.J., Parsons, D.R., Sumner, E.J., Clare, M.A., Simmons, S.M., Cooper, C., Pope, E.L., 2017. Newly recognized turbidity current structure can explain prolonged flushing of submarine canyons. Sci. Adv. 3, e1700200. https://doi.org/10.1126/sciadv.1700200

Bachu, S., Underschultz, J.R., 1993. Hydrogeology of formation waters, northeastern Alberta Basin. Am. Assoc. Pet. Geol. Bull. https://doi.org/10.1306/bdff8f24-1718-11d7-8645000102c1865d

Badhani, S., 2020. Seafloor instabilities in the Gulf of Lions , Western Mediterranean.

Badhani, S., Cattaneo, A., Dennielou, B., Leroux, E., Colin, F., Thomas, Y., Jouet, G., Rabineau, M., Droz, L., 2020. Morphology of retrogressive failures in the Eastern Rhone interfluve during the last glacial maximum (Gulf of Lions, Western Mediterranean). Geomorphology 351, 106894. https://doi.org/10.1016/j.geomorph.2019.106894

Bahr, A., Jimenez-Espejo, F.J., Kolasinac, N., Grunert, P., 2014. Deciphering bottom current velocity and paleoclimate signals from contourite deposits in the Gulf of C?adiz during the last 140 kyr: An inorganic geochemical approach. Geochemistry, Geophys. Geosystems 15, 3145–3160. https://doi.org/10.1002/2015GC005918

Bahr, A., Kaboth, S., Jiménez-Espejo, F.J., Sierro, F.J., Voelker, A.H.L., Lourens, L., Röhl, U., Reichart, G.J., Escutia, C., Hernández-Molina, F.J., Pross, J., Friedrich, O., 2015. Persistent monsoonal forcing of mediterranean outflow water dynamics during the late Pleistocene. Geology 43, 951–954. https://doi.org/10.1130/G37013.1

Baptista, M.A., Heitor, S., Miranda, J.M., Miranda, P., Mendes Victor, L., 1998. The 1755 Lisbon tsunami; Evaluation of the tsunami parameters. J. Geodyn. 25, 143–157. https://doi.org/10.1016/s0264-3707(97)00019-7

Baptista, M.A., Miranda, J.M., 2009. Revision of the portuguese catalog of tsunamis. Nat. Hazards Earth Syst. Sci. 9, 25–42. https://doi.org/10.5194/nhess-9-25-2009

Baringer, M.O., Price, J.F., 2002. Mixing and Spreading of the Mediterranean Outflow. J. Phys. Oceanogr. 27, 1654–1677. https://doi.org/10.1175/1520-0485(1997)027<1654:masotm>2.0.co;2

Barley, B., 1999. Deepwater problems around the world. Lead. Edge 18, 488–494.

Bartoli, G., Sarnthein, M., Weinelt, M., Erlenkeuser, H., Garbe-Schönberg, D., Lea, D.W., 2005. Final closure of Panama and the onset of northern hemisphere glaciation. Earth Planet. Sci. Lett. 237, 33–44. https://doi.org/10.1016/j.epsl.2005.06.020

Bartolome, R., Gràcia, E., Stich, D., Martínez-Loriente, S., Klaeschen, D., de Lis Mancilla, F., Lo Iacono, C., Dañobeitia, J.J., Zitellini, N., 2012. Evidence for active strike-slip faulting along the Eurasia-Africa convergence zone: Implications for seismic hazard in the southwest Iberian margin. Geology 40, 495–498. https://doi.org/10.1130/G33107.1

Basili, R., Kastelic, V., Demircioglu, M.B., Garcia Moreno, D., Nemser, E.S., Petricca, P., Sboras, S.P., Besana-Ostman, G.M., Cabral, J., Camelbeek, T., Caputo, R., Danciu, L., Domac, H., Fonseca, J., Garcìa-Mayordomo, J., Giardini, D., Glavatovic, B., Gulen, L., Ince, Y., Pavlides, S., Sesetyan, K., Tarabusi, G., Tiberti, M.M., Utkucu, M., Vanneste, K., Vilanova, S., Wössner, J., 2013. The European Database of Seismogenic Faults (EDSF) compiled in the framework of the Project SHARE. https://doi.org/10.6092/INGV.IT-SHARE-EDSF

Becker, K., Davis, E.E., 2005. A review of CORK designs and operations during the Ocean Drilling Program. Proc. IODP, 301 301. https://doi.org/10.2204/iodp.proc.301.104.2005

Behrmann, J.H., Flemings, P.B., John, C.M., Behrmann, J.H., Flemings, P.B., John, C.M., Iturrino, G.J., Aizawa, Y., Binh, N.T.T., De Silva, N., Dugan, B., Edeskär, T.M., Franke, C., Gay, A., Gilhooly, W.P., Gutierrez-Pastor, J., Jiang, S.Y., Long, H., Moore, J.C., Nonoura, T., Pirmez, C., Reichow, M., Sawyer, D.E., Schneider, J., Shumnyk, A. V., Suzuki, T., Takano, Y., Urgeles, R., Yamamoto, Y., Zampetti, V., 2006. Rapid sedimentation, overpressure, and focused fluid flow, gulf of mexico continental margin. Sci. Drill. 1, 12–17. https://doi.org/10.2204/iodp.sd.3.03.2006

Bellwald, B., Urlaub, M., Hjelstuen, B.O., Sejrup, H.P., Sørensen, M.B., Forsberg, C.F.,

Vanneste, M., 2019. NE Atlantic continental slope stability from a numerical modeling perspective. Quat. Sci. Rev. 203, 248–265. https://doi.org/10.1016/j.quascirev.2018.11.019

Berndt, C., 2005. Focused fluid flow in passive continental margins. Philos. Trans. R. Soc. A Math. Phys. Eng. Sci. 363, 2855–2871. https://doi.org/10.1098/rsta.2005.1666

Best, A.I., Gunn, D.E., 1999. Calibration of marine sediment core loggers for quantitative acoustic impedance studies belonging to Southampton Oceanography Centre. Mar. Geol. 160, 137–146.

Bethke, C.M., Corbet, T.F., 1988. Linear and nonlinear solutions for one-dimensional compaction flow in sedimentary basins. Water Resour. Res. 24, 461–467.

Biscontin, G., Pestana, J.M., Nadim, F., 2004. Seismic triggering of submarine slides in soft cohesive soil deposits. Mar. Geol. 203, 341–354. https://doi.org/10.1016/S0025-3227(03)00314-1

Bitzer, K., 1999. Two-dimensional simulation of clastic and carbonate sedimentation, consolidation, subsidence, fluid flow, heat flow and solute transport during the formation of sedimentary basins. Comput. Geosci. 25, 431–447. https://doi.org/10.1016/S0098-3004(98)00147-2

Bitzer, K., 1996. Modeling Consolidation Sedimentary and Fluid Basins Flow. Comput. Geosci. 22, 467–478.

Bjørlykke, K., Høeg, K., 1997. Effects of burial diagenesis on stresses, compaction and fluid flow in sedimentary basins. Mar. Pet. Geol. 14, 267–276. https://doi.org/10.1016/S0264-8172(96)00051-7

Blum, P., 1997. Physical Properties Handbook: A Guide to the Shipboard Measurement of Physical Properties of Deep-Sea Cores, ODP Tech. Note, Ocean Drilling Program Technical Notes. Ocean Drilling Program. https://doi.org/10.2973/odp.tn.26.1997

Borge, H., Sylta, Ø., 1998. 3D Modelling of Fault Bounded Pressure Compartments in the North Viking Graben. Energy Explor. Exploit. 16, 301–323.

Boudon, G., Le Friant, A., Komorowski, J.C., Deplus, C., Semet, M.P., 2007. Volcano flank instability in the Lesser Antilles Arc: Diversity of scale, processes, and temporal recurrence. J. Geophys. Res. Solid Earth 112. https://doi.org/10.1029/2006BJ004674

Bowen, A.J., Normark, W.R., Piper, D.J.W., 1984. Modelling of turbidity currents on Navy Submarine Fan, California Continental Borderland. Sedimentology 31, 169–185.

Bowers, G.L., 2002. Detecting high overpressure. Lead. Edge 21, 174–177. https://doi.org/10.1190/1.1452608

Brackenridge, R.E., Hernández-Molina, F.J., Stow, D.A.V., Llave, E., 2013. A Pliocene mixed contourite-turbidite system offshore the Algarve Margin, Gulf of Cadiz: Seismic response, margin evolution and reservoir implications. Mar. Pet. Geol. 46, 36–50. https://doi.org/10.1016/j.marpetgeo.2013.05.015

Brackenridge, R.E., Stow, D.A.V., Hernández-Molina, F.J., Jones, C., Mena, A., Alejo, I., Ducassou, E., Llave, E., Ercilla, G., Nombela, M.A., Perez-Arlucea, M., Frances, G., 2018. Textural characteristics and facies of sand-rich contourite depositional systems. Sedimentology 2223–2252. https://doi.org/10.1111/sed.12463

Bredehoeft, J.D., Hanshaw, B.B., 1968. On the Maintenance of Anomalous Fluid Pressures: I. Thick Sedimentary Sequences. Geol. Soc. Am. Bull. 79, 1097–1106.

British Standards Institution, 1990. Consolidation and permeability test in hydraulic cells and with pore pressure measurement, in: Soils for Civil Engineering Purposes. p. 61.

Broichhausen, H., Littke, R., Hantschel, T., 2005. Mudstone compaction and its influence on

overpressure generation, elucidated by a 3D case study in the North Sea. Int. J. Earth Sci. 94, 956–978. https://doi.org/10.1007/s00531-005-0014-1

Brown, K.M., Tryon, M.D., DeShon, H.R., Dorman, L.R.M., Schwartz, S.Y., 2005. Correlated transient fluid pulsing and seismic tremor in the Costa Rica subduction zone. Earth Planet. Sci. Lett. 238, 189–203. https://doi.org/10.1016/j.epsl.2005.06.055

Brunet, M., Le Friant, A., Boudon, G., Lafuerza, S., Talling, P., Hornbach, M., Ishizuka, O., Lebas, E., Guyard, H., 2016. Composition, geometry, and emplacement dynamics of a large volcanic island landslide offshore Martinique: From volcano flank-collapse to seafloor sediment failure? Geochemistry, Geophys. Geosystems 17, 699–724. https://doi.org/10.1002/2015GC006034

Bryn, P., Berg, K., Forsberg, C.F., Solheim, A., Kvalstad, T.J., 2005. Explaining the Storegga Slide. Mar. Pet. Geol. 22, 11–19. https://doi.org/10.1016/j.marpetgeo.2004.12.003

Bugge, T., Befring, S., Belderson, R.H., Eidvin, T., Jansen, E., Kenyon, N.H., Holtedahl, H., Sejrup, H.P., 1987. A giant three-stage submarine slide off Norway. Geo-Marine Lett. 7, 191–198. https://doi.org/10.1007/BF02242771

Cacho, I., Grimalt, J.O., Sierro, F.J., Shackleton, N., Canals, M., 2000. Evidence for enhanced Mediterranean thermohaline circulation during rapid climatic coolings. Earth Planet. Sci. Lett. 183, 417–429. https://doi.org/10.1016/S0012-821X(00)00296-X

Calais, E., DeMets, C., Nocquet, J.M., 2003. Evidence for a post-3.16-Ma change in Nubia-Eurasia-North America plate motions? Earth Planet. Sci. Lett. 216, 81–92. https://doi.org/10.1016/S0012-821X(03)00482-5

Camerlenghi, A., Rebesco, M., Pudsey, C.J., 1997. High Resolution Terrigenous Sedimentary Record of a Sediment Drift on the Antarctic Peninsula Pacific Margin (Initial Results of the "SEDANO" Program), The Antarctic Region: Geological Evolution and Processes. Terra Antarctica Pubblication.

Canals, M., Lastras, G., Urgeles, R., Casamor, J.L., Mienert, J., Cattaneo, A., De Batist, M., Haflidason, H., Imbo, Y., Laberg, J.S., Locat, J., Long, D., Longva, O., Masson, D.G., Sultan, N., Trincardi, F., Bryn, P., 2004. Slope failure dynamics and impacts from seafloor and shallow sub-seafloor geophysical data: Case studies from the COSTA project. Mar. Geol. 213, 9–72. https://doi.org/10.1016/j.margeo.2004.10.001

Carlton, B.D., Price, K., Vanneste, M., Forsberg, C.F., 2017. Development and application of a regional slope stability assessment screening tool. Adv. Nat. Technol. Hazards Res. 46, 267–276. https://doi.org/10.1007/978-3-319-56487-6_24

Carter, L., Gavey, R., Talling, P.J., Liu, J.T., 2014. Insights into submarine geohazards from breaks in subsea telecommunication cables. Oceanography 27, 58–67. https://doi.org/10.5670/oceanog.2014.40

Carter, L., Milliman, J.D., Talling, P.J., Gavey, R., Wynn, R.B., 2012. Near-synchronous and delayed initiation of long run-out submarine sediment flows from a record-breaking river flood, offshore Taiwan. Geophys. Res. Lett. 39, 6–10. https://doi.org/10.1029/2012GL051172

Casagrande, A., 1932. Research on the Atterberg limits of soils. Public Roads 12, 121–136.

Casas, D., Casalbore, D., Yenes, M., Urgeles, R., 2015. Submarine mass movements around the iberian Peninsula. The building of continental margins through hazardous processes. Bol. Geol. y Min. 126, 257–278.

Cattaneo, A., Babonneau, N., Ratzov, G., Dan-Unterseh, G., Yelles, K., Bracane, R., Mercier De Lapinay, B., Boudiaf, A., Daverchare, J., 2012. Searching for the seafloor signature of the 21 May 2003 Boumerdas earthquake offshore central Algeria. Nat. Hazards Earth Syst. Sci. 12, 2159–2172. https://doi.org/10.5194/nhess-12-2159-2012

Chillarige, A.R. V., Morgenstern, N.B., Robertson, P.K., Christian, H.A., 1997. Seabed instability due to flow liquefaction in the Fraser River delta. Can. Geotech. J. 34, 520–533. https://doi.org/10.1139/T97-019

Clare, M., Lintern, D.G., Rosenberger, K., Clarke, J.E.H., Paull, C., Gwiazda, R., Cartigny, M.J.B., Talling, P.J., Perara, D., Xu, J., Parsons, D., Jacinto, R.S., Apprioual, R., 2020. Lessons learned from the monitoring of turbidity currents and guidance for future platform designs. Geol. Soc. Spec. Publ. 500, 605–634. https://doi.org/10.1144/SP500-2019-173

Clare, M.A., Hughes Clarke, J.E., Talling, P.J., Cartigny, M.J.B., Pratomo, D.G., 2016. Preconditioning and triggering of offshore slope failures and turbidity currents revealed by most detailed monitoring yet at a fjord-head delta. Earth Planet. Sci. Lett. 450, 208–220. https://doi.org/10.1016/j.epsl.2016.06.021

Clare, M.A., Vardy, M.E., Cartigny, M.J.B., Talling, P.J., Himsworth, M.D., Dix, J.K., Harris, J.M., Whitehouse, R.J.S., Belal, M., 2017. Direct monitoring of active geohazards: Emerging geophysical tools for deep-water assessments. Near Surf. Geophys. 15, 427–444. https://doi.org/10.3997/1873-0604.2017033

Clark, P.U., Archer, D., Pollard, D., Blum, J.D., Rial, J.A., Brovkin, V., Mix, A.C., Pisias, N.G., Roy, M., 2006. The middle Pleistocene transition: characteristics, mechanisms, and implications for long-term changes in atmospheric pCO2. Quat. Sci. Rev. 25, 3150–3184. https://doi.org/10.1016/j.quascirev.2006.07.008

Collico, S., Arroyo, M., Urgeles, R., Gràcia, E., Devincenzi, M., Peréz, N., 2020. Probabilistic mapping of earthquake-induced submarine landslide susceptibility in the South-West Iberian margin. Mar. Geol. 429. https://doi.org/10.1016/j.margeo.2020.106296

Colton-Bradley, V.A.C., 1987. Role of pressure in smectite dehydration-Effects on geopressure and smectite-to-illite transition. Am. Assoc. Pet. Geol. Bull. 71, 1414–1427.

Cossu, F.R., Wells, M.G., Peakall, J., 2015. Latitudinal variations in submarine channel sedimentation patterns: The role of coriolis forces. J. Geol. Soc. London. 172, 161–174. https://doi.org/10.1144/jgs2014-043

Cossu, R., Wells, M.G., Whlin, A.K., 2010. Influence of the coriolis force on the velocity structure of gravity currents in straight submarine channel systems. J. Geophys. Res. Ocean. 115, 1–15. https://doi.org/10.1029/2010JC006208

D4318-10, A., 2010. Standard Test Methods for Liquid Limit, Plastic Limit, and Plasticity Index of Soils, in: ASTM Standard. ASTM International, West Conshohocken, USA, pp. 1–14.

Daines, S.R., 1982. Aquathermal pressuring and geopressure evaluation. Am. Assoc. Pet. Geol. Bull. 66, 931–939. https://doi.org/10.1306/03B5A35E-16D1-11D7-8645000102C1865D

Davis, E.E., Becker, K., Wang, K., Obara, K., Ito, Y., Kinoshita, M., 2006. A discrete episode of seismic and aseismic deformation of the Nankai trough subduction zone accretionary prism and incoming Philippine Sea plate. Earth Planet. Sci. Lett. 242, 73–84. https://doi.org/10.1016/j.epsl.2005.11.054

Davis, E.E., Villinger, H.W., 2006. Transient formation fluid pressures and temperatures in the Costa Rica forearc prism and subducting oceanic basement: CORK monitoring at ODP Sites 1253 and 1255. Earth Planet. Sci. Lett. 245, 232–244. https://doi.org/10.1016/j.epsl.2006.02.042

De Blasio, F. V., 2004. Hydroplaning and submarine debris flows. J. Geophys. Res. 109, C01002. https://doi.org/10.1029/2002JC001714

de Castro, S., Hernández-Molina, F.J., Rodríguez-Tovar, F.J., Llave, E., Ng, Z.L., Nishida, N., Mena, A., 2020. Contourites and bottom current reworked sands: Bed facies model and implications. Mar. Geol. 428. https://doi.org/10.1016/j.margeo.2020.106267

de Stigter, H.C., Jesus, C.C., Boer, W., Richter, T.O., Costa, A., van Weering, T.C.E., 2011.

Recent sediment transport and deposition in the Lisbon-Setúbal and Cascais submarine canyons, Portuguese continental margin. Deep. Res. Part II Top. Stud. Oceanogr. 58, 2321–2344. https://doi.org/10.1016/j.dsr2.2011.04.001

De Vicente, G., Cloetingh, S., Van Wees, J.D., Cunha, P.P., 2011. Tectonic classification of Cenozoic Iberian foreland basins. Tectonophysics 502, 38–61. https://doi.org/10.1016/j.tecto.2011.02.007

Demers, D., Leroueil, S., 2002. Evaluation of preconsolidation pressure and the overconsolidation ratio from piezocone tests of clay deposits in Quebec. Can. Geotech. J. 39, 174–192. https://doi.org/10.1139/t01-071

DeMets, C., Gordon, R.G., Argus, D.F., 2010. Geologically current plate motions. Geophys. J. Int. 181, 1–80. https://doi.org/10.1111/j.1365-246X.2009.04491.x

Deplus, C., Le Friant, A., Boudon, G., Komorowski, J.C., Villemant, B., Harford, C., Ségoufin, J., Cheminée, J.L., 2001. Submarine evidence for large-scale debris avalanches in the Lesser Antilles Arc. Earth Planet. Sci. Lett. 192, 145–157. https://doi.org/10.1016/S0012-821X(01)00444-7

Dickinson, G., 1953. Geological aspects of abnormal reservoir pressures in Gulf Coast Louisiana. Am. Assoc. Pet. Geol. Bull. 37, 410–432.

Dugan, B., Flemings, P.B., 2002. Fluid flow and stability of the US continental slope offshore New Jersey from the Pleistocene to the present. Geofluids 2, 137–146. https://doi.org/10.1046/j.1468-8123.2002.00032.x

Dugan, B., Flemings, P.B., 2000. Overpressure and fluid flow in the New Jersey continental, slope: Implications for slope failure and cold seeps. Science (80-.). 289, 288–291. https://doi.org/10.1126/science.289.5477.288

Dugan, B., Germaine, J.T., 2008. Near-seafloor overpressure in the deepwater Mississippi Canyon, northern Gulf of Mexico. Geophys. Res. Lett. 35, 1–5. https://doi.org/10.1029/2007GL032275

Dugan, B., Sheahan, T.C., 2012. Offshore sediment overpressures of passive margins: Mechanisms, measurement, and models. Rev. Geophys. 50, 1–20. https://doi.org/10.1029/2011rg000379

Edwards, C., McQuaid, S., Easton, S., Scott, D., Couch, A., Evans, R., Hart, S., 2018. Lateral accretion in a straight slope channel system: An example from the Forties Sandstone of the Huntington Field, UK Central North Sea. Pet. Geol. Conf. Proc. 8, 413–428. https://doi.org/10.1144/PGC8.33

Encyclopedia Britanica, 2021. Encyclopedia Britanica.

Escutia, C., Nelson, C.H., Acton, G.D., Eittreim, S.L., Cooper, A.K., Warnke, D.A., Jaramillo, J.M., 2002. Current controlled deposition on the Wilkes Land continental rise, Antarctica. Geol. Soc. Mem. 22, 373–384. https://doi.org/10.1144/GSL.MEM.2002.022.01.26

Expedition 308 Scientists, 2006. Expedition 308 summary. Proc. IODP, 308 308. https://doi.org/10.2204/iodp.proc.308.101.2006

Expedition 308 Scientists, 2005. Overpressure and fluid flow processes in the deepwater Gulf of Mexico: slope stability, seeps, and shallow-water flow. Integr. Ocean Drill. Progr. Exped. 308 Sci. Prospect.

Expedition 340 Scientists, 2013. Expedition 340 summary 340. https://doi.org/10.2204/iodp.proc.340.101.2013

Faugères, J.C., Stow, D.A.V., 2008. Contourite drifts: nature, evolution and controls, in: Rebesco, M., Camerlenghi, A. (Eds.), Developments in Sedimentology. Elsevier, Amsterdam, pp. 257–288. https://doi.org/10.1016/S0070-4571(08)10014-0

Faugères, J.C., Stow, D.A.V., Imbert, P., Viana, A., 1999. Seismic features diagnostic of contourite drifts. Mar. Geol. 162, 1–38. https://doi.org/10.1016/S0025-3227(99)00068-7

Flecker, R., Krijgsman, W., Capella, W., de Castro Martíns, C., Dmitrieva, E., Mayser, J.P., Marzocchi, A., Modestu, S., Ochoa, D., Simon, D., Tulbure, M., van den Berg, B., van der Schee, M., de Lange, G., Ellam, R., Govers, R., Gutjahr, M., Hilgen, F., Kouwenhoven, T., Lofi, J., Meijer, P., Sierro, F.J., Bachiri, N., Barhoun, N., Alami, A.C., Chacon, B., Flores, J.A., Gregory, J., Howard, J., Lunt, D., Ochoa, M., Pancost, R., Vincent, S., Yousfi, M.Z., 2015. Evolution of the Late Miocene Mediterranean-Atlantic gateways and their impact on regional and global environmental change. Earth-Science Rev. 150, 365–392. https://doi.org/10.1016/j.earscirev.2015.08.007

Flemings, P., Behrmann, J., John, C., Expedition 308 Scientists, 2006. Proceedings of the Ocean Drilling Program. IODP Manag. Int. Inc., Coll. Stn. TX.

Flemings, P.B., John, C., Behrmann, J., 2012. Expedition 308 synthesis: overpressure, consolidation, and slope stability on the continental slope of the Gulf of Mexico 308. https://doi.org/10.2204/iodp.proc.308.215.2012

Flemings, P.B., Liu, X., Winters, W.J., 2003. Critical pressure and multiphase flow in Blake Ridge gas hydrates. Geology 31, 1057–1060. https://doi.org/10.1130/G19863.1

Flemings, P.B., Long, H., Dugan, B., Germaine, J., John, C.M., Behrmann, J.H., Sawyer, D., 2008. Pore pressure penetrometers document high overpressure near the seafloor where multiple submarine landslides have occurred on the continental slope, offshore Louisiana, Gulf of Mexico. Earth Planet. Sci. Lett. 274, 269–283. https://doi.org/10.1016/j.epsl.2008.06.027

Flemming, B.W., 2000. A revised textural classification of gravel-free muddy sediments on the basis of ternary diagrams. Cont. Shelf Res. 20, 1125–1137. https://doi.org/10.1016/S0278-4343(00)00015-7

Fonnesu, M., Palermo, D., Galbiati, M., Marchesini, M., Bonamini, E., Bendias, D., 2020. A new world-class deep-water play-type, deposited by the syndepositional interaction of turbidity flows and bottom currents: The giant Eocene Coral Field in northern Mozambique. Mar. Pet. Geol. 111, 179–201. https://doi.org/10.1016/j.marpetgeo.2019.07.047

Ford, J., Urgeles, R., Camerlenghi, A., Gràcia, E., 2021. Seismic diffraction imaging to characterise mass-transport complexes: examples from the Gulf of Cadiz, south west Iberian Margin. J. Geophys. Res. Solid Earth. https://doi.org/10.1029/2020JB021474

Freeze, R.A., 1979. Groundwater. Prentice Hall, Englewood Cliffs, N.J.

Freudenthal, T., Wefer, G., 2013. Drilling cores on the sea floor with the remote-controlled sea floor drilling rig MeBo. Geosci. Instrumentation, Methods Data Syst. 2, 329–337. https://doi.org/10.5194/gi-2-329-2013

Frigola, J., Canals, M., Mata, P., 2015. Techniques for the non-destructive and continuous analysis of sediment cores. Application in the Iberian continental margin. Bol. Geol. y Min. 126, 609–634.

Fuhrmann, A., Kane, I.A., Clare, M.A., Ferguson, R.A., Schomacker, E., Bonamini, E., Contreras, F.A., 2020. Hybrid turbidite-drift channel complexes : An integrated multiscale model. Geology 48, 562–568. https://doi.org/10.1130/G47179.1/4967910/g47179.pdf

García-Mayordomo, J., Insua-Arévalo, J.M., Martínez-Díaz, J.J., Jiménez-Díaz, A., Martín-Banda, R., Martín-Alfageme, S., Álvarez-Gómez, J.A., Rodríguez-Peces, M., Pérez-López, R., Rodríguez-Pascua, M.A., Masana, E., Perea, H., Martín-González, F., Giner-Robles, J., Nemser, E.S., Cabral, J., Sanz de Galdeano, C., Peláez, J.A., García-Tortosa, F.J., Gràcia, E., Bartolomé, R., González, Azañón, J.M., Alfaro, P., Moreno, X., Ferrero-Vega, A., Dias, R., Martínez, S., Gutiérrez, F., Ortuño, M., Booth-Rea, G., Giaconia, F., Martínez-Martínez, J.M., Villegas, I., Lo Iacono, C., Pérez-Peña, J. V., Brum da Silveira, A., García-Meléndez,

E., Lafuente, P., Simón, J.L., Arlegui, L.E., Liesa, C.L., Bach, J., Linares, R., 2012. The Quaternary Active Faults Database of Iberia (QAFI v.2.0). J. Iber. Geol. 38, 285–302. https://doi.org/10.5209/rev_JIGE.2012.v38.n1.39219

Garcia-Orellana, J., Gràcia, E., Vizcaino, A., Masqué, P., Olid, C., Martínez-Ruiz, F., Piñero, E., Sanchez-Cabeza, J.A., Dañobeitia, J., 2006. Identifying instrumental and historical earthquake records in the SW Iberian margin 210Pb turbidite chronology. Geophys. Res. Lett. 33. https://doi.org/10.1029/2006GL028417

Gatter, R., Clare, M.A., Hunt, J.E., Watts, M., Madhusudhan, B.N., Talling, P.J., Huhn, K., 2020. A multi-disciplinary investigation of the AFEN slide: The relationship between contourites and submarine landslides. Geol. Soc. Spec. Publ. 500, 173–193. https://doi.org/10.1144/SP500-2019-184

Gerland, S., Villinger, H., 1995. Nondestructive density determination on marine sediment cores from gamma-ray attenuation measurements. Geo-Marine Lett. 15, 111–118. https://doi.org/10.1007/BF01275415

Germa, A., Quidelleur, X., Labanieh, S., Chauvel, C., Lahitte, P., 2011. The volcanic evolution of Martinique Island: Insights from K-Ar dating into the Lesser Antilles arc migration since the Oligocene. J. Volcanol. Geotherm. Res. 208, 122–135. https://doi.org/10.1016/j.jvolgeores.2011.09.007

Germa, A., Quidelleur, X., Labanieh, S., Lahitte, P., Chauvel, C., 2010. The eruptive history of Morne Jacob volcano (Martinique Island, French West Indies): Geochronology, geomorphology and geochemistry of the earliest volcanism in the recent Lesser Antilles arc. J. Volcanol. Geotherm. Res. 198, 297–310. https://doi.org/10.1016/j.jvolgeores.2010.09.013

Gibson, R.E., 1958. The Progress of Consolidation in a Clay Layer Increasing in Thickness with Time. Géotechnique 8, 171–182. https://doi.org/10.1680/geot.1958.8.4.171

Gong, C., Wang, Y., Zhu, W., Li, W., Xu, Q., 2013. Upper Miocene to Quaternary unidirectionally migrating deep-water channels in the Pearl River Mouth Basin, northern South China Sea. Am. Assoc. Pet. Geol. Bull. 97, 285–308. https://doi.org/10.1306/07121211159

Gracia, E., Danobeitia, J., 2001. High-Resolution Imaging of Tsunamigenic Structures in the Southwest Iberian Margin (Eurasia-Africa Convergence): Implications for Seismic Hazard Assessment, in: American Geophysical Union, Fall Meeting.

Gràcia, E., Danobeitia, J., Vergés, J., 2003a. Mapping active faults offshore Portugal (36 Њ N – 38 Њ N): Implications for seismic hazard assessment along the southwest Iberian margin. Geology 31, 83–86. https://doi.org/10.1130/0091-7613(2003)031<0083

Gràcia, E., Dañobeitia, J., Vergés, J., Bartolomé, R., Córdoba, D., 2003b. Crustal architecture and tectonic evolution of the Gulf of Cadiz (SW Iberian margin) at the convergence of the Eurasian and African plates. Tectonics 22, 1033–1056. https://doi.org/10.1029/2001TC901045

Gràcia, E., Urgeles, R., Shipboard Scientific Party, 2018. INSIGHT-Leg1 Cruise Report.

Gràcia, E., Vizcaino, A., Escutia, C., Asioli, A., Rodés, Á., Pallàs, R., Garcia-Orellana, J., Lebreiro, S., Goldfinger, C., 2010. Holocene earthquake record offshore Portugal (SW Iberia): testing turbidite paleoseismology in a slow-convergence margin. Quat. Sci. Rev. 29, 1156–1172. https://doi.org/10.1016/j.quascirev.2010.01.010

Grauls, D., 2001. Gas hydrates: Importance and applications in petroleum exploration. Mar. Pet. Geol. 18, 519–523. https://doi.org/10.1016/S0264-8172(00)00075-1

Grauls, D.J., Baleix, J.M., 1994. Role of overpressures and in situ stresses in fault-controlled hydrocarbon migration: a case study. Mar. Pet. Geol. 11, 734–742.

https://doi.org/10.1016/0264-8172(94)90026-4

Griffiths, D. V., Lane, P.A., 1999. Slope stability analysis by finite elements. Géotechnique 49, 387–403.

Grützner, J., Rebesco, M.A., Cooper, A.K., Forsberg, C.F., Kryc, K.A., Wefer, G., 2003. Evidence for orbitally controlled size variations of the East Antarctic Ice Sheet during the late Miocene. Geology 31, 777–780. https://doi.org/10.1130/G19574.1

Gutierrez, M., Wangen, M., 2005. Modeling of compaction and overpressuring in sedimentary basins. Mar. Pet. Geol. 22, 351–363. https://doi.org/10.1016/j.marpetgeo.2005.01.003

Gutscher, M.A., 2004. What caused the Great Lisbon earthquake? Science (80-.). 305, 1247–1248. https://doi.org/10.1126/science.1101351

Gutscher, M.A., Malod, J.A., Rehault, J.P., Contrucci, I., Klingelhoefer, F., Mendes-Victor, L., Spakman, W., 2002. Evidence for active subduction beneath Gibraltar. Geology 30, 1071–1074. https://doi.org/10.1130/0091-7613-31.1.e22

Haflidason, H., Sejrup, H.P., Nygård, A., Mienert, J., Bryn, P., Lien, R., Forsberg, C.F., Berg, K., Masson, D.G., 2004. The Storegga Slide: Architecture, geometry and slide development. Mar. Geol. 213, 201–234. https://doi.org/10.1016/j.margeo.2004.10.007

Hampton, M.A., Lee, H.J., Locat, J., 1996. Submarine landslides. Rev. Geophys. 34, 33–59. https://doi.org/10.1029/95RG03287

Hanquiez, V., Mulder, T., Lecroart, P., Gonthier, E., Marchès, E., Voisset, M., 2007. High resolution seafloor images in the Gulf of Cadiz, Iberian margin. Mar. Geol. 246, 42–59. https://doi.org/10.1016/j.margeo.2007.08.002

Hanquiez, V., Mulder, T., Toucanne, S., Lecroart, P., Bonnel, C., Marchès, E., Gonthier, E., 2010. The sandy channel-lobe depositional systems in the Gulf of Cadiz: Gravity processes forced by contour current processes. Sediment. Geol. 229, 110–123. https://doi.org/10.1016/j.sedgeo.2009.05.008

Harris, P.T., Macmillan-Lawler, M., Rupp, J., Baker, E.K., 2014. Geomorphology of the oceans. Mar. Geol. 352, 4–24. https://doi.org/10.1016/j.margeo.2014.01.011

Harris, P.T., Whiteway, T., 2011. Global distribution of large submarine canyons: Geomorphic differences between active and passive continental margins. Mar. Geol. 285, 69–86. https://doi.org/10.1016/j.margeo.2011.05.008

Hart, B.S., Flemings, P.B., Deshpande, A., 1995. Porosity and pressure: role of compaction disequilibrium in the development of geopressures in a Gulf coast Pleistocene basin. Geology 23, 45–48. https://doi.org/10.1130/0091-7613(1995)023<0045:PAPROC>2.3.CO;2

He, Y., Xie, X., Kneller, B.C., Wang, Z., Li, X., 2013. Architecture and controlling factors of canyon fills on the shelf margin in the Qiongdongnan Basin, northern South China Sea. Mar. Pet. Geol. 41, 264–276. https://doi.org/10.1016/j.marpetgeo.2012.03.002

Heidarzadeh, M., Muhari, A., Wijanarto, A.B., 2019. Insights on the Source of the 28 September 2018 Sulawesi Tsunami, Indonesia Based on Spectral Analyses and Numerical Simulations. Pure Appl. Geophys. 176, 25–43. https://doi.org/10.1007/s00024-018-2065-9

Heijnen, M.S., Clare, M.A., Cartigny, M.J.B., Talling, P.J., Hage, S., Lintern, D.G., Stacey, C., Parsons, D.R., Simmons, S.M., Chen, Y., Sumner, E.J., Dix, J.K., Clarke, J.E.H., 2020. Rapidly-migrating and internally-generated knickpoints can control submarine channel evolution. Nat. Commun. 1–15. https://doi.org/10.1038/s41467-020-16861-x

Hernández-Molina, F.J., Llave, E., Preu, B., Ercilla, G., Fontan, A., Bruno, M., Serra, N., Gomiz, J.J., Brackenridge, R.E., Sierro, F.J., Stow, D.A.V., García, M., Juan, C., Sandoval, N., Arnaiz, A., 2014a. Contourite processes associated with the Mediterranean Outfl ow Water

after its exit from the Strait of Gibraltar: Global and conceptual implications. Geology 42, 227–230. https://doi.org/10.1130/G35083.1

Hernández-Molina, F.J., Serra, N., Stow, D.A.V., Llave, E., Ercilla, G., van Rooij, D., 2011. Along-slope oceanographic processes and sedimentary products around the Iberian margin. Geo-Marine Lett. 31, 315–341. https://doi.org/10.1007/s00367-011-0242-2

Hernández-Molina, F.J., Sierro, F.J., Llave, E., Roque, C., Stow, D.A.V., Williams, T., Lofi, J., Van der Schee, M., Arnáiz, A., Ledesma, S., Rosales, C., Rodríguez-Tovar, F.J., Pardo-Igúzquiza, E., Brackenridge, R.E., 2016a. Evolution of the gulf of Cadiz margin and southwest Portugal contourite depositional system: Tectonic, sedimentary and paleoceanographic implications from IODP expedition 339. Mar. Geol. 377, 7–39. https://doi.org/10.1016/j.margeo.2015.09.013

Hernández-Molina, F.J., Somoza, L., Vazquez, J.T., Lobo, F., Fernández-Puga, M.C., Llave, E., Díaz-del Río, V., 2002. Quaternary stratigraphic stacking patterns on the continental shelves of the southern Iberian Peninsula: Their relationship with global climate and palaeoceanographic changes. Quat. Int. 92, 5–23. https://doi.org/10.1016/S1040-6182(01)00111-2

Hernández-Molina, F.J., Soto, M., Piola, A.R., Tomasini, J., Preu, B., Thompson, P., Badalini, G., Creaser, A., Violante, R.A., Morales, E., Paterlini, M., De Santa Ana, H., 2016b. A contourite depositional system along the Uruguayan continental margin: Sedimentary, oceanographic and paleoceanographic implications. Mar. Geol. 378, 333–349. https://doi.org/10.1016/j.margeo.2015.10.008

Hernández-Molina, F.J., Stow, D.A.V., Alvarez-Zarikian, C.A., Acton, G., Bahr, A., Balestra, B., Ducassou, E., Flood, R., 2014b. Onset of Mediterranean outflow into the North Atlantic. Science (80-.). 344, 1244–1250.

Hickman, S., Mooney, W. ~D., Hsieh, P. ~A., Enomoto, C., Nelson, P. ~H., McNutt, M., 2010. Scientific Studies in Support of Shutting In the Macondo Well (Deepwater Horizon) Blowout, Gulf of Mexico (Invited), in: AGU Fall Meeting Abstracts. pp. NH43B-06.

Hitchcock, C., Givler, R., Angell, M., Hooper, J., 2010. GIS-Based Assessment of Submarine Mudflow Hazard Offshore of the Mississippi Delta, Gulf of Mexico, in: Mosher, D.C., Shipp, R.C., Moscardelli, L., Chaytor, J.D., Baxter, C.D.P., Lee, H.J., Urgeles, R. (Eds.), Submarine Mass Movements and Their Consequences, Advances in Natural and Technological Hazards Research. Springer Netherlands, pp. 353–364. https://doi.org/10.1007/978-90-481-3071-9

Hughes Clarke, J.E., 2018. Multibeam Echosounders, in: Micallef, A., Krastel, S., Savini, A. (Eds.), Submarine Geomorphology. Springer International Publishing, Cham, pp. 25–41. https://doi.org/10.1007/978-3-319-57852-1_3

Hüpers, A., Brune, R., Magalhaes, V., Freitas, M., Fleischmann, T., Freudenthal, T., Gonzales Lanchas, A., Haberkorn, P., Heine, L., Klaembt, C., Mazerath, P., Menapace, W., Meservy, W., Moreno, K., Pereira, S., Schmidt, J.N., Stanislowski, K., Stelzner, M., 2020. Preliminary results of R/V METEOR cruise M149: Shipboard and Post-Cruise Analysis, Recurrence of tsunamigenic hazards from MeBo drilling records and hazard mitigation using MeBo observatories, Las Palmas (Canary Islands) – Cadiz (Spain), 24.07.2018 – 24.0. Bremen.

Hurtado, J.E., Barbat, A.H., 1998. Monte Carlo techniques in computational stochastic mechanics. Arch. Comput. Methods Eng. 5, 3–29. https://doi.org/10.1007/bf02736747

Hustoft, S., Dugan, B., Mienert, J., 2009. Effects of rapid sedimentation on developing the Nyegga pockmark field: Constraints from hydrological modeling and 3-D seismic data, offshore mid-Norway. Geochemistry, Geophys. Geosystems 10. https://doi.org/10.1029/2009GC002409

Inverno, C.M., Manupella, G., Zbyszewski, G., Pais, J., Ribeiro, M.L., 1993. Notícia explicativa

da folha 42-C, Santiago do Cacém, 1:50.000.

IODP Expedition 339 Scientists, 2013a. Expedition 339 summary, in: Stow; Dorrik A.V.; Hernandez-Molina; F. J.; Alvarez-Zarikian; Carlos A; Expedition 308 Scientists (Ed.), Proc. IODP, 339. Integrated Ocean Drilling Program Management International, Inc., Tokyo. https://doi.org/10.2204/iodp.proc.339.101.2013

IODP Expedition 339 Scientists, 2013b. Site U1391 - Smear slides, in: Stow, D.A.V., Hernandez-Molina, F.J., Alvarez-Zarikian, C.A., Expedition 308 Scientists (Eds.), Proc. IODP, 339. Integrated Ocean Drilling Program Management International, Inc., Tokyo.

IODP Expedition 339 Scientists, 2013c. Site U1391 - Visual core description, in: Stow, D.A.V., Hernandez-Molina, F.J., Alvarez-Zarikian, C.A., Scientists, E. 308 (Eds.), Proc. IODP, 339. Integrated Ocean Drilling Program Management International, Inc., Tokyo, pp. 1–107.

Jibson, R.W., 2011. Methods for assessing the stability of slopes during earthquakes-A retrospective. Eng. Geol. 122, 43–50. https://doi.org/10.1016/j.enggeo.2010.09.017

Jibson, R.W., Harp, E.L., Michael, J.A., 2000. A method for producing digital probabilistic seismic landslide hazard maps. Eng. Geol. 58, 271–289. https://doi.org/10.1016/S0013-7952(00)00039-9

Jiménez-Espejo, F.J., Pardos-Gené, M., Martínez-Ruiz, F., García-Alix, A., van de Flierdt, T., Toyofuku, T., Bahr, A., Kreissig, K., 2015. Geochemical evidence for intermediate water circulation in the westernmost Mediterranean over the last 20kyrBP and its impact on the Mediterranean Outflow. Glob. Planet. Change 135, 38–46. https://doi.org/10.1016/j.gloplacha.2015.10.001

Johnson, J., Ambar, I., Serra, N., Stevens, I., 2002. Comparative studies of the spreading of Mediterranean Water through the Gulf of Cadiz. Deep. Res. Part II Top. Stud. Oceanogr. 49, 4179–4193. https://doi.org/10.1016/S0967-0645(02)00149-2

Johnson, P. a, Mcevilly, T. V, 1995. Parkfield seismicity : Fluid-driven ? Abstract . Characteristics of microearthquake occurrence along studies at Parkfield have defined attenuating fault zone and a high Vp / Vs ratio in the nucleation zone of the repeating Most of the ongoing seismicity i. Network 100, 937–950.

Jorgensen, D.G., 1980. Relationships betwa Basic Soils-Engineering Equations and Basic Ground-Water Flow Equations. Geol. Surv. Water-Supply.

Jowett, E.C., Cathles III, L.M., Davis, B.W., 1993. Predicting Depths of Gypsum Dehydration in Evaporitic Sedimentary Basins 1. Am. Assoc. Pet. Geol. Bull. 77, 402–413. https://doi.org/10.1306/BDFF8C22-1718-11D7-8645000102C1865D

Kane, I A, Kane, Ian A, Clare, M.A., Miramontes, E., Wogelius, R., Rothwell, J.J., Garreau, P., Pohl, F., 2020. Seafloor microplastic hotspots controlled by deep-sea circulation. Science (80-.). 5899, 1–11.

Kennett, J.P., 1982. Marine Geology. Prentice Hall, Englewood Cliffs, N.J.

Kimura, H., Yamaguchi, Y., 2000. Detection of landslide areas using satellite radar interferometry. Photogramm. Eng. Remote Sensing 66, 337–344.

Kitajima, H., Saffer, D.M., 2012. Elevated pore pressure and anomalously low stress in regions of low frequency earthquakes along the Nankai Trough subduction megathrust. Geophys. Res. Lett. 39, 1–5. https://doi.org/10.1029/2012GL053793

Knutz, P.C., 2008. Chapter 24 Palaeoceanographic Significance of Contourite Drifts. Dev. Sedimentol. 60, 511–535. https://doi.org/10.1016/S0070-4571(08)10024-3

Kopf, A., Asshoff, K., Belke-Brea, M., Bergenthal, M., Bohrmann, G., Bräuning, A., Düssmann, R., Feseker, T., Fleischmann, T., Franke, P., Geprägs, P., Hammerschmidt, S., Heesemann, B., Herschelmann, O., Hüpers, A., Ikari, M., Kaszemaik, K., Kaul, M., Kimura, T., Kitada,

K., Klar, S., Lange, M., Madison, M., Mai, A., Noorlander, C., Pape, T., Rehage, R., Reuter, C., Reuter, M., Rosiak, U., Saffer, D., Schmidt, W., Seiter, C., Spiesecke, U., Stachowski, A., Takanori, O., Tryon, M., Vahlenkamp, M., Wei, J., Wiemer, G., Wintersteller, P., Zarrouk, M., 2013. MeBo drilling and in situ Long-term Monitoring in the Nankai Trough accretionary complex, Japan. Berichte aus dem MARUM und dem Fachbereich Geowissenschaften der Universität Bremen.

Kopf, A., Freudenthal, T., Ratmeyer, V., Bergenthal, M., Lange, M., Fleischmann, T., Hammerschmidt, S., Seiter, C., Wefer, G., 2015. Simple, affordable, and sustainable borehole observatories for complex monitoring objectives. Geosci. Instrumentation, Methods Data Syst. 4, 99–109. https://doi.org/10.5194/gi-4-99-2015

Kopf, A.J., 2002. Significance of mud volcanism. Rev. Geophys. 40, 1005. https://doi.org/10.1029/2000RG000093

Krijgsman, W., Hilgen, F.J., Raffi, I., Sierro, F.J., Wilson, D.S., 1999. Chronology, causes and progression of the Messinian salinity crisis. Nature 400, 652–655. https://doi.org/10.1038/23231

Kunze, E., Rosenfeld, L.K., Carter, G.S., Gregg, M.C., 2002. Internal waves in Monterey Submarine Canyon. J. Phys. Oceanogr. 32, 1890–1913. https://doi.org/10.1175/1520-0485(2002)032<1890:IWIMSC>2.0.CO;2

Kvalstad, T.J., Andresen, L., Forsberg, C.F., Berg, K., Bryn, P., Wangen, M., 2005. The Storegga slide: Evaluation of triggering sources and slide mechanics. Mar. Pet. Geol. 22, 245–256. https://doi.org/10.1016/j.marpetgeo.2004.10.019

Kvenvolden, K.A., 1993. Gas hydrates-geological perspective and global change. Rev. Geophys. 31, 173–187. https://doi.org/10.1029/93RG00268

Laberg, J.S., Camerlenghi, A., 2008. The Significance of Contourites for Submarine Slope Stability, in: Developments in Sedimentology. Elsevier, pp. 537–556. https://doi.org/10.1016/S0070-4571(08)10025-5

Laberg, J.S., Stoker, M.S., Dahlgren, K.I.T., de Haas, H., Haflidason, H., Hjelstuen, B.O., Nielsen, T., Shannon, P.M., Vorren, T.O., van Weering, T.C.E., Ceramicola, S., 2005. Cenozoic alongslope processes and sedimentation on the NW European Atlantic margin. Mar. Pet. Geol. 22, 1069–1088. https://doi.org/10.1016/j.marpetgeo.2005.01.008

Lafuerza, S., Le Friant, A., Manga, M., Boudon, G., Villemant, B., Stroncik, N., Voight, B., Hornbach, M., Ishizuka, O., 2014. Geomechanical Characterization of Submarine Volcano-Flank Sediments, Martinique, Lesser Antilles Arc BT - Submarine Mass Movements and Their Consequences: 6th International Symposium, in: Krastel, S., Behrmann, J.-H., Völker, D., Stipp, M., Berndt, C., Urgeles, R., Chaytor, J., Huhn, K., Strasser, M., Harbitz, C.B. (Eds.), . Springer International Publishing, Cham, pp. 73–81. https://doi.org/10.1007/978-3-319-00972-8_7

Lafuerza, S., Sultan, N., Canals, M., Frigola, J., Berné, S., Jouet, G., Galavazi, M., Sierro, F.J., 2009. Overpressure within upper continental slope sediments from CPTU data, Gulf of Lion, NW Mediterranean Sea. Int. J. Earth Sci. 98, 751–768. https://doi.org/10.1007/s00531-008-0376-2

Le Friant, A., Boudon, G., Deplus, C., Villemant, B., 2003. Large-scale flank collapse events during the activity of Montagne Pelée, Martinique, Lesser Antilles. J. Geophys. Res. Solid Earth 108, 1–15. https://doi.org/10.1029/2001jb001624

Le Friant, A., Ishizuka, O., Boudon, G., Palmer, M.R., Talling, P.J., Villemant, B., Adachi, T., Aljahdali, M., 2015. Submarine record of volcanic island construction and collapse in the Lesser Antilles arc: First scientific drilling of submarine volcanic island landslides by IODP Expedition 340. Geochemistry Geophys. Geosystems 16, 420–442. https://doi.org/10.1002/2014GC005684.Key

Le Friant, A., Ishizuka, O., Stroncik, N., IODP Expedition 340 Scientists, 2013. Proc. IODP, 340, in: Integrated Ocean Drilling Program (Ed.), Proceedings of the IODP, 340. Tokyo.

Lebreiro, S.M., Mccave, N.I., Weaver, P.P.E., 1997. Late Quaternary Turbidite Emplacement on the Horseshoe Abyssal Plain (Iberian Margin). SEPM J. Sediment. Res. 67, 856–870. https://doi.org/10.1306/d4268658-2b26-11d7-8648000102c1865d

Lee, H., Baraza, J., 1999. Geotechnical characteristics and slope stability in the Gulf of Cadiz. Mar. Geol. 155, 173–190. https://doi.org/10.1016/S0025-3227(98)00146-7

Leonard, M., 2014. Self-Consistent Earthquake Fault-Scaling Relations: Update and Extension to Stable Continental Strike-Slip Faults. Bull. Seismol. Soc. Am. 104, 2953–2965. https://doi.org/10.1785/0120140087

Leynaud, D., Sultan, N., Mienert, J., 2007. The role of sedimentation rate and permeability in the slope stability of the formerly glaciated Norwegian continental margin: The Storegga slide model. Landslides 4, 297–309. https://doi.org/10.1007/s10346-007-0086-z

Liu, J.T., Wang, Y.H., Yang, R.J., Hsu, R.T., Kao, S.J., Lin, H.L., Kuo, F.H., 2012. Cyclone-induced hyperpycnal turbidity currents in a submarine canyon. J. Geophys. Res. Ocean. 117, 1–12. https://doi.org/10.1029/2011JC007630

Liu, X., Flemings, P., 2009. Dynamic response of oceanic hydrates to sea level drop. Geophys. Res. Lett. 36, 1–5. https://doi.org/10.1029/2009GL039821

Llave, E., Hernández-Molina, F.J., García, M., Ercilla, G., Roque, C., Juan, C., Mena, A., Preu, B., Van Rooij, D., Rebesco, M., Brackenridge, R., Jané, G., Gómez-Ballesteros, M., Stow, D., 2019. Contourites along the Iberian continental margins: conceptual and economic implications, Geological Society, London, Special Publications. https://doi.org/10.1144/sp476-2017-46

Llave, E., Hernández-Molina, F.J., Somoza, L., Stow, D.A.V., Díaz Del Río, V., Mar, D.C., Vigo, U. De, Southampton, S., 2007a. Quaternary evolution of the contourite depositional system in the Gulf of Cadiz. Geol. Soc. Spec. Publ. 276, 49–79. https://doi.org/10.1144/GSL.SP.2007.276.01.03

Llave, E., Hernández-Molina, F.J., Stow, D.A.V., Fernández-Puga, M.C., García, M., Vázquez, J.T., Maestro, A., Somoza, L., Díaz del Río, V., 2007b. Reconstructions of the Mediterranean Outflow Water during the quaternary based on the study of changes in buried mounded drift stacking pattern in the Gulf of Cadiz. Mar. Geophys. Res. 28, 379–394. https://doi.org/10.1007/s11001-007-9040-7

Llave, E., Matias, H., Hernández-Molina, F.J., Ercilla, G., Stow, D.A.V., Medialdea, T., 2011. Pliocene-Quaternary contourites along the northern Gulf of Cadiz margin: Sedimentary stacking pattern and regional distribution. Geo-Marine Lett. 31, 377–390. https://doi.org/10.1007/s00367-011-0241-3

Llave, E., Schönfeld, J., Hernández-Molina, F.J., Mulder, T., Somoza, L., Díaz Del Río, V., Sánchez-Almazo, I., 2006. High-resolution stratigraphy of the Mediterranean outflow contourite system in the Gulf of Cadiz during the late Pleistocene: The impact of Heinrich events. Mar. Geol. 227, 241–262. https://doi.org/10.1016/j.margeo.2005.11.015

Llopart, J., Lafuerza, S., Le Friant, A., Urgeles, R., Watremez, L., 2021. Long-term and long-distance deformation in submarine volcanoclastic sediments: coupling of hydrogeology and debris avalanche emplacement off W Martinique Island. Basin Res. 53. https://doi.org/10.1111/bre.12553

Llopart, J., Urgeles, R., Forsberg, C.F., Camerlenghi, A., Vanneste, M., Rebesco, M., Lucchi, R.G., Rüther, D.C., Lantzsch, H., 2019. Fluid flow and pore pressure development throughout the evolution of a trough mouth fan, western Barents Sea. Basin Res. 31, 487–513. https://doi.org/10.1111/bre.12331

Lo Iacono, C., Gràcia, E., Zaniboni, F., Pagnoni, G., Tinti, S., Bartolomé, R., Masson, D.G., Wynn, R.B., Lourenccedil, N., de Abreu, M.P., Dañobeitia, J.J., Zitellini, N., 2012. Large, deepwater slope failures: Implications for landslide-generated tsunamis. Geology 40, 931–934. https://doi.org/10.1130/G33446.1

Locat, J., Lee, H., Kayen, R., Israel, K., Savoie, M.C., Boulanger, É., 2002. Shear strength development with burial in Eel River margin slope sediments. Mar. Georesources Geotechnol. 20, 111–135. https://doi.org/10.1080/03608860290051831

Locat, J., Lee, H.J., 2002. Submarine landslides: Advances and challenges. Can. Geotech. J. 39, 193–212. https://doi.org/10.1139/t01-089

Locat, J., Leroueil, S., Locat, A., Lee, H., 2014. Weak Layers: Their Definition and Classification from a Geotechnical Perspective, in: Krastel, S., Behrmann, J.-H., Völker, D., Stipp, M., Berndt, C., Urgeles, R., Chaytor, J., Huhn, K., Strasser, M., Harbitz, C.B. (Eds.), Submarine Mass Movements and Their Consequences: 6th International Symposium. Springer International Publishing, Cham, pp. 3–12. https://doi.org/10.1007/978-3-319-00972-8_1

Locat, J., Tanaka, H., Tan, T., Dasari, G.R., Lee, H.J., 2003. Natural soils: geotechnical behavior and geological knowledge, in: Tan, T., Phoon, K., Hight, D., Leroueil, S. (Eds.), Characterisation and Engineering Properties of Natural Soils. Swets & Zeitlinger B.V., Lisse. The Netherlands, pp. 3–28.

Locker, S.D., Laine, E.P., 1992. Paleogene-Neogene depositional history of the middle U.S. Atlantic continental rise: mixed turbidite and contourite depositional systems. Mar. Geol. 103, 137–164. https://doi.org/10.1016/0025-3227(92)90013-8

Lofi, J., Voelker, A.H.L., Ducassou, E., Hernández-Molina, F.J., Sierro, F.J., Bahr, A., Galvani, A., Lourens, L.J., Pardo-Igúzquiza, E., Pezard, P., Rodríguez-Tovar, F.J., Williams, T., 2016. Quaternary chronostratigraphic framework and sedimentary processes for the Gulf of Cadiz and Portuguese Contourite Depositional Systems derived from Natural Gamma Ray records. Mar. Geol. 377, 40–57. https://doi.org/10.1016/j.margeo.2015.12.005

Loncke, L., Gaullier, V., Bellaiche, G., Mascle, J., 2002. Recent depositional patterns o the Nile deep-sea fan from echo-character mapping. Am. Assoc. Pet. Geol. Bull. 86, 1165–1186.

Long, H., Flemings, P.B., Germaine, J.T., 2007. Interpreting in situ pressure and hydraulic properties with borehole penetrometers in ocean drilling: DVTPP and piezoprobe deployments at southern Hydrate Ridge, offshore Oregon. J. Geophys. Res. Solid Earth 112, 1–17. https://doi.org/10.1029/2005JB004165

Long, H., Flemings, P.B., Germaine, J.T., Saffer, D.M., 2011. Consolidation and overpressure near the seafloor in the Ursa Basin, Deepwater Gulf of Mexico. Earth Planet. Sci. Lett. 305, 11–20. https://doi.org/10.1016/j.epsl.2011.02.007

Long, H., Flemings, P.B., Germaine, J.T., Saffer, D.M., Dugan, B., 2008. Data report: consolidation characteristics of sediments from IODP Expedition 308, Ursa Basin, Gulf of Mexico 308. https://doi.org/10.2204/iodp.proc.308.204.2008

Lucchi, R.G., Rebesco, M., 2007. Glacial contourites on the Antarctic Peninsula margin: Insight for palaeoenvironmental and palaeoclimatic conditions. Geol. Soc. Spec. Publ. 276, 111–127. https://doi.org/10.1144/GSL.SP.2007.276.01.06

Lunne, T., Robertson, P.K., Powell, J.J.M., 1997. Cone Penetration Testing in geotechnical practice. SponPress, London.

Maldonado, A., Somoza, L., Pallarés, L., 1999. The Betic orogen and the Iberian-African boundary in the Gulf of Cadiz: Geological evolution (central North Atlantic). Mar. Geol. 155, 9–43. https://doi.org/10.1016/S0025-3227(98)00139-X

Malod, J.A., Mauffret, A., 1990. Iberian plate motions during the Mesozoic. Tectonophysics 184, 261–278. https://doi.org/10.1016/0040-1951(90)90443-C

Mankelow, J.M., Murphy, W., 1998. Using gis in the probabilistic assessment of earthquake triggered landslide hazards. J. Earthq. Eng. 2, 593–623. https://doi.org/10.1080/13632469809350336

Marchès, E., Mulder, T., Cremer, M., Bonnel, C., Hanquiez, V., Gonthier, E., Lecroart, P., 2007. Contourite drift construction influenced by capture of Mediterranean Outflow Water deep-sea current by the Portimão submarine canyon (Gulf of Cadiz, South Portugal). Mar. Geol. 242, 247–260. https://doi.org/10.1016/j.margeo.2007.03.013

Marchès, E., Mulder, T., Gonthier, E., Cremer, M., Hanquiez, V., Garlan, T., Lecroart, P., 2010. Perched lobe formation in the Gulf of Cadiz: Interactions between gravity processes and contour currents (Algarve Margin, Southern Portugal). Sediment. Geol. 229, 81–94. https://doi.org/10.1016/j.sedgeo.2009.03.008

Marín-Moreno, H., Minshull, T.A., Edwards, R.A., 2013. A disequilibrium compaction model constrained by seismic data and application to overpressure generation in The Eastern Black Sea Basin. Basin Res. 25, 331–347. https://doi.org/10.1111/bre.12001

Marine, I.W., Fritz, S.J., 1981. Osmotic model to explain anomalous hydraulic heads. Water Resour. Res. 17, 73–82. https://doi.org/10.1029/WR017i001p00073

Martínez-Loriente, S., 2013. Geophysical and geological characterization of the active structures and of the nature of the basement in the Eurasia-Africa plate boundary (SW Iberian Margin): Implications for regional geodynamics and seismic hazard assessment Geophysical and geologic 353.

Martínez-Loriente, S., Gràcia, E., Bartolome, R., Perea, H., Klaeschen, D., Dañobeitia, J.J., Zitellini, N., Wynn, R.B., Masson, D.G., 2018. Morphostructure, tectono-sedimentary evolution and seismic potential of the Horseshoe Fault, SW Iberian Margin. Basin Res. 30, 382–400. https://doi.org/10.1111/bre.12225

Martínez-Loriente, S., Gràcia, E., Bartolome, R., Sallarès, V., Connors, C., Perea, H., Lo Iacono, C., Klaeschen, D., Terrinha, P., Dañobeitia, J.J., Zitellini, N., 2013. Active deformation in old oceanic lithosphere and significance for earthquake hazard: Seismic imaging of the Coral Patch Ridge area and neighboring abyssal plains (SW Iberian Margin). Geochemistry, Geophys. Geosystems 14, 2206–2231. https://doi.org/10.1002/ggge.20173

Martínez-Loriente, S., Sallarès, V., Gràcia, E., 2021. The Horseshoe Abyssal plain Thrust could be the source of the 1755 Lisbon earthquake and tsunami. Commun. Earth Environ. 2, 1–9. https://doi.org/10.1038/s43247-021-00216-5

Maslin, M., Owen, M., Betts, R., Day, S., Jones, T.D., Ridgwell, A., 2010. Gas hydrates: Past and future geohazard? Philos. Trans. R. Soc. A Math. Phys. Eng. Sci. 368, 2369–2393. https://doi.org/10.1098/rsta.2010.0065

Maslin, M., Owen, M., Day, S., Long, D., 2004. Linking continental-slope failures and climate change: Testing the clathrate gun hypothesis. Geology 32, 53–56. https://doi.org/10.1130/G20114.1

Masson, D.G., Harbitz, C.B., Wynn, R.B., Pedersen, G., Løvholt, F., 2006. Submarine landslides: processes, triggers and hazard prediction. Philos. Trans. R. Soc. A Math. Phys. Eng. Sci. 364, 2009–2039. https://doi.org/10.1098/rsta.2006.1810

Masson, D.G., Wynn, R.B., Talling, P.J., 2010. Large landslides on passive continental margins: Processes, hypotheses and outstanding questions. Submar. Mass Movements Their Consequences - 4th Int. Symp. 28, 153–165. https://doi.org/10.1007/978-90-481-3071-9_13

McBride, R.A., 2002. 2.9 Atterberg Limits. Methods Soil Anal., SSSA Book Series. https://doi.org/https://doi.org/10.2136/sssabookser5.4.c17

McCave, I.N., 1984. Erosion, transport and deposition of fine-grained marine sediments. Geol. Soc. Spec. Publ. 15, 35–69. https://doi.org/10.1144/GSL.SP.1984.015.01.03

McCave, I.N., Hall, I.R., 2002. Turbidity of waters over the Northwest Iberian continental margin. Prog. Oceanogr. 52, 299–313. https://doi.org/10.1016/S0079-6611(02)00012-5

Mencaroni, D., Llopart, J., Urgeles, R., Lafuerza, S., Gràcia, E., Le Friant, A., Urlaub, M., 2020. From gravity cores to overpressure history: the importance of measured sediment physical properties in hydrogeological models. Geol. Soc. London, Spec. Publ. SP500-2019–176. https://doi.org/10.1144/sp500-2019-176

Mencaroni, D., Urgeles, R., Camerlenghi, A., Llopart, J., Ford, J., Sanchez Serra, C., Meservy, W., Gràcia, E., Rebesco, M., Zitellini, N., 2021. A mixed turbidite – contourite system related to a major submarine canyon: The Marquês de Pombal Drift (south-west Iberian margin). Sedimentology sed.12844. https://doi.org/10.1111/sed.12844

Mestdagh, T., Lobo, F.J., Llave, E., Hernández-Molina, F.J., García Ledesma, A., Puga-Bernabéu, Á., Fernández-Salas, L.M., Rooij, D. Van, 2020. Late Quaternary multi-genetic processes and products on the northern Gulf of Cadiz upper continental slope (SW Iberian Peninsula). Mar. Geol. 427, 106214. https://doi.org/10.1016/j.margeo.2020.106214

Mestdagh, T., Lobo, F.J., Llave, E., Hernández-Molina, F.J., Van Rooij, D., 2019. Review of the late Quaternary stratigraphy of the northern Gulf of Cadiz continental margin: New insights into controlling factors and global implications. Earth-Science Rev. 198, 102944. https://doi.org/10.1016/j.earscirev.2019.102944

Micallef, A., Masson, D.G., Berndt, C., Stow, D.A.V., 2009. Development and mass movement processes of the north-eastern Storegga Slide. Quat. Sci. Rev. 28, 433–448. https://doi.org/10.1016/j.quascirev.2008.09.026

Michels, K.H., Rogenhagen, J., Kuhn, G., 2001. Recognition of contour-current influence in mixed contourite-turbidite sequences of the western Weddell Sea , Antarctica. Mar. Geophys. Researhes 22, 465–485.

Miller, K.G., Kominz, M.A., Browning, J. V., Wright, J.D., Mountain, G.S., Katz, M.E., Sugarman, P.J., Cramer, B.S., Christie-Blick, N., Pekar, S.F., 2005. The phanerozoic record of global sea-level change. Science (80-.). 310, 1293–1298. https://doi.org/10.1126/science.1116412

Miller, M.C., McCave, I.N., Komar, P.D., 1977. Threshold of Sediment Motion under Unidirectional Currents. Sedimentology 24, 507–527.

Minning, M., Hebbeln, D., Hensen, C., Kopf, A., 2006. Geotechnical and geochemical investigations of the Marquês de Pombal landslide at the Portuguese continental margin. Nor. Geol. Tidsskr. 86, 187–198.

Miramontes, E., Cattaneo, A., Jouet, G., Garziglia, S., 2016a. Implications of sediment dynamics in mass transport along the Pianosa Ridge (Northern Tyrrhenian Sea). Adv. Nat. Technol. Hazards Res. 41, 301–309. https://doi.org/10.1007/978-3-319-20979-1_30

Miramontes, E., Cattaneo, A., Jouet, G., Théreau, E., Thomas, Y., Rovere, M., Cauquil, E., Trincardi, F., 2016b. The Pianosa Contourite Depositional System (Northern Tyrrhenian Sea): Drift morphology and Plio-Quaternary stratigraphic evolution. Mar. Geol. 378, 20–42. https://doi.org/10.1016/j.margeo.2015.11.004

Miramontes, E., Eggenhuisen, J.T., Silva Jacinto, R., Poneti, G., Pohl, F., Normandeau, A., Campbell, D.C., Hernández-Molina, F.J., 2020. Channel-levee evolution in combined contour current–turbidity current flows from flume-tank experiments. Geology 48, 353–357. https://doi.org/10.1130/G47111.1

Miramontes, E., Garreau, P., Caillaud, M., Jouet, G., Pellen, R., Hernández-Molina, F.J., Clare, M.A., Cattaneo, A., 2019. Contourite distribution and bottom currents in the NW Mediterranean Sea: Coupling seafloor geomorphology and hydrodynamic modelling. Geomorphology 333, 43–60. https://doi.org/10.1016/j.geomorph.2019.02.030

Miramontes, E., Garziglia, S., Sultan, N., Jouet, G., Cattaneo, A., 2018. Morphological control of slope instability in contourites: a geotechnical approach. Landslides 15, 1085–1095. https://doi.org/10.1007/s10346-018-0956-6

Mougenot, D., 1979. La marge continentale sud-portugaise: évolution structurale et sédimentaire. Ciências da Terra 5, 223–246.

Mulder, T., Cochonat, P., 1996. Classification of offshore mass movements. J. Sediment. Res. https://doi.org/10.1306/D42682AC-2B26-11D7-8648000102C1865D

Mulder, T., Faugères, J.C., Gonthier, E., 2008. Mixed Turbidite-Contourite Systems. Dev. Sedimentol. 60, 435–456. https://doi.org/10.1016/S0070-4571(08)10021-8

Mulder, T., Lecroart, P., Hanquiez, V., Marches, E., Gonthier, E., Guedes, J.C., Thiébot, E., Jaaidi, B., Kenyon, N., Voisset, M., Perez, C., Sayago, M., Fuchey, Y., Bujan, S., 2006. The western part of the Gulf of Cadiz: Contour currents and turbidity currents interactions. Geo-Marine Lett. 26, 31–41. https://doi.org/10.1007/s00367-005-0013-z

Mulder, T., Voisset, M., Lecroart, P., Le Drezen, E., Gonthier, E., Hanquiez, V., Faugres, J.C., Habgood, E., Hernández-Molina, F.J., Estrada, F., Llave-Barranco, E., Poirier, D., Gorini, C., Fuchey, Y., Voelker, A., Freitas, P., Sanchez, F.L., Fernandez, L.M., Kenyon, N.H., Morel, J., 2003. The Gulf of Cadiz: an unstable giant contouritic levee. Geo-Marine Lett. 23, 7–18. https://doi.org/10.1007/s00367-003-0119-0

Nadim, F., 2015. Accounting for Uncertainty and Variability in Geotechnical Characterization of Offshore Sites. Geotech. Saf. Risk V 23–34. https://doi.org/10.3233/978-1-61499-580-7-23

Nardin, T.R., Hein, F.J., Gorsline, D.S., Edwards, B.D., 1979. A review of mass movement processes, sediment and acoustic characteristics, and contrasts in slope and base-of-slope systems versus canyon- fan- basin floor systems, in: Doyle, L.J., Pilkey, O.H. (Eds.), Geology of Continental Slopes, SEPM Special Publication. SEPM (Society for Sedimentary Geology), pp. 61–73. https://doi.org/10.2110/pec.79.27

Nelson, C.H., Baraza, J., Maldonado, A., Rodero, J., Escutia, C., Barber, J.H., 1999. Influence of the Atlantic inflow and Mediterranean outflow currents on Late Quaternary sedimentary facies of the Gulf of Cadiz continental margin. Mar. Geol. 155, 99–129. https://doi.org/10.1016/S0025-3227(98)00143-1

Neuzil, C.E., 2000. Osmotic generation of “anomalous” fluid pressures in geological environments. Nature 403, 182–184. https://doi.org/10.1038/35003174

Neuzil, C.E., 1995. Abnormal pressures as hydrodynamic phenomena. Am. J. Sci. 295, 742–786. https://doi.org/10.2475/ajs.295.6.742

Neves, M.C., Roque, C., Luttrell, K.M., Vázquez, J.T., Alonso, B., 2016. Impact of sea-level rise on earthquake and landslide triggering offshore the Alentejo margin (SW Iberia). Geo-Marine Lett. 36, 415–424. https://doi.org/10.1007/s00367-016-0459-1

Nichol, J., Wong, M.S., 2005. Satellite remote sensing for detailed landslide inventories using change detection and image fusion. Int. J. Remote Sens. 26, 1913–1926. https://doi.org/10.1080/01431160512331314047

Nichols, M.D., Xuan, C., Crowhurst, S., Hodell, D.A., Richter, C., Acton, G.D., Wilson, P.A., 2020. Climate-Induced Variability in Mediterranean Outflow to the North Atlantic Ocean During the Late Pleistocene. Paleoceanogr. Paleoclimatology 35, 1–17. https://doi.org/10.1029/2020PA003947

Nicholson, U., Libby, S., Tappin, D.R., McCarthy, D., 2020. The Subantarctic Front as a sedimentary conveyor belt for tsunamigenic submarine landslides. Mar. Geol. 424, 106161. https://doi.org/10.1016/j.margeo.2020.106161

Nielsen, T., Knutz, P.C., Kuijpers, A., 2008. Chapter 16 Seismic Expression of Contourite Depositional Systems. Dev. Sedimentol. 60, 301–321. https://doi.org/10.1016/S0070-

4571(08)10016-4

Nihous, G.C., Masutani, S.M., 2006. Notes on the dissolution rate of gas hydrates in undersaturated water. Chem. Eng. Sci. 61, 7827–7830. https://doi.org/10.1016/j.ces.2005.09.010

Obana, K., Kodaira, S., 2009. Low-frequency tremors associated with reverse faults in a shallow accretionary prism. Earth Planet. Sci. Lett. 287, 168–174. https://doi.org/10.1016/j.epsl.2009.08.005

Ochoa, J., Bray, N.A., 1991. Water mass exchange in the Gulf of Cadiz. Deep Sea Res. Part A. Oceanogr. Res. Pap. 38, S465–S503. https://doi.org/10.1016/s0198-0149(12)80021-5

Oliveira, J.T., 1984. Notícia explicativa de carta geológica de Portugal, folha 7, 1:200.000.

Orange, D.L., Saffer, D., Jeanjean, P., Al-Khafaji, Z., Humphrey, G., Riley, G., 2003. Measurements and modeling of the shallow pore pressure regime at the Sigsbee escarpment: Successful prediction of overpressure and ground-truthing with borehole measurements. Lead. Edge 22, 906–913. https://doi.org/10.1190/1.1614157

Osborne, M.J., Swarbrick, R.E., 1997. Mechanisms for generating overpressure in sedimentary basins: A reevaluation. Am. Assoc. Pet. Geol. Bull. 81, 1023–1041.

Öser, C., 2020. Determining the plasticity properties of high plastic clays: a new empirical approach. Arab. J. Geosci. 13. https://doi.org/10.1007/s12517-020-05412-9

Paull, C.K., Talling, P.J., Maier, K.L., Parsons, D., Xu, J., Caress, D.W., Gwiazda, R., Lundsten, E.M., Anderson, K., Barry, J.P., Chaffey, M., O'Reilly, T., Rosenberger, K.J., Gales, J.A., Kieft, B., McGann, M., Simmons, S.M., McCann, M., Sumner, E.J., Clare, M.A., Cartigny, M.J., 2018. Powerful turbidity currents driven by dense basal layers. Nat. Commun. 9, 1–9. https://doi.org/10.1038/s41467-018-06254-6

Peacock, S.M., Christensen, N.I., Bostock, M.G., Audet, P., 2011. High pore pressures and porosity at 35 km depth in the Cascadia subduction zone. Geology 39, 471–474. https://doi.org/10.1130/G31649.1

Peakall, J., Kane, I.A., Masson, D.G., Keevil, G., Mccaffrey, W., Corney, R., 2012. Global (latitudinal) variation in submarine channel sinuosity. Geology 40, 11–14. https://doi.org/10.1130/G32295.1

Pereira, R., 2013. Continental rifting and post breakup evolution of Southwest Iberia: Tectono-stratigraphic record of the first segment of the North Atlantic Ocean. PhD Thesis 343.

Pereira, R., Alves, T.M., 2013. Crustal deformation and submarine canyon incision in a Meso-Cenozoic first-order transfer zone (SW Iberia, North Atlantic Ocean). Tectonophysics 601, 148–162. https://doi.org/10.1016/j.tecto.2013.05.007

Pereira, R., Alves, T.M., 2011. Margin segmentation prior to continental break-up: A seismic-stratigraphic record of multiphased rifting in the North Atlantic (Southwest Iberia). Tectonophysics 505, 17–34. https://doi.org/10.1016/j.tecto.2011.03.011

Piper, D.J.W., Aksu, A.E., 1987. The source and origin of the 1929 grand banks turbidity current inferred from sediment budgets. Geo-Marine Lett. 7, 177–182. https://doi.org/10.1007/BF02242769

Piper, D.J.W., Cochonat, P., Morrison, M.L., 1999. The sequence of events around the epicentre of the 1929 Grand Banks earthquake: Initiation of debris flows and turbidity current inferred from sidescan sonar. Sedimentology 46, 79–97. https://doi.org/10.1046/j.1365-3091.1999.00204.x

Polito, C.P., Green, R.A., Lee, J., 2008. Pore Pressure Generation Models for Sands and Silty Soils Subjected to Cyclic Loading. J. Geotech. Geoenvironmental Eng. 134, 1490–1500. https://doi.org/10.1061/(asce)1090-0241(2008)134:10(1490)

Premchitt, J., Ho, K.S., Evans, N.C., 1995. Conventional and CRS Rowe cell consolidation test on some Hong Kong Clays.

Prior, D.B., Coleman, J.M., 1982. Active Slides and Flows in Underconsolidated Marine Sediments on the Slopes of the Mississippi Delta, in: Saxov, S., Nieuwenhuis, J.K. (Eds.), Marine Slides and Other Mass Movements. Springer US, Boston, MA, pp. 21–49. https://doi.org/10.1007/978-1-4613-3362-3_3

Puig, P., Palanques, A., Guillén, J., El Khatab, M., 2004. Role of internal waves in the generation of nepheloid layers on the northwestern Alboran slope: Implications for continental margin shaping. J. Geophys. Res. C Ocean. 109, 1–11. https://doi.org/10.1029/2004JC002394

Rampello, S., Callisto, L., Fargnoli, P., 2010. Evaluation of slope performance under earthquake loading conditions. Riv. Ital. di Geotec. 44, 29–41.

Rasmussen, S., Lykke-Andersen, H., Kuijpers, A., Troelstra, S.R., 2003. Post-miocene sedimentation at the continental rise of Southeast Greenland: The interplay between turbidity and contour currents. Mar. Geol. 196, 37–52. https://doi.org/10.1016/S0025-3227(03)00043-4

Rebesco, M., Camerlenghi, A., 2008. Late Pliocene margin development and mega debris flow deposits on the Antarctic continental margins: Evidence of the onset of the modern Antarctic Ice Sheet? Palaeogeogr. Palaeoclimatol. Palaeoecol. 260, 149–167. https://doi.org/10.1016/j.palaeo.2007.08.009

Rebesco, M., Camerlenghi, A. (Eds.), 2006. Contourites, Developments in Sedimentology, 60. Elsevier, Amsterdam.

Rebesco, M., Camerlenghi, A., Volpi, V., Neagu, C., Accettella, D., Lindberg, B., Cova, A., Zgur, F., Party, M., 2007. Interaction of processes and importance of contourites: Insights from the detailed morphology of sediment Drift 7, Antarctica. Geol. Soc. Spec. Publ. 276, 95–110. https://doi.org/10.1144/GSL.SP.2007.276.01.05

Rebesco, M., Hernández-Molina, F.J., Van Rooij, D., Wåhlin, A., 2014. Contourites and associated sediments controlled by deep-water circulation processes: State-of-the-art and future considerations. Mar. Geol. 352, 111–154. https://doi.org/10.1016/j.margeo.2014.03.011

Rebesco, M., Larter, R.D., Camerlenghi, A., Barker, P.F., 1996. Giant sediment drifts on the continental rise west of the Antarctic Peninsula. Geo-Marine Lett. 16, 65–75. https://doi.org/10.1007/bf02202600

Reddy, J.N., 2011. Numerical Methods, Finite Element, in: Gupta, H.. (Ed.), Encyclopedia of Solid Earth Geophysics. Springer, Dordrecht, Netherlands, pp. 892–895. https://doi.org/10.1007/978-90-481-8702-7

Reece, J.S., Flemings, P.B., Dugan, B., Long, H., Germaine, J.T., 2012. Permeability-porosity relationships of shallow mudstones in the Ursa Basin, northern deepwater Gulf of Mexico. J. Geophys. Res. B Solid Earth 117, 1–13. https://doi.org/10.1029/2012JB009438

Reed, A.H., Briggs, K.B., Lavoie, D.L., 2002. Porometric properties of siliciclastic marine sand: A comparison of traditional laboratory measurements with image analysis and effective medium modeling. IEEE J. Ocean. Eng. 27, 581–592. https://doi.org/10.1109/JOE.2002.1040940

Revil, A., Cathles, L.M., Shosa, J.D., Pezard, P.A., de Larouzière, F.D., 1998. Capillary sealing in sedimentary basins: A clear field example. Geophys. Res. Lett. 25, 389–392. https://doi.org/10.1029/97GL03775

Revil, A., Pezard, P.A., de Larouziere, F.D., 1999. Fluid overpressures in Western Mediterranean sediments, sites 974-979. Proc. Ocean Drill. Progr. Sci. Results 161, 117–128. https://doi.org/10.2973/odp.proc.sr.161.274.1999

Ribeiro, A., Oliveira, J.T., Ramalho, M., Ribeiro, M.L., Silva, L., 1987. Notícia explicativa de folha 48-D, Bordeira, 1:50.000.

Ribó, M., Puig, P., Muñoz, A., Lo Iacono, C., Masqué, P., Palanques, A., Acosta, J., Guillén, J., Gómez Ballesteros, M., 2016. Morphobathymetric analysis of the large fine-grained sediment waves over the Gulf of Valencia continental slope (NW Mediterranean). Geomorphology 253, 22–37. https://doi.org/10.1016/j.geomorph.2015.09.027

Ribó, M., Puig, P., Salat, J., Palanques, A., 2013. Nepheloid layer distribution in the Gulf of Valencia, northwestern Mediterranean. J. Mar. Syst. 111–112, 130–138. https://doi.org/10.1016/j.jmarsys.2012.10.008

Riboulot, V., Cattaneo, A., Sultan, N., Garziglia, S., Ker, S., Imbert, P., Voisset, M., 2013. Sea-level change and free gas occurrence influencing a submarine landslide and pockmark formation and distribution in deepwater Nigeria. Earth Planet. Sci. Lett. 375, 78–91. https://doi.org/10.1016/j.epsl.2013.05.013

Rodrigues, S., Roque, C., Hernández-Molina, F.J., Llave, E., Terrinha, P., 2020. The sines contourite depositional system along the SW Portuguese margin: Onset, evolution and conceptual implications. Mar. Geol. 430, 106357. https://doi.org/10.1016/j.margeo.2020.106357

Rodrigues, S.M., 2017. Seismostratigraphic model of the Sines Contourite Drift (SW Portuguese margin)-depositional evolution, structural control and paleoceanographic implications Mestrado em Geologia Especialização em Estratigrafia, Sedimentologia e Paleontologia. M.Sc Thesis.

Roest, W.R., Srivastava, S.P., 1991. Kinematics of the plate boundaries between Eurasia, Iberia, and Africa in the North Atlantic from the Late Cretaceous to the present. Geology 19, 613–616. https://doi.org/10.1130/0091-7613(1991)019<0613:KOTPBB>2.3.CO;2

Rogerson, M., Bigg, G.R., Rohling, E.J., Ramirez, J., 2012a. Vertical density gradient in the eastern North Atlantic during the last 30,000 years. Clim. Dyn. 39, 589–598. https://doi.org/10.1007/s00382-011-1148-4

Rogerson, M., Rohling, E.J., Bigg, G.R., Ramirez, J., 2012b. Paleoceanography of the Atlantic-Mediterranean exchange: Overview and first quantitative assessment of climatic forcing. Rev. Geophys. 50, RG2003. https://doi.org/10.1029/2011RG000376

Rogerson, M., Rohling, E.J., Weaver, P.P.E., Murray, J.W., 2005. Glacial to interglacial changes in the settling depth of the Mediterranean Outflow plume. Paleoceanography 20, 1–12. https://doi.org/10.1029/2004PA001106

Rovere, M., Ranero, C.R., Sartori, R., Torelli, L., Zitellini, N., 2004. Seismic images and magnetic signature of the Late Jurassic to Early Cretaceous Africa-Eurasia plate boundary off SW Iberia. Geophys. J. Int. 158, 554–568. https://doi.org/10.1111/j.1365-246X.2004.02339.x

Roveri, M., Flecker, R., Krijgsman, W., Lofi, J., Lugli, S., Manzi, V., Sierro, F.J., Bertini, A., Camerlenghi, A., De Lange, G., Govers, R., Hilgen, F.J., Hübscher, C., Meijer, P.T., Stoica, M., 2014. The Messinian Salinity Crisis: Past and future of a great challenge for marine sciences. Mar. Geol. 352, 25–58. https://doi.org/10.1016/j.margeo.2014.02.002

Rowe, P.W., Barden, L., 1966. A New Consolidation Cell. Géotechnique 16, 162–170. https://doi.org/10.1680/geot.1966.16.2.162

Rubey, W.W., Hubbert, M.K., 1959. Role of fluid pressure in mechanics of overthrust faulting, Part 2. Overthrust belt in geosynclinal area ofwestern Wyoming in light of fluid-pressure hypothesis. Geol. Soc. Am. Bull. 70, 167–205.

Saffer, D.M., 2003. Pore pressure development and progressive dewatering in underthrust sediments at the Costa Rican subduction margin: Comparison with northern Barbados and Nankai. J. Geophys. Res. Solid Earth 108, 1–16. https://doi.org/10.1029/2002jb001787

Saffer, D.M., Tobin, H.J., 2011. Hydrogeology and mechanics of subduction zone forearcs: Fluid flow and pore pressure. Annu. Rev. Earth Planet. Sci. 39, 157–186. https://doi.org/10.1146/annurev-earth-040610-133408

Sallarès, V., Gràcia, E., Urgelés, R., 2010. Active Faulting and Slope Failure in the Iberian Margins : Towards offshore geohazard mitigation 1–12.

Sallarès, V., Martínez-Loriente, S., Prada, M., Gràcia, E., Ranero, C., Gutscher, M.A., Bartolome, R., Gailler, A., Dañobeitia, J.J., Zitellini, N., 2013. Seismic evidence of exhumed mantle rock basement at the Gorringe Bank and the adjacent Horseshoe and Tagus abyssal plains (SW Iberia). Earth Planet. Sci. Lett. 365, 120–131. https://doi.org/10.1016/j.epsl.2013.01.021

Sammartini, M., Camerlenghi, A., Budillon, F., Insinga, D.D., Zgur, F., Conforti, A., Iorio, M., Romeo, R., Tonielli, R., 2019. Open-slope, translational submarine landslide in a tectonically active volcanic continental margin (Licosa submarine landslide, southern tyrrhenian sea). Geol. Soc. Spec. Publ. 477, 133–150. https://doi.org/10.1144/SP477.34

Sanchez-Cabeza, J.A., Masqué, P., Ani-Ragolta, I., 1998. 210Pb and210Po analysis in sediments and soils by microwave acid digestion. J. Radioanal. Nucl. Chem. 227, 19–22. https://doi.org/10.1007/BF02386425

Sánchez-Leal, R.F., Bellanco, M.J., Fernández-Salas, L.M., García-Lafuente, J., Gasser-Rubinat, M., González-Pola, C., Hernández-Molina, F.J., Pelegrí, J.L., Peliz, A., Relvas, P., Roque, D., Ruiz-Villarreal, M., Sammartino, S., Sánchez-Garrido, J.C., 2017. The Mediterranean Overflow in the Gulf of Cadiz: A rugged journey. Sci. Adv. 3, 1–12. https://doi.org/10.1126/sciadv.aao0609

Sánchez-Leal, R.F., Bellanco, M.J., Naranjo, C., García-Lafuente, J., González-Pola, C., 2020. On the seasonality of waters below the seasonal thermocline in the Gulf of Cádiz. Cont. Shelf Res. 204. https://doi.org/10.1016/j.csr.2020.104190

Sandoval, G.F.B., Galobardes, I., Teixeira, R.S., Toralles, B.M., 2017. Comparison between the falling head and the constant head permeability tests to assess the permeability coefficient of sustainable Pervious Concretes. Case Stud. Constr. Mater. 7, 317–328. https://doi.org/10.1016/j.cscm.2017.09.001

Sansom, P., 2018. Hybrid turbidite–contourite systems of the Tanzanian margin. Pet. Geosci. 24, 258–276.

Sartori, R., Torelli, L., Zitellini, N., Peis, D., Lodolo, E., 1994. Eastern segment of the Azores-Gibraltar line (central-eastern Atlantic): an oceanic plate boundary with diffuse compressional deformation. Geology 22, 555–558. https://doi.org/10.1130/0091-7613(1994)022<0555:ESOTAG>2.3.CO;2

Sawyer, D.E., Devore, J.R., 2015. M argins : Evidence for seismic strengthening 216–221. https://doi.org/10.1002/2015GL066603.Received

Sawyer, D.E., Flemings, P.B., Shipp, R.C., Winker, C.D., 2007. Seismic geomorphology, lithology, and evolution of the late Pleistocene Mars-Ursa Turbidite region, Mississippi Canyon Area, Northern Gulf of Mexico. Am. Assoc. Pet. Geol. Bull. 91, 215–234.

Sayers, C.M., Johnson, G.M., Denyer, G., 2002. Predrill pore-pressure prediction using seismic data. Geophysics 67, 1286–1292. https://doi.org/10.1190/1.1500391

Schettino, A., Turco, E., 2009. Breakup of Pangaea and plate kinematics of the central Atlantic and Atlas regions. Geophys. J. Int. 178, 1078–1097. https://doi.org/10.1111/j.1365-246X.2009.04186.x

Schönfeld, J., Zahn, R., 2000. Late Glacial to Holocene history of the Mediterranean outflow. Evidence from benthic foraminiferal assemblages and stable isotopes at the Portuguese margin. Palaeogeogr. Palaeoclimatol. Palaeoecol. 159, 85–111.

https://doi.org/10.1016/S0031-0182(00)00035-3

Schönfeld, J., Zahn, R., De Abreu, L., 2003. Surface and deep water response to rapid climate changes at the Western Iberian margin. Glob. Planet. Change 36, 237–264. https://doi.org/10.1016/S0921-8181(02)00197-2

Schultheiss, P.J., 1990. Pore pressures in marine sediments: An overview of measurement techniques and some geological and engineering applications. Mar. Geophys. Res. 12, 153–168. https://doi.org/10.1007/BF00310570

Screaton, E.J., 2010. Recent advances in subseafloor hydrogeology: Focus on basement-sediment interactions, subduction zones, and continental slopes. Hydrogeol. J. 18, 1547–1570. https://doi.org/10.1007/s10040-010-0636-7

Screaton, E.J., Carson, B., Lennon, G.P., 1995. Hydrogeologic properties of a thrust fault within the Orogen accretionary prism. J. Geophys. Res. 100. https://doi.org/10.1029/95jb02152

Seed, H.B., Idriss, I.M., 1971. Simplified Procedure for Evaluating Soil Liquefaction Potential. J. Soil Mech. Found. Div. 97, 1249–1273. https://doi.org/10.1061/JSFEAQ.0001662

Seed, H.B., Woodward, R., Lundgren, R., 1964. Fundamental Aspects of the Atterberg Limits. J. Soil Mech. Found. Div. 90, 75–106. https://doi.org/10.1061/JSFEAQ.0000685

Serra, C.S., Martínez-Loriente, S., Gràcia, E., Urgeles, R., Vizcaino, A., Perea, H., Bartolome, R., Pallàs, R., Lo Iacono, C., Diez, S., Dañobeitia, J., Terrinha, P., Zitellini, N., 2020. Tectonic evolution, geomorphology and influence of bottom currents along a large submarine canyon system: The São Vicente Canyon (SW Iberian margin). Mar. Geol. 426, 106219. https://doi.org/10.1016/j.margeo.2020.106219

Serra, C.S., Martínez-Loriente, S., Gràcia, E., Urgeles, R., Gómez de la Peña, L., Maesano, F.E., Basili, R., Volpe, M., Romano, F., Scala, A., Piatanesi, A., Lorito, S., 2021. Sensitivity of Tsunami Scenarios to Complex Fault Geometry and Heterogeneous Slip Distribution: Case-Studies for SW Iberia and NW Morocco. J. Geophys. Res. Solid Earth 1–19. https://doi.org/10.1029/2021jb022127

Serra, N., Ambar, I., Käse, R.H., 2005. Observations and numerical modelling of the Mediterranean outflow splitting and eddy generation. Deep. Res. Part II Top. Stud. Oceanogr. 52, 383–408. https://doi.org/10.1016/j.dsr2.2004.05.025

Shimobe, S., Spagnoli, G., 2019. A global database considering Atterberg limits with the Casagrande and fall-cone tests. Eng. Geol. 260, 105201. https://doi.org/10.1016/j.enggeo.2019.105201

Sibson, R.H., 1990. Conditions for fault-valve behaviour. Geol. Soc. London, Spec. Publ. 54, 15–28. https://doi.org/10.1144/GSL.SP.1990.054.01.02

Silva, S., Terrinha, P., Matias, L., Duarte, J.C., Roque, C., Ranero, C.R., Geissler, W.H., Zitellini, N., 2017. Micro-seismicity in the Gulf of Cadiz: Is there a link between micro-seismicity, high magnitude earthquakes and active faults? Tectonophysics 717, 226–241. https://doi.org/10.1016/j.tecto.2017.07.026

Singh, A.D., Rai, A.K., Tiwari, M., Naidu, P.D., Verma, K., Chaturvedi, M., Niyogi, A., Pandey, D., 2015. Fluctuations of Mediterranean Outflow Water circulation in the Gulf of Cadiz during MIS 5 to 7: Evidence from benthic foraminiferal assemblage and stable isotope records. Glob. Planet. Change 133, 125–140. https://doi.org/10.1016/j.gloplacha.2015.08.005

Sleep, N.H., Blanpied, M.L., 1992. Creep, compaction and the weak rheology of major faults. Nature 359, 687–692. https://doi.org/10.1038/359687a0

Solheim, A., Berg, K., Forsberg, C.F., Bryn, P., 2005. The Storegga Slide complex: Repetitive large scale sliding with similar cause and development. Mar. Pet. Geol. 22, 97–107.

https://doi.org/10.1016/j.marpetgeo.2004.10.013

Spinelli, G.A., Mozley, P.S., Tobin, H.J., Underwood, M.B., Hoffman, N.W., Bellew, G.M., 2007. Diagenesis, sediment strength, and pore collapse in sediment approaching the Nankai Trough subduction zone. Bull. Geol. Soc. Am. 119, 377–390. https://doi.org/10.1130/B25920.1

Spinelli, G.A., Saffer, D.M., Underwood, M.B., 2006. Hydrogeologic responses to three-dimensional temperature variability, Costa Rica subduction margin. J. Geophys. Res. Solid Earth 111, 1–15. https://doi.org/10.1029/2004JB003436

Srivastava, S.P., Schouten, H., Roest, W.R., Klitgord, K.D., Kovacs, L.C., Verhoef, J., Macnab, R., 1990. Iberian plate kinematics: A jumping plate boundary between Eurasia and Africa. Nature 344, 756–759. https://doi.org/10.1038/344756a0

Stich, D., Mancilla, F. de L., Morales, J., 2005. Crust-mantle coupling in the Gulf of Cadiz (SW-Iberia). Geophys. Res. Lett. 32, 1–4. https://doi.org/10.1029/2005GL023098

Stich, D., Mancilla, F. de L., Pondrelli, S., Morales, J., 2007a. Source analysis of the February 12th 2007, Mw 6.0 Horseshoe earthquake: Implications for the 1755 Lisbon earthquake. Geophys. Res. Lett. 34, L12308. https://doi.org/10.1029/2007GL030012

Stich, D., Mancilla, F. de L., Pondrelli, S., Morales, J., 2007b. Source analysis of the February 12th 2007, Mw 6.0 Horseshoe earthquake: Implications for the 1755 Lisbon earthquake. Geophys. Res. Lett. 34, 1–5. https://doi.org/10.1029/2007GL030012

Stigall, J., Dugan, B., 2010. Overpressure and earthquake initiated slope failure in the Ursa region, northern Gulf of Mexico. J. Geophys. Res. 115, B04101. https://doi.org/10.1029/2009JB006848

Stow, D.A.V., Faugères, J.C., Gonthier, E., 1986. Facies distribution and textural variation in Faro Drift contourites: Velocity fluctuation and drift growth. Mar. Geol. 72, 71–100. https://doi.org/10.1021/ma981754p

Stow, D.A.V., Faugères, J.C., Howe, J.A., Pudsey, C.J., Viana, A.R., 2002. Bottom currents, contourites and deep-sea sediment drifts: Current state-of-the-art. Geol. Soc. Mem. 22, 7–20. https://doi.org/10.1144/GSL.MEM.2002.022.01.02

Stow, D.A.V., Hernández-Molina, F.J., Alvarez Zarikian, C.A., 2013a. Site U1391. Proc. Integr. Ocean Drill. Progr. 339. https://doi.org/10.2204/iodp.proc.339.109.2013

Stow, D.A.V., Hernández-Molina, F.J., Llave, E., Bruno, M., García, M., Díaz del Rio, V., Somoza, L., Brackenridge, R.E., 2013b. The Cadiz Contourite Channel: Sandy contourites, bedforms and dynamic current interaction. Mar. Geol. 343, 99–114. https://doi.org/10.1016/j.margeo.2013.06.013

Stow, D.A.V., Hernández-Molina, F.J., Llave, E., Sayago-Gil, M., Díaz-del Río, V., Branson, A., 2009. Bedform-velocity matrix: The estimation of bottom current velocity from bedform observations. Geology 37, 327–330. https://doi.org/10.1130/G25259A.1

Strout, J.M., Tjelta, T.I., 2005. In situ pore pressures: What is their significance and how can they be reliably measured? Mar. Pet. Geol. 22, 275–285. https://doi.org/10.1016/j.marpetgeo.2004.10.024

Sultan, N., 2007. Excess Pore Pressure and Slope Failures Resulting From Gas-Hydrates Dissociation and Dissolution, in: Offshore Technology Conference. https://doi.org/10.4043/18532-ms

Sultan, N., Cochonat, P., Canals, M., Cattaneo, A., Dennielou, B., Haflidason, H., Laberg, J.S., Long, D., Mienert, J., Trincardi, F., Urgeles, R., Vorren, T.O., Wilson, C., 2004a. Triggering mechanisms of slope instability processes and sediment failures on continental margins: A geotechnical approach. Mar. Geol. https://doi.org/10.1016/j.margeo.2004.10.011

Sultan, N., Cochonat, P., Foucher, J.P., Mienert, J., 2004b. Effect of gas hydrates melting on seafloor slope instability. Mar. Geol. 213, 379–401. https://doi.org/10.1016/j.margeo.2004.10.015

Sultan, N., Lafuerza, S., 2013. In situ equilibrium pore-water pressures derived from partial piezoprobe dissipation tests in marine sediments. Can. Geotech. J. 50, 1294–1305. https://doi.org/10.1139/cgj-2013-0062

Sultan, N., Marsset, B., Ker, S., Marsset, T., Voisset, M., Vernant, A.M., Bayon, G., Cauquil, E., Adamy, J., Colliat, J.L., Drapeau, D., 2010. Hydrate dissolution as a potential mechanism for pockmark formation in the Niger delta. J. Geophys. Res. Solid Earth 115, 1–33. https://doi.org/10.1029/2010JB007453

Takagi, H., Pratama, M.B., Kurobe, S., Esteban, M., Aránguiz, R., Ke, B., 2019. Analysis of generation and arrival time of landslide tsunami to Palu City due to the 2018 Sulawesi earthquake. Landslides 983–991. https://doi.org/10.1007/s10346-019-01166-y

Talling, P., Clare, M., Urlaub, M., Pope, E., Hunt, J., Watt, S., 2014. Large Submarine Landslides on Continental Slopes: Geohazards, Methane Release, and Climate Change. Oceanography 27, 32–45. https://doi.org/10.5670/oceanog.2014.38

Talling, P.J., 2014. On the triggers, resulting flow types and frequencies of subaqueous sediment density flows in different settings. Mar. Geol. 352, 155–182. https://doi.org/10.1016/j.margeo.2014.02.006

Talling, P.J., Paull, C.K., Piper, D.J.W., 2013. How are subaqueous sediment density flows triggered, what is their internal structure and how does it evolve? Direct observations from monitoring of active flows. Earth-Science Rev. 125, 244–287. https://doi.org/10.1016/j.earscirev.2013.07.005

Tanaka, H., Locat, J., 1999. A microstructural investigation of Osaka Bay clay: the impact of microfossils on its mechanical behaviour. Can. Geotech. J. 36, 493–508. https://doi.org/10.1139/t99-009

Teixeira, M., Terrinha, P., Roque, C., Rosa, M., Ercilla, G., Casas, D., 2019. Interaction of alongslope and downslope processes in the Alentejo Margin (SW Iberia) – Implications on slope stability. Mar. Geol. 410, 88–108. https://doi.org/10.1016/j.margeo.2018.12.011

Teixeira, M., Terrinha, P., Roque, C., Voelker, A.H.L., Silva, P., Salgueiro, E., Abrantes, F., Naughton, F., Mena, A., Ercilla, G., Casas, D., 2020. The Late Pleistocene-Holocene sedimentary evolution of the Sines Contourite Drift (SW Portuguese Margin): A multiproxy approach. Sediment. Geol. 407, 105737. https://doi.org/10.1016/j.sedgeo.2020.105737

Terrinha, P., Matias, L., Vicente, J., Duarte, J., Luís, J., Pinheiro, L., Lourenço, N., Diez, S., Rosas, F., Magalhães, V., Valadares, V., Zitellini, N., Roque, C., Víctor, L.M., 2009. Morphotectonics and strain partitioning at the Iberia-Africa plate boundary from multibeam and seismic reflection data. Mar. Geol. 267, 156–174. https://doi.org/10.1016/j.margeo.2009.09.012

Terrinha, P., Pinheiro, L.M., Henriet, J.P., Matias, L., Ivanov, M.K., Monteiro, J.H., Akhmetzhanov, A., Volkonskaya, A., Cunha, T., Shaskin, P., Rovere, M., 2003. Tsunamigenic-seismogenic structures, neotectonics, sedimentary processes and slope instability on the southwest Portuguese Margin. Mar. Geol. 195, 55–73. https://doi.org/10.1016/S0025-3227(02)00682-5

Terrinha, P., Ribeiro, C., Kullberg, J.C., Lopes, C., Rocha, R., Ribeiro, A., 2002. Compressive episodes and faunal isolation during rifting, Southwest Iberia. J. Geol. 110, 101–113. https://doi.org/10.1086/324206

Terzaghi, K., 1926. Principles of soil mechanics: A summary of experimental studies of clay and sand. McGraw-Hill.

Tessarolo, L. de F., Innocentini, V., Barreto, F.T.C., Gonçalves, I.A., 2021. Formation, dissolution, and decomposition of gas hydrates in a numerical model for oil and gas from deepwater blowouts. Mar. Pollut. Bull. 165, 112103. https://doi.org/10.1016/j.marpolbul.2021.112103

TGS, 2005. PD00: Non-exclusive 2D Survey. Acquisition Parameters. https://map.tgs.com/specsheets/PD-00_Spec.pdf 1–2.

Thorpe, S.A., 1975. Variability of the mediterranean undercurrent in the Gulf of Cadiz. Deep Sea Res. Oceanogr. Abstr. 23, 711-IN1. https://doi.org/10.1016/s0011-7471(76)80016-2

Tømmerås, A., Sylta, Ø., Daszinnies, M.C., Mencaroni, D., 2018. Prewell and postwell predictions of oil and gas columns using an iterative Monte Carlo technique with three-dimensional petroleum systems modeling. Am. Assoc. Pet. Geol. Bull. 102, 545–547. https://doi.org/10.1306/0503171616717078

Tréhu, A.M., Long, P.E., Torres, M.E., Bohrmann, G., Rack, F.R., Collett, T.S., Goldberg, D.S., Milkov, A. V., Riedel, M., Schultheiss, P., Bangs, N.L., Barr, S.R., Borowski, W.S., Claypool, G.E., Delwiche, M.E., Dickens, G.R., Gracia, E., Guerin, G., Holland, M., Johnson, J.E., Lee, Y.J., Liu, C.S., Su, X., Teichert, B., Tomaru, H., Vanneste, M., Watanabe, M., Weinberger, J.L., 2004. Three-dimensional distribution of gas hydrate beneath southern Hydrate Ridge: Constraints from ODP Leg 204. Earth Planet. Sci. Lett. 222, 845–862. https://doi.org/10.1016/j.epsl.2004.03.035

Urgeles, R., Camerlenghi, A., 2013. Submarine landslides of the Mediterranean Sea: Trigger mechanisms, dynamics, and frequency-magnitude distribution. J. Geophys. Res. Earth Surf. 118, 2600–2618. https://doi.org/10.1002/2013JF002720

Urgeles, R., Canals, M., Roberts, J., 2000. Fluid flow from pore pressure measurements off La Palma, Canary Islands. J. Volcanol. Geotherm. Res. 101, 253–271. https://doi.org/10.1016/S0377-0273(00)00176-1

Urgeles, R., Leynaud, D., Lastras, G., Canals, M., Mienert, J., 2006. Back-analysis and failure mechanisms of a large submarine slide on the ebro slope, NW Mediterranean. Mar. Geol. 226, 185–206. https://doi.org/10.1016/j.margeo.2005.10.004

Urgeles, R., Locat, J., Dugan, B., 2007. Recursive Failure Of The Gulf Of Mexico Continental Slope: Timing And Causes, in: Lykousis, V., Sakellariou, D., Locat, J. (Eds.), Submarine Mass Movements and Their Consequences. Springer Netherlands, Dordrecht, pp. 209–219. https://doi.org/10.1007/978-1-4020-6512-5_22

Urgeles, R., Locat, J., Sawyer, D.E., Flemings, P.B., Dugan, B., Binh, N.T.T., 2010. History of Pore Pressure Build Up and Slope Instability in Mud-Dominated Sediments of Ursa Basin, Gulf of Mexico Continental Slope BT - Submarine Mass Movements and Their Consequences, in: Mosher, D.C., Shipp, R.C., Moscardelli, L., Chaytor, J.D., Baxter, C.D.P., Lee, H.J., Urgeles, R. (Eds.), Submarine Mass Movements and Their Consequences. Springer Netherlands, Dordrecht, pp. 179–190. https://doi.org/10.1007/978-90-481-3071-9_15

Urgeles, R., Shipboard Scientific Party, 2019. INSIGHT-Leg2 Cruise Report.

Urlaub, M., 2013. The role of sedimentation rate on the stability of low gradient submarine continental slopes. Ph.D 188.

Urlaub, M., Talling, P.J., Masson, D.G., 2013. Timing and frequency of large submarine landslides: Implications for understanding triggers and future geohazard. Quat. Sci. Rev. 72, 63–82. https://doi.org/10.1016/j.quascirev.2013.04.020

Urlaub, M., Talling, P.J., Zervos, A., Masson, D.G., 2015. What causes large submarine landslides on low gradient (<2∘) continental slopes with large submarine landslides on low gradient (<2∘) continental slopes with slow (~0.15 m/kyr) sediment gradient (<2∘) continental slopes with slow (~0.15 m/kyr) sediment ac. J. Geophys. Res. Solid Earth 120,

1–18. https://doi.org/10.1002/2015JB012347.Received

Urlaub, M., Zervos, A., Talling, P.J., Masson, D.G., Clayton, C.I., 2012. How Do ~2° Slopes Fail in Areas of Slow Sedimentation? A Sensitivity Study on the Influence of Accumulation Rate and Permeability on Submarine Slope Stability, in: Yamada, Y., Kawamura, K., Ikehara, K., Ogawa, Y., Urgeles, R., Mosher, D., Chaytor, J., Strasser, M. (Eds.), Submarine Mass Movements and Their Consequences. Springer Netherlands, Dordrecht, pp. 277–287. https://doi.org/10.1007/978-94-007-2162-3_25

Van Hinte J. E., 1978. Geohistory Analysis--Application of Micropaleontology in Exploration Geology. Am. Assoc. Pet. Geol. Bull. 62, 201–222. https://doi.org/10.1306/c1ea4815-16c9-11d7-8645000102c1865d

Vanoudheusden, E., Sultan, N., Cochonat, P., 2004. Mechanical behaviour of unsaturated marine sediments: Experimental and theoretical approaches. Mar. Geol. 213, 323–342. https://doi.org/10.1016/j.margeo.2004.10.012

Vatandoost, A., Fullagar, P., Walters, S., Kojovic, T., 2009. Towards Petrophysical Characterization of Comminution Behavior. 41st Annu. Meet. Can. Miner. Process.

Veeken, P.C.H., 2007. Seismic stratigraphy, basin analysis and reservoir characterisation, 1st ed. ed, Handbook of Geophysical Exploration, Handbook of geophysical exploration. Seismic exploration. Elsevier, Amsterdam ; Boston. https://doi.org/10.1016/S0950-1401(07)80025-5

Viana, A.R., Rebesco, M., 2007. Economic and Palaeoceanographic Significance of Contourite Deposits. Geological Society, London.

Viesca, R.C., Rice, J.R., 2012. Nucleation of slip-weakening rupture instability in landslides by localized increase of pore pressure. J. Geophys. Res. Solid Earth 117, 1–21. https://doi.org/10.1029/2011JB008866

Vizcaino, A., Gràcia, E., Pallàs, R., Garcia-Orellana, J., Escutia, C., Casas, D., Willmott, V., Diez, S., Asioli, A., Dañobeitia, J., 2006. Sedimentology, physical properties and age of mass transport deposits associated with the Marquês de Pombal Fault, Southwest Portuguese Margin. Nor. Geol. Tidsskr. 86, 177–186. https://doi.org/ISI:000242300000004

Voelker, A.H.L., Jimenez-espejo, F.J., Bahr, A., Acton, G.D., Rebotim, A., Röhl, U., Escutia, C., 2014. Mediterranean Outflow Water changes in the Gulf of Cadiz during the Mid-Pleistocene Transition – The role of insolation. pp. 2013–2014.

Voelker, A.H.L., Salgueiro, E., Rodrigues, T., Jimenez-Espejo, F.J., Bahr, A., Alberto, A., Loureiro, I., Padilha, M., Rebotim, A., Röhl, U., 2015. Mediterranean Outflow and surface water variability off southern Portugal during the early Pleistocene: A snapshot at Marine Isotope Stages 29 to 34 (1020-1135ka). Glob. Planet. Change 133, 223–237. https://doi.org/10.1016/j.gloplacha.2015.08.015

Volpi, V., Camerlenghi, A., Hillenbrand, C.D., Rebesco, M., Ivaldi, R., 2003. Effects of biogenic silica on sediment compaction and slope stability on the Pacific margin of the Antarctic Peninsula. Basin Res. 15, 339–363. https://doi.org/10.1046/j.1365-2117.2003.00210.x

Wang, K., Davis, E.E., 1996. Theory for the propagation of tidally induced pore pressure variations in layered subseafloor formations. J. Geophys. Res. B Solid Earth 101, 11483–11495. https://doi.org/10.1029/96jb00641

Wangen, M., 1997. A simple model of pressure build-up caused by porosity reduction during burial. Geophys. J. Int. 130, 757–764. https://doi.org/10.1111/j.1365-246X.1997.tb01870.x

Wentworth, C.K., 1922. A Scale of Grade and Class Terms for Clastic Sediments. J. Geol. 30, 377–392. https://doi.org/10.1086/622910

Westercamp, D., d'Archimbaud, J.D., de Lapparent, A.F., Marinelli, G., Tazieff, H., Brousse, R.,

1972. Contribution à l'étude du volcanisme en Martinique.

Wiemer, G., Kopf, A., 2015. Altered marine tephra deposits as potential slope failure planes? Geo-Marine Lett. 35, 305–314. https://doi.org/10.1007/s00367-015-0408-4

Winker, C.D., Booth, J.R., 2000. Sedimentary dynamics of the salt-dominated continental slope, Gulf of Mexico: Integration of observations from the seafloor, near surface, and deep surface, in: Weimer, P., Slatt, R.M., Coleman, J., Rosen, N.C., Nelson, H., Bouma, A.H., Styzen, M.J., Lawrence, D.T. (Eds.), Deep-Water Reservoirs of the World: SEPM Gulf Coast Section 20th Annual Research Conference. pp. 1059–1086.

Worrall, D.M., Snelson, S., 1989. Evolution of the northern Gulf of Mexico, with emphasis on Cenozoic growth faulting and the role of salt, in: Bally, A.W., Paler, A.R. (Eds.), The Geology of North America—An Overview (Vol A). Geological Society of America, Boulder,.

Wynn, R.B., Stow, D.A.V., 2002. Classification and characterisation of deep-water sediment waves. Mar. Geol. 192, 7–22. https://doi.org/10.1016/S0025-3227(02)00547-9

Yu, X., Stow, D., Smillie, Z., Esentia, I., Brackenridge, R., Xie, X., Bankole, S., Ducassou, E., Llave, E., 2020. Contourite porosity, grain size and reservoir characteristics. Mar. Pet. Geol. 117, 104392. https://doi.org/10.1016/j.marpetgeo.2020.104392

Zachos, J., Pagani, H., Sloan, L., Thomas, E., Billups, K., 2001. Trends, rhythms, and aberrations in global climate 65 Ma to present. Science (80-.). 292, 686–693. https://doi.org/10.1126/science.1059412

Zitellini, N., Berton, E., Bortoluzzi, G., Calafato, N., Centorami, G., Chierici, F., Landuzzi, V., Ligi, M., Penitenti, D., Scipionii, E., Rovere, M., Casoni, L., Correggiari, A., Magagnoli, A., Marozzi, G., Vigliotti, L., Jornet, P., Rodriguez, P., Thompson, I., Zahinos, A., Bartolome, R., Gracia, E., Terrinha, P., Ribeiro, A.C.N.-G.-G.-T. 1.-6383, 2010. PROJECT BIGSETS: REPORT ON SEISMIC AND MAGNETIC INVESTIGATIONS DURING CRUISE BS98 WITH R/V Urania. Rapp. Ismar 17.

Zitellini, N., Chierici, F., Sartori, R., Torelli, L., 1999. The tectonic source of the 1755 Lisbon earthquake and tsunami. Ann. Di Geofis.

Zitellini, N., Gràcia, E., Matias, L., Terrinha, P., Abreu, M.A., De Alteriis, G., Henriet, J.P., Dañobeitia, J.J., Masson, D.G., Mulder, T., Ramella, R., Somoza, L., Diez, S., 2009. The quest for the Africa-Eurasia plate boundary west of the Strait of Gibraltar. Earth Planet. Sci. Lett. 280, 13–50. https://doi.org/10.1016/j.epsl.2008.12.005

Zitellini, N., Ligi, M., Matias, L., Rovere, M., Shipboard Scientific Party, 2002. VOLTAIRE 2002 Cruise Report.

Zitellini, N., Mendes, L.A., Cordoba, D., Danobeitia, J., Nicolich, R., Pellis, G., Ribeiro, A., Sartori, R., Torelli, L., Bartolome, R., Bortoluzzi, G., Calafato, A., Carrilho, F., Casoni, L., Chierici, E., Corela, C., Correggiari, A., Delia Vedova, B., Gracia, E., Jornet, P., Landuzzi, M., Ligi, M., Magagnoli, A., Marozzi, G., Matias, L., Penitenti, D., Rodriguez, P., Rovere, M., Terrinha, P., Vigliotti, L., Ruiz, A.Z., 2001. Source of 1755 lisbon earthquake and tsunami investigated. Eos (Washington. DC). 82, 285–291. https://doi.org/10.1029/EO082i026p00285-01

Zitellini, N., Rovere, M., Terrinha, P., Chierici, F., Matias, L., Victor, L.M., Corela, C., Ribeiro, A., Cordoba, D., Danobeitia, J.J., Grácia, E., Bartolomé, R., Nicolich, R., Pellis, G., Della Vedova, B., Sartori, R., Torelli, L., Correggiari, A., Vigliotii, L., 2004. Neogene through quaternary tectonic reactivation of SW Iberian passive margin. Pure Appl. Geophys. 161, 565–587. https://doi.org/10.1007/s00024-003-2463-4